UNIVERSITY OF CALIFORNIA, SAN DIEGO

Mechanical Properties of Semiconducting Polymers

A Dissertation submitted in partial satisfaction of the requirements for the degree of Doctor of Philosophy

in

Chemical Engineering

by

Samuel E. Root

Committee in charge:

Professor Darren Lipomi, Chair
Professor Michael Gilson
Professor Ying Shirley Meng
Professor Tse Nga Ng
Professor Shyue Ping Ong

2018

This Dissertation of Samuel E. Root is approved, and it is acceptable in quality and form for publication on microfilm and electronically:

_____

_____

_____

_____

_____

Chair

University of California, San Diego

2018

DEDICATION

This thesis is dedicated to Grandpa Mo.

ת ק וע לם

TABLE OF CONTENTS

LIST OF FIGURES

LIST OF TABLES

LIST OF IMAGES

ACKNOWLEDGEMENTS

Thank you. For my entire life, I have had the good fortune of being surrounded by a close circle of family and friends. It is with sincere gratitude that I thank everyone in my life for all the support that they have provided for me. I am lucky to have all of you and I would not have gotten this far without you.

Siblings. Since before I can remember I've been the middle child of a tight-knit crew of 'rootlets.' My three siblings: Zach, Jared, and Sara have been my built-in best friends and partners in crime. My older brother, Zach, helped to toughen me, giving me thick skin and teaching me street-smarts. My little brother, Jared, through unshakable morality, showed me how to be just and fair. And my little sister, Sara, through unwavering sweetness and empathy, showed me how to be kind and understanding. My central position as the middle child of this cohort is likely where my independence as an individual and a scientist came from.

Parents. Having four children within three years is no small challenge for two parents to handle, but I am thankful to my parents for doing so. It is without question that my Mom and Dad have been the most important role models in my life. They have made so many sacrifices to ensure that my siblings and I have all received the best possible education and opportunities. My Dad passed along his creative and artistic spirit, along with an even-handed temperament a relaxed personality. My Mom passed along her incredible work ethic and frugality, endowing me with a set of values that were built upon hard work, rather than material possessions and social standing. My decision to pursue a

Ph. D. in the first place hinged on the fact that Mom knew me better than I did, and convinced me that a Ph. D. was the right career path for me.

Family. Of my extended family, there have been two important figures in my life that have directed me towards a scientific style of thinking: Grandpa Mo and Uncle Beamer. My Grandpa Mo immigrated to New York from Israel as a teenager. He came here looking for a better life and worked hard as an airplane mechanic—when he quite clearly should have been an aerospace engineer. The hard work and sacrifices that he made are what made my education as an engineer possible. The mechanical/tinkering skills that he taught me from a young age ended up being much more valuable for my career than I would have expected when he first taught me how to fix a flat tire on my bicycle. I wish he could have been around to bounce research ideas off. My Uncle Beamer, the department 'chef,' was my first research mentor, when I volunteered in his hospital during high school. He has been a constant source of support and advice throughout my life.

Friends. Throughout high school, college and my Ph. D., I have always been surrounded by a great group of friends. I am greatly indebted Mark Biatreh, Steven Wald, Ayal Gabbay, Michael Saulle, Donovan Van Eetveldt and many more friends for listening to me incessantly prattle on about whatever scientific topic I was interested in at the time.

University of Rochester. During my time at University of Rochester, I had the opportunity to work as a researcher in two academic laboratories. I am grateful to Professor Alexander Shestopalov, and Kenneth Marshall for mentoring me and providing me with my first real research experiences. While working with Ken's group at the Laboratory for

Laser Energetics, I had the great pleasure of working alongside Abbas Shikari, whom I know will remain a close friend and colleague for the rest of my life.

Darren. I will never forget the day that I received my first email from Darren Lipomi. I was sitting in my stat. mech. class at the time and I was so excited to hear from him that I immediately left the class and called my Mom. Darren gave me the opportunity of a lifetime: a reason to move to California, and a position doing the exact type of research that I wanted in a highly-collaborative group with a diverse and fun team. Over the past four years Darren and I have built a close relationship upon our mutual love for molecules. My thesis research has mainly originated from conversations we had while running ~1000 miles together on the beach. Darren has been a constant source of both professional and personal mentorship, helping me to grow as a researcher and a person. He has taught me how to effectively communicate the motivation, results, and implications of my research. He also got me started on the path to meditation and mindfulness which well be important to maintain a balance during my future research career. I am excited to see where the Lipomi Lab will go from here, I expect big things.

The Lipomi Group. It is a rare and precious experience to be a part of a cohesive team, where there is a level of trust, comfort, and comradery that allows for collaboration without conflict or competition. I was extremely fortunate to join the Lipomi Lab at the time that I did. I was welcomed with open arms by TimM O'Connor, Suchol Savagatrup, Adam Printz, and Alex Zaretski, who immediately made me feel right at home within the lab. TimM (AKA Momma TimM) added me to his well-developed social circle in San Diego, allowing me to forgo that awkward first month of trying to find some friends in a

new place. We were close friends throughout my entire stay in San Diego and went on some wild adventures. Suchol and Adam were my guides to the vast literature, status quo, and experimental considerations surrounding the mechanical of semiconducting polymers. They both helped me to plan my theoretical research and push forward on this important and interesting topic. Alex was an important mentor for me in the laboratory where he taught me many pro-tips and helped guide me through my first experimental project in the Lipomi Lab.

Collaborators. Collaboration is one of the main reason that I enjoy research. While working in the Lipomi Lab I have had the privilege of collaborating with many inspiring researchers. When I started my thesis research I had no formal experience doing any kind of computational research. Right from the start, Professor Gaurav Arya took me under his wing and gave me important guidance that allowed me to learn how to make molecular dynamics simulations and design computational experiments. Gaurav would meet with me weekly to discuss my progress and help plan the next steps. The discussions we had helped to broaden my view on computational theory and its place in scientific research as a whole. I would also like to thank Nicholas Jackson, for all of the help he provided with my atomistic simulations.

After two initial years of doing purely computational work, I decided that I wanted to get back into the laboratory. This transition required a lot of help from many individuals. I would like to sincerely thank Suchol Savagatrup, Daniel Rodriquez, Alex Zaretski, and Brandon Marin for helping me to get up to speed and comfortable working in the lab. Suchol and Daniel taught me many of the techniques and processes surround mechanical

characterization. Alex and Brandon taught me about many important nanofabrication processes and characterization techniques related to the nanoislands and barriers projects. (Brandon also gets a special shout out for distracting me to go snatch some crumbs, breath through my mouth, toot it and boot it, etc.) I would also like to thank Andrew Kleinschmidt for taking over as the computational specialist within the group, I know you will make some beautiful simulations and I hope that you keep your eye out for other interesting oscillations that could occur in the correlation functions. I would also like to thank the group members who joined the group after me and helped me to finish up my PhD strongly. Thank you to Laure Kayser for teaching me about chemistry and synthesis. Thank you to Cody Carpenter for teaching me to surf, showing me how to shock myself (safely) and helping me to lead a balanced life outside of research. Thank you to Mickey Finn, Julian Ramirez, and Charles Dhong for always being available and eager to help troubleshoot technical issues and just generally helping out around the lab. Finally, thank you to Rory Runser for taking over the interfacial drawing and barrier project for me, I hope you make the first solar tarp!

Over the past couple of years, I have also received a lot of mentorship, advice, and direction from faculty members in the department. I would like to thank Prof. Vlado Lubarda for the discussions we had on mechanics: they were valuable in cementing my understanding of the subject. I would also like to thank all of my committee members for their suggestions and encouragement. Finally, I want to thank Tod Pascal for helping to sharpen my blade the day before my defense, I wish we had more overlapping time here for collaboration.

Another reason I enjoy research is mentorship. Over the past three years I have had the honor of mentoring several skilled younger researchers. C.J. Pais was my first hire. With his computer science background, he helped me to turn my initial code into reusable and modular software allowing me to spend less time on coding and more time in the lab. I met Mohammad Alkhadra (aka Mo aka Big Mo $$) in the polymeric materials class that I was the TA for. He always aksed me the most challenging questions and spurred the best discussions in office hours. It was only when I hired Mo that I truly realized how savage he actually was. The speed in which Mo picked up experimental skills and completed tasks was unparalleled. I've never seen anybody work as hard as he did during his first year as a researcher. Mo's discipline, focus, and attention-to-detail have become standards that I strive to emulate in the future. I can't wait to see what he accomplishes as a doctoral student. I'm not sure how I will continue to write papers without your sharp eye for grammatical mistakes. Finally, I would also like to thank Kristan Hilby, Derick Ober, Armando Urbina, and Eden Alkile for all their help performing experiments and working in the lab.

Chapter 1, in full, is a reprint of the material as it appears in *Chemical Reviews*, 2017, 117, 6467-6499. The American Chemical Society, 2017. Samuel E. Root, Suchol Savagatrup, Adam D. Printz, Daniel Rodriquez, and Darren J. Lipomi. The dissertation author was the primary author of this paper.

Chapter 2, in full, is a reprint of the material as it appears in *Macromolecules*, 2016, 49, 2866-2894. The American Chemical Society, 2016. Samuel E. Root, Suchol

Savagatrup, Christopher J. Pais, Gaurav Arya, and Darren J. Lipomi. The dissertation author was the primary investigator and author of this paper.

Chapter 3, in full, is a reprint of the material as it appears in *Energy & Environmental Sciences*, 2017, 10, 558-569. The Royal Society of Chemistry, 2017. Samuel E. Root, Nicholas E. Jackson, Suchol Savagatrup , Gaurav Arya, and Darren J. Lipomi. The dissertation author was the primary investigator and author of this paper.

Chapter 4, in full, is a reprint of the material as it appears in *Chemistry of Materials*, 2017, 28, 2646-2654. The American Chemical Society, 2017. Samuel E. Root,‡ Mohammad A. Alkhadra,‡ Daniel Rodriquez, Adam D. Printz, and Darren J. Lipomi (‡ Equal contribution). The dissertation author was a primary investigator and author of this paper.

Chapter 5, in full, is a reprint of the material as it appears in *Chemistry of Materials*, 2017, 29, 10139–10149. The American Chemical Society, 2017. Mohammad A. Alkhadra,† Samuel E. Root,† Kristan M. Hilby, Daniel Rodriquez, Fumitaka Sugiyama, and Darren J. Lipomi*(† Equal contribution). The dissertation author was a primary investigator and author of this paper.

VITA

2014	Bachelor of Science in Chemical Engineering, University of Rochester
2016	Master of Science in Chemical Engineering, University of California, San Diego
2014–2018	Graduate Researcher, University of California, San Diego
2018	Doctor of Philosophy in Chemical Engineering, University of California, San Diego

PUBLICATIONS

Root, S. E.; Carpenter, C.W.; Kayser, L. V.; Rodriquez, D.; Davies, D. M.; Wang, S.; Tan, S. T. M.; Meng, Y. S.; Lipomi, D. J. Ionotactile Stimulation: Ionic Gels for Haptic Human-Machine Interfaces *ACS Omega* **2018**, 3, 662-666

Alkhadra, M. A.; **Root, S. E.;** Hilby, K. M.; Rodriquez, D.; Sugiyama, F.; Lipomi, D. J. Quantifying the Fracture Behavior of Brittle and Ductile Thin Films of Semiconducting Polymers. **2017**, *29*, 10139–10149.

Marin, B. C.; Ramirez, J.; **Root, S. E.**, Aklile, E.; Lipomi, D. J. Metallic Nanoislands on Graphene: A Metamaterial for Chemical, Mechanical, Optical, and Biological Applications. *Nanoscale Horizons* **2017**, 2, 311-318

O'Connor, T. F.; Fach, M. E.; Miller, R.; **Root, S. E**.; Mercier, P. P.; Lipomi, D. J. The Language of Glove: Wireless gesture decoder with low-power and stretchable hybrid electronics *PloS one* **2017**, 12, 1-12

Root, S. E.; Savagatrup, S.; Printz, A. D.; Rodriquez, D.; Lipomi, D. J. Mechanical Properties of Organic Semiconductors for Stretchable, Highly Flexible, and Mechanically Robust Electronics. *Chemical Reviews* **2017**, 117, 6467- 6499

Root, S. E.; Alkhadra, M. A.; Rodriquez, D.; Printz, A. D.; Lipomi, D. J. Measuring the Glass Transition Temperature of Conjugated Polymer Films with Ultraviolet-Visible Spectroscopy. *Chemistry of Materials* **2017**, 28, 2646-2654

Rodriquez, D.; Kim, J.H.; **Root, S. E.**; Fei, Z.; Boufflet, P.; Heeney, M.; Kim, T. S.; Lipomi, D. J. Comparison of Methods for Determining the Mechanical Properties of Semiconducting Polymer Films for Stretchable Electronics *Applied Materials & Interfaces* **2017**, 9, 8855-8862.

Marin, B. C.; **Root, S. E.**; Urbina, A. D.; Alklile, E.; Miller, R.; Zaretski, A. V.; Lipomi, D. J. Graphene-Metal Composites with Near-Zero Temperature Coefficient of Resistance *ACS Omega* **2017**, 2, 626-630.

Root, S. E.; Jackson, N. E.; Savagatrup, S.; Arya, G.; Lipomi, D. J. Modelling the Morphology and Mechanical Behaviour of Low-Bandgap Conjugated Polymers and Bulk Heterojunction Films. *Energy & Environmental Science* **2017**, 10, 558-569

Kleinschmidt, A. T.; **Root, S. E.**; Lipomi, D. J. Poly (3-hexylthiophene) (P3HT): Fruit Fly or Outlier in Organic Solar Cell Research? *Journal of Materials Chemistry A* **2017**, 5, 11396-11400

Root, S. E.; Savagatrup, S.; Pais, C. J.; Arya, G.; Lipomi, D. J. Predicting the Mechanical

Properties of Organic Semiconductors Using Coarse-Grained Molecular Dynamics Simulations. *Macromolecules* **2016**, 49, 2886-2894

Zaretski, A. V.; **Root, S. E.**; Savchenko, A.; Molokanova, E.; Printz, A. D.; Jibril, L.; Arya, G.; Mercola, M.; Lipomi, D. J. Metallic Nanoislands on Graphene as Highly Sensitive Transducers of Mechanical, Biological, and Optical Signals. *Nano Letters* **2016**,16, 1375-1380

Savagatrup, S.; Printz, A. D.; O'Connor, T. F.; Zaretski, A. V.; Rodriquez, D.; Sawyer, E. J.; Rajan, K. M.; Acosta, R. I.; **Root, S. E.**; Lipomi, D. J. Mechanical Degradation and Stability of Organic Solar Cells: Molecular and Microstructural Determinants. *Energy & Environmental Science* **2015**, *8*, 55–80.

ABSTRACT OF THE DISSERTATION

Mechanical Properties of Semiconducting Polymers

by

Samuel E. Root

Doctor of Philosophy in Chemical Engineering

University of California, San Diego, 2018

Professor Darren J. Lipomi, Chair

Mechanical softness and deformability underpin most of the advantages offered by semiconducting polymers. A detailed understanding of the mechanical properties of these materials is crucial for the design and manufacturing of robust, thin-film devices such as solar cells, displays, and sensors. The mechanical behavior of polymers is a complex function of many interrelated factors that span multiple scales, ranging from molecular

structure, to microstructural morphology, and device geometry. This thesis builds a comprehensive understanding of the thermomechanical properties of polymeric semiconductors through the development and experimental-validation of computational methods for mechanical simulation. A predictive computational methodology is designed and encapsulated into open-sourced software for automating molecular dynamics simulations on modern supercomputing hardware. These simulations are used to explore the role of molecular structure/weight and processing conditions on solid-state morphology and thermomechanical behavior. Experimental characterization is employed to test these predictions—including the development of simple, new techniques for rigorously characterizing thermal transitions and fracture mechanics of thin films.

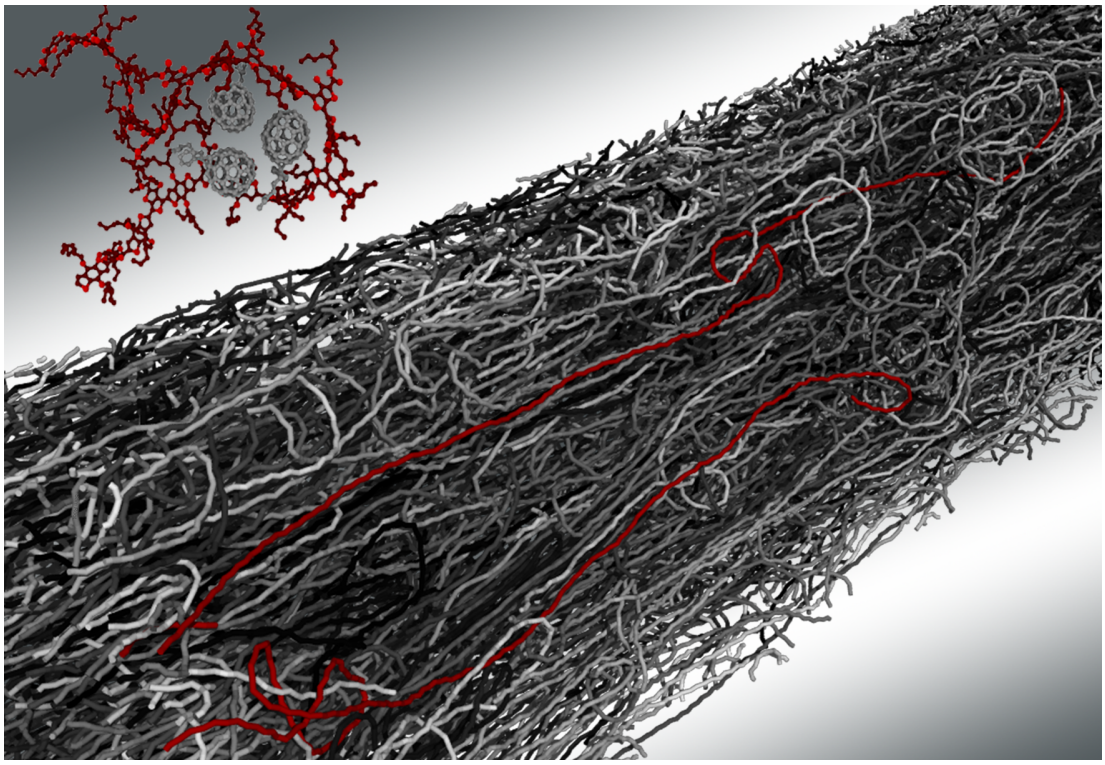

Image 1. Artistic representation of a simulated semiconducting polymer thin film under tensile loading.

Chapter 1

Mechanical Properties of Organic Semiconductors for Stretchable, Highly Flexible, and Mechanically Robust Electronics

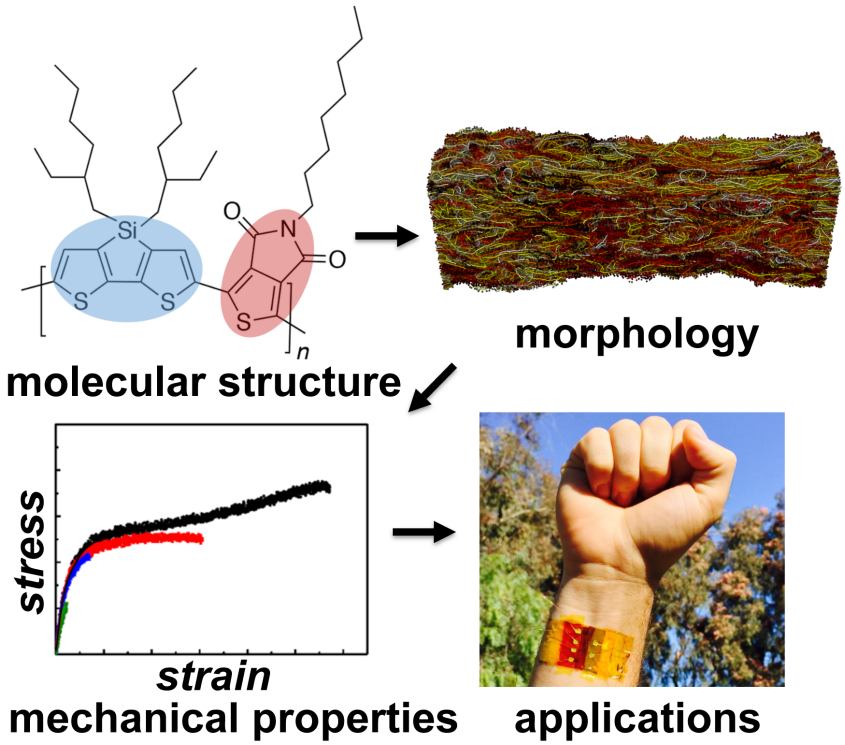

Image 2. Table of contents artwork for Chapter 1. Schematic diagram showing the relevant scales, properties and applications of mechanically robust semiconducting polymers.

Samuel E. Root, Suchol Savagatrup, Adam D. Printz, Daniel Rodriquez, and Darren J. Lipomi

Department of NanoEngineering, University of California, San Diego

9500 Gilman Drive, Mail Code 0448, La Jolla, CA 92093-0448

Abstract

Mechanical deformability underpins many of the advantages of organic semiconductors. The mechanical properties of these materials are, however, diverse, and the molecular characteristics that permit charge transport can render the materials stiff and brittle. This review is a comprehensive description of the molecular and morphological parameters that govern the mechanical properties of organic semiconductors. Attention is paid to ways in which mechanical deformability and electronic performance can coexist. The review begins with a discussion of flexible and stretchable devices of all types, and in particular the unique characteristics of organic semiconductors. It then discusses the mechanical properties most relevant to deformable devices. In particular, it describes how low modulus, good adhesion, and absolute extensibility prior to fracture enable robust performance, along with mechanical "imperceptibility" if worn on the skin. A description of techniques of metrology precedes a discussion of the mechanical properties of three classes of organic semiconductors: π-conjugated polymers, small molecules, and composites. The discussion of each class of materials focuses on molecular structure and how this structure (and postdeposition processing) influences the solid-state packing structure and thus the mechanical properties. The review concludes with applications of organic semiconductor devices in which every component is intrinsically stretchable or highly flexible.

1.1. Introduction

Developments in semiconductor technology have left few aspects of modern life untouched.[1] These developments have been driven by the concerted efforts of chemists, physicists, and engineers over the last fifty years. The fruit of this labor is reflected in an exponential rate of progress, which was identified by Intel's Gordon Moore in 1965.[1,2] Moore predicted that the density of transistors on an integrated circuit would double approximately every two years. The technologies that have enabled this periodic doubling underpins several other exponential improvements, for example, the capacity of memory circuits, the resolution of digital imaging, and the overall cost-per-function of semiconductor devices. The outcome in all cases is an increase in electronic performance. One can imagine, however, analogous trends describing the evolution of other physical parameters of importance for semiconducting devices—not just performance and efficiency derived from miniaturization. One such parameter could be mechanical compliance.[3-5] Development of electronic materials and devices with the goal of deformability, for example, would permit the fabrication of robust devices for portable electronics,[6,7] the production of flexible solar modules[8] and displays[7,9,10] using roll-to-roll printing methodologies,[11,12] and the property of "mechanical invisibility"[13] for wearable[3,14] and implantable[15,16] applications. The research done on rigid semiconductor systems is,[17,18] of course, a prerequisite for deformable electronics to achieve a useful level of function, but mechanical resilience or toughness would be the goal.[19]

One class of materials that since its inception has been associated with flexible, printed electronics is organic semiconductors.[20] In fact, deformability is the characteristic that underpins most touted advantages of organic electronic materials, especially if they are to

be manufactured by roll-to-roll printing.[21-23] While it might be natural to assume that the carbon framework common to all organic molecules would afford some level of softness—by analogy to biological materials—the diversity of structures of organic semiconductors embodies a rich mechanical behavior that is only sometimes best described as "plastic" (in the sense of "deformable").[5] Even semiconducting polymers, whose repeating structures evoke comparisons to engineering plastics, do not exhibit high strength and toughness characteristic of, for example, high molecular weight polyethylene or nylon.[24-27] The requirement that π-conjugated organics still transport charge with efficiency that is comparable to structurally simpler inorganic semiconductors seems to necessitate rigidity in the molecular backbone[28] and assembly into ordered aggregates in the solid state.[29-31] Moreover, the presence of side chains—required for processing from solution—nearly always reduces the cohesion of these materials by reducing strong van der Waals forces that would exist between unsubstituted main chains.[32-34] Mechanical performance is also limited by synthetic procedures. That is, the synthesis of semiconducting polymers often leads to degrees of polymerization that can be both more broadly distributed and significantly smaller than those obtained for commodity polymers and engineering plastics. Low degrees of polymerization are a consequence of the poor solubility of π-conjugated systems with increased molecular weight. Additionally, there are the practical difficulties of combining AA and BB monomers in a ratio of exactly 1:1 (as required by the Carothers equation to achieve high molecular weight) when performing polycondensation reactions at a small scale.[35] Solid samples comprising short polymer chains and high dispersity exhibit reduced densities of entanglements, which limit the cohesion[26] and extensibility.[36]

While it may seem from this discussion that organic semiconductors could never have the excellent thermomechanical properties characteristic of engineering plastics (which are, after all, optimized for some combination of toughness, strength, extensibility, high-temperature operation, and other parameters), there is a reason to be optimistic. That is, in most thin-film devices, the active layer is not responsible for bearing the load. The substrate and encapsulant[37] are usually one or more orders of magnitude thicker than the active material,[38] and are responsible for providing the strength to keep the device intact. Thus, properties that describe the ability of a material to store or dissipate mechanical energy (resilience and toughness) take on significantly less importance for organic semiconductors than for engineering plastics. Instead, the properties that seem to be of increased importance in thin-film organic semiconductors are low tensile modulus in the elastic regime (to minimize interfacial stresses upon deformation and to permit mechanical imperceptibility when worn on the skin[13]) and absolute extensibility prior to fracture. (We note, however, that intentional fracture of organic semiconductors is one possible route toward producing stretchable devices.[39]) In many cases, consideration of the strain in the active materials is more important than consideration of the stress, because the deformations in the active materials are driven by the deformations of the substrate. Because of the mismatch in thickness between the substrate-encapsulant and the active material, the force needed to deform the ultra-thin active layer is vanishingly small. Toughness and cohesive fracture energy take on increased importance in twisting and shear deformations (and deformations that act to delaminate the device stack),[27,40,41] and during thermal cycling, when unequal coefficients of thermal expansion place stress on the layers.

In such scenarios, metrics related to the energy density absorbed during the course of deformation should of course be maximized to the extent possible.[42]

This review takes the position that despite the apparent mutual incompatibility of charge transport and mechanical deformability in organic electronic materials, the chemistry of these materials nevertheless provides several routes to achieving mechanical softness combined with state-of-the-art electronic properties. Such approaches include tailoring of the chemical structure (e.g., the lengths and composition of the side chains and rigidity of the backbones) and tuning properties familiar to the polymer engineering community (e.g., molecular weight, polydispersity, and crosslinking).[43] Quite often, the mechanical properties of organic semiconductors are determined not only by molecular structure, but also by the ways in which the molecules pack in the solid state.[28,30,31] The solid-state packing structure is determined by the phase behavior of the molecules and the conditions of deposition and processing post deposition.[44-47] Moreover, organic semiconductors accommodate mechanical energy by a range of mechanisms across many length scales, from sub-T_g bond rotations to the breakage of covalent bonds. **Figure 1.1** illustrates the molecular mechanisms by which strain is accommodated across various length scales and strain regimes.

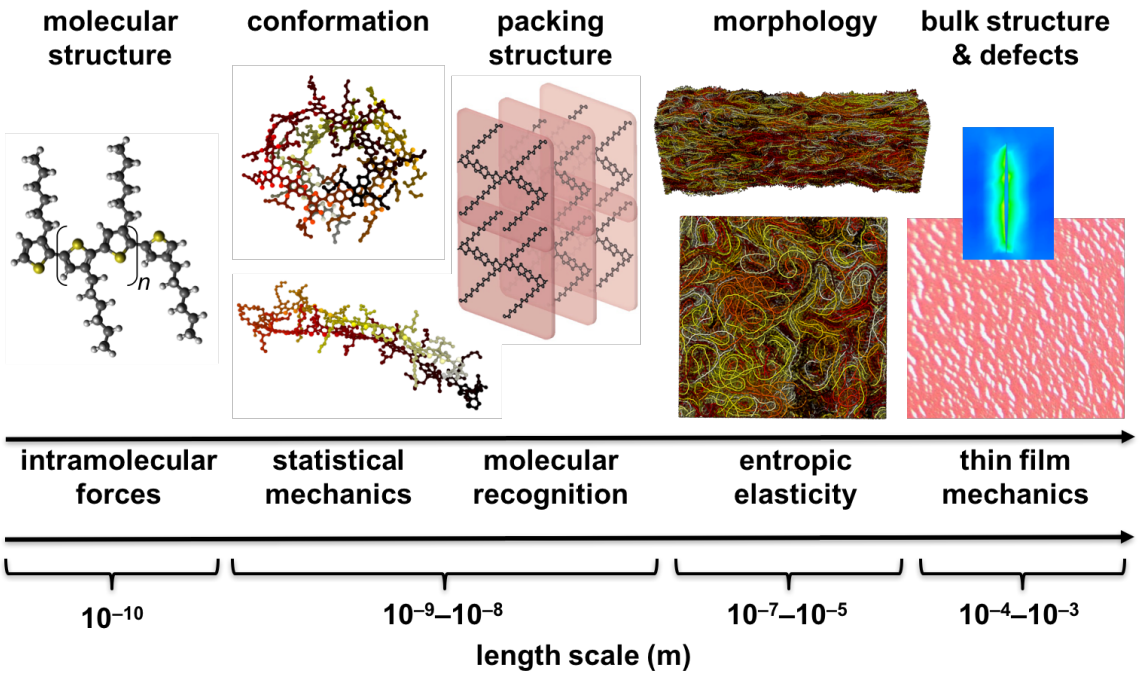

Figure 1.1. Length scales and molecular mechanisms for storage or dissipation of mechanical energy. Embodied in the molecular structure are the restoring forces of covalent bonds, but also the intramolecular forces manifested in electrostatic interactions between distal units and dihedral potential energies between adjacent ones. The conformation of molecules in solution influences the structure and mechanical properties of the film upon the process of solidification, and is in turn predicted by statistical thermodynamics. The packing structure is determined by sterics, electrostatic interactions, and molecular recognition. This structure produces the overall morphology of the solid film. Amorphous chains within the bulk store elastic energy entropically. Finally, the deformability of the bulk structure is determined in large part by defects. The effective mechanical properties of a thin film can be treated using thin-film mechanics. (Drawing illustrating "packing structure" reproduced with permission from ref [31]. Copyright 2010, American Chemical Society.)

This paper is a comprehensive review of the literature related to the mechanical properties of organic semiconductors. The focus is on the molecular and morphological determinants of these properties, the relevant physics of polymeric solids, theoretical and computational approaches to predicting these properties, techniques for metrology, examples of materials that have been synthesized that exhibit especially high deformability, and applications in devices. Progress in this field can benefit from what is

known about the mechanical properties of commodity polymers and engineering plastics; however, the necessity to retain optoelectronic properties in organic semiconductors substantially constricts the available options for designing new materials. For example, rigid molecular chains and highly aggregated morphologies, which are conducive to charge transport, tend to make materials stiff and brittle.[31]

In examining the literature, we found that work related to determining the mechanical properties of π-conjugated materials went through three distinct phases. The first phase (1980s) coincided with the advent of conductive polymers, during which time it first seemed possible to combine metal-like conductivity with the processability of plastics.[48-51] The second phase (1990s-2000s) saw a lull in interest in the thermomechanical properties of organic semiconductors, possibly because of the development of the organic thin-film transistor,[52] light-emitting device,[53] and solar cell.[54-56] Synthesizing new materials, understanding their charge-transport physics, and producing optimized devices required significant resources, which in general were not allocated toward understanding the mechanical properties. The third phase (2010s-present) was characterized by a reaction to activity in the field of soft electronics based on metals and inorganic semiconductors. Inorganic materials can be rendered stretchable using specialized device layouts, i.e., wavy interconnects and topographic features.[17,18,57-60] These strain-relief structures permit the use of metallic films, semiconductor nanoribbons, and whole integrated circuits, which though not quite deformable by themselves (especially under tensile deformation), can be rendered stretchable and highly flexible using the appropriate layout.[10,61] This work suggested to the community interested in organic semiconductors that it no longer had a monopoly on deformability. Moreover, the success of these devices highlighted the inferiority of organic

semiconductors with respect to both charge transport (the mobility of silicon is 2-3 orders of magnitude higher than even the best organic semiconductors[62]) and lifetime (organics are susceptible to degradation when unencapsulated[63]).[64] These results spurred activity on increasing the mechanical deformability of organic semiconductors, and in pursuing areas in which organics retained their advantages against competition from conventional electronic materials.

1.1.1. Deformable Organic Electronics as a Subset of All Deformable Electronics

Stretchable and ultra-flexible electronics originated in the late 1990s and early 2000s, and are primarily attributed to the work of Wagner and Suo.[18,57,58,65-68] Early systems of materials included films of metals and other materials on thin flexible foils[18] and elastomers. Such thin films could accommodate strain by intentional fracture[58,68] or mechanical buckling.[57] Exploiting these routes of deformation was facilitated by the development of the theory of "film-on-foil" mechanics.[18,66] This vein of research was later substantially developed by the work of Rogers and coworkers,[60] who developed device layouts using fractal,[69] interconnecting structures,[3,70] and topographically patterned island-bridge approaches[8] to direct strain away from the active components of devices. This work produced a number of impressive demonstrations, including an electronic eye camera,[71,72] implantable devices for in vivo electrophysiological mapping of the heart[73] and brain,[15] and myriad examples in energy[8] and healthcare.[3,15,73-76] An effort in parallel by Someya and coworkers used organic active materials and stretchable composite interconnects[77] whose goal was also largely to direct strain away from the active components[78-82] (though the same authors were also among the first to study the effect of mechanical strain on the charge-transport properties of organic semiconductors[83]). Bauer and coworkers[4,84] have

also made significant contributions to this field, especially in the area of stretchable batteries,[85] soft actuators,[86,87] solar cells,[38,88] and metrology.[89] **Figure 1.2** illustrates the approaches taken by members of the community to permit semiconductor devices to accommodate strain.

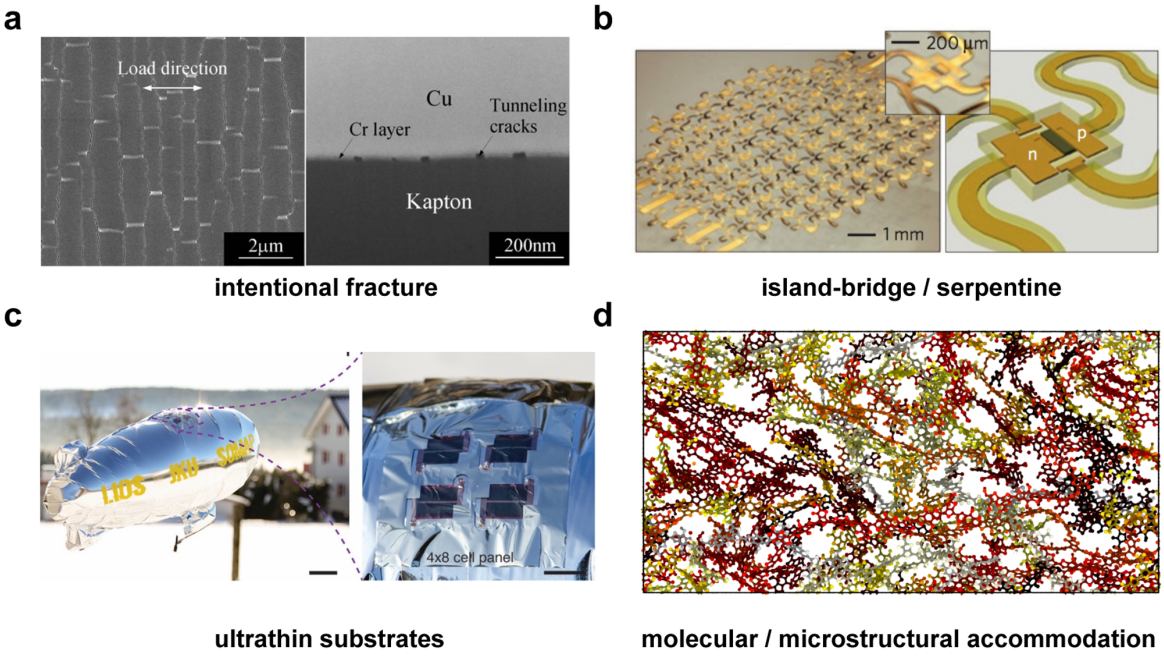

Figure 1.2. Approaches taken by the community to impart stretchability or extraordinary flexibility to electronic devices. (a) Intentional fracture can produce percolated conductive pathways that open and close with strain. Reproduced with permission from ref [90]. Copyright 2007, American Institute of Physics. (b) Wavy, fractal, and island-bridge type geometries have been used extensively for stretchable devices based on inorganic thin films. Reproduced with permission from ref [10]. Copyright 2010, Nature Publishing Group. (c) Ultrathin substrates can be used for lightweight, flexible, and low-cost electronics. Reproduced with permission from ref [88]. Copyright 2015, Nature Publishing Group. (d) Intrinsically or molecularly stretchable materials use the materials themselves to accommodate strain. Reproduced with permission from ref [25]. Copyright 2015, American Chemical Society.

An alternative approach to these composite systems—in which the conductors or semiconductors are dispersed in or on top of a matrix—is one in which the active material itself accommodates the strain.[5,9] Such an approach would simplify patterning, as all

materials could be printed in the same layer without relief structures. The ability to avoid patterning interconnects in complex serpentine patterns, which occupy a large footprint, could also increase the density of the active components. In this approach, which might be selected when digital patterning and low cost are more important considerations than complex function or high-performance operation, organic materials are a logical option. In addition to facile replication by screen,[91] gravure,[92] or slot-die printing,[93] rapid tailorability in circuit design can be accomplished by digital inkjet printing.[94] The advantages of low cost and rapid fabrication are complimented by several other characteristics unique to organics: tailorability by synthesis,[95] tunable color[96] and bandgap,[97] oxide-free interfaces for biological integration,[98,99] low-cost disposal or recycling,[100] and the potential for self-repair[101,102] and biodegradability.[103]

The challenges associated with organics for ultra-compliant applications include, significantly, that the molecular and microstructural characteristics needed for charge transport—namely rigid, π-conjugated polymer chains and highly ordered aggregates in the solid state—also tend to render such materials stiff and brittle. This apparent trade-off is not a fundamental rule, however, and can be negotiated. The simple fact that charge-transport and brittleness or elastic modulus are not directly correlated (**Figure 1.3**) admits of several conceivable strategies to combine charge transport and deformability. These strategies (to be covered in detail in this review) include the use of plasticizers,[34,104] various processing techniques (for example, to improve the entanglement density),[30,105] and the use of flexible side chains and unconjugated linkers in the main chain.[102,106,107] It is first, however, necessary to understand the relevant mechanical properties of existing organic semiconductors—and how they are similar or different from those of other organic solids—

using a combination of experimental and theoretical techniques. Success in understanding the molecular and microstructural determinants of both charge transport and mechanical properties would bring the field closer to achieving electronics with truly "plastic"—i.e., deformable—character. Such an outcome would have two major consequences. The first is that it would permit devices that are destined for commercialization to be more mechanically robust. The second is that it would permit a new class of electronic materials and devices that exhibited extraordinary deformability for devices like electronic skin and wearable and implantable health monitors.

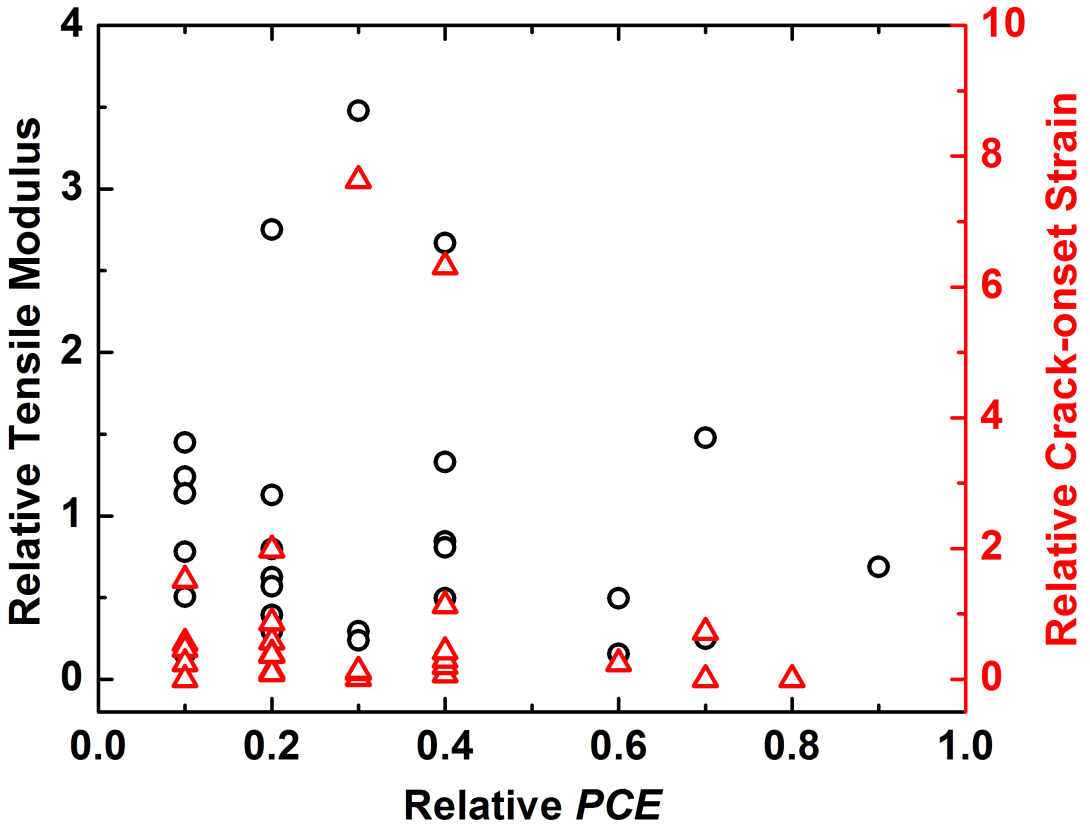

Figure 1.3. Plot of relative tensile modulus (black circles) and crack-onset strain (red triangles) for a library of semiconducting polymers described in ref [108]. vs. relative power conversion efficiency of a bulk heterojunction consisting of the polymer mixed with $PC_{61}BM$. The lack of correlation suggests that it should be possible to co-engineer mechanical deformability with electronic performance.

1.2. Thermal and Mechanical Properties and How to Measure Them

In considering which mechanical properties are desirable for deformable applications of organic electronics, we find that the terminology in this field is not always used consistently.[19] The field sometimes refers to qualities such as "stiffness," "compliance," "hardness," "resilience," "toughness," "ductility," and "elasticity" in ways that differ from the precise meanings used in the mechanics community, whose lexicon is well established. On the other hand, the descriptor "flexible" is so inclusive in that it does not distinguish qualities afforded by the dimensions of the material from qualities afforded by the material itself. That is, any material can be made flexible if it is sufficiently thin.[18] The descriptor "stretchable" is imprecise because it does not convey whether the deformation is elastic (reversible) or plastic (irreversible), and does not define the range over which it exhibits one or the other behavior. In this review, we use "flexible" to mean any form of any device that can be bent to radii of curvature smaller than 1 cm, regardless of the thickness of the substrate, and "stretchable" to mean a device or material that can be elongated by approximately 5 percent or more, regardless of whether the deformation is elastic or plastic. The rarity of the term "deformable" in this field has preserved its generality, and we use it liberally throughout this review in its colloquial sense. A material or device that is "deformable" is thus taken to be an order of magnitude more flexible and stretchable than a typical silicon wafer with a thickness of ~200 μm. The adjective "extensible" will be used to mean "having a high strain at fracture" (in a pull test) or "having a high crack-onset strain" (if the film is measured on an elastomer).

The mechanical properties of organic solids most relevant to deformable devices include the elastic modulus (usually obtained as the tensile or Young's modulus),[109] elastic range and yield point,[110] toughness,[111] and strain to fracture[31] (**Figure 1.4**). These properties are determined not only by the structure of individual molecules, but how these molecules pack in the solid state.[30] Measuring the mechanical properties of thin films poses particular challenges because (1) it is difficult to handle thin films for a conventional pull test[112,113] and (2) pilot-scale synthetic procedures usually do not produce enough material for more than a few films. These challenges have been met by the development of "film-on-elastomer" methods for approximating the range of behavior to tensile strain.[110] These "film-on-elastomer" methods provide the benefits of simplicity to perform and applicability to a range of materials, but require multiple techniques to reconstruct the stress-strain behavior.[110] There are other methods, which may require specialized equipment, however, that obtain these data directly. For example, a method resembling a conventional pull test using a thin film supported by water can obtain a stress-strain curve in a single step (**Figure 1.5**).[114] For measurements of cohesion and adhesion using stresses applied perpendicular to the plane of the films, double-cantilever beam and four-point bending experiments have proven to be valuable.[25-27,40,41,115-117] Comparisons of the results between methods do not always yield the same values, but these discrepancies often produce insights, and the results of one measurement may be more relevant than the results of another to a particular application. The section will conclude with a discussion of which mechanical properties are desirable for deformable applications.

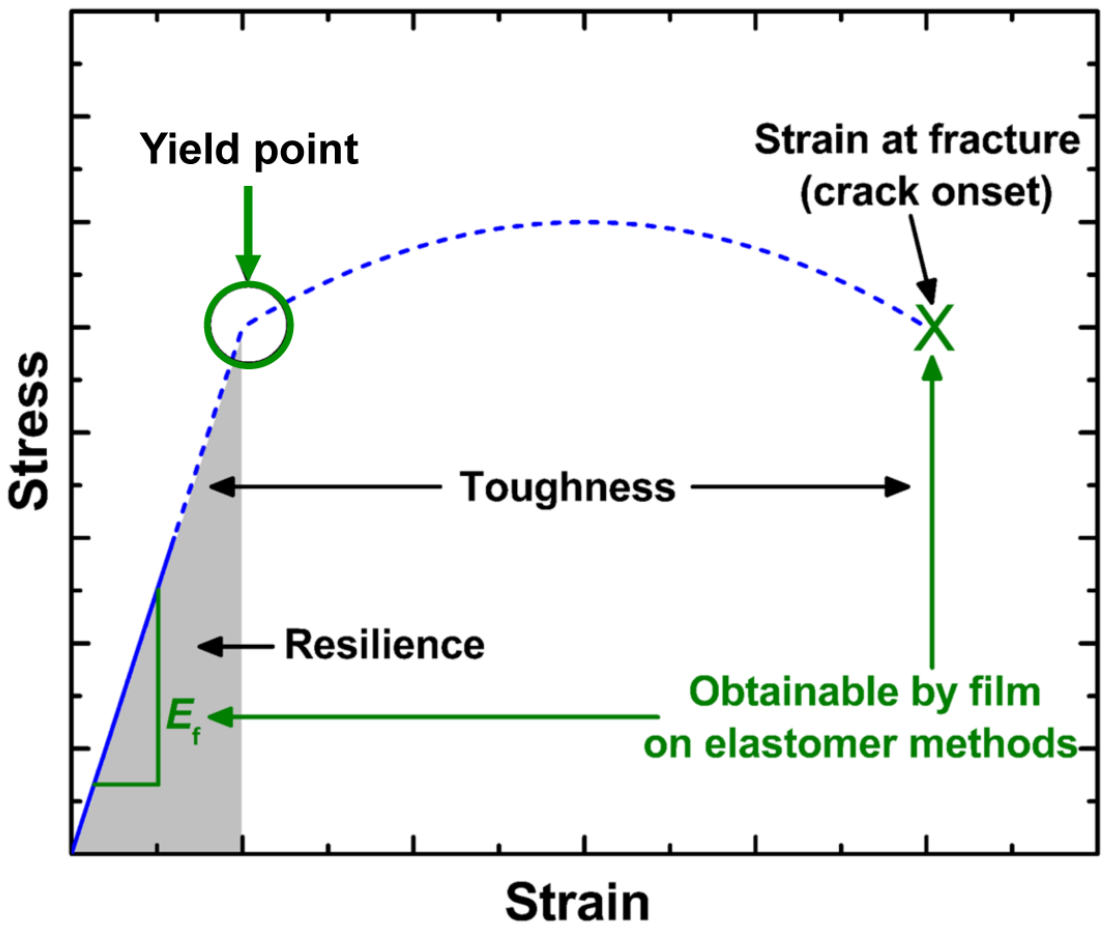

Figure 1.4. Hypothetical stress-strain curve showing the critical features. The stress is an intensive property equal to the force per unit area normal to the load. The strain is the engineering strain, $(l - l_0)/l_0$, where l is the deformed length and l_0 is the length at equilibrium. The elastic modulus of a film, E_f, is the slope of the curve in the linear, elastic regime. The area under the curve in this region is the resilience, which has units of energy per volume. The yield point represents the stress and strain at which the material undergoes irreversible deformation. The strain at fracture represents mechanical bifurcation of the specimen. The area under the entire curve is called the toughness, and has units of energy per volume. Quantities labeled in green can be obtained using film-on-elastomer methods, that is, the modulus by buckling, the yield point by onset of buckling, and the strain at fracture by the crack-onset strain. Reproduced with permission from ref [110]. Copyright 2015, American Chemical Society.

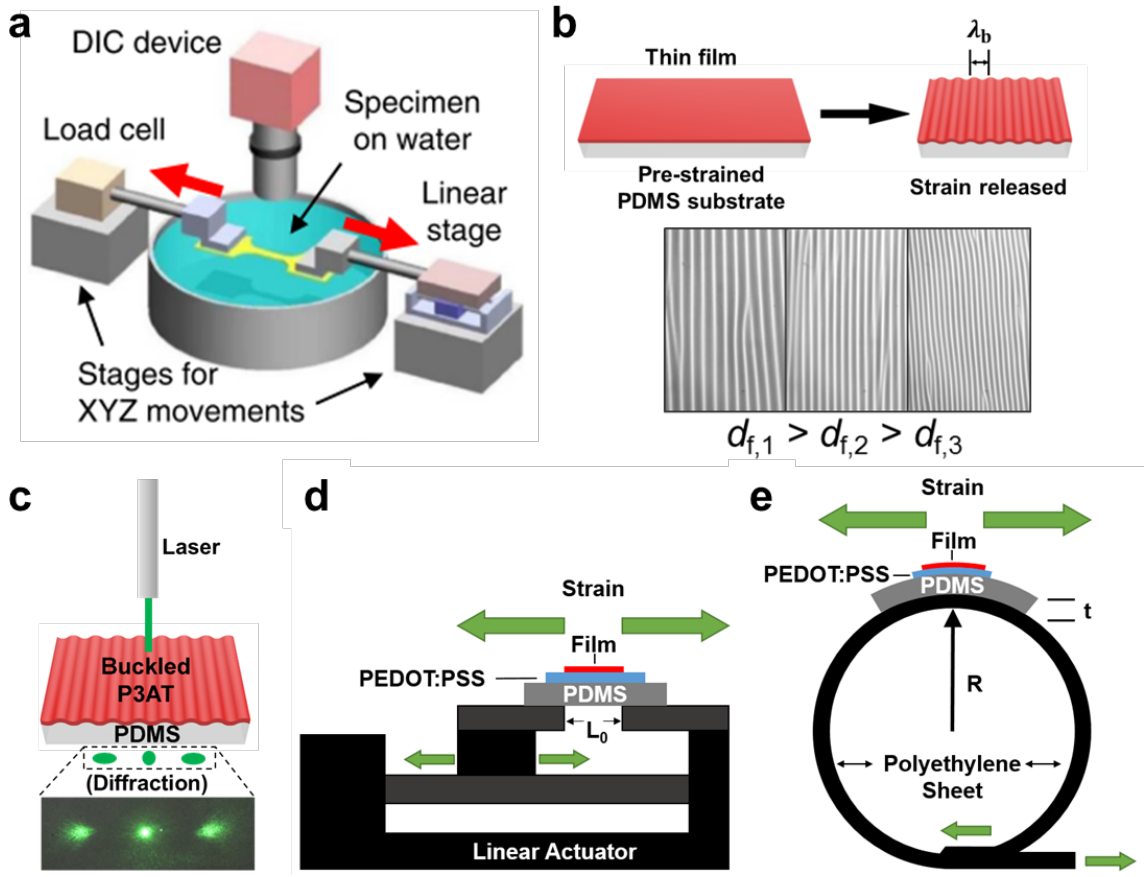

Figure 1.5. Tools for measuring the mechanical properties of organic thin films. (a) The film-on-water method. Reproduced with permission from ref [111]. Copyright 2015, Nature Publishing Group. (b) Schematic diagram of surface wrinkling used to determine the tensile modulus of films. The thickness of the film (d_f) and the modulus determines the buckling wavelength. (c) Buckling wavelength can be determined by the spacing of the diffraction pattern for measurements of modulus or in the technique of buckle-onset to determine the yield point. Reproduced with permission from ref [110]. Copyright 2016, American Chemical Society. (d) A linear actuator or (e) bending experiment can be used to determine the crack-onset strain at the high- and low-strain regimes. Reproduced with permission from ref. [118] Copyright 2016, American Chemical Society.

1.2.1. Glass Transition Temperature

The glass transition temperature (T_g) is a second-order phase transition that ultimately describes the thermally activated reorganization of chains in the amorphous domains of a polymer specimen.[119] A plot of density vs. temperature exhibits a change in slope in the

vicinity of T_g.[35] Similarly, a plot of heat flow vs. temperature measured by differential scanning calorimetry (DSC) reveals an increase in heat capacity. Below T_g, a polymer is said to be glassy; above the T_g, it is rubbery. In a purely amorphous sample (e.g., atactic polystyrene), the material flows readily above its T_g. A semicrystalline sample above its T_g, but below the temperature at which its crystalline domains melt (T_m), exists as a solid at ordinary timescales and is said to be in its elastomeric state. The position of the T_g of a polymer relative to its operating temperature is thus an important predictor of the mechanical properties of a polymer. The T_g also influences the morphological stability of the solid state of the polymer, which can be problematic if the morphology that is most conducive to device performance is not the most thermodynamically stable one.[119] Devices based on composite systems, e.g., bulk heterojunction solar cells, can phase separate with deleterious consequences if operated above their T_g.[119] The requirement that a bulk heterojunction solar cell have a high T_g for morphological stability and a low T_g for mechanical stability is another competing criterion. For an account of the role of T_g in the operation and stability of organic photovoltaic devices, see the comprehensive review by Müller.[119]

Despite its importance, the glass transition of many organic semiconductors is not easily determined. The change in heat capacity in the vicinity of T_g for organic semiconductors is often too weak to detect by DSC.[106,120-125] Other techniques, such as dynamic mechanical analysis (DMA),[126] or variable-temperature ellipsometry (which has been applied to polyolefins[127,128] as well as conjugated polymers[129]), are often required. The glass transition can also be predicted computationally, as atomistic and coarse-grained

molecular dynamics (MD) simulations have been used to obtain values that are in good agreement with experiment (**Figure 1.6**).[130]

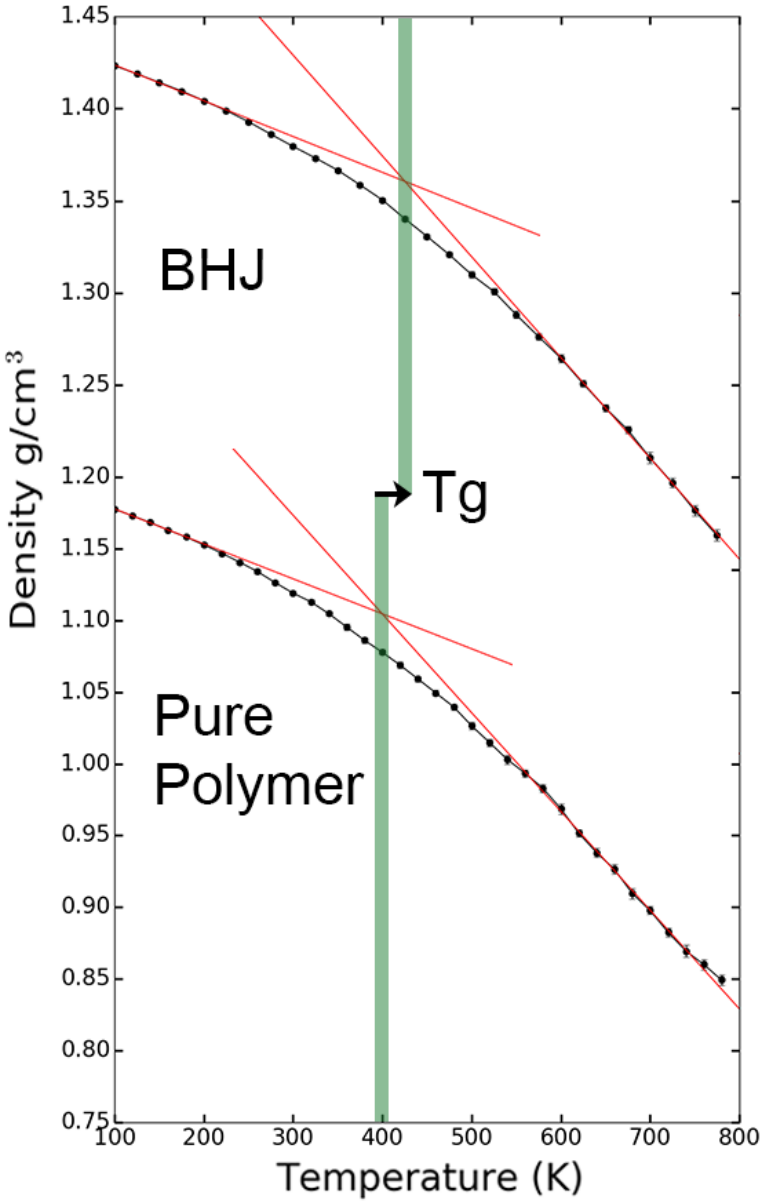

Figure 1.6. Theoretical prediction of glass transition temperature (T_g) for the semiconducting polymer PTB7 based on molecular dynamics simulations. The density is estimated by the intersection of the linear fits to the glassy (low T) and rubbery (high T) regions. The plot also shows the increase in T_g upon mixing with PCBM, which behaves as an antiplasticizer, in a bulk heterojunction (BHJ) film. Reproduced with permission from ref [105]. Copyright 2016, Royal Society of Chemistry.

1.2.2. Elastic Modulus, Poisson Ratio and Elastic Range

Several bulk mechanical properties can influence the mechanical robustness of organic semiconductor films for deformable applications (**Figure 1.4**). The elastic moduli quantify the ability of a material to reversibly store mechanical energy. They can be expressed in three common forms depending on the mode of deformation: the tensile modulus (E), the shear modulus (G), and the bulk modulus (K). For isotropic solids, these quantities can be interconverted. In thin films, the easiest to measure and perhaps the most relevant property is the tensile (Young's) modulus, E. This quantity refers to the force required per unit area normal to the load (stress, σ) to deform the material a fraction of its initial length (strain, ε) reversibly under uniaxial deformation. The shear modulus describes the response of a material to shear stress and is defined as the ratio of shear stress to shear strain. The bulk modulus describes the volume change of a material undergoing an infinitesimal change under uniform (i.e., hydrostatic) pressure. For isotropic, homogeneous materials, the elastic moduli, along with the Poisson ratio (ν), which describes the negative fractional deformation of a material along the two axes perpendicular to the strained axis, are sufficient to fully describe the elastic behavior of a material. That is, a material stretched axially by 1 percent with concomitant reduction of the transverse dimension by 0.5 percent has a Poisson ratio of 0.5. The tensile modulus is expressed in units of force per cross sectional area (N m^{-2} or Pa). A typical value of E for polycarbonate is ~1 GPa; for silicone rubber it is ~1 MPa. Values for the common semiconducting polymer regioregular poly(3-hexylthiophene) (P3HT) range from 0.1 – 1 GPa, depending on the sample and—given its T_g near room temperature of 12 °C—the temperature at which the measurement was taken. The elastic moduli and Poisson ratio are valid only for small strains within the elastic

regime of the material, or less than approximately 10 percent. The area under the curve for the linear portion of the stress strain curve is called the modulus of resilience (U_r), and represents the total amount of energy per unit volume (e.g., J m^{-3}) storable by the solid before the onset of plastic deformation.

The tensile modulus is highly relevant for deformable applications because it can be tuned to minimize interfacial stresses (among other layers in the device or between the device and another surface, i.e., the skin) and it is closely related to molecular structure and solid-state packing structure. The modulus is often correlated to other mechanical properties and even to optoelectronic properties. The molecular mechanisms responsible for storing mechanical energy in the elastic regime depend on the phase of the solid. For crystalline solids and the crystalline phases of semicrystalline solids, displacement of the molecules from their equilibrium positions in the lattice produces a restoring force. For van der Waals solids, the restoring force can be described by a Lennard-Jones or similar potential. For glassy phases below T_g, elastic deformation is mediated by van der Waals forces, but also by deformation of covalent bonds. For semicrystalline polymeric phases above T_g, in which the polymer chains are unfrozen, chains are aligned along the axis of tensile deformation; this reduction in degrees of freedom produces a restoring force, as polymer chains tend toward increasing their configurational entropy. Elastomers thus behave as "entropic springs," in which changes in internal energy are negligible, and changes in entropy dominate.

The tensile modulus can be measured using several different techniques, and in many cases the technique chosen depends on the amount of material available and the forms into which it can be processed. If enough material is available for a conventional

pull test, a typical specimen can be cast into the appropriate—e.g., dog-bone—size and shape, and its force-displacement curve can be measured and transformed into its stress-strain curve using the dimensions of the sample.[24,36] In practice, this method is limited to simple polymeric structures like the P3ATs, whose synthetic procedures comprising only a few steps can produce quantities of material large enough (e.g., >100 mg) for a bulk measurement. Designer materials—i.e., low-bandgap polymer exhibiting the alternating donor-acceptor motif[95]—are synthesized at laboratory scale in only modest quantities. The quantities of materials available at the laboratory scale are limited in the case of conventional reactions by the low concentrations, and in the case of microwave-assisted reactions by small reaction vessels. Moreover, vastly greater quantities of material are required for conventional mechanical tests, which requires a bulk sample, than for a charge-transport measurement,[131,132] which require a thin film (~10 μg, excluding a 10-fold greater fraction of wasted material if the film is produced by spin coating). Given the importance of mechanical properties in determining the lifetime and stability of organic devices, there has thus been a drive toward obtaining properties directly from thin films.

Pull testing of bulk samples of organic electronic materials was used extensively in early work using materials such as poly(acetylene)[48,49] and unsubstituted polyaromatic[50] species synthesized by simple routes, such as oxidative polymerization. An early test of regiorandom poly(3-alkylthiophene) synthesized in this way revealed a striking decrease in tensile modulus with increasing length of the alkyl side chain,[33] which is a common theme among P3ATs and other conjugated polymers.[34,133,134] More recently, block copolymers of P3HT and poly(ethylene) have been synthesized and determined by conventional pull testing to exhibit decreasing tensile modulus with increasing fraction of

the insulating component, but also extraordinary ductility and toughness.[24] The effect of molecular weight on the mechanical properties of P3HT has also been measured on bulk samples (**Figure 1.7a**);[36] greatly increased ductility and toughness with molecular weight (though similar tensile modulus) measurements pointed to the importance of entanglements, even in semi-rigid polymers such as P3HT. Direct tensile testing of bulk samples of low-bandgap polymers or semiconducting small molecule films has not been reported.

Techniques used to determine the tensile moduli of thin films circumvent the need to produce large amounts of material and also the need to manipulate fragile, freestanding films.[112] Moreover, the mechanical properties of thin films often differ from those of bulk samples of the same material,[135] and thus direct measurements on thin films may produce results that are more in line with the properties exhibited by the materials in working devices. Techniques that have been developed include direct pull testing of thin films on water,[111,114] nanoindentation,[136-138] and the buckling-based method.[112] Kim and coworkers have pioneered the use of the water-based technique, in which a film is coated on a flat substrate and then gently floated onto the surface of water (**Figure 1.7b**).[111,114] A highly sensitive load cell coupled to a linear actuator is used to obtain a plot of force vs. displacement. Critical to this method is ensuring that the contacts do not tear the delicate thin film; slabs of poly(dimethylsiloxane) (PDMS), which adhere to top surfaces of the termini of the floating thin films by van der Waals forces, are used in place of a clamp, and thus minimize mechanical damage. The water-based technique has been used to measure the stress-strain behavior of P3HT as a function of regioregularity[114] (the films become more deformable with increasing regiorandomness, though the charge-carrier mobility

decreases) and also of all-polymer active layers for intrinsically stretchable solar cells.[111] As the film is not bonded to a solid substrate in the water-based method, the results may thus be influenced by concentration of strain in thin areas and defects within the thin film.[139] The force required to stretch the sample will thus be lowered, as will the stress, which is calculated on the assumption that the cross section of the sample is mathematically uniform. For example, the water-based method produced values of tensile moduli that were 3-6 times lower than values produced by the buckling method (described below). In a recent study that compared the results of the two methods,[139] the difference in modulus were attributed to the combined effects of inhomogeneities in film thickness, void space in the films behaving differently under tension and compression, and differences in strain rate. Nevertheless, the advantage of the water-based technique is that it provides the full stress-strain behavior (not just the tensile modulus), it is simple to perform, and provides convenient comparisons between materials.

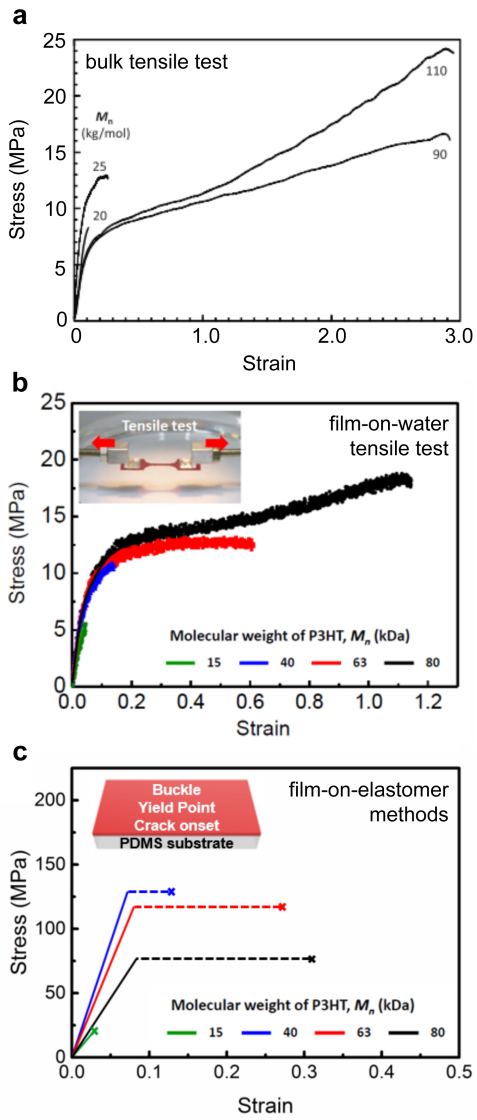

Figure 1.7. Stress-strain curves for P3HT obtained by three different metrology techniques. (a) Bulk tensile test of P3HT samples with different molecular weights. Reproduced with permission from ref [36]. Copyright 2013, Elsevier. (b) Tensile test obtained using the film-on-elastomer technique. (c) Stress-strain behavior reconstructed using film-on-elastomer techniques: the buckling technique, determination of yield point by the onset of buckling, and crack-onset strain. Reproduced with permission from ref [139]. Copyright 2017, American Chemical Society.

The buckling technique uses the wavelength of the sinusoidal wrinkles that form in a thin film when it is compressed on a compliant substrate and has been implemented

successfully to measure the tensile moduli of a variety of organic thin films, including several examples of semiconducting polymers and small molecules.[112,113] The buckling phenomenon was described for metal films on PDMS substrates by Whitesides and Hutchinson,[140] and the mechanics were adapted into a metrology technique for measuring the elastic properties of thin films by Stafford and coworkers.[113] The method was extended to organic semiconductors by Khang and coworkers,[109] and then used extensively by O'Connor and coworkers,[30,31,141] along with our group,[34,104,134,142] for a variety of materials.[42] The technique has been reviewed before by Stafford and coworkers,[112] and a description of it was included in an earlier review by our group in the context of the mechanical stability of organic solar cells,[42] so here we will focus on the practical issues related to measurement of tensile modulus for organic semiconductors.

Briefly, the buckling wavelength increases with the stiffness (modulus and thickness) of the thin film, and thus the modulus (E_f) can be obtained by plotting the buckling wavelength (λ) vs. film thickness (d_f); the slope λ/d_f increases with the third power of E_f, according to **equation 1**.[113]

$$E_f = 3E_s\left(\frac{1-\nu_f^2}{1-\nu_s^2}\right)\left(\frac{\lambda}{2\pi d_f}\right)^3 \qquad (1) \qquad \textbf{Equation 1}$$

Accurate values of the modulus of the PDMS substrate (E_s) and the Poisson ratios of the film (ν_f) and the substrate (ν_s) are needed for the determination of E_f. There is a practical difficulty in casting films directly on the elastomeric substrate—typically PDMS—because it swells when in contact with organic solvents. This challenge can be overcome by first casting the film on a passivated glass or Si/SiO_2 substrate, and transferring the films by kinetic (rapid) transfer[143] using PDMS as a carrier substrate. It is

often best to cure the PDMS (Sylgard 184 cured at the normal ratio of 10:1 base:crosslinker) for 36 h at room temperature, so that the bulk structure is solid, but that the top surface is still somewhat tacky. If the film is too strongly adhered to the original substrate to remove using fast transfer, transfer can be facilitated by using immersion in water. If direct transfer fails, it may be necessary to form a bilayer film using a second material with a known tensile modulus ($E_{f,2}$) and thickness ($d_{f,2}$). The modulus of the film (E_f) can then be related to the modulus of the bilayer film (E_{eff}) using **equation 2**.

$$E_{\text{eff}} = \frac{1 + m^2n^4 + 2mn(2n^2 + 3n + 2)}{(1+n)^3(1+mn)} E_{\text{f}};\ \text{where}\ m = \frac{E_{\text{f},2}}{E_{\text{f}}},\ n = \frac{d_{\text{f},2}}{d_{\text{f}}} \qquad (\mathbf{2})$$

The small compressive strain is typically generated by pre-straining the PDMS and then releasing the strain once the thin film has been transferred. The buckling wavelength should be measured immediately (within 1 h) after the film is transferred to the PDMS and compressed, so that time-dependent relaxation of the PDMS, thin film, or both, does not affect the result.

The advantage of the buckling technique is that it does not require specialized equipment for measuring mechanical properties; all that is required is a microscope and a technique for measuring the thickness of thin films, such as stylus profilometry, atomic force microscopy, or ellipsometry. While it is necessary to know the tensile modulus of the PDMS substrate, this quantity can be measured using a conventional pull tester available to most laboratories (or in principle simply by suspending weights from a sample and measuring the displacement). Moreover, the buckling-based measurement provides a measure of the tensile modulus that is not subject to the influence of defects. The buckling wavelength is usually measured at multiple locations using image analysis, and reported

results are usually averages. A disadvantage of the technique (unlike water-supported pull testing or nanoindentation) is that it measures only a single mechanical property. The buckling technique is thus one of three techniques that can be used in concert to approximate the key features of the stress-strain curve (**Figure 1.7c**), which also include determination of yield point by onset of buckling (Section 2.3) and crack-onset strain (Section 2.4).

In the development of the buckling-based method, Stafford and coworkers showed that the tensile modulus of plasticized polystyrene as measured by nanoindentation was in good agreement with the buckling-based method.[113] Nanoindentation is one of the standard measurement techniques for thin films and has been successfully used to measure the hardness and tensile modulus of thin films of ceramics and metals. Typically, the material properties are calculated from the shape of the curve of the load vs. depth of penetration and indenter type. Significant challenges arise when the method is applied to materials with submicron thickness. Such measurements are complicated by effects of the substrate, along with viscoelastic behavior, which produces a dependence of the mechanical properties on the rate of the displacement of the indenter tip. In order to eliminate the effect of the underlying substrate on the measurement of the tensile modulus, one strategy is to use films thicker than 1 μm. For example, Venkatanarayanan et al. measured the tensile modulus of two conjugated polymers, poly(*p*-phenylene vinylene) (PPV) and polyacetylene (PA), using nanoindentation on films thicker than 3 μm and observed good agreement to the values they obtained by molecular dynamics simulations.[144]

1.2.3. Yield and Ductility

The elastic behavior of a solid material terminates with either brittle fracture or plastic yield. At the yield point, the energy stored during elastic deformation (i.e., the modulus of resilience, U_r) is converted to plastic deformation. That is, this energy overcomes the barrier imposed by intermolecular forces and entropic effects in the elastic regime and the molecules adopt a new configuration at mechanical equilibrium. For van der Waals solids, yield corresponds to molecules sliding past each other, and is facilitated by a low glass transition, for example, by the presence of side chains. In semicrystalline semiconducting polymers whose structure permits interdigitation between the side chains in the crystallites, there are strong intermolecular forces along all axes in the lattice, and these materials tend to exhibit brittle behavior as opposed to plastic deformation.[31]

The yield point in conjugated polymers has practical consequences.[110] The lower limit of this quantity—generally expressed as a strain—defines the elastic range, up to which a material can be expected to be deformed many times over its lifetime with little change in performance.[145] In applications requiring repeated deformation (e.g., devices integrated with the moving parts of the body or of machines) it is thus desirable to operate within the elastic range. For applications that require only one-time bonding to curved surfaces (e.g., windshields, lenses, and architectural elements),[9,146] permanent plastic deformation may be acceptable.[147] Whether or not the effects of plastic deformation are deleterious depend on the ways in which the deformed microstructure influence optical absorption[148] or charge transport.[149] During tensile loading, polymer chains tend to align along the axis of strain; this alignment corresponds to increased tensile strength along the strained axis and birefringence in semiconducting polymers. O'Connor and coworkers have used this

approach to generate organic photovoltaic devices based on a stretched P3HT:fullerene active layer. This device behaves essentially as a polarization-dependent photodetector.[148] Strain alignment also produces anisotropy in elastic modulus[150] and charge transport.[151] Generally, the molecular axis is the most efficient one, and thus measurements of field-effect mobility have been highest along the strained axis for stretched samples of P3ATs.[151,152] The extent of chain alignment in strained films of P3HT has been measured experimentally by O'Connor et al.[151] and has been predicted computationally using coarse-grained molecular dynamics;[130] the results of both of these techniques yield excellent agreement. Mechanical strain can also produce changes in texture, as has been observed in P3HT, in which molecules partially reorient with their π-stacking axes perpendicular to the substrate. Gargi et al. demonstrated that this reorientation increased the mobility in samples of biaxially strained P3HT, which exhibited highly face-on stacking, relative to samples that were unstrained, which comprised a blend of face-on and edge-on stacking.[149]

The yield point can be measured using a variety of techniques. In a pull test, the yield point occurs just after the end of the linear portion of the stress-strain curve. Using film-on-elastomer techniques, the yield point can be estimated by the onset of buckling.[110] In this experiment, a thin film on an elastomeric substrate is cyclically strained by incrementally increasing amounts, e.g., 0% → 1% → 0% → 2%, etc. At the first appearance of buckles upon returning the film to 0% strain, it can be assumed that the yield point has been surpassed. The appearance of buckles can be determined by inspection using optical microscopy for stiff and highly absorbing materials (i.e., easy-to-see films). In the case of transparent or hard-to-see films, the onset of buckling can be inferred from the production of a diffraction pattern when passing a laser beam through the sample (**Figure 1.5c**). Printz

et al. found a dependence of the yield point on the length of the alkyl side chain, namely that the elastic limit increases with increasing length of the side chain.[110] Interestingly, the yield point also increased with decreasing thickness, as observed in films of poly(3-dodecylthiophene) (P3DDT, **Figure 1.8b**).

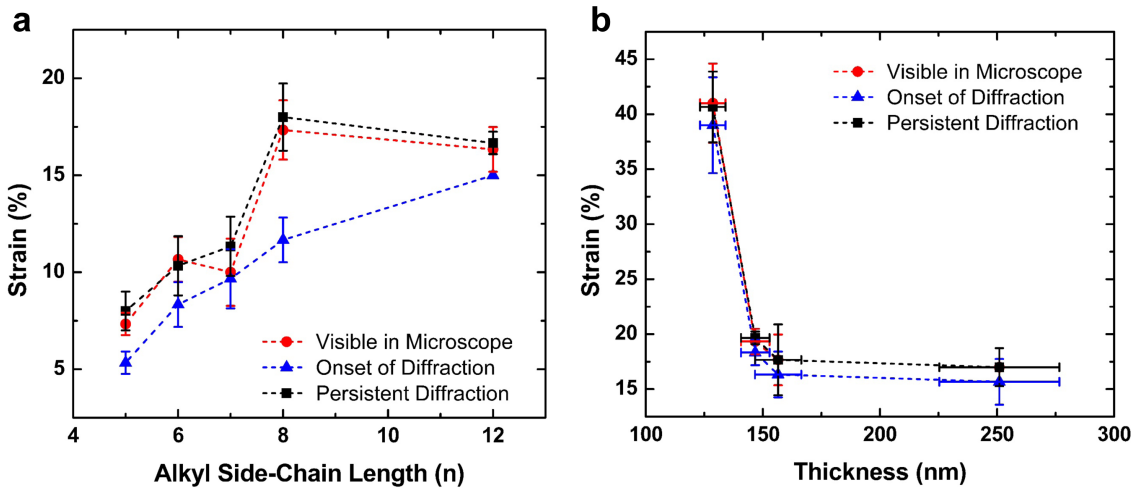

Figure 1.8. Yield point as determined by onset of buckling. (a) Strain at the yield point vs. alkyl side-chain length for P3ATs. The three plots refer to the onset of diffraction, persistent diffraction, and the strains at which the buckles were visible by optical microscopy. The onset of diffraction occurs at smaller strains because the buckles form and then recede because of the viscoelasticity of the polymer films and the PDMS substrate. (b) Strain at the yield point vs. thickness for poly(3-dodecylthiophene). The yield point of the material exhibits a strong dependence on thickness, with films thinner than approximately 140 nm exhibiting greater elastic limit. Reproduced with permission from ref [110]. Copyright 2015, American Chemical Society.

1.2.4. Moduli of Resilience and Toughness

The deformation of a sample is characterized by two energy densities: modulus of resilience (U_r) and modulus of toughness (U_t). The modulus of resilience is the total energy stored by the sample within the elastic regime, and is calculated as the area under the linear portion of the stress-strain curve. The modulus of toughness is the total energy absorbable by the sample at the point of fracture, and is the total area under the stress-strain curve from

0% strain to the point of fracture. The toughness increases with the product of strength and extensibility, and generally increases with increasing intermolecular forces and with molecular weight. The absolute extensibility prior to fracture, however, may not be the most important predictor of the ability of encapsulated devices to survive extreme deformation. Rather, the substrate and encapsulant, rather than the active layer, bear the load. For extreme deformations, it may be sufficient for a material to be neither strong nor tough, assuming the active materials are at least as deformable as—and have good adhesion to—the substrates and encapsulants.[37]

1.2.5. Crack-Onset and Fracture

Once the mechanical energy density absorbed by a specimen exceeds its modulus of toughness, its bulk structure fractures. The molecular mechanisms responsible for fracture of organic structures depend on the molecular weight and phase of the solid sample. For small molecular semiconductors,[118] fracture occurs when the van der Waals forces between molecules are overcome. For crystalline solids, the van der Waals cohesive pressure is theoretically greater than 10^8 Pa (>1000 atm),[153] and thus it is likely that fracture initiates at boundaries between crystallites. In samples of semicrystalline polymers, scission of covalent bonds and pulling out of chains can both be active:[154] chain scission[155] is favored with high T_g and density of entanglements (which scales with molecular weight), and pullout is favored with low T_g and low molecular weight.[156,157]

Catastrophic decohesion of a sample is generally measured by the strain at failure in a bulk tensile test—i.e., when the sample bifurcates. For thin films, the strain at fracture can be measured using the water-supported tensile test, or indirectly by measuring the

strain at which the first crack appears when the film is bonded to an elastomer (the crack-onset strain). The water-based method generally produces a smaller value for fracture strain than the crack-onset strain.[139] The origin of the discrepancy is that thin films have inhomogeneities in thickness that can be a significant fraction of the thickness of the film. Concentration of strain at thin areas and defects produce cracking at smaller strains than would be expected for a mathematically smooth film. This argument is analogous to the one given for the lower tensile moduli obtained using the water-based method. This effect is counterbalanced somewhat by the fact that the fracture strain in the water-based method represents complete bifurcation of the sample, whereas the crack-onset strain where the film is bonded to an elastomer represents only the first appearance of a crack as visible by optical microscopy.

While it might seem that fracture would mean the demise of a device based on organic semiconductors, fracture is not always catastrophic. The extent to which fracture is deleterious to performance depends on the extent of the cracks and the direction of charge-transport in the device. For example, in organic solar cells and light-emitting devices, charge-transport is perpendicular to the plane of the device; for field-effect transistors, it is in-plane. Thus, cracking in devices with perpendicular charge transport is not necessarily catastrophic, as cracked devices can in principle behave as multiple devices connected in parallel.[158] Short-circuiting of the electrodes through the active layer, however, will eventually lead to complete failure of such devices. In devices operating using lateral, in-plane transport, operation will continue if there is a percolated pathway between electrodes.[159] Intentional fracture has long been a method for introducing

stretchability into metallic thin films, [58,68,160] and such an approach has also proven effective in organic field-effect transistors.[39]

1.2.6 Cyclic Loading and Fatigue

A device in outdoor or on-body environments will be subjected to cyclic deformations.[3,145] The ultimate effects of cyclic loading in engineering materials are deleterious.[160] That is, strain hardening produced by the accumulation of dislocations within crystalline grains harden and embrittle metallic samples,[160] and chain scission embrittles plastics. Like engineering plastics, semiconducting polymers also undergo fatigue, as Printz et al. showed for poly(3-heptylthiophene) (P3HpT, **Figure 1.9**).[161] When cyclically strained 10,000 cycles above the yield point, P3HpT exhibited a loss in tensile modulus (as deduced by a decrease in buckling wavelength) and increase in brittleness (as deduced by an increase in the linear density of cracks at a given applied strain). Interestingly, fatigued films of P3HpT exhibited a correlation between tensile modulus and brittleness that was opposite to what was expected for other conjugated polymers, including P3ATs with increasing length of the alkyl chain (for which stiffness increases with brittleness).[161] For fatigued films, low tensile modulus correlated with brittleness. Moreover, analysis of the UV-vis spectra by the weakly interacting H-aggregate model showed de-aggregation of the polymer chains by a reduction in the vibronic absorptions characteristic of π-π stacking. Thus cyclic loading and fatigue have dually detrimental effects: by degrading the microstructure in a way that is deleterious to charge transport, but also increasing the susceptibility to mechanical failure.[161]

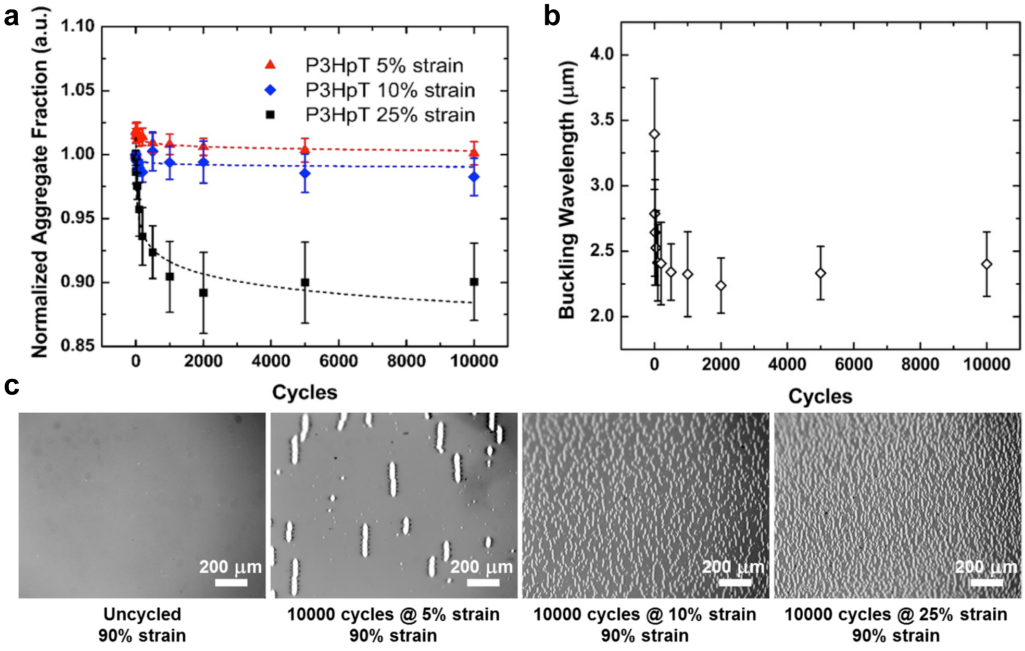

Figure 1.9. Fatigue in poly(3-heptylthiophene) (P3HpT). (a) Normalized fraction of H-aggregates as a function of number of cycles of strain to 5, 10, and 25%. The greatest change is observed for a strain above the yield point, or 25%. (b) The buckling wavelength decreases significantly as a function of cycles of strain, which is indicative of a tensile modulus that decreases with cyclic loading. (c) Micrographs showing the density of cracks as a function of maximum strain before fatigue (left image), and after 10,000 cycles of 5, 10, and 25% strain. Reproduced with permission from ref [161]. Copyright 2016, Elsevier.

1.2.7 Adhesive and Cohesive Fracture Energy

The Dauskardt laboratory has described extensively the adhesive and cohesive energies of organic semiconductors and devices.[25-27,40,41,115-117] Films with poor adhesion[115] or cohesion produce delamination, which results in catastrophic failure of devices. Adhesion (cohesion) is a function of their interlayer (intralayer) chemical bonding (if any), van der Waals interactions, and chain entanglements. Methods for probing the adhesion and cohesion of thin films include the four-point bending technique (FPB, **Figure 1.10a**) and the double-cantilever beam technique (DCB, **Figure 1.10b**). Briefly, FPB is most appropriate for measuring the interfacial adhesion between layers, although it can be used

to measure layer cohesion as well. It involves placing (or sandwiching) a thin film between two beams and applying load using bending pins with inner and outer symmetry. The thin film/beam sandwich has a starter notch equidistant from the pins on the side under tension. To prevent the fracture from propagating from the notch through the film and to the other beam, a small area of material known to have poor adhesion is sometimes added to direct the fracture to the interface of interest.

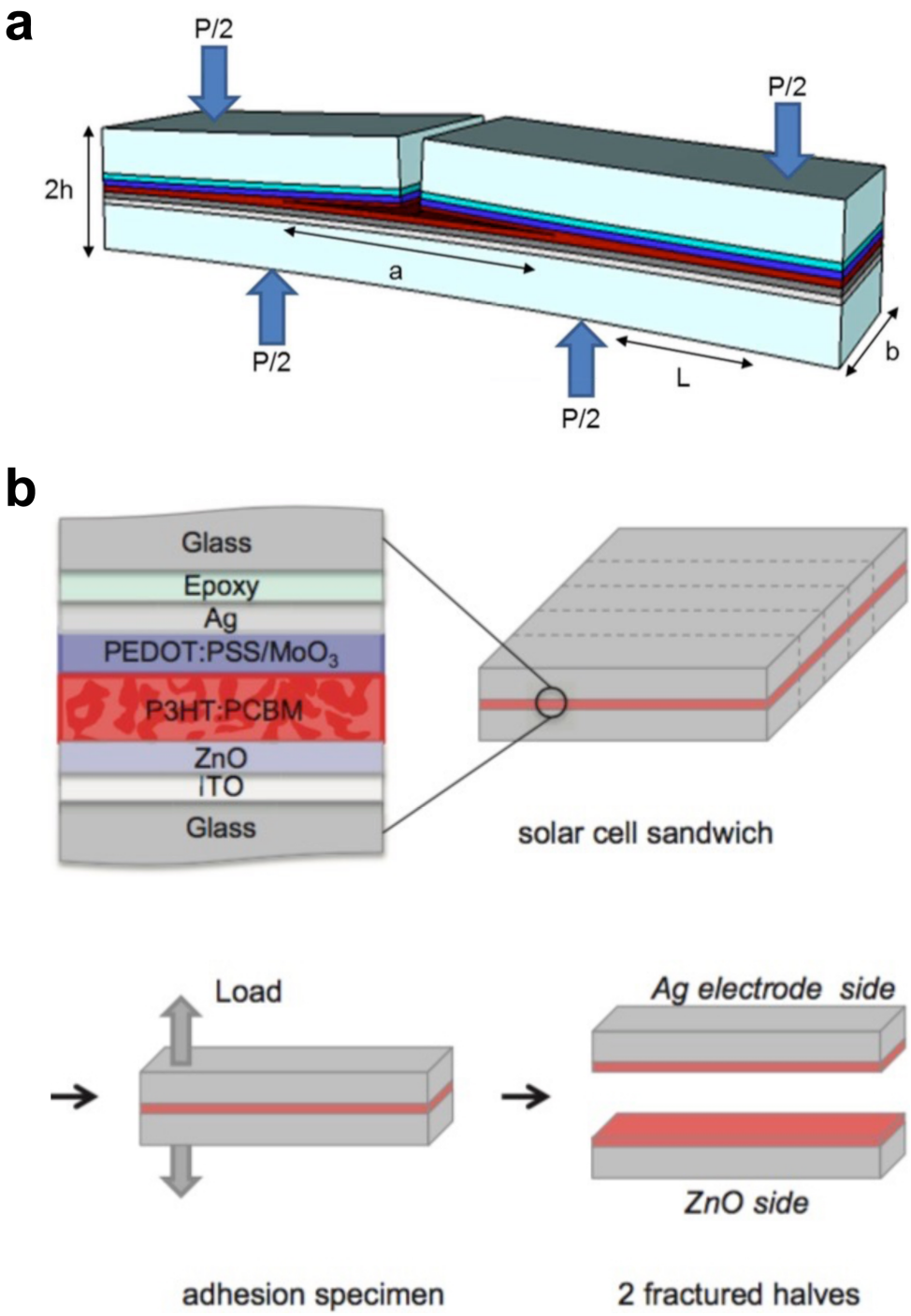

Figure 1.10. Schematic drawings of the (a) double-cantilever beam and (b) four-point bend tests. Reproduced with permission from refs [25] and [115]. Copyright 2015 and 2013, Elsevier and American Chemical Society, respectively.

The experimental setup for DCB is a thin film or films being sandwiched between two beams with loads applied normal to the beam surfaces at one end of the beams and it can be utilized to probe either adhesive or cohesive failure. The cohesive fracture energy determined by DCB can be considered to be essentially the same as toughness in the case of a homogeneous thin film sandwiched between two essentially rigid beams. However, in the case where additional layers are sandwiched between the beams, these layers can plastically deform ahead of the fracture path and results in a measured fracture energy greater than the film toughness. Typical values for the cohesive energy obtained using the DCB and FPB tests for organic electronics are typically less than 5 J m^{-2}, with PEDOT:PSS measured to be 2.5 J m^{-2},[116] and P3HT:PCBM blends measured as high at 4.9 J m^{-2} after high-temperature annealing for a short duration (200 °C for 15 s).[27]

1.2.8 Viscoelasticity

All polymers, especially those above or near their glass transition temperatures, are at least partially viscoelastic, and thus exhibit mechanical behavior that depends on time. A viscoelastic solid is solid-like at short timescales and small deformations, and fluid-like at long timescales and large deformations. Viscoelastic properties of polymeric materials can be characterized using dynamic mechanical analysis (DMA).[154] This technique measures the complex dynamic modulus (composed of the storage and loss modulus) by monitoring the ratio of an oscillating stress and strain—either tensile, compressive, flexural, or shear—in a deformed sample as a function of frequency and temperature (<0.5% strain). DMA is typically performed on free-standing films and has been used to study only a few conjugated polymers, which include P3ATs,[162-166] polytriarylamine,[167] and poly(diphenylacetylene)[168] derivatives.

Chen and Ni performed some of the earliest work aimed at corrleating the structure and viscoelastic properties of regiorandom P3ATs. The authors performed temperature-dependent DMA on a series of bulk samples of regiorandom P3ATs with varying side-chain lengths (P3BT, P3OT, and P3DDT). Three characteristic thermal transitions were observed: a γ-transition associated with methylene linkages in side chains (< –150 °C), a β-transition associated with side chains, and an α-transition (T_g) associated with dihedral twists of the thiophene backbone. The β-transition was observed to increase with length of the side chain, while the α-transition exhibited the opposite trend. In going from P3BT to P3OT the T_g decreased to below room temperature, enabling P3OT and P3DDT to undergo viscoelastic stress relaxation under ambient conditions.[162] van der Leur et al. investigated the frequency dependence of the α relaxation mode for a series of P3ATs (P3HT, P3OT, and P3DDT), and observed a 15-20 °C increase in the glass transition when increasing the frequency from 0.1 to 10 Hz.[166] More recently, Smith et al. have used DMA to measure the room-temperature storage and loss modulus of a series of P3ATs containing randomly incorporated unsubstituted thiophene rings along the backbone. In all cases, at room temperature the storage modulus was observed to be on the order of 10 times larger than the loss modulus indicating that the response was predominately elastic.[164]

A particularly striking example of a soft, viscoelastic conjugated polymer was a poly(diphenylacetylene) derivative reported by Jin et al. that was shown to exhibit gum-like mechanical behavior at room temperature. The authors found that the addition of long alkyl side to the off-axis phenyl units resulted in fluorescent materials that exhibited significant viscoelastic relaxation at room temperature. Room temperature DMA revealed

placement of the side chain at the meta position of the phenyl unit led to a much softer and stickier materials than the para position. Unfortunately, the diphenyl acetylene backbone has poor charge-transport characteristics, so these materials would principally be of use for their fluorescence properties.[168]

1.2.8 Which Properties Are Desirable?

For an engineering plastic, the desired mechanical behavior is straightforward to specify. For example, automotive plastic in a dashboard must survive high temperatures in the summer, while plastic used in machinery must have high mechanical strength and temperature stability. Semiconducting polymers, however, exist as a thin film and are not expected to bear significant mechanical loads. (These polymers would not be able to do so anyhow because their electronic function requires them to be very thin.) For materials expected to endure only tensile modes of deformation (e.g., stretching and bending), it is sufficient in most cases for a material to have a low tensile modulus and high crack-onset strain. Each material in a multi-material stack will have different tensile moduli, and the magnitude of these differences will determine the interlayer stresses, which contribute to delamination. As deformation of the substrate (and encapsulant) will dictate the deformation in the active materials due to the much greater thicknesses of the substrate, the simplest route to minimizing interfacial stresses is to lower the modulus of the active material. For stretchable substrates (e.g., PDMS or thermoplastic polyurethane, $E \leq 1$ MPa), the typical modulus of an organic semiconductor would have to be lowered by several orders of magnitude to achieve the elastic response of the elastomeric substrate. For skin-wearable devices, the concept of "mechanical invisibility"—imperceptibility of

the device by the wearer—requires low stiffness, or a combination of low modulus and low thickness, and an elastic range that is commensurate with that of skin. Depending on the region on the body and the axis along which it is stretched, human skin exhibits an extensibility of ca. 30%. In all cases, the extensibility (i.e., the crack-onset strain) of the active material should be equal to or greater than that of the substrate, unless cracking itself is used as a means to impart stretchability.

In modes of deformation characterized by bending and stretching, it is the absolute extensibility prior to fracture—rather than the energy absorbed over this range—that will determine the failure of devices. It may, for example, be acceptable to have an organic semiconductor with properties resembling those of a hydrogel:[169] low modulus, large extensibility, and either low or high toughness. Modes of deformation that generate significant shear (i.e., twisting) or forces normal to the plane of the active layer, in effect require the active layer to behave as glue, and thus toughness and cohesive energy play a critical role.

Adhesion is a parameter that depends on the characteristics of both the active material and the adjacent layers.[40,115] It is critical in all forms of deformation, as strong bonding between adjacent layers can mitigate unequal elastic moduli and hold the device stack together. For obvious reasons, it increases the stability of devices in twisting and shear modes of deformation. For example, DuPont et al. found that interpenetration of PEDOT:PSS electrodes into P3HT:PCBM active layers shifts the plane in which the device stack was most likely to fracture from the interface between PEDOT:PSS and the active layer to the bulk of the active layer (**Figure 1.11a**).[115] Adhesion also plays a role in the fracture behavior within thin films under tensile and bending deformations. It is well

known that adhesion layers act to distribute strain, and mitigate cracking. Lu et al. showed that copper films on polyimide substrates could be stretched to 50% with an adhesion layer of chromium.[90] The same concept applies in organic thin films.[34] For example, PEDOT:PSS similarly behaves as an adhesion promoter for P3AT:PCBM films on PDMS.[147] Encapsulation layers also play a significant role in reducing the occurrence of cracks. For example, Sawyer et al. was able to increase the crack-onset strain of both PEDOT:PSS and P3HpT:PCBM by a factor of three simply by encapsulating the stack in an overlayer of thermoplastic polyurethane (**Figure 1.11b**).[37]

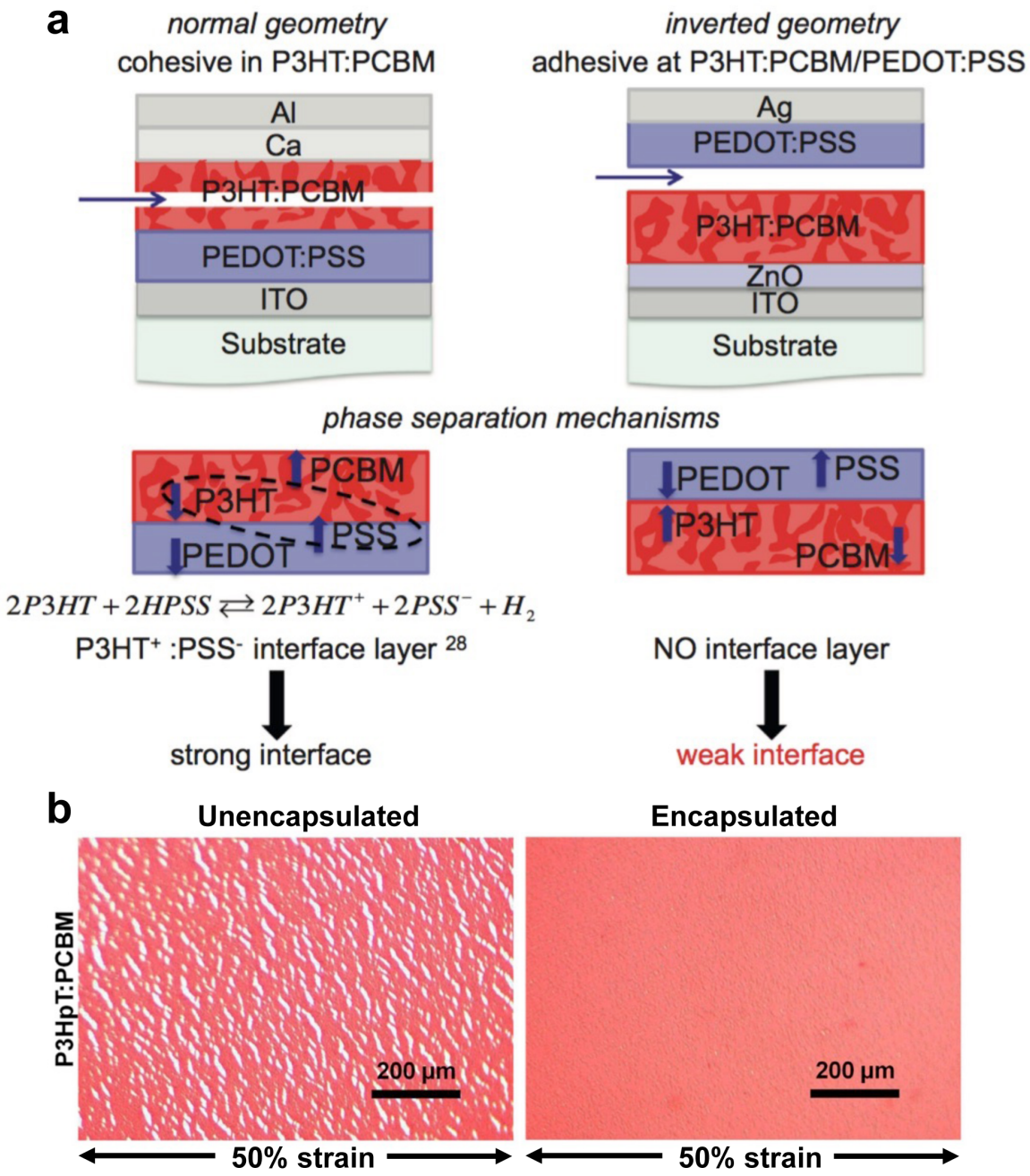

Figure 1.11. Influence of interfaces in the mechanical behavior of polymer films. (a) Interpenetration of P3HT:PCBM into PEDOT:PSS. Reproduced with permission from ref [115]. Copyright 2013, Elsevier. (b) Effect of encapsulation on the cracking behavior of P3HpT:PCBM films. Reproduced with permission from ref [37]. Copyright 2016, Elsevier.

1.3 Theoretical Models

Experimental characterization techniques have been complemented by a variety of theoretical treatments to provide a more detailed understanding of the thermal and mechanical properties of organic semiconductors. These methods range in sophistication from back-of-the-envelope calculations using semi-empirical bond-connectivity indices[155] to large-scale molecular dynamics simulations (both atomistic[25] and coarse-grained[170]) and sophisticated finite-element models for device-scale deformation and fracture phenomena.[170] Insights obtained from computation have the potential to augment the understanding of experimental findings. Computational resources available at the time of this writing[171] can simulate solid-state structures with good resemblance to experimental thin films, and are now able to make experimentally testable predictions. It can be expected that computation will play an increasing role in developing experimentally testable hypotheses, and co-optimizing the mechanical and optoelectronic properties of organic semiconductors.

1.3.1. Semi-Empirical Approaches Using Connectivity Indices

A simple model for estimating the mechanical properties of polymeric materials, using structure-property relationships, has been developed by Seitz.[155] These predictions are based on five molecular properties: the molecular weight, van der Waals volume, the length and number of rotational bonds in the repeat unit, and the glass transition temperature of the polymer. While originally developed for amorphous polymers, the method was applied successfully (though unmodified) to semicrystalline semiconducting polymers.[109] Despite the ability to predict the tensile moduli of simple polymers such as P3ATs, significant problems in predicting the properties of polymers with complex

molecular structures limit the transferability of the method.[134] Details of the implementation of this method can be found in previous publications.[34,109,155] Such simple methods are useful for quick predictions on paper—which may save researchers time in the laboratory—but are only practical for relatively simple molecular structures. For more sophisticated polymers, computation is required.

1.3.2. Molecular Dynamics Simulations of P3ATs

Molecular dynamics (MD) simulations use the numerical solution of Newton's equations of motion to model interactions between organic molecules based on semi-empirical atomistic force fields. Such simulations have been successfully used to predict the mechanical properties of conjugated polymers and composites. For polymeric systems, due to the difference in timescales between fast dynamic modes (e.g., vibrations of covalent bonds) and slow modes (e.g., reptation of chains), simulations using coarse-grained (CG) models are often used for the sake of computational efficiency. In a CG model, groups of covalently bonded atoms are mapped into representative CG beads.[172] The resolution of the model decreases when these beads are used to represent greater numbers of atoms. The resolution can range from a united-atom treatment—where all hydrogen atoms are grouped into the atom to which they are bonded[173]—to extremely coarse models in which several monomers are mapped to a single coarse-grained bead.[174] Coarse-graining thus represents a compromise between atomistic detail and computational efficiency. For example, P3HT could be simulated using a fully atomistic model (**Figure 1.12**, left), a three-site model

(middle), or a single-site model (right). A CG procedure allows for the simulation of larger systems and longer time steps than can be achieved using atomistic models.

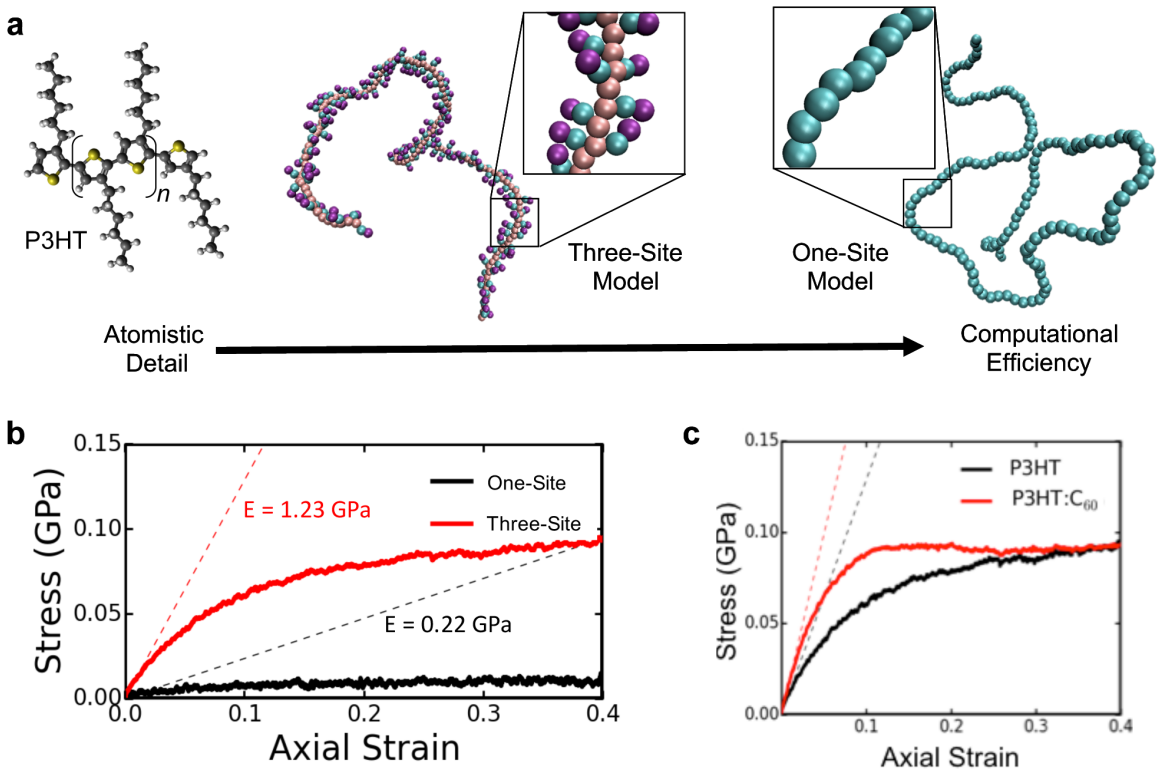

Figure 1.12. Coarse-grained molecular dynamics simulations of poly(3-hexylthiophene) (P3HT). (a) Schematic diagram showing the competition between atomistic detail and computational efficiency when one decreases the resolution. (b) Calculated stress-strain behavior of P3HT using one-site and three-site coarse-grained models. The three-site model reproduced the experimental value of the tensile modulus. (c) Calculated stress-strain behavior of P3HT and P3HT:C_{60} bulk heterojunction. The model correctly predicts the stiffening effect of the fullerene on the polymer. Reproduced with permission from ref [130]. Copyright 2016, American Chemical Society.

Tummala et al. described the first use of MD simulations to predict the mechanical properties of P3HT and its blends with fullerenes.[25] In one study, the authors used atomistic models to predict the effects of molecular weight and entanglement on the uniaxial tensile response.[170] They have additionally simulated the effect of various fullerene-based electron

acceptors on the mechanical properties of the composite film.[25] The authors found that degrees of polymerization of at least 50 were required to obtain elastic behavior. To predict the solid-state structure of larger systems comprising longer polymer chains, two CG models have been proposed: the one-site model of Lee et al.,[175] and the three-site model of Huang et al.[176 177] We compared the abilities of these two models to predict the glass-transition temperature, density, and tensile modulus of P3HT and its blend with C_{60}.[130] The three-site model gave values close to the experimentally determined values for these quantities, whereas the one-site model overestimated the density and underestimated the tensile modulus. An important observation that arose from this study was that there were a significantly lower number of calculated interior kinks per chain[178]—proportional to the density of entanglements—in the P3HT:C_{60} blend films (2.4 kinks per chain) compared to films of the neat polymer (7.0). This observation is consistent with increased brittleness that is always observed in bulk heterojunction films compared to films of pure polymers. One limitation of the CG approach is its limited transferability. When the three-site model was extended to attempt to predict the tensile modulus of P3ATs with longer side chains, the absolute values were overestimated when compared to experiment. This lack of transferability is possibly due to the inadequacy of representing the thiophene ring as a symmetrical CG bead and implies that at this level of resolution, predictive models for materials with even minor changes to the molecular structure require parameterization from atomistic simulations. Nevertheless, it seems that CG models are adequate to predict a wide range of thermomechanical properties of the P3ATs with degrees of polymerization of 150 or more. Potential future work in this area includes, simulating the effect of substrate interactions and including a realistic polydispersity in the simulations.

1.3.3. Molecular Dynamics Simulations of Low-Bandgap Polymers

Atomistic MD simulations have been applied to low-bandgap polymers exhibiting the donor-acceptor (DA) motif. Using the quantum mechanically informed force fields computed by Jackson et al., our group recently simulated the mechanical properties of PDTSTPD, PTB7, and TQ1 (**Figure 1.13a**).[105,179] These materials were chosen to represent a range of solid-state packing structures adopted by DA polymers, from the semicrystalline PDTSTPD, to PTB7, which exhibits local order, and TQ1, which is amorphous. Perhaps the most striking finding of this study was the importance of the ways in which a film solidifies from solution or from the melt influence the mechanical properties (**Figure 1.13b**). For example, we have shown that glassy morphologies of the low-bandgap polymers PDTSTPD, PTB7, and TQ1 can be prepared in two ways (**Figure 1.13c**).[105] In the first way, an equilibrated melt is quenched rapidly, to generate a thermodynamically favored glass (melt-quenched morphology). In the second way, implicitly solvated polymer molecules are permitted to self-aggregate prior to deposition (self-aggregated morphology). This process, which is intended to mimic casting from a poor solvent, generates a kinetically trapped structure. Compared to the melt-quenched morphology, the self-aggregated morphology contains a greater fraction of void space (~10% greater) and a significant reduction in the fraction of entanglements.[105] These two structural features are predicted to decrease the elastic modulus and extensibility.

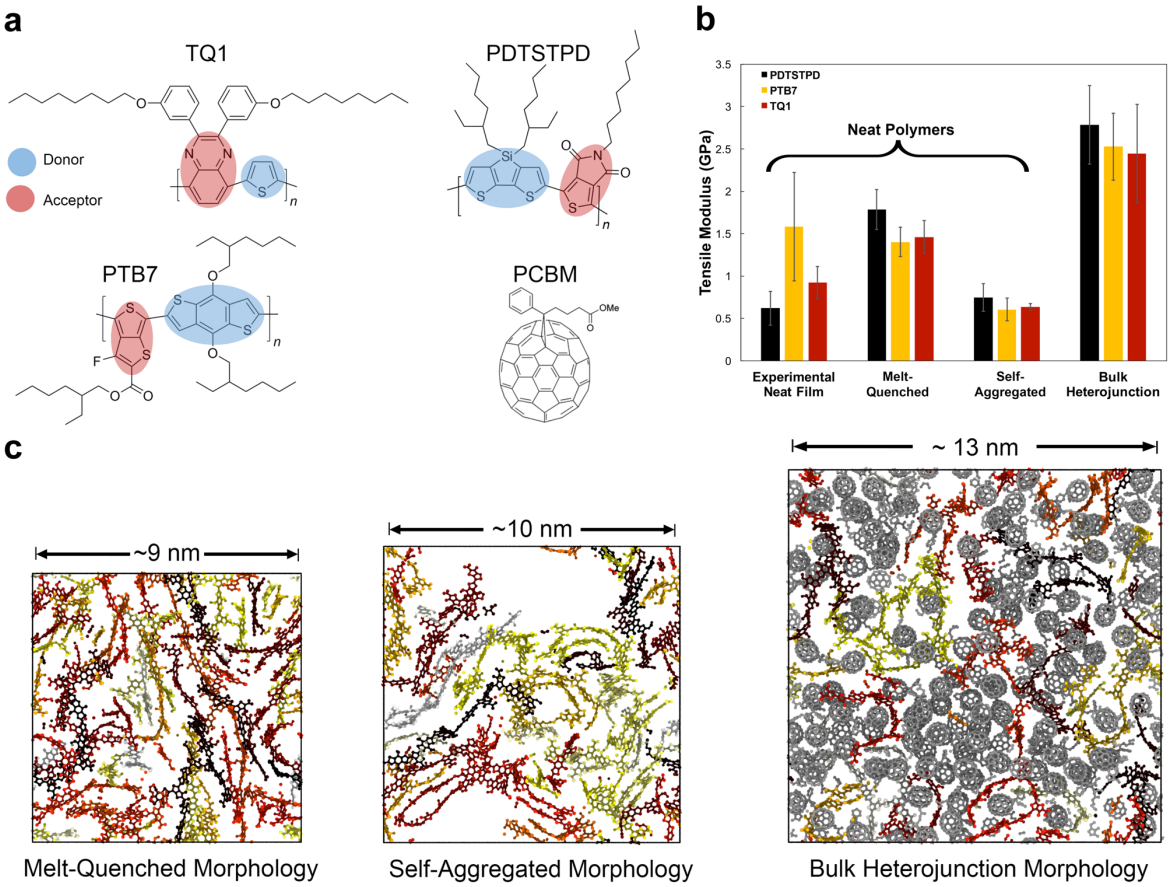

Figure 1.13. Atomistic molecular dynamics approaches to predicting the mechanical behavior of donor-acceptor polymers and bulk heterojunction films. (a) Molecular structures of the structures simulated. (b) Tensile moduli of the three conjugated polymers grouped by the way in which the solid films were prepared. The bulk heterojunction of the polymers mixed with PCBM is also shown. (c) Visualization of the melt-quenched, self-aggregated and bulk heterojunction morphologies. Reproduced with permission from ref [105]. Copyright 2016, Royal Society of Chemistry.

1.4. Mechanical Properties of Conjugated Polymers

This section is the first of three (4–6) that focus on particular classes of organic semiconductors. In this section, we examine the most attractive from a mechanical stability standpoint: conjugated polymers. Important differences between conjugated polymers and engineering plastics—e.g., polyolefins—suggest that lessons learned from many years of research in the polymer research community to increase the elasticity and toughness of

materials are not directly applicable to organic semiconductors, in part because of the requirement that elastic and tough conjugated polymers must retain charge transport properties. Significant work has been done in the last three years to elucidate the effects of molecular structure on the bulk properties in the categories of molecular parameters covered in this section.

1.4.1 Molecular Weight

Along with molecular structure, the most important molecular parameter used to improve the mechanical performance of commodity polymers and engineering plastics is molecular weight. The molecular weight of a polymer is most commonly described by one of two measures, the number-average molecular weight (M_n) and the weight-average molecular weight (M_w). The M_n is a conventional average. It is obtained by summing the molecular weights of every molecule in the system, and dividing by the number of molecules. It can be an inaccurate predictor of the mechanical properties of a polymeric sample, however, because one or more fractions with a given molecular weight may comprise the bulk of the weight of the entire sample. (For example, a system comprising a single chain with a molecular weight of 1000 kDa, and ten unreacted monomers.) The M_w, on the other hand, is biased toward the fraction of the sample with the greatest molecular weight, and is thus a more accurate predictor of the mechanical properties of the system. The two molecular weights are calculated using the equations below:

$$M_n = \frac{\sum M_i N_i}{\sum N_i}$$

$$M_w = \frac{\sum M_i^2 N_i}{\sum M_i N_i}$$

In these equations, i is the degree of polymerization, and thus M_i and N_i are the weight and number of molecules with degree of polymerization i. As M_w is always greater than M_n, the ratio of M_w/M_n is greater than 1, and this quantity is termed the dispersity ($Đ$), which reflects the narrowness of the distribution in molecular weight for a given sample.

The principal effect of the molecular weight on the mechanical properties is to increase its strength and toughness by increasing the density and quality of entanglements. The effects of molecular weight on the mechanical properties have been characterized most thoroughly for P3HT (see **Figure 1.7**). These properties have been assayed by traditional pull testing of bulk samples,[36] but also on thin films using the film-on-water and film-on-elastomer techniques.[139] Pull testing of bulk samples revealed similar moduli for samples from 20 to 110 kDa, though the high molecular weight samples (90 and 110 kDa) exhibited very high extensibilities (nearly 300%) prior to fracture, with the greatest toughness for the 110 kDa sample.[36] A similar trend was observed for films tested while suspended on water. In that case, the modulus increased with molecular weight, but saturated at approximately 40 kDa, while the maximum extensibility increases (>100%) for 80 kDa, the highest molecular weight tested.[139] Results from pull testing mirrored the key features of those obtained using film-on-elastomer methods. However, the compressive mode of deformation used in the buckling technique produced values of moduli that were 3-6 times greater than those obtained using pull testing. Microstructurally, low molecular weight is correlated with the presence of highly ordered needle-like aggregates, which in principle could stiffen the films. However, the opposite effect is usually observed, and some high-molecular-weight samples exhibit significant aggregation characteristic of extensive π-stacking.[139]

We close this section with a caveat on measuring molecular weights. Because of the ubiquity of the equipment and experimental simplicity, it is common practice to measure M_n and M_w using size-exclusion (gel-permeation) chromatography (SEC or GPC), which uses a column filled with porous beads. The molecules with the largest hydrodynamic volumes bypass a large fraction of the pores, and thus have the smallest retention time (i.e., they elute first). Conversely, molecules with the smallest hydrodynamic volumes have the longest integrated pathways through the pores, and elute later. The apparatus is calibrated using polystyrene samples of molecular weights that are well known (i.e., by light scattering). As SEC/GPC provides a measure of the hydrodynamic volume—not the molecular weight—the technique is subject to inaccuracies when the solution-phase conformations of the polymers under study are significantly different from those of the standards. This procedure overestimates the molecular weight of conjugated polymers by a factor of approximately 2,[180] because these structures adopt an extended conformation in solution, i.e., when the molecular weights of rigid conjugated polymers are compared to standards that adopt ideal random coils in solution. Heeney and coworkers found that the molecular weights of P3HT are overestimated by a factor of 1.67 when the results of SEC/GPC are compared with those of NMR or matrix-assisted laser desorption ionization time-of-flight secondary ion mass spectrometry (MALDI-TOF-SIMS).[181] Since P3HT is expected to be more flexible than most donor-acceptor polymers (which contain fused rings and significantly higher barriers to rotation), the factor by which the molecular weight determined by SEC/GPC is greater than the actual molecular weight is expected to be greater than 1.67.

1.4.2 Entanglements

The excluded volume of long polymer chains gives rise to a structure in the solid and melt phase in which the molecules can be highly entangled, as chains can slide past, but not through, each other. Consequently, the motion of an individual polymer chain consists of reptation through a tube-like region along the chain contour called a primitive path.[182,183] Interior kinks are defined as nodes along the primitive path that represent the limit to which the contour can be reduced to a minimum length without violating the topological constraint of excluded volume of the chains.[178] The density of entanglements is proportional to the number of interior kinks per chain, and can be quantified in MD simulations using the Z1 algorithm of Kröger and coworkers.[184,185] This quantity thus increases with degree of polymerization, and it manifests physically in the rheological properties of polymer melts and solutions, and in the mechanical properties of solid films. A polymeric solid with a highly entangled microstructure exhibits high viscosity, tensile strength, toughness, and extensibility. A metric that describes the likelihood that a polymeric sample will exhibit entanglements is termed the entanglement molecular weight, which is believed to have a value of ~10 kDa for P3HT in principle, though ~20 kDa as typically measured by GPC. The density of entanglements is also affected by blending, and a MD study by our laboratory showed that BHJ films of P3HT:PCBM are significantly less entangled than pure P3HT. This finding is consistent with increased brittleness of the BHJ relative to the pure polymer. Polymers such as donor-acceptor materials, which have substantially greater radii of gyration than P3HT with a similar contour length, also exhibit entanglements (**Figure 1.14**), the density of which depends strongly on the way in which the solid film was formed. For example, MD simulations predict that a thermodynamic

glass prepared by quenching an equilibrated melt structure will exhibit a significantly greater density of entanglements than a solid structure prepared by depositing pre-aggregated polymer chains from solution (i.e., from a poor solvent). These simulated results in particular suggested prescriptions for increasing the entanglement density—and hence the mechanical stability—through the judicious choice of solvents and thermal treatments.

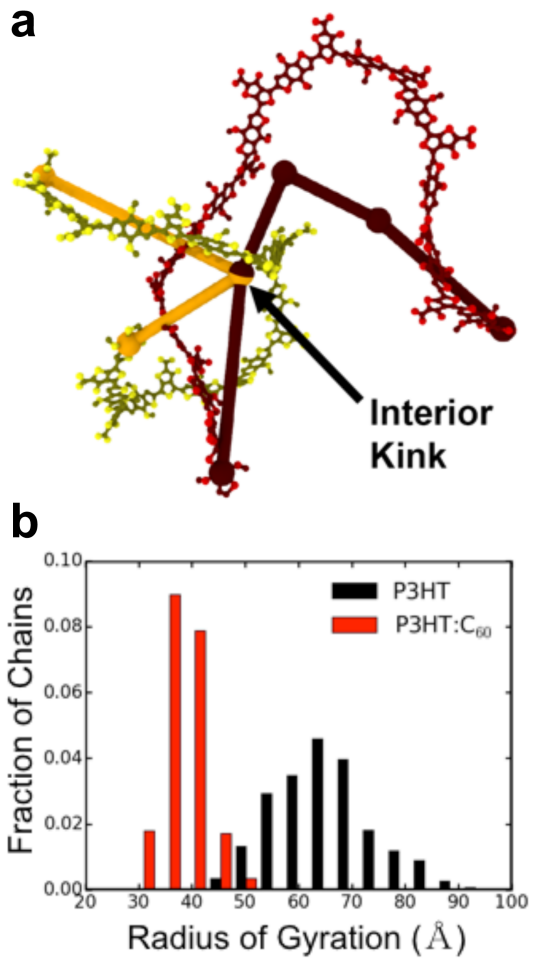

Figure 1.14. Entanglements and radius of gyration. (a) Graphical representation of interior kinks as the intersection of the primitive paths for two polymer chains. Reproduced with permission from ref [105]. Copyright 2017, Royal Society of Chemistry (b) Fraction of polymer chains as a function of radius of gyration for both pure P3HT and the P3HT:C_{60} bulk heterojunction. Reproduced with permission from ref [130]. Copyright 2016, American Chemical Society.

1.4.3 Side-Chain Length, Branching, and Attachment Density

The unsubstituted π-conjugated main chain of a semiconducting polymer is generally insoluble. To render semiconducting polymers soluble, alkyl side chains are usually attached. Side chains afford solubility by reducing strong van der Waals forces between the main chains, and also permit greater entropic freedom of the polymer structure in the solution phase.[186] These side chains also have a strong effect on the thermomechanical properties.[32] In general, the effect of increasing lengths of side chains is to decrease the tensile modulus and increase the crack-onset strain for materials with a common backbone structure and similar molecular weights. This effect was observed strikingly in both regiorandom[33] and regioregular[34] P3ATs, as the tensile modulus was found to decrease significantly from poly(3-butylthiophene) to poly(3-dodecylthiophene), the material with the longest side chain tested.[133] The decrease in tensile modulus, and increase in extensibility, mirrored a similar trend in glass transition temperature, which decreases with increasing length of the side chain.[133] The intuitive rationale for the decrease in glass transition temperature and increase in softness is similar to its effect on solubility: longer side chains decrease the van der Waals energy between the main chains, and in the case of mechanical deformation, reduce the density of load-bearing carbon-carbon bonds along the strained axis.[32]

For regioregular P3ATs, the largest reduction in stiffness and increase in extensibility with increasing length of the side chain occurs between P3HT and P3HpT, where Hp = heptyl (see **Figure 1.6a**).[134] This behavior is reflected in the glass transition temperature. In particular, the T_g of P3HT is ca. 12 °C, while that of P3HpT is ca. –5 °C, significantly below room temperature.[133] Given this extensibility, P3HpT:PCBM has been

used in the active layer in the first solar cell in which each polymeric component is an elastomer[37]—i.e., an "all-rubber solar cell"—and P3OT has been used in biaxially stretchable solar cells that can be bonded to hemispherical surfaces without cracking or wrinkling.[147] Copolymers that exhibit side chains of mixed lengths have also been examined for their mechanical properties. Savagatrup and Printz et al. measured the tensile moduli of block and statistical copolymers of poly(3-hexylthiophene) and poly(3-octylthiophene), along with physical blends of these materials.[134] This approach produced compromises—as opposed to the "best of both worlds"—between mechanical deformability and optoelectronic properties. Recently Smith et al. have reported a detailed study of a series of rr-P3ATs with randomly incorporated unsubstituted thiophene units.[164] The authors found that 1:1 random copolymer containing P3DDT and PT led to a co-optimization of the electrical and mechanical properties. Compared to the P3DDT homopolymer, there was approximately a 5-fold increase in both the conductivity and mobility. This improvement in electrical performance was accompanied by a 760% increase in toughness.[164] This study clearly demonstrated the importance of side chain length, and grafting density on the bulk material properties.

The effects of side chains on the mechanical properties of semiconducting polymers with molecular structures that are significantly more complex than P3AT have also been studied. With these materials too, one finds a strong role of side chains. Savagatrup et al. measured the tensile modulus and crack-onset strains of a library of over 50 low-bandgap polymers,[108] whose photovoltaic properties were described by the Krebs laboratory[187] (**Figure 1.15**). A trend in the data was increased deformability for polymer structures bearing branched side chains, as opposed to linear ones. An interesting historical note is

that the softening effect of the side chains in comb-like polymers included for processability was regarded as catastrophic for materials intended for structural applications.[32] In the case of deformable organic semiconductors, however, we argue that increased compliance and extensibility produced by side chains is desirable.

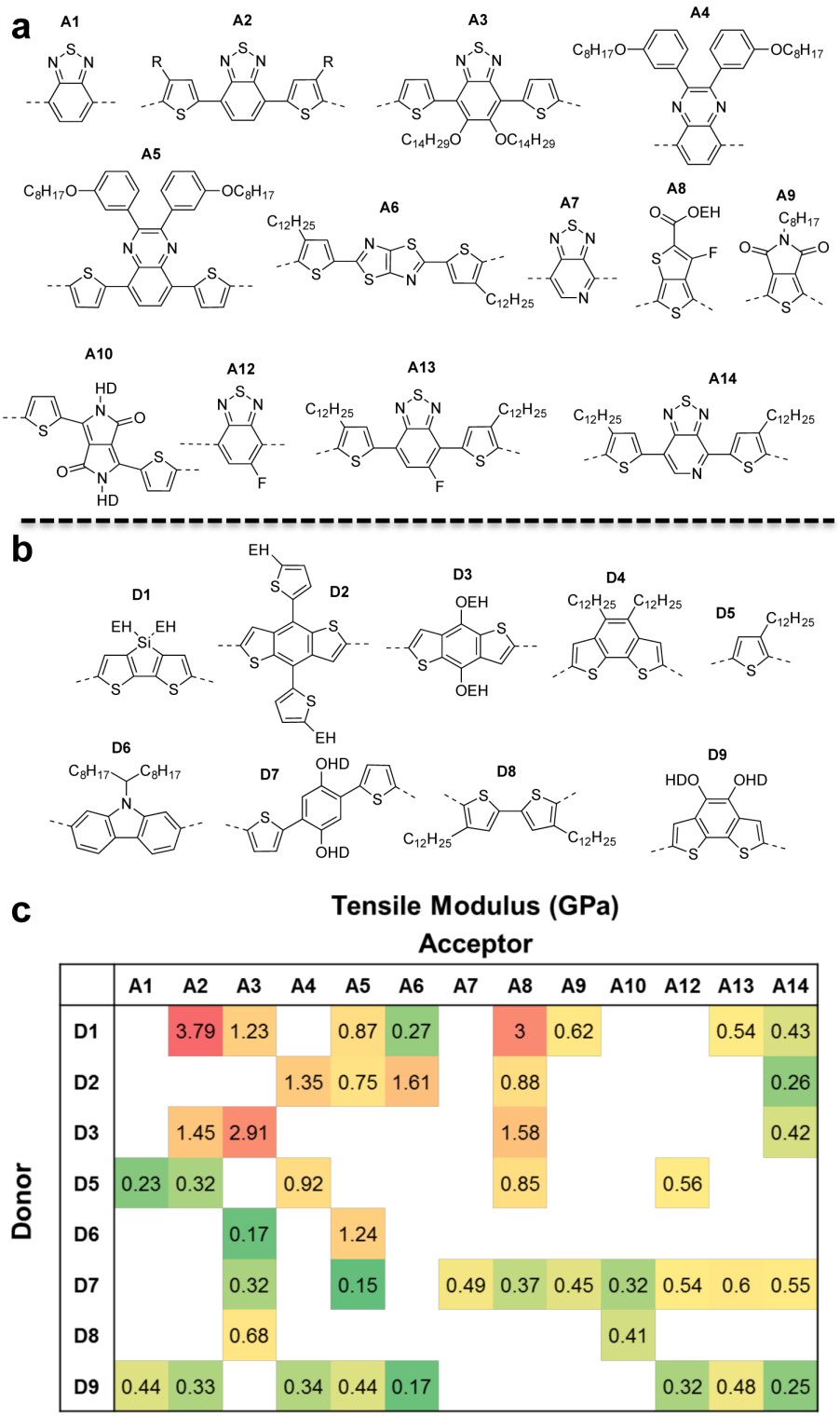

Figure 1.15. Structures of acceptor (a) and donor (b) units, and mechanical properties (c), of low-bandgap library. Reproduced with permission from ref [108]. Copyright 2016, American Chemical Society.

1.4.4 Regioregularity

In the early 1990s, McCullough[188,189] and Rieke[190] independently published methods leading to the regioregular synthesis of P3ATs (rr-P3ATs, in which the monomers are all coupled with the same head-to-tail configuration such that all of the side chains point in the same direction). Given a large improvement in conductivity, mobility, and performance in solar cells of rr-P3ATs compared to regiorandom material (rra-P3AT), there has been limited interest in materials exhibiting less-than-high regioregularity. The principle way in which regiorandom couplings reduce the abilities of these materials to transport charge is to twist the backbone out of planarity, and thus decrease the bandgap and mobility. Increased flexibility of the chains also prevents crystallization—rra-P3ATs are amorphous[141]—and also has a softening effect on the solid films. Kim and coworkers recently published a study in which the regioregularity of P3HT was varied from 64% to 98%.[114] They observed a monotonic increase in both the degree of crystallinity, from 0% to 48.4%, and hole mobility, from 4.84×10^{-8} cm^2 V^{-1} s^{-1} to 1.81×10^{-1} cm^2 $V^{-}1$ s^{-1}.[114] These increases in crystallinity and mobility were coupled with a decrease in the extensability from 5.3% to 0.6% and an increase in the tensile modulus from 13 MPa to 287 MPa, indicating that as regioregularity increased and ordering improved, the films became less soft and more brittle.[114]

1.4.5 Main-Chain Rigidity: Fused Rings, Isolated Rings, and Aliphatic Spacers

One would expect based on intuition that the deformability of the solid film would be a manifestation of the flexibility of the individual polymer chains. This intuition has been supported in a few studies, but the conclusions are not easily generalizable. In one of

the first contributions to the field of intrinsically stretchable organic semiconductors, Müller et al. synthesized a block copolymer of polyethylene and P3HT. Films of these materials exhibited still-unmatched extensibilities (up to 600%), and retained charge-carrier mobilities of up to 2×10^{-2} cm^2 V^{-1} s^{-1} with as great as 90 wt % of the insulating fraction.[24] For polymers in which every atom in the backbone is conjugated, much less is known. The deformability of PBTTT—which contains the fused thienothiophene (TT) unit—is substantially less than that of P3HT, as noted by O'Connor et al.,[31] but a direct comparison of the effect of the rigidity of the backbone is problematic because the space provided by the unsubstituted TT unit permits intercalation of the side chains of PBTTT, which also increases the stiffness and brittleness (**Figure 1.16a**). In an early measurement involving low-bandgap polymers comprising the DPP unit, Lipomi et al. observed that the incorporation of the TT unit produced a somewhat (~25%) lower modulus than the bithiophene (2T)-containing polymer.[158] In a large-scale screening of a combinatorial library of low-bandgap polymers, it was again observed that structures comprising fused rings were stiffer and more fragile than similar compounds with isolated rings.[108] While this effect is intuitive and provides a foundation for future work in this area, it should be noted that other parameters, e.g., molecular weight, were not rigorously controlled. In a more controlled study, Lu et al. reported a detailed characterization of a series of DPP-based polymers containing tetrathienoacene units.[191] They found that the addition of an extra unsubstituted thiophene spacer along the conjugated improved the ductility (in comparison to a control without the spacer), enabling the film to accommodate up to 40% strain without cracking. The improved ability to accommodate strain while retaining good charge-transport characteristics was attributed to an increased propensity for edge-on

backbone configurations compared to the control which exhibited a bimodal distribution of crystallite orientations.[191]

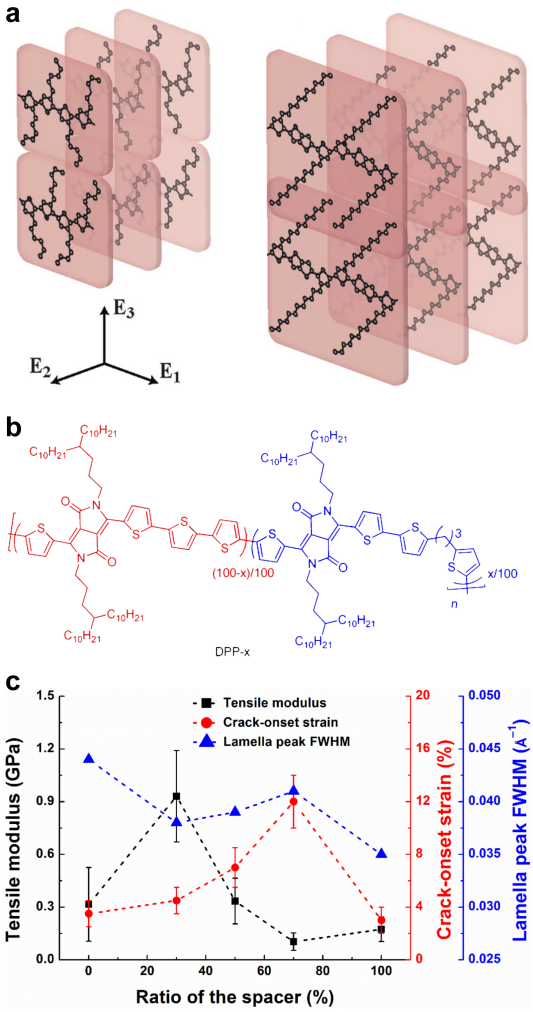

Figure 1.16. Effect of interdigitation of side chains on the mechanical properties of conjugated polymers. (a) The non-interdigitated structure of P3HT (left) and the interdigitated structure of PBTTT. Reproduced with permission from ref [31]. Copyright 2010, American Chemical Society. (b) The structure of polymers bearing flexible conjugation-break spacers. (c) Tensile modulus, crack-onset strain, and lamellar full width at half maximum (FWHM) vs. ratio of the conjugation break spacer. Reproduced with permission from ref [28]. Copyright 2016, Wiley-VCH Verlag, GmbH & Co. KGaA.

Recently, Mei and coworkers introduced the concept of conjugation-break spacers (CBSs) to increase the flexibility of DPP-based low-bandgap polymers. A series of polymers starting with the fully rigid DPP-0 and the fully flexible DPP-100 containing aliphatic propylene groups in every repeat unit (**Figure 1.16b**).[192] The hypothesis was that such flexible units would increase the entropy of the melt phase compared to fully conjugated analogues, and thus decrease the melting temperature (T_m).[192] Because of the rigidity of most conjugated polymers, they tend to decompose at a lower temperature than that at which they melt. The high melting temperatures of conjugated polymers precludes possible benefits of melt processing—e.g., highly crystalline samples crystallized from the melt, injection molding, hot embossing, and extrusion-based printing. Savagatrup et al. hypothesized that the melt-processible films containing the flexible CBS units would produce a deformable thin film.[28] What was found instead (**Figure 1.16c**) was that the fully flexible DPP-100—which contains an aliphatic spacer within every monomer residue—formed the stiffest, most brittle solid! This finding was rationalized by comparison to GIXS data, which showed that the DPP-100 had the smallest lamellar spacing (and thus possibly interdigitation the strongest secondary interactions between the main chains) and the greatest lamellar order (smallest full-width at half maximum, FWHM). This study highlights the dual roles of the main chain, as it simultaneously determines the flexibility of the isolated molecules—which is easy to predict—and also the solid-state packing structure—which is not.[28]

The concept of a conjugation-break spacer has also been explored by the Bao laboratory.[106] Aliphatic spacers along the axis of the conjugated backbone were first employed to improve the solution processibility of isoindigo based conjugated polymers

without compromising device performance.[106] This concept was further expanded upon through the synthesis a series of DPP-based polymers were synthesized with a variety of conjugation-break spacers containing different molecular structures.[102] The hypothesis was that the addition of chemical moieties with the ability to form dynamic non-covalent crosslinking sites would help dissipate mechanical energy due to tensile loading and potentially enable self-healing properties. The authors found that the incorporation of a 2,6-pyridine dicarboxamide unit as the conjugation-break spacer along the backbone (10 mol%) led to the best improvement in extensibility without a significant sacrifice in the charge transport properties. Additionally, this material was reported to exhibit healing characteristics when a damaged film was exposed to high temperature and solvent vapor.[102]

1.4.6 Small-Molecule Additives

One commonly used strategy in polymer engineering to increase the deformability of the solid is the use of plasticizers. These compounds are small molecules—e.g., phthalates—that suppress the T_g by increasing the free volume, and produce a concomitant increase in the compliance and extensibility. Semiconducting polymers are frequently processed with small molecule additives, especially in solar cells. These compounds, which have included 1,8-dithiooctane[193] and diiodooctane,[20] and low-molecular-weight PDMS,[194] have various effects that under favorable circumstances promote the formation of an ideal donor-acceptor morphology between the conjugated polymer and electron acceptor, typically a methanofullerene. Several of these compounds have also been found to have a plasticizing effect on bulk heterojunction films of P3HT:[60]PCBM.[34] It is unclear, however, if the plasticizing effect is because of the effect of the additive on the morphology, or because additive remaining in the film behaves as a conventional

plasticizer. It is possible that both mechanisms are operative. We will return to the effects of plasticizers, namely the strong effect of Capstone (formerly Zonyl) fluorosurfactant on the deformability of PEDOT:PSS,[104] and of polystyrene additives on bulk heterojunctions consisting only of semiconducting small molecules.[118]

1.4.7 Special Case: PEDOT:PSS

The conductive polyelectrolyte complex known as poly(3,4-ethylenedioxythiophene):poly(styrenesulfonate) (PEDOT:PSS) is ubiquitous in organic electronics.[98,99,195-199] This material consists of long chains of PSS^- complexed with shorter chains of $PEDOT^+$,[200] and in neat form exhibits stiff, brittle behavior characteristic of PSS.[104] Several stretchable composite materials have been generated using PEDOT:PSS as the conductive phase, and an elastomeric component as the stretchable matrix.[201,202] While the mechanical properties of neat PEDOT:PSS are unfavorable,[104] it is only moderately conductive in its native state (<1 S cm^{-1}), and is thus nearly always processed with a high-boiling, polar additive, such as dimethylsulfoxide (DMSO). This solvent has the effect of encouraging the growth of conductive PEDOT grains;[203] increased percolation improves the conductivity of the film (>1000 S cm^{-1}). PEDOT:PSS is coated as a commercial suspension in water, and thus cannot be printed on hydrophobic substrates. In order to decrease the surface tension, PEDOT:PSS is often mixed with a fluorosurfactant of the general form $CF_3(CF_2)_n(CH_2CH_2O)_mH$ (called Capstone by DuPont, formerly called Zonyl), which in small weight fractions (≥0.1%) permits wetting on hydrophopic substrates.[204,205] These additives—DMSO and Capstone—are ubiquitous in the solution processing of PEDOT:PSS, and also have effects on the mechanical properties. In particular, DMSO has a small stiffening and embrittling effect, which is overwhelmed by

the strong plasticizing effect of the fluorosurfactant.[104] This additive, in concentrations between 1% and 10%, has the effect of decreasing the tensile modulus by a factor of 100, and the extensibility by a factor of 10.[104]

1.4 Mechanical Properties of Small-Molecule Semiconductors

This section focuses on molecular semiconductors, which have purported advantages of high purity, monodispersity, and high crystallinity. The absence of entanglements and other morphological features of polymers that confer mechanical benefits have suggested that solid films of molecular materials could not be deformed significantly. Recent work, however, suggests that while the energy required to deform or fracture these materials is lower than that of polymers, the range over which these materials can be deformed is quite high (>10% for some materials), but only if the molecules contain solubilizing pendant groups.[118] The role of the substrate and encapsulant to bear mechanical loads partially reduces the requirement that the active materials themselves be strong or tough. The small amount of energy required to deform or fracture films of small-molecule semiconductors relative to polymers thus does not imply that small molecules cannot be used for deformable applications. This section discusses the molecular mechanisms by which van der Waals solids, such as these, accommodate mechanical energy.

1.5.1 Unsubstituted Acenes

The semiconducting cores of small-molecular semiconductors tend to comprise multiple fused rings. An early calculation of the tensile modulus of naphthalene and anthracene produced values of 8.1 and 8.4 GPa.[206] Tahk et al. measured the mechanical properties of a vapor deposited thin film of pentacene using the buckling technique.[109]

While the film cracked extensively under the small compressive strains (<4%) required for the measurement, the authors were nevertheless able to extract a value for tensile modulus of 16 GPa, one of the highest values ever measured for an organic semiconductor. Pendant groups, installed on conjugated cores for solubility, increase the free volume in solid films and permit greater deformability. The modulus of TIPS-pentacene is only 3.0 GPa, as measured by the buckling technique.[118] Cun et al. used a combination of STM and density functional theory (DFT) calculations to determine a modulus of *N,N'*-dihexadecyl-quinacridone—whose conjugated core is isosteric with pentacene—of 0.92 GPa.[207]It thus seems from these measurements that the newest generation of low-bandgap small-molecule semiconductors (which all bear pendant groups) would have significant deformability.

1.5.2 Solution-Processable Small Molecules

Our research group recently measured the mechanical properties (modulus and crack-onset strain) for several high-performance small-molecule organic semiconductors (**Figure 1.17**).[118] There materials were the electron donors SMDPPEH and DTS($FBTTh_2$)$_2$, and the acceptors HPI-BT and $PC_{71}BM$. We also measured the mechanical properties of the donor:acceptor blends, and determined the effect of additives (diiodooctane and polystyrene) on the properties of BHJ films of DTS($FBTTh_2$)$_2$:$PC_{71}BM$. For all small-molecule films beside $PC_{71}BM$, we found surprisingly low tensile modulu (<3 GPa) and high crack onset strains (>5%, and as high as 14.28% for DTS($FBTTh_2$)$_2$).[118] We attributed the ability of these materials to accommodate such large plastic deformations by molecules sliding past each other in the solid films, as facilitated by the presence of alkyl pendant groups. Blending the two donor materials with $PC_{71}BM$ had the effect of increasing the modulus and lowering the crack-onset strain, which is also observed in polymer:fullerene

BHJ films. While blending of the two donor materials with HPI-BT produced compliant (<1 GPa) and ductile (7-12% strain) films, they were not efficient (*PCE* < 1%), though there are potentially many alternative non-fullerene acceptors. The deformability of DTS(FBTTh$_2$)$_2$:PC$_{71}$BM films could be increased somewhat to a maximum of 4.67% strain with a corresponding modulus of 12.5 GPa using diiodocotane and polystyrene with a molecular weight of 900 kDa.[118] While the extensibility of DTS(FBTTh$_2$)$_2$ is promising for some applications, more work is required to understand the molecular mechanisms for the accommodation of plastic strain without cracking.

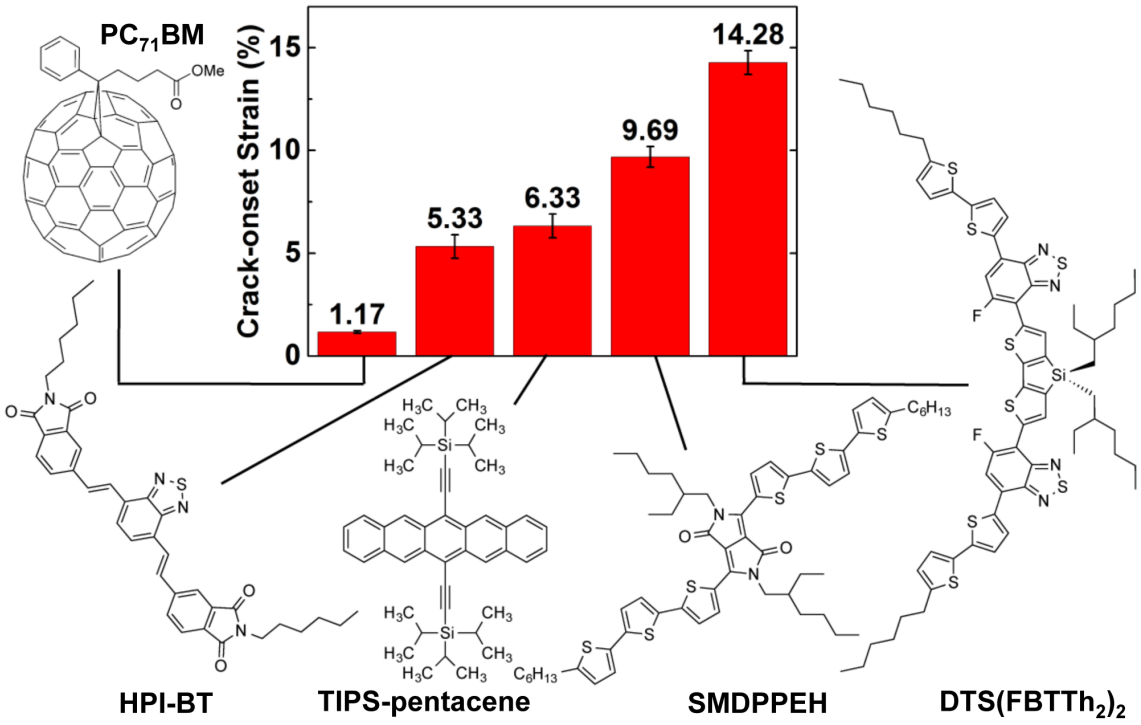

Figure 1.17. Crack-onset strains of several solution-processible semiconducting small molecules. Reproduced with permission from ref [118]. Copyright 2016, American Chemical Society.

1.5.3 Fullerenes and Soluble Fullerenes

By far the most common electron-transporting materials in organic electronics are fullerenes. These materials have the advantage of high electron mobilities and solubilities when appropriately derivatized, as in the methanofullerene $PC_{61}BM$. In solar cells, soluble fullerenes often adopt a ternary morphology with conjugated polymers—comprising fullerene-rich, polymer-rich, and mixed phases—that are beneficial for charge separation.[44,47,208,209] Unfortunately, solid films of pure methanofullerenes such as $PC_{61}BM$ and $PC_{71}BM$ have high moduli and crack and very low strains.[142] For example, pure films of $PC_{61}BM$ were measured to have a tensile modulus of 25.6 GPa, and a crack-onset strain of 3.5%.[142] Owing to its oblong shape and the fact that it exists as a mixture of isomers, films of $PC_{71}BM$ are more deformable (modulus of 5.39 GPa and crack-onset strain of 5.25%).[142] Given the observation that some disorder may actually be beneficial for lowering the modulus and increasing the extensibility, we tested the hypothesis that blending $PC_{61}BM$ with $PC_{71}BM$ would produce films with increased deformability compared to pure films of either material. This outcome would be beneficial for an additional reason in that "technical grades" of methanofullerenes, which are incompletely separated (but otherwise pure) blends of the two materials.[142] Indeed, the maximum extensibility (14.7%) was achieved for a 1:1 mixture, and the lowest modulus (5.13 GPa) was achieved for a technical grade comprising 93.5% $PC_{71}BM$ and the remainder $PC_{61}BM$.[142] We attributed the increased deformability of the blends to void space created by inefficient packing of dissimilar molecules. While the mechanical properties of films of pure fullerenes and their derivatives are not favorable, simple modifications can recover some deformability.

1.6 Composite Systems

This section describes the mechanical properties of blends of polymers, and of polymers with small molecules. The importance of composite films is exemplified by the bulk heterojunction—e.g., blends of conjugated polymers with methanofullerenes—used in organic solar cells.[210,211] Composite structures introduce additional challenges and constraints to the goal of maximizing the deformability of the active layers without sacrificing electronic performance. Some small molecules behave as plasticizers in a polymeric matrix; others behave as anti-plasticizers. In fact, the stiffening and embrittling effects of fillers can have multiple origins. The details of molecular recognition (i.e., whether or not a small molecule intercalates in a regular way between the side chains of a polymer[117,212,213]) also have an effect on the mechanical properties of the bulk structure.[214] This section describes the molecular and microstructural bases for the mechanical properties of composite films compared to those of the pure components. To avoid repetition, interested readers are referred to the discussion of composite systems comprising two small molecules in Section 5.2.

1.6.1 Polymer:Fullerene (Bulk Heterojunction) Composites

One of the most well known classes of organic electronic devices is the organic solar cell (OSC).[215] The active layer of an OSC comprises an electron-donating material and an electron-accepting material. In the vast majority of devices, the donor is a semiconducting polymer and the acceptor is a methanofullerene (e.g., $PC_{61}BM$), which can be present in amounts as great as 80%, by weight.[216] The mechanical properties of the methanofullerene thus have a strong effect on the deformability of the composite film, called the bulk heterojunction (BHJ).[34,109] The current model for the solid structure of the

BHJ for many systems of polymers and fullerenes (exemplified by P3AT:PCBM) comprises three phases: an ordered polymer phase, a fullerene-rich phase, and a mixed phase.[45] Methanofullerenes in general behave as anti-plasticizers for conjugated polymers.[142] That is, they lower the glass transition temperature of the blend, increase the elastic modulus, and decrease the crack-onset strain.[133,142]

The effect on the mechanical behavior can be predicted using a simple composite theory first applied to the bulk heterojunction by Khang and coworkers.[109] This theory includes a large role for the mechanical properties of the filler itself, in this case, the methanofullerene. As we have seen in Section 5.3., the mechanical properties of pure methanofullerenes vary on the basis of the size and shape of the fullerene—e.g., films of $PC_{71}BM$ are more deformable than $PC_{61}BM$—and also by the extent of separation between fullerenes of different sizes and shapes. That is, deformability is maximized with some intermediate combination of $PC_{71}BM$ and $PC_{61}BM$, which can be obtained naturally in an incompletely separated sample—so-called "technical grade" material.[142] The mechanical properties of the pure films thus influence the mechanical properties of the BHJ, and even the microstructure of the polymeric phase. Analysis of the UV-vis spectra of P3HT with different blends of methanofullerenes, ranging from pure $PC_{61}BM$ to pure $PC_{71}BM$, showed that technical grades of $PC_{71}BM$ (contaminated with 6.5% $PC_{61}BM$) had a favorable combination of deformability and power conversion efficiency (*PCE*). Interestingly, analysis of the UV-vis spectra of these BHJ films using the weakly interacting H-aggregate model revealed that the order in the polymer phase was correlated with order in the fullerene phase (**Figure 1.18**).[142] It is possible that reduced order in the polymer phase allowed recruiting of polymer chains from the polymer crystallites into the

disordered mixed phase because of the partial miscibility of the fullerene and amorphous polymer. Increased deformability for BHJs comprising incompletely separated fullerenes may thus arise from two effects: inefficiently packed fullerene in the fullerene-rich phases and reduced aggregation of the polymer phases. The net effect of the fullerenes on the mechanical properties of the BHJ is still nonetheless deleterious, and these effects amount to one of the reasons that the research community is seeking non-fullerene acceptors (NFAs),[217] some of which have achieved performance equal to that of fullerenes in solar cells.[218] As of this writing, the mechanical properties of polymer:NFA BHJs have not been explored.

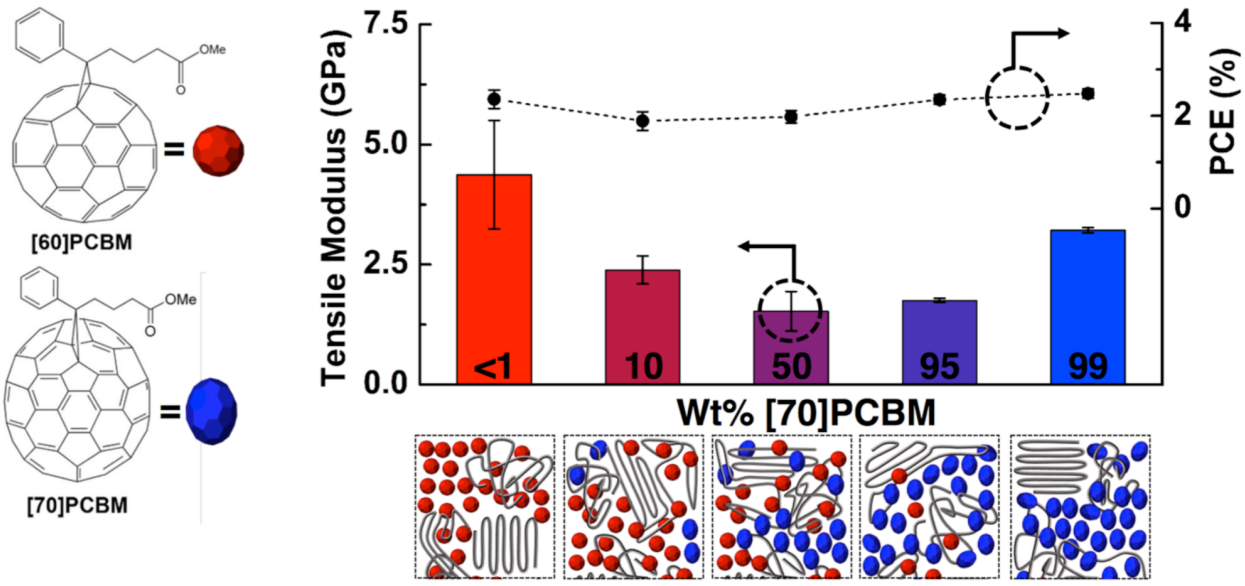

Figure 1.18. Tensile modulus and power conversion efficiency of P3HT:PCBM blends with different weight fractions of $PC_{71}BM$. Reproduced with permission from ref [142]. Copyright 2015, American Chemical Society.

1.6.2 Polymer:Polymer Composites

The favorability of the mechanical properties of polymeric materials derive from their high degrees of polymerization, which facilitates coordination of many van der Waals interactions along adjacent molecules, along with entanglements. It is thus reasonable that using an all-polymer blend would lead to a significantly more deformable semiconducting composite—i.e., for solar cells—than one in which one of the components was a small molecule. The Kim group recently described the mechanical properties of a blend of PBDTTTPD (donor) and P(NDI2HD-T) (acceptor) for an intrinsically stretchable solar cell, and measured the mechanical properties of the blend using the film-on-water method.[111] The all-polymer active layer exhibited a maximum extensibility of 7.2% and tensile modulus of 0.43 GPa, compared to 0.12% and 1.76 GPa for the PBDTTTPD:$PC_{61}BM$ film (**Figure 1.19**).[111] Moreover, the blend containing $PC_{61}BM$ exhibited significantly increased brittleness.

Blends of polymers have also been investigated as a means improve the extensibility of organic semiconductors for transistor applications. The O'Connor group recently reported a new composite design strategy in which a brittle high performance donor-acceptor polymer (PCDTPT) was blended with a more ductile semiconducting polymer (P3HT) to improve extensibility without sacrificing the charge-transport characteristics.[219] When supported by an elastomeric substrate, the composite was shown to reversibly orient and relax under large tensile strains up to 75% and up to 100 strain cycles. When subsequently transferred to a rigid test bed, the film was shown to exhibit high charge-carrier mobility in both an unstrained and strained states. The high mobility was attributed to vertical phase segregation of PCDTPT towards the interphase with the gate dielectric.[219]

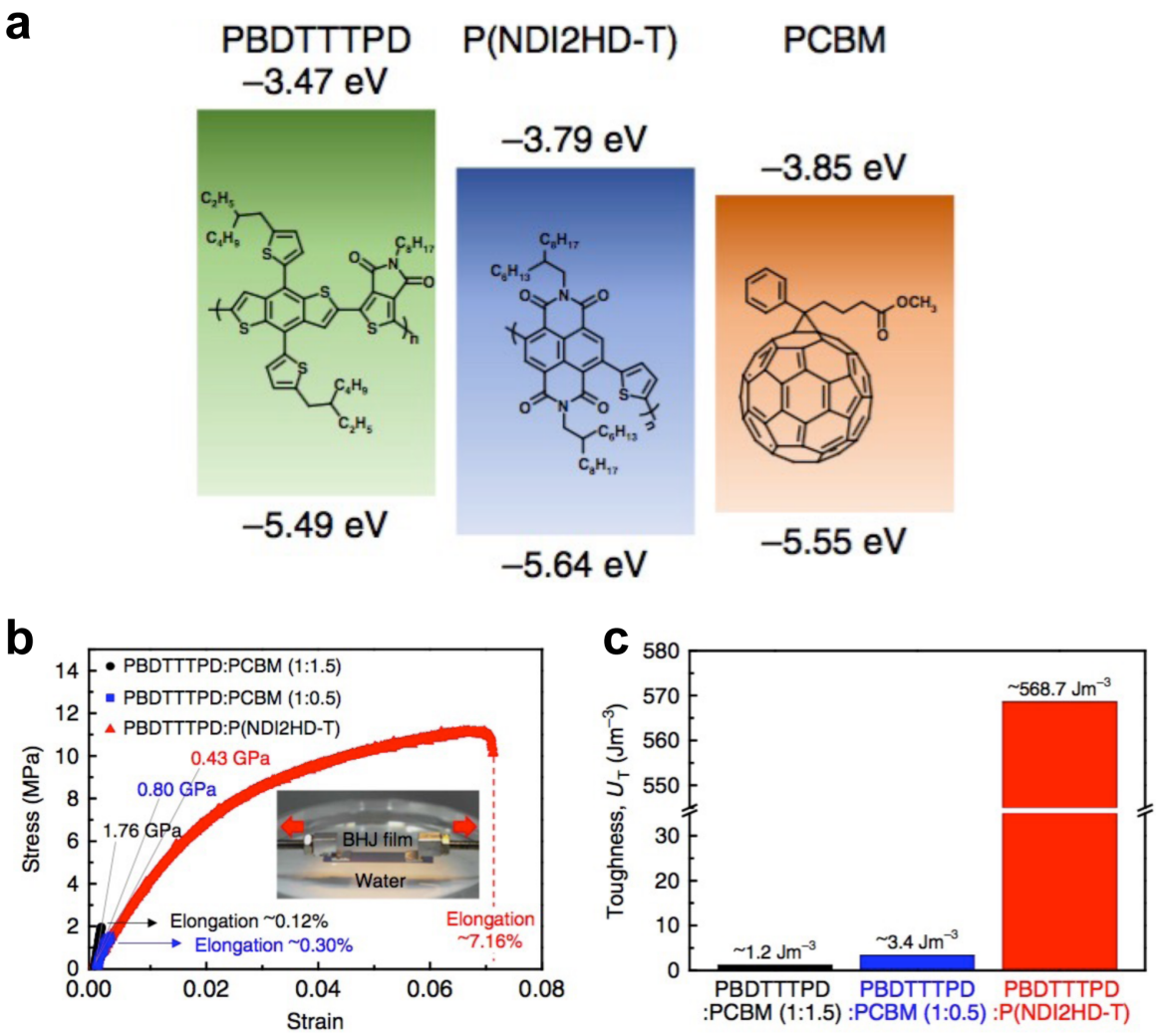

Figure 1.19. All-polymer stretchable solar cells. (a) Chemical structures of PBDTTTPD, P(NDI2HD-T), and $PC_{61}BM$, along with the positions of their frontier molecular orbitals. (b) Stress-strain behavior of the bulk heterojunction composites obtained by the film-on-water method. The all-polymer blend had the lowest modulus and the greatest extensibility. (c) Toughness of the bulk heterojunction blends, again, greatest for the all-polymer blend. Reproduced with permission from ref [111]. Copyright 2015, Nature Publishing Group.

1.7 Effect of Microstructure and Morphology

The solid-state packing structure has a large influence on the mechanical properties of an organic semiconductor. The microstructure and morphology is, in turn, strongly influenced by the processing conditions—e.g., solvent used, kinetics of solidification, and post-deposition treatment. In many cases, the molecular structure plays a subordinate role to the solid-state microstructure. Indeed, the ease with which the mechanical properties can be manipulated by the conditions of processing suggests that in some cases, the most important role of the molecular structure is to influence self-aggregation in solution and packing in the solid state. Results of MD simulations from which one can derive similar conclusions are discussed in Section 3.3.

1.7.1 Correlation of Mechanical Properties with Aggregation

Spectroscopic and micrographic tools have been used to correlate solid structure to mechanical properties. For example, O'Connor and coworkers have used the weakly interacting H-aggregate model, originally developed by Spano and coworkers,[29] to correlate the order present in P3HT and P3HT:PCBM films to the stiffness and ductility (**Figure 1.20**).[30] In particular, when the UV-vis spectra are deconvoluted into signals originating from vibronic transitions of aggregated material and amorphous material, spectra with the greatest aggregated fraction are associated with the stiffest and least extensible films. The aggregated fraction, and hence the mechanical properties, can be controlled using the rate of solvent evaporation. Our group employed the weakly interacting H-aggregate model in our studies on the effects of mixed ratios of side chains

in P3ATs,[134] the purity of the fullerene component,[142] cyclic loading and fatigue,[161] and the role of interdigitation of side chains and intercalation of small molecules.[214]

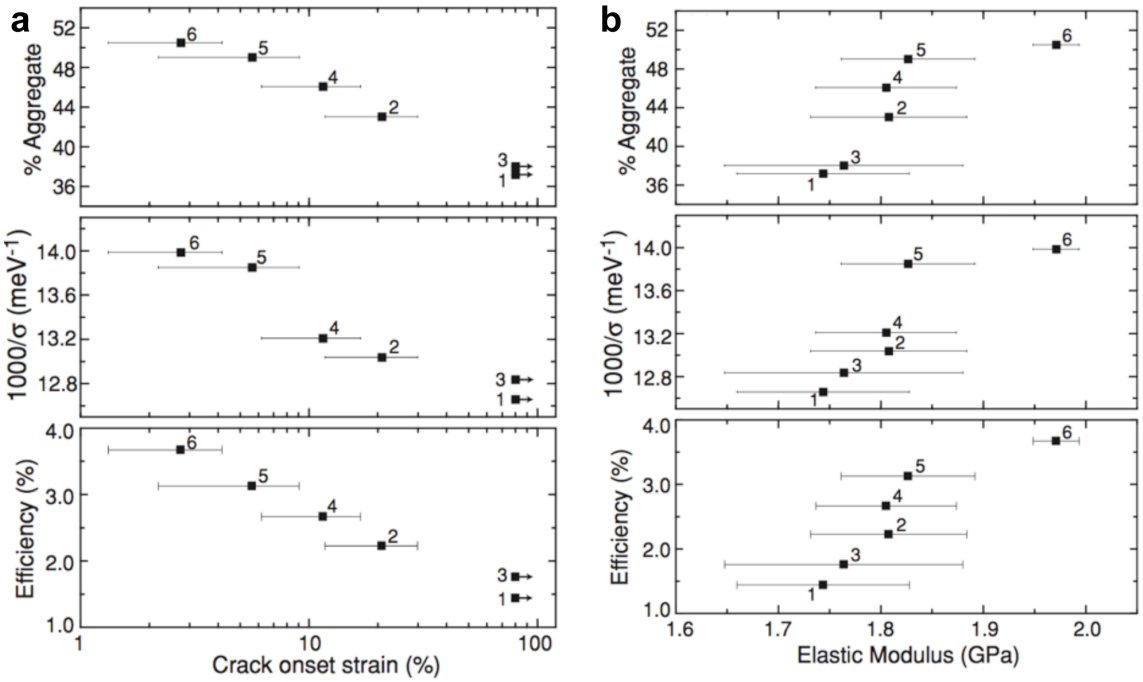

Figure 1.20. Correlations between mechanical properties, photovoltaic efficiency, and solid-state ordering. Percent aggregate, order parameter ($100/\sigma$, where σ is the Gaussian bandwidth), and efficiency vs. extensibility (left) and elastic modulus (right) for P3HT:$PC_{61}BM$ blends processed using a combination of spin-coating speed and concentration to produce BHJ films with different degrees of ordering of the polymer phase. Reproduced with permission from ref [30]. Copyright 2013, Wiley-VCH Verlag GmbH & Co. KGaA.

While the electronic properties of the most deformable films generated by manipulating the processing conditions were generally inferior to those of the stiffer films,[30] Awartani et al. was nevertheless able to use films with low levels of local order to make polarization-dependent organic photodetectors in which the active layer could be stretched by 100% without fracturing.[148] Birefringent absorption in these films was the result of strain-alignment of polymer chains. In addition to aligning of the main axis of the

polymer chains along the strained direction, stretching can also produce changes in texture. Indeed, partial reorientation of P3HT chains from predominantly edge-on to partially face-on has been observed under both uniaxial[151] and biaxial tension.[149]

1.7.2 Interdigitation of Side Chains

In most semiconducting polymers, the lamellar stacking axis, along which the side chains point, shows that the side chains are pointed end-to-end, i.e., they do not interdigitate. In the case of decreased attachment density of the side chains, however, or under the right conditions of processing, it is possible for the side chains to interdigitate.[220-222] Polymers exhibiting interdigitation—e.g., PBTTT—often exhibit highly crystalline microstructures, with highly developed vibronic peaks by UV-vis, which are indicative of H-aggregates. The interdigitated microstructural motif is indicated by a shortening of the lamellar reflection by grazing-incidence X-ray scattering (GIXS). As Cates-Miller et al. has shown in a series of publications, interdigitation can be disrupted by the intercalation of fullerenes (and perhaps other molecules) between the side chains of the polymers, which decreases the scattering angle (i.e., indicates a larger distance) of the lamellar reflection.[117,212] While stereotypically non-interdigitated, the side chains of P3HT will interdigitate in samples with low degrees of polymerization ($i \leq 36$)[220] or if treated with the vapor of carbon disulfide.[223] The interdigitated structure of P3HT—called "form II"—was remarked to have brittle mechanical properties, though these were not quantified.[220]

1.7.3 Intercalation of Fullerenes and Small Molecules

When semiconducting polymers with low attachment density of side chains are blended with fullerenes or small molecules, intercalation of these small molecules along

the polymer backbone can occur.[212] Depending on the relative size of the small molecule and the free volume available between the side chains, this intercalation can either prevent polymer crystallization or produce bimolecular crystallites.[212] As an example, the polymers PT2T and PBTTT (**Figure 1.21a**)—both of which allowed intercalation of the fullerenes—were inspected by UV-vis spectroscopy (**Figure 1.21b**).[214] The spectra of the neat polymers showed vibronic peaks indicative of aggregation; upon the addition of fullerene, the vibronic peaks completely disappeared in the PT2T spectrum indicating disruption or polymer ordering, yet remained in the PBTTT spectrum; the retention of these peaks hinted at at bimolecular crystallization, which degrades the photovoltaic performance at low loadings of fullerenes because the bicontinuity of the blend is destroyed (**Figure 1.21c**).[214] These observations were attributed to differences in the molecular structures of the polymers. PT2T is a poly(terthiophene) with a similar structure to P3HT,[224] except every third thiophene is without a side-chain, and the 3-alkylthiophenes are tail-to-tail coupled rather than head-to-tail. This molecular structure created a large enough free volume between side-chains for fullerene to intercalate, however, the spacing was still relatively small and the co-facial π-stacking—and likely the lamellar stacking—was disrupted.[224] Conversely, PBTTT, which has a larger distance between side-chains due to the thienothiophene spacer, was able to accommodate intercalation of fullerenes without the disruption of aggregation.[225] When the tensile moduli of these polymers and their blends with fullerene were compared to P3HT and P3HpT, the surprising result that the moduli of the blends were linearly correlated with the moduli of the neat polymer was found (**Figure 1.21d**).[214] This observation suggested that—at least for polythiophenes—the tensile modulus of polymer:fullerene blends was dominated by the same molecular interactions

that determined the tensile modulus in the neat polymers rather than the extent of molecular mixing.

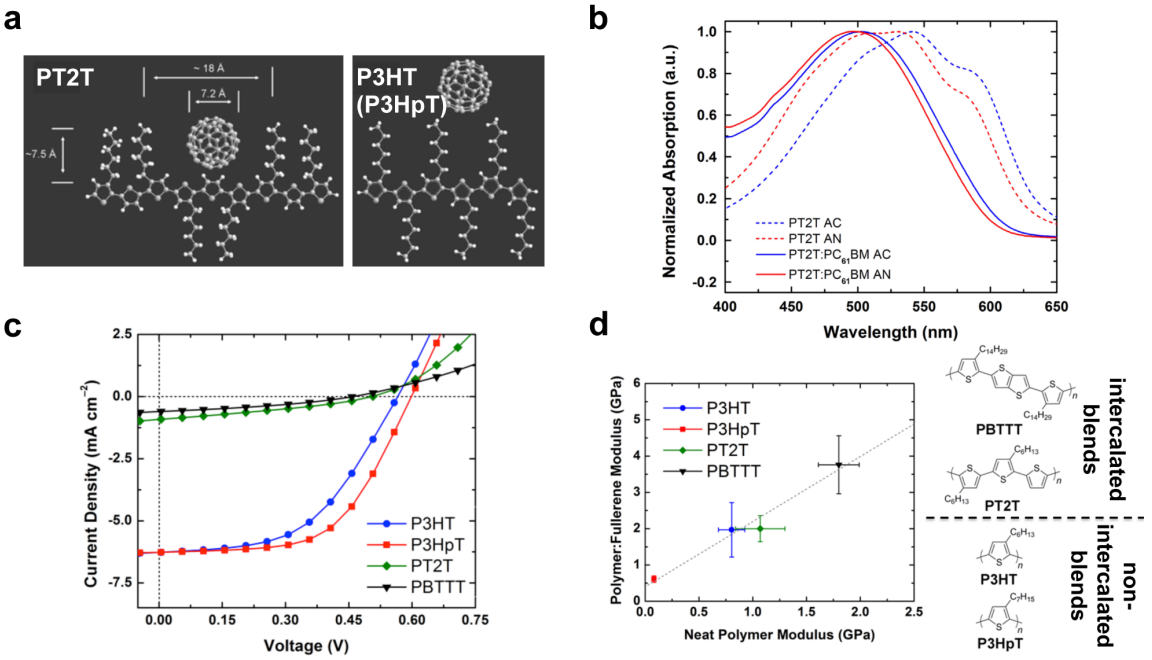

Figure 1.21. Effects of intercalation on the mechanical properties of semiconducting polymers. (a) Structures of the poly(terthiophene) PT2T and P3HT showing intercalation and non-intercalation. Reproduced with permission from ref [224]. Copyright 2007, Wiley-VCH Verlag, GmbH & Co. KGaA. (b) UV-vis spectra of pure PT2T as-cast and annealed, and PT2T:$PC_{61}BM$ as-cast and annealed. (c) Current-voltage characteristics for 1:1 bulk heterojunction blends of P3HT, P3HpT, PT2T, and PBTTT and $PC_{61}BM$. (d) Plot of the modulus of the BHJ blend vs. the modulus of the neat polymer, which shows that the modulus of the blend depends linearly on the modulus of the neat polymer, independent of the details of the packing structure. Reproduced with permission from ref [214]. Copyright 2015, Elsevier.

1.8 Intrinsically Deformable Organic Devices

While the focus of this review is on chemical physical parameters that determine the ability of organic solids to store or absorb strain energy, the ultimate goal of researchers in the field of organic electronics is to construct useful devices (**Figure 1.22**).[226 5,227] This section describes examples of whole organic devices that have the characteristic that the

active layer accommodates significant (≥10%) deformation intrinsically. This criterion is strict in that it requires each component—substrate, electrodes, and active materials—to accommodate strain. Examples of intrinsically deformable devices include solar cells (**Figure 1.22a**), [111,159,228] light-emitting devices,[9,146,229] thin-film transistors (**Figure 1.22b**), [39 145,230] and biosensors.[13,231] We find that devices with the greatest performance, the choice of materials was made with regard to the molecular structures and solid-state packing structures that were known to produce the greatest deformability.

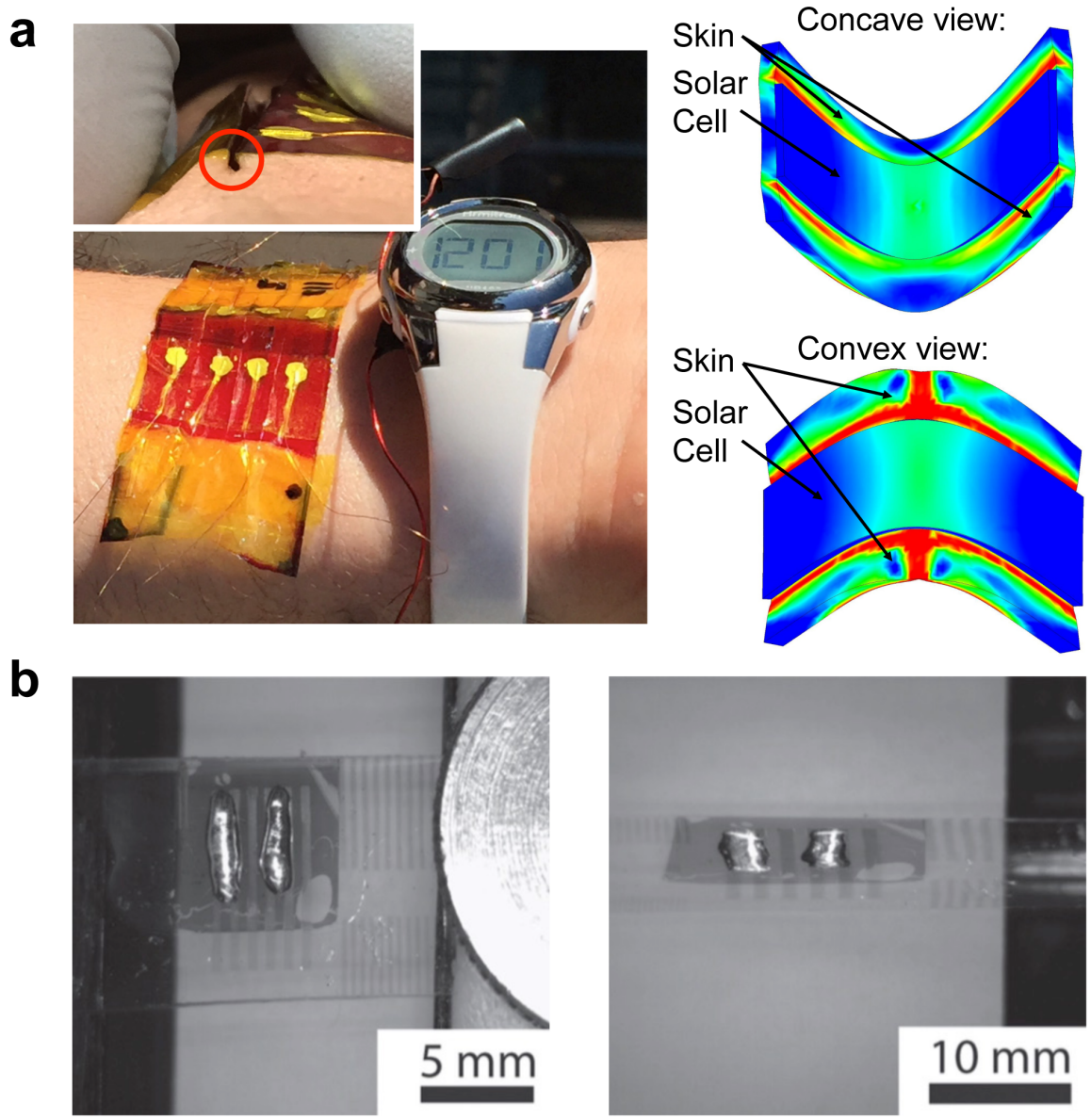

Figure 1.22. Examples of intrinsically deformable devices. (a) A skin-wearable solar cell capable of surviving 1,000 cycles of compression, which produced bending radii of ~100 μm, as indicated in the finite-element model shown. Reproduced with permission from ref. [145] Copyright 2015, Elsevier. (b) A stretchable organic thin-film transistor using carbon nanotube electrodes. Reproduced with permission from ref. [39] Copyright 2014, Wiley-VCH Verlag, GmbH & Co. KGaA.

1.8.1 Solar Cells

The organic electronic device for which the greatest amount of effort has been spent to increase the deformability is the solar cell.[42] Truly deformable organic solar cells would

be beneficial for three reasons. First, the ability of multilayer modules to survive the rigors of roll-to-roll coating would increase the attractiveness of solution-based printing.[12,23,40,108,232] Second, the use of mechanically robust active materials would reduce the burden on the substrate and encapsulant[37] to supply the mechanical stability, and it would thus be possible to reduce the thickness of these layers.[38] (The substrate and the encapsulant presently account for the greatest fraction of the cost and embodied energy of organic solar modules.[233,234]) Moreover, reduction in the weight of solar modules by using ultrathin substrates would reduce the cost of support racks and thus the so-called balance-of-system costs. Third, deformable organic semiconductors would increase the lifetime of devices in both portable applications[235] and in the outdoor environment,[11] where modules must be stable against the forces of the environment.

The first stretchable organic solar cell was not intrinsically stretchable; rather it used microscale wrinkles to accommodate strain.[159] This device was rendered stretchable by spin-coating the layers on a PDMS substrate pre-strained by up to 30%. Upon release of the pre-strain, the stiff active materials buckled. The active layer used (P3HT and $PC_{61}BM$) was stiff and brittle, and cracked readily when the device was stretched beyond the level of the pre-strain.[159] Kaltenbrunner et al. used a similar approach to make stretchable solar cells on ultra-thin poly(ethylene terephthalate) (PET) foil.[38] The first report of stretchable solar cells using intrinsically stretchable organic components (except for the cathode, which used liquid eutectic gallium-indium) compared the evolution in photovoltaic properties of cells with active layers of both P3HT:$PC_{61}BM$ and DPPT-TT:$PC_{61}BM$.[158] The DPP-based polymer exhibited larger extensibilities in part because of the large, branched alkyl side chain.[158] The effect of side chains in stretchable solar cells

was later found to be critical, and a direct comparison of P3HT and P3DDT containing bulk heterojunctions revealed highly stretchable behavior in uniaxially deformed cells.[34]

Biaxial stretchability for bonding to hemispherical substrates at room temperature was demonstrated using P3OT, owing to its low T_g.[147] This report was unique at the time in its use of an inverted architecture, which had PEDOT:PSS as a transparent anode (top contact in the inverted architecture) and PEDOT:PSS treated with poly(ethyleneimine) (PEI) as the transparent cathode (bottom contact). The stretchability of solar cells could be further enhanced using a stretchable encapsulant, e.g., thermoplastic polyurethane, as was demonstrated by Sawyer et al. in the first "all-rubber" solar cell, which was composed of components that were entirely elastomeric (except for the $PC_{61}BM$).[37] In the absence of the encapsulant, strain is concentrated to thin areas and defects in the active film, and it thus cracks at strains smaller than would be observed for a mathematically uniform film. The ultimate extensibility of these devices was limited by the use of methanofullerenes as electron acceptors, which embrittle the films.[142] To avoid the embrittling effects of methanofullerenes on the mechanical properties of semiconducting polymers, all-polymer active layers can be employed. To this end, the KAIST group fabricated cells with active layers consisting entirely of polymers, which was the highest performing—and most stretchable—organic solar cell produced to date.[111] In order for these extraordinarily robust and compliant devices to have an impact in portable and outdoor applications, however, stretchable substrates and encapsulants must be developed that have impermeability to water vapor and oxygen.

1.8.2 Light-Emitting Devices

The arguments in favor of intrinsically highly deformable organic light-emitting devices (OLEDs) are largely similar as they are for organic solar cells: displays based on organic materials could be fabricated at low cost by printing, as could inexpensive panels for solid-state lighting. Rollable, foldable, portable, lightweight, and mechanically robust displays would be useful in consumer electronics devices, along with military and disaster relief applications. The first example of a stretchable organic light-emitting device was described by Someya and coworkers.[79] These authors used stretchable composite materials based on carbon nanotubes to provide electrical connections in a stretchable active matrix display. In this case, however, the emissive organic semiconductors were not deformable. The first intrinsically stretchable organic light-emitting device—and perhaps the first intrinsically stretchable organic electronic device of any kind—was an organic light-emitting electrochemical device produced by Pei and coworkers.[9] The authors demonstrated the ability to shape this device with heating. The electrodes that enabled this technology were based on silver nanowires in an early demonstration,[146] and later carbon nanotubes.[215] The blue emissive polymer used was PF-B, a polyfluorene copolymer. This structure has long alkyl side chains, which is consistent with the level of deformability possible, and was also mixed with the ionic conductor poly(ethylene oxide)dimethacrylate ether (PEO-DMA) and lithium trifluoromethanesulfonate (LiTf). It is likely that the ionic conductive polymer behaved as a plasticizer, though the authors did not investigate the mechanical properties of the emissive layer. The authors later showed a yellow emissive device using the poly(phenylene vinylene) (PPV) derivative "super yellow," which achieved impressive extensabilities of 120%.[236] An ultra-flexible device was demonstrated

by White et al. using the paradigm of ultrathin substrates previously demonstrated by the same laboratories for organic solar cells.[7]

1.8.3 Thin-Film Transistor

Perhaps the most fundamental organic electronic device is the thin-film transistor (OTFT).[52] That is for its practical importance as well as its usefulness in establishing charge-transport characteristics of materials.[132] Several approaches have surfaced in the literature whose goals have been to impart stretchability to OTFTs.[237] An advantage to mechanical deformability for OTFTs is the ability to pattern devices directly on flexible and stretchable substrates without the need for complex, patterned interconnects and relief features.[13] For example, the Bettinger laboratory used the buckled, wavy approach to generate the first stretchable OTFT,[238] which Chortos et al. showed that the cracks in the channel layer produced by stretching in P3HT devices were not sufficient to destroy charge transport.[39] Other composite approaches based on conjugated polymer nanofibers[239-241] have also been used, but the intrinsic deformability of the semiconductor is masked in cases where a stiff material is cast into a nanofiber. Goffri et al. have reported a multicomponent design strategy in which the semiconducting polymer is mixed with a commodity semi-crystalline polymer to obtain vertically stratified structures in a one step process. They found that the fraction of semiconducting polymer could be reduced to as low as 3 wt% without any degradation in device performance. It can be expected that the mechanical properties of this composite system would be dominated by the semi-crystalline commodity polymer, however, no mechanical characterization was performed.[242]

Approaches toward intrinsically stretchable OTFTs have their roots in measurement of the effects of strain on charge-transport properties of flexible devices.[151]

Early work by Someya elucidated the effect of mechanical strain on the charge-transport properties of small molecular semiconductors.[83] Among the authors findings were the importance of compressive strain on decreasing the intermolecular separation and hence increasing the charge-carrier mobility.[83] In a later study, Sokolov et al. introduced the metric of mobility factor, $F_M = \Delta\%\mu/\%\text{strain}$, which quantifies the relationship between mobility and strain.[243] In experiments on flexible transistors under tensile and compressive strain, the authors uncovered an important role of strain on the strain-evolved surface energy of the dielectric layer, which depending on the materials selected for the device produced a value of F_M that was either positive or negative.[243] The effects of strain could be mitigated by using an inorganic dielectric layer bearing a dense alkyl monolayer.

It has long been known that stretched films of conjugated polymers exhibit anisotropic charge transport, with the most facile direction being parallel to the stretched axis.[152] The microstructural rationale is alignment of chains,[152] which has been confirmed by X-ray diffraction,[149,151] by birefringent absorption by UV-vis,[148] and molecular dynamics simulations.[130] The Bao laboratory used a method based on soft contact lamination and delamination to measure the hole mobility of conjugated polymers,[244] which, though not a device, will be a useful tool for the efficient determination of the effect of strain on the transport properties of organic semiconductors. One of the most successful examples of an intrinsically stretchable semiconductive polymers for TFT applications was that of Wu et al., who used an isoindigo-based donor-acceptor polymer bearing long, branched carbosilane side chains to achieve mobilities ≥ 1 $cm^2\ V^{-1}\ s^{-1}$ even at strains as large as 60%.[107] Jeong and coworkers comprehensively reviewed approaches to generating active layers for deformable transistors.[237]

1.8.4 Biosensors

Integration of π-conjugated materials with biological systems—"organic bioelectronics"[99]—requires seamless interfaces between devices and the biological milieu.[231] In the case of wearable devices, materials must accommodate the natural stretchability of the skin,[245] which extends by 30 percent or more, depending on the location and axis of strain.[246] Low stiffness—i.e., the combination of low thickness with low tensile modulus—would permit a strong chemical interface, which would be required for the detection of biological signals.[13] One of the advantages of stretchable thin-film and patch-like devices is imperceptibility by the user.[13] This attribute, sometimes called "mechanical invisibility," would lower the barriers to use and increase compliance of patients and the willingness of other users to adopt these wearable technologies.[3] Work on of ultra-flexible and stretchable devices using intrinsically deformable organic semiconductors is still in its early stages, but several proof-of-concept devices have been demonstrated. The description that follows includes on a few prominent examples in which a π-conjugated semiconductor plays a key role in an integrated device.

Using ultrathin (1.4 μm) plastic foils, Kaltenbrunner et al. showed extraordinary bending stability of OTFTs for eventual use in "imperceptible" biological applications.[13] Schwartz et al. combined an organic transistor with a microstructured compressible gate dielectric in a flexible OTFT that was sufficiently sensitivity to measure the pulse pressure waveform of the human radial artery.[247] Malliaras and coworkers have used the organic electrochemical transistor (OECT) for a variety of wearable device for healthcare.[99] For example, PEDOT:PSS can be use to transduce electrical signals from the cardiac cycle (electrocardiography, ECG), eye movements (electrooculography, EOG), and neurological

rhythyms (electroencephalography, EEG).[98,199,248] Small electrical potentials drive ions in and out of the PEDOT:PSS channel to modulate the conductivity.[98] The mechanical interfaces in this type of device are unexplored, though typical formulations of PEDOT:PSS tend to be brittle.[104] While PEDOT:PSS is not a semiconductor, it is widely used for neural interfacing as exemplified by the work of Martin and coworkers.[198,249]

1.9 Conclusions and Outlook

Mechanical deformability is the property that enables essentially all advantages of organic electronic materials. Printed organic solar cells, light-emitting devices, thin-film transistors, and radio-frequency identification tags must survive the rigors of roll-to-roll coating, and also the mechanical insults of portable applications and in the outdoor environment. Furthermore, organic bioelectronic devices must conform to the skin or the surfaces of internal organs to transduce biochemical signals; without a conformal mechanical interface, however, there can be no chemical interface. Achieving mechanical robustness in thin film devices is tantamount to minimizing the elastic modulus, increasing the toughness, elastic range, ductility, or other mechanical property, depending on the application and the expected modes of deformation. These mechanical properties depend on molecular structure and the ways that these structures pack in solid films.

While molecular structure of course plays a role in determining the mechanical properties—e.g., the size of side chains for a given attachment density is a good predictor of softness—the influence of molecular manifests especially strongly in its effect on structure in the solid state. Indeed, a recurring theme is the influence of how processing conditions influence mechanical properties. The conditions of spin coating can, for example, influence ordering and degree of crystallinity in a thin film. Self-aggregation in

solution may produce kinetically trapped films upon solidification that exhibit a density of entanglements that is not idea for robust applications. Interdigitation of side chains can produce stiffer and more brittle films. A complete understanding of the mechanical properties of π-conjugated materials must include expectations about how a given molecular structure will assemble in solution and then in the solid state.

The challenges associated with measuring the mechanical properties of delicate thin films of organic semiconductors has led to the development of metrological techniques that have broad applicability to other types of thin solid films. For example, the film-on-elastomer and film-on-water methods can be readily applied to films of other technologically important polymers, such as optical coatings, photoresists, paints, and scratch-resistant layers. One aspect of organic semiconductors that is still poorly understood is time-dependent mechanical behavior. In order to understand the ways in which the microstructure of an organic semiconductor evolves over time when strained—i.e., creep—experiments should be designed specifically for thin films to anticipate these effects.

Organic semiconductor devices are already commercial in the form of large-area ultra-high-definition display panels. Whether or not organic electronics meet their expectations in the areas of large-area solar panels or biosensors, it seems likely that at least some of these applications will be realized eventually. In the near term, we expect that a deeper knowledge of the mechanical properties of these materials will facilitate production of flexible devices on thin plastic foil, and enable their long-term reliability against mechanical and theromomechanical deformations. In the long term, work directed toward understanding and improving the thermomechanical properties of these materials

may suggest ways in which other properties might be brought about that are reminiscent of biological materials, including biodegradability and self-repair. Thus π-conjugated materials could more fully embody colloquial meanings of "organic" and "plastic," by which they are often referred.

1.10 Acknowledgements

This work was supported by a grant from the Air Force Office of Scientific Research grant number FA9550-16-1-0220. S. S. and D. A. were supported in part by the Graduate Research Fellowship Program of the National Science Foundation (DGE-1144086).

Chapter 1, in full, is a reprint of the material as it appears in *Chemical Reviews*, 2017, 117, 6467-6499. The American Chemical Society, 2017. Samuel E. Root, Suchol Savagatrup, Adam D. Printz, Daniel Rodriquez, and Darren J. Lipomi. The dissertation author was the primary investigator and author of this paper.

1.11 References

(1) Kagan, C. R.; Fernandez, L. E.; Gogotsi, Y.; Hammond, P. T.; Hersam, M. C.; Nel, A. E.; Penner, R. M.; Willson, C. G.; Weiss, P. S.: Nano Day: Celebrating the Next Decade of Nanoscience and Nanotechnology. *ACS Nano* **2016**, *10*, 9093-9103.

(2) Willson, C. G.; Roman, B. J.: The Future of Lithography: Sematech Litho Forum 2008. *ACS Nano* **2008**, *2*, 1323-1328.

(3) Kim, D. H.; Lu, N. S.; Ma, R.; Kim, Y. S.; Kim, R. H.; Wang, S. D.; Wu, J.; Won, S. M.; Tao, H.; Islam, A. et al.: Epidermal Electronics. *Science* **2011**, *333*, 838-843.

(4) Bauer, S.; Bauer-Gogonea, S.; Graz, I.; Kaltenbrunner, M.; Keplinger, C.; Schwodiauer, R.: 25th Anniversary Article: A Soft Future: From Robots and Sensor Skin to Energy Harvesters. *Adv. Mater.* **2014**, *26*, 149-162.

(5) Savagatrup, S.; Printz, A. D.; O'Connor, T. F.; Zaretski, A. V.; Lipomi, D. J.: Molecularly Stretchable Electronics. *Chem. Mater.* **2014**, *26*, 3028-3041.

(6) Ying, M.; Bonifas, A. P.; Lu, N.; Su, Y. W.; Li, R.; Cheng, H. Y.; Ameen, A.; Huang, Y. G.; Rogers, J. A.: Silicon Nanomembranes for Fingertip Electronics. *Nanotechnology* **2012**, *23*, 344004-1-344004-7.

(7) White, M. S.; Kaltenbrunner, M.; Glowacki, E. D.; Gutnichenko, K.; Kettlgruber, G.; Graz, I.; Aazou, S.; Ulbricht, C.; Egbe, D. A. M.; Miron, M. C. et al.: Ultrathin, Highly Flexible and Stretchable Pleds. *Nat. Photonics* **2013**, *7*, 811-816.

(8) Lee, J.; Wu, J. A.; Shi, M. X.; Yoon, J.; Park, S. I.; Li, M.; Liu, Z. J.; Huang, Y. G.; Rogers, J. A.: Stretchable Gaas Photovoltaics with Designs That Enable High Areal Coverage. *Adv. Mater.* **2011**, *23*, 986-991.

(9) Yu, Z. B.; Niu, X. F.; Liu, Z.; Pei, Q. B.: Intrinsically Stretchable Polymer Light-Emitting Devices Using Carbon Nanotube-Polymer Composite Electrodes. *Adv. Mater.* **2011**, *23*, 3989-3994.

(10) Kim, R. H.; Kim, D. H.; Xiao, J. L.; Kim, B. H.; Park, S. I.; Panilaitis, B.; Ghaffari, R.; Yao, J. M.; Li, M.; Liu, Z. J. et al.: Waterproof AlInGaP Optoelectronics on Stretchable Substrates with Applications in Biomedicine and Robotics. *Nat. Mater.* **2010**, *9*, 929-937.

(11) Krebs, F. C.; Espinosa, N.; Hosel, M.; Sondergaard, R. R.; Jorgensen, M.: 25th Anniversary Article: Rise to Power - Opv-Based Solar Parks. *Adv. Mater.* **2014**, *26*, 29-39.

(12) Galagan, Y.; Coenen, E. W. C.; Zimmermann, B.; Slooff, L. H.; Verhees, W. J. H.; Veenstra, S. C.; Kroon, J. M.; Jorgensen, M.; Krebs, F. C.; Andriessen, R.: Scaling up ITO-Free Solar Cells. *Adv. Energy Mater.* **2014**, *4*, 1300498.

(13) Kaltenbrunner, M.; Sekitani, T.; Reeder, J.; Yokota, T.; Kuribara, K.; Tokuhara, T.; Drack, M.; Schwodiauer, R.; Graz, I.; Bauer-Gogonea, S. et al.: An Ultra-Lightweight Design for Imperceptible Plastic Electronics. *Nature* **2013**, *499*, 458-463.

(14) Yang, Z. B.; Deng, J.; Sun, X. M.; Li, H. P.; Peng, H. S.: Stretchable, Wearable Dye-Sensitized Solar Cells. *Adv. Mater.* **2014**, *26*, 2643-2647.

(15) Kim, D. H.; Viventi, J.; Amsden, J. J.; Xiao, J. L.; Vigeland, L.; Kim, Y. S.; Blanco, J. A.; Panilaitis, B.; Frechette, E. S.; Contreras, D. et al.: Dissolvable Films of Silk Fibroin for Ultrathin Conformal Bio-Integrated Electronics. *Nat. Mater.* **2010**, *9*, 511-517.

(16) Fu, K. K.; Wang, Z. Y.; Dai, J. Q.; Carter, M.; Hu, L. B.: Transient Electronics: Materials and Devices. *Chem. Mater.* **2016**, *28*, 3527-3539.

(17) Kim, D. H.; Ahn, J. H.; Choi, W. M.; Kim, H. S.; Kim, T. H.; Song, J. Z.; Huang, Y. G. Y.; Liu, Z. J.; Lu, C.; Rogers, J. A.: Stretchable and Foldable Silicon Integrated Circuits. *Science* **2008**, *320*, 507-511.

(18) Suo, Z.; Ma, E. Y.; Gleskova, H.; Wagner, S.: Mechanics of Rollable and Foldable Film-on-Foil Electronics. *Appl. Phys. Lett.* **1999**, *74*, 1177-1179.

(19) Lipomi, D. J.: Stretchable Figures of Merit in Deformable Electronics. *Adv. Mater.* **2016**, *28*, 4180-4183.

(20) Peet, J.; Heeger, A. J.; Bazan, G. C.: "Plastic" Solar Cells: Self-Assembly of Bulk Heterojunction Nanomaterials by Spontaneous Phase Separation. *Acc. Chem. Res.* **2009**, *42*, 1700-1708.

(21) Krebs, F. C.; Tromholt, T.; Jorgensen, M.: Upscaling of Polymer Solar Cell Fabrication Using Full Roll-to-Roll Processing. *Nanoscale* **2010**, *2*, 873-886.

(22) Krebs, F. C.; Gevorgyan, S. A.; Alstrup, J.: A Roll-to-Roll Process to Flexible Polymer Solar Cells: Model Studies, Manufacture and Operational Stability Studies. *J. Mater. Chem.* **2009**, *19*, 5442-5451.

(23) Krebs, F. C.: All Solution Roll-to-Roll Processed Polymer Solar Cells Free from Indium-Tin-Oxide and Vacuum Coating Steps. *Org. Electron.* **2009**, *10*, 761-768.

(24) Muller, C.; Goffri, S.; Breiby, D. W.; Andreasen, J. W.; Chanzy, H. D.; Janssen, R. A. J.; Nielsen, M. M.; Radano, C. P.; Sirringhaus, H.; Smith, P. et al.: Tough, Semiconducting Polyethylene-Poly(3-Hexylthiophene) Diblock Copolymers. *Adv. Funct. Mater.* **2007**, *17*, 2674-2679.

(25) Tummala, N. R.; Bruner, C.; Risko, C.; Bredas, J. L.; Dauskardt, R. H.: Molecular-Scale Understanding of Cohesion and Fracture in P3HT:Fullerene Blends. *ACS Appl. Mater. Interfaces* **2015**, *7*, 9957-9964.

(26) Bruner, C.; Dauskardt, R. H.: Role of Molecular Weight on the Mechanical Device Properties of Organic Polymer Solar Cells. *Macromolecules* **2014**, *47*, 1117-1121.

(27) Brand, V.; Bruner, C.; Dauskardt, R. H.: Cohesion and Device Reliability in Organic Bulk Heterojunction Photovoltaic Cells. *Sol. Energy Mater. Sol. Cells* **2012**, *99*, 182-189.

(28) Savagatrup, S.; Zhao, X. K.; Chan, E.; Mei, J. G.; Lipomi, D. J.: Effect of Broken Conjugation on the Stretchability of Semiconducting Polymers. *Macromol. Rapid Commun.* **2016**, *37*, 1623-1628.

(29) Clark, J.; Silva, C.; Friend, R. H.; Spano, F. C.: Role of Intermolecular Coupling in the Photophysics of Disordered Organic Semiconductors: Aggregate Emission in Regioregular Polythiophene. *Phys. Rev. Lett.* **2007**, *98*, 206406.

(30) Awartani, O.; Lemanski, B.; Ro, H. W.; Richter, L. J.; DeLongchamp, D. M.; O'Connor, B. T.: Correlating Stiffness, Ductility, and Morphology of

Polymer:Fullerene Films for Solar Cell Applications. *Adv. Energy Mater.* **2013**, *3*, 399-406.

(31) O'Connor, B.; Chan, E. P.; Chan, C.; Conrad, B. R.; Richter, L. J.; Kline, R. J.; Heeney, M.; McCulloch, I.; Soles, C. L.; DeLongchamp, D. M.: Correlations between Mechanical and Electrical Properties of Polythiophenes. *ACS Nano* **2010**, *4*, 7538-7544.

(32) Postema, A. R.; Liou, K.; Wudl, F.; Smith, P.: Highly Oriented, Low-Modulus Materials from Liquid Crystalline Polymers: The Ultimate Penalty for Solubilizing Alkyl Side Chains. *Macromolecules* **1990**, *23*, 1842-1845.

(33) Moulton, J.; Smith, P.: Electrical and Mechanical Properties of Oriented Poly(3-Alkylthiophenes): 2. Effect of Side-Chain Length. *Polymer* **1992**, *33*, 2340-2347.

(34) Savagatrup, S.; Makaram, A. S.; Burke, D. J.; Lipomi, D. J.: Mechanical Properties of Conjugated Polymers and Polymer-Fullerene Composites as a Function of Molecular Structure. *Adv. Funct. Mater.* **2014**, *24*, 1169-1181.

(35) Hiemenz, P. C.; Lodge, T. P.: *Polymer Chemistry*; 2nd ed.; CRC Press, 2007.

(36) Koch, F. P. V.; Rivnay, J.; Foster, S.; Müller, C.; Downing, J. M.; Buchaca-Domingo, E.; Westacott, P.; Yu, L. Y.; Yuan, M. J.; Baklar, M. et al.: The Impact of Molecular Weight on Microstructure and Charge Transport in Semicrystalline Polymer Semiconductors--Poly(3-Hexylthiophene), a Model Study. *Prog. Polym. Sci.* **2013**, *38*, 1978-1989.

(37) Sawyer, E. J.; Zaretski, A. V.; Printz, A. D.; de los Santos, N. V.; Bautista-Gutierrez, A.; Lipomi, D. J.: Large Increase in Stretchability of Organic Electronic Materials by Encapsulation. *Extreme Mech. Lett.* **2016**, *8*, 78-87.

(38) Kaltenbrunner, M.; White, M. S.; Glowacki, E. D.; Sekitani, T.; Someya, T.; Sariciftci, N. S.; Bauer, S.: Ultrathin and Lightweight Organic Solar Cells with High Flexibility. *Nat. Commun.* **2012**, *3*, 770.

(39) Chortos, A.; Lim, J.; To, J. W. F.; Vosgueritchian, M.; Dusseault, T. J.; Kim, T. H.; Hwang, S. W.; Bao, Z. N.: Highly Stretchable Transistors Using a Microcracked Organic Semiconductor. *Adv. Mater.* **2014**, *26*, 4253-4259.

(40) Dupont, S. R.; Oliver, M.; Krebs, F. C.; Dauskardt, R. H.: Interlayer Adhesion in Roll-to-Roll Processed Flexible Inverted Polymer Solar Cells. *Sol. Energy Mater. Sol. Cells* **2012**, *97*, 171-175.

(41) Brand, V.; Levi, K.; McGehee, M. D.; Dauskardt, R. H.: Film Stresses and Electrode Buckling in Organic Solar Cells. *Sol. Energy Mater. Sol. Cells* **2012**, *103*, 80-85.

(42) Savagatrup, S.; Printz, A. D.; O'Connor, T. F.; Zaretski, A. V.; Rodriquez, D.; Sawyer, E. J.; Rajan, K. M.; Acosta, R. I.; Root, S. E.; Lipomi, D. J.: Mechanical Degradation and Stability of Organic Solar Cells: Molecular and Microstructural Determinants. *Energy Environ. Sci.* **2015**, *8*, 55-80.

(43) Onorato, J.; Pakhnyuk, V.; Luscombe, C.: Structure and Design of Polymer for Durable, Stretchable Organic Electronics. *Polym. J.* **2017**, *49*, 41-60.

(44) Liu, F.; Gu, Y.; Shen, X. B.; Ferdous, S.; Wang, H. W.; Russell, T. P.: Characterization of the Morphology of Solution-Processed Bulk Heterojunction Organic Photovoltaics. *Prog. Polym. Sci.* **2013**, *38*, 1990-2052.

(45) Treat, N. D.; Chabinyc, M. L.: Phase Separation in Bulk Heterojunctions of Semiconducting Polymers and Fullerenes for Photovoltaics. *Annu. Rev. Phys. Chem.* **2014**, *65*, 59-81.

(46) Takacs, C. J.; Brady, M. A.; Treat, N. D.; Kramer, E. J.; Chabinyc, M. L.: Quadrites and Crossed-Chain Crystal Structures in Polymer Semiconductors. *Nano Lett.* **2014**, *14*, 3096-3101.

(47) Treat, N. D.; Varotto, A.; Takacs, C. J.; Batara, N.; Al-Hashimi, M.; Heeney, M. J.; Heeger, A. J.; Wudl, F.; Hawker, C. J.; Chabinyc, M. L.: Polymer-Fullerene Miscibility: A Metric for Screening New Materials for High-Performance Organic Solar Cells. *J. Am. Chem. Soc* **2012**, *134*, 15869-15879.

(48) Cao, Y.; Smith, P. A.; Heeger, A. J.: Mechanical and Electrical Properties of Highly Oriented Polyacetylene Films. *Synth. Met.* **1991**, *41-43*, 181-184.

(49) Cao, Y.; Smith, P.; Heeger, A. J.: Mechanical and Electrical Properties of Polyacetylene Films Oriented by Tensile Drawing. *Polymer* **1991**, *32*, 1210-1218.

(50) Tokito, S.; Smith, P.; Heeger, A. J.: Mechanical and Electrical Properties of Poly(2,5-Thienylene Vinylene) Fibers. *Synth. Met.* **1990**, *36*, 183-194.

(51) Fred Wudl, G. S.: Conducting Polymer Formed of Poly(2-Methoxy,5-(2'-Ethyl-Hexyloxy)-P-Phenylenevinylene). Office, U. S. P., Ed.; The Regents Of The University of California, Oakland, California: United States of America, 1993; Vol. 5189136; pp 6.

(52) Bao, Z. N.; Dodabalapur, A.; Lovinger, A. J.: Soluble and Processable Regioregular Poly(3-Hexylthiophene) for Thin Film Field-Effect Transistor Applications with High Mobility. *Appl. Phys. Lett.* **1996**, *69*, 4108-4110.

(53) Burroughes, J. H.; Bradley, D. D. C.; Brown, A. R.; Marks, R. N.; Mackay, K.; Friend, R. H.; Burns, P. L.; Holmes, A. B.: Light-Emitting Diodes Based on Conjugated Polymers. *Nature* **1990**, *347*, 539-541.

(54) Halls, J. J. M.; Walsh, C. A.; Greenham, N. C.; Marseglia, E. A.; Friend, R. H.; Moratti, S. C.; Holmes, A. B.: Efficient Photodiodes from Interpenetrating Polymer Networks. *Nature* **1995**, *376*, 498-500.

(55) Yu, G.; Gao, J.; Hummelen, J. C.; Wudl, F.; Heeger, A. J.: Polymer Photovoltaic Cells - Enhanced Efficiencies Via a Network of Internal Donor-Acceptor Heterojunctions. *Science* **1995**, *270*, 1789-1791.

(56) Sariciftci, N. S.; Smilowitz, L.; Heeger, A. J.; Wudl, F.: Photoinduced Electron-Transfer from a Conducting Polymer to Buckminsterfullerene. *Science* **1992**, *258*, 1474-1476.

(57) Jones, J.; Lacour, S. P.; Wagner, S.; Suo, Z. G.: Stretchable Wavy Metal Interconnects. *J. Vac. Sci. Technol., A* **2004**, *22*, 1723-1725.

(58) Lacour, S. P.; Wagner, S.; Huang, Z. Y.; Suo, Z.: Stretchable Gold Conductors on Elastomeric Substrates. *Appl. Phys. Lett.* **2003**, *82*, 2404-2406.

(59) Khang, D. Y.; Xiao, J. L.; Kocabas, C.; MacLaren, S.; Banks, T.; Jiang, H. Q.; Huang, Y. Y. G.; Rogers, J. A.: Molecular Scale Buckling Mechanics in Individual Aligned Single-Wall Carbon Nanotubes on Elastomeric Substrates. *Nano Lett.* **2008**, *8*, 124-130.

(60) Khang, D. Y.; Jiang, H. Q.; Huang, Y.; Rogers, J. A.: A Stretchable Form of Single-Crystal Silicon for High-Performance Electronics on Rubber Substrates. *Science* **2006**, *311*, 208-212.

(61) Jung, I.; Shin, G.; Malyarchuk, V.; Ha, J. S.; Rogers, J. A.: Paraboloid Electronic Eye Cameras Using Deformable Arrays of Photodetectors in Hexagonal Mesh Layouts. *Appl. Phys. Lett.* **2010**, *96*, -.

(62) Tseng, H. R.; Phan, H.; Luo, C.; Wang, M.; Perez, L. A.; Patel, S. N.; Ying, L.; Kramer, E. J.; Nguyen, T. Q.; Bazan, G. C. et al.: High-Mobility Field-Effect Transistors Fabricated with Macroscopic Aligned Semiconducting Polymers. *Adv. Mater.* **2014**, *26*, 2993-2998.

(63) Jorgensen, M.; Norrman, K.; Gevorgyan, S. A.; Tromholt, T.; Andreasen, B.; Krebs, F. C.: Stability of Polymer Solar Cells. *Adv. Mater.* **2011**, *24*, 580-612.

(64) Rogers, J. A.; Someya, T.; Huang, Y. G.: Materials and Mechanics for Stretchable Electronics. *Science* **2010**, *327*, 1603-1607.

(65) Lacour, S. P.; Chan, D.; Wagner, S.; Li, T.; Suo, Z.: Mechanisms of Reversible Stretchability of Thin Metal Films on Elastomeric Substrates. *Appl. Phys. Lett.* **2006**, *88*, 204103.

(66) Gleskova, H.; Cheng, I. C.; Wagner, S.; Sturm, J. C.; Suo, Z. G.: Mechanics of Thin-Film Transistors and Solar Cells on Flexible Substrates. *Solar Energy* **2006**, *80*, 687-693.

(67) Lacour, S. P.; Jones, J.; Wagner, S.; Li, T.; Suo, Z. G.: Stretchable Interconnects for Elastic Electronic Surfaces. *Proc. IEEE* **2005**, *93*, 1459-1467.

(68) Lacour, S. P.; Jones, J.; Suo, Z.; Wagner, S.: Design and Performance of Thin Metal Film Interconnects for Skin-Like Electronic Circuits. *IEEE Electr. Device L.* **2004**, *25*, 179-181.

(69) Fan, J. A.; Yeo, W. H.; Su, Y. W.; Hattori, Y.; Lee, W.; Jung, S. Y.; Zhang, Y. H.; Liu, Z. J.; Cheng, H. Y.; Falgout, L. et al.: Fractal Design Concepts for Stretchable Electronics. *Nat. Commun.* **2014**, *5*, 3266.

(70) Xu, S.; Zhang, Y.; Cho, J. H.; Lee, J.; Huang, X.; Jia, L.; Fan, J. A.; Su, Y. W.; Su, J.; Zhang, H. et al.: Stretchable Batteries with Self-Similar Serpentine Interconnects and Integrated Wireless Recharging Systems. *Nat. Commun.* **2013**, *4*, 1543.

(71) Shin, G.; Jung, I.; Malyarchuk, V.; Song, J. Z.; Wang, S. D.; Ko, H. C.; Huang, Y. G.; Ha, J. S.; Rogers, J. A.: Micromechanics and Advanced Designs for Curved Photodetector Arrays in Hemispherical Electronic-Eye Cameras. *Small* **2010**, *6*, 851-856.

(72) Ko, H. C.; Stoykovich, M. P.; Song, J. Z.; Malyarchuk, V.; Choi, W. M.; Yu, C. J.; Geddes, J. B.; Xiao, J. L.; Wang, S. D.; Huang, Y. G. et al.: A Hemispherical Electronic Eye Camera Based on Compressible Silicon Optoelectronics. *Nature* **2008**, *454*, 748-753.

(73) Viventi, J.; Kim, D. H.; Moss, J. D.; Kim, Y. S.; Blanco, J. A.; Annetta, N.; Hicks, A.; Xiao, J. L.; Huang, Y. G.; Callans, D. J. et al.: A Conformal, Bio-Interfaced Class of Silicon Electronics for Mapping Cardiac Electrophysiology. *Sci. Transl. Med.* **2010**, *2*, 24.

(74) Kim, D. H.; Lu, N.; Huang, Y. G.; Rogers, J. A.: Materials for Stretchable Electronics in Bioinspired and Biointegrated Devices. *MRS Bull.* **2012**, *37*, 226-235.

(75) Hwang, S. W.; Tao, H.; Kim, D. H.; Cheng, H. Y.; Song, J. K.; Rill, E.; Brenckle, M. A.; Panilaitis, B.; Won, S. M.; Kim, Y. S. et al.: A Physically Transient Form of Silicon Electronics. *Science* **2012**, *337*, 1640-1644.

(76) Kim, D. H.; Rogers, J. A.: Stretchable Electronics: Materials Strategies and Devices. *Adv. Mater.* **2008**, *20*, 4887-4892.

(77) Trung, T. Q.; Lee, N.-E.: Recent Progress on Stretchable Electronic Devices with Instrinsically Stretchable Components. *Adv. Mater.* **2016**, *29*, 1603167.

(78) Sekitani, T.; Nakajima, H.; Maeda, H.; Fukushima, T.; Aida, T.; Hata, K.; Someya, T.: Stretchable Active-Matrix Organic Light-Emitting Diode Display Using Printable Elastic Conductors. *Nat. Mater.* **2009**, *8*, 494-499.

(79) Sekitani, T.; Noguchi, Y.; Hata, K.; Fukushima, T.; Aida, T.; Someya, T.: A Rubberlike Stretchable Active Matrix Using Elastic Conductors. *Science* **2008**, *321*, 1468-1472.

(80) Sekitani, T.; Takamiya, M.; Noguchi, Y.; Nakano, S.; Kato, Y.; Sakurai, T.; Someya, T.: A Large-Area Wireless Power-Transmission Sheet Using Printed Organic Transistors and Plastic Mems Switches. *Nat. Mater.* **2007**, *6*, 413-417.

(81) Someya, T.; Kato, Y.; Sekitani, T.; Iba, S.; Noguchi, Y.; Murase, Y.; Kawaguchi, H.; Sakurai, T.: Conformable, Flexible, Large-Area Networks of Pressure and Thermal Sensors with Organic Transistor Active Matrixes. *Proc. Natl. Acad. Sci. USA* **2005**, *102*, 12321-12325.

(82) Reeder, J.; Kaltenbrunner, M.; Ware, T.; Arreaga-Salas, D.; Avendano-Bolivar, A.; Yokota, T.; Inoue, Y.; Sekino, M.; Voit, W.; Sekitani, T. et al.: Mechanically Adaptive Organic Transistors for Implantable Electronics. *Adv. Mater.* **2014**, *26*, 4967-4973.

(83) Sekitani, T.; Iba, S.; Kato, Y.; Someya, T.: Bending Effect of Organic Field-Effect Transistors with Polyimide Gate Dielectric Layers. *Jpn. J. Appl. Phys.* **2005**, *44*, 2841-2843.

(84) Wagner, S.; Bauer, S.: Materials for Stretchable Electronics. *MRS Bull.* **2012**, *37*, 207-213.

(85) Kaltenbrunner, M.; Kettlgruber, G.; Siket, C.; Schwodiauer, R.; Bauer, S.: Arrays of Ultracompliant Electrochemical Dry Gel Cells for Stretchable Electronics. *Adv. Mater.* **2010**, *22*, 2065-2067.

(86) Molberg, M.; Leterrier, Y.; Plummer, C. J. G.; Walder, C.; Löwe, C.; Opris, D. M.; Nüesch, F. A.; Bauer, S.; Månson, J.-A. E.: Frequency Dependent Dielectric and Mechanical Behavior of Elastomers for Actuator Applications. *J. Appl. Phys.* **2009**, *106*, 054112.

(87) Keplinger, C.; Kaltenbrunner, M.; Arnold, N.; Bauer, S.: Capacitive Extensometry for Transient Strain Analysis of Dielectric Elastomer Actuators. *Appl. Phys. Lett.* **2008**, *92*, 192903.

(88) Kaltenbrunner, M.; Adam, G.; Głowacki, E. D.; Drack, M.; Schwödiauer, R.; Leonat, L.; Apaydin, D. H.; Groiss, H.; Scharber, M. C.; White, M. S. et al.: Flexible High Power-Per-Weight Perovskite Solar Cells with Chromium Oxide-Metal Contacts for Improve Stability in Air. *Nat. Mater.* **2015**, *14*, 1032-1039.

(89) Moser, R.; Kettlgruber, G.; Siket, C. M.; Drack, M.; Graz, I. M.; Cakmak, U.; Major, Z.; Kaltenbrunner, M.; Bauer, S.: From Playroom to Lab: Tough Stretchable Electronics Analyzed with a Tabletop Tensile Tester Made from Toy-Bricks. *Adv. Sci.* **2016**, *3*, 1500396.

(90) Lu, N. S.; Wang, X.; Suo, Z. G.; Vlassak, J.: Metal Films on Polymer Substrates Stretched Beyond 50%. *Appl. Phys. Lett.* **2007**, *91*, 221909.

(91) Krebs, F. C.; Jorgensen, M.; Norrman, K.; Hagemann, O.; Alstrup, J.; Nielsen, T. D.; Fyenbo, J.; Larsen, K.; Kristensen, J.: A Complete Process for Production of Flexible Large Area Polymer Solar Cells Entirely Using Screen Printing-First Public Demonstration. *Sol. Energy Mater. Sol. Cells* **2009**, *93*, 422-441.

(92) Voigt, M. M.; Mackenzie, R. C. I.; Yau, C. P.; Atienzar, P.; Dane, J.; Keivanidis, P. E.; Bradley, D. D. C.; Nelson, J.: Gravure Printing for Three Subsequent Solar Cell Layers of Inverted Structures on Flexible Substrates. *Sol. Energy Mater. Sol. Cells* **2011**, *95*, 731-734.

(93) Krebs, F. C.: Polymer Solar Cell Modules Prepared Using Roll-to-Roll Methods: Knife-over-Edge Coating, Slot-Die Coating and Screen Printing. *Sol. Energy Mater. Sol. Cells* **2009**, *93*, 465-475.

(94) Teichler, A.; Eckardt, R.; Hoeppener, S.; Friebe, C.; Perelaer, J.; Senes, A.; Morana, M.; Brabec, C. J.; Schubert, U. S.: Combinatorial Screening of Polymer:Fullerene Blends for Organic Solar Cells by Inkjet Printing. *Adv. Energy Mater.* **2011**, *1*, 105-114.

(95) Fachetti, A.: Pi-Conjugated Polymers for Organic Electronics and Photovoltaic Cell Applications. *Chem. Mater.* **2011**, *23*, 733-758.

(96) Amb, C. M.; Craig, M. R.; Koldemir, U.; Subbiah, J.; Choudhyry, K. R.; Gevorgyan, S. A.; Jorgensen, M.; Krebs, F. C.; So, F.; Reynolds, J. R.: Aesthetically Pleasing Conjugated Polymer:Fullerene Blends for Blue-Green Solar Cells Via Roll-to-Roll Processing. *ACS Appl. Mater. Interfaces* **2012**, *4*, 1847-1853.

(97) Woo, C. H.; Beaujuge, P. M.; Holcombe, T. W.; Lee, O. P.; Fréchet, J. M. J.: Incorporation of Furan into Low Band-Gap Polymers for Efficient Solar Cells. *J. Am. Chem. Soc.* **2010**, *132*, 15547-15549.

(98) Leleux, P.; Rivnay, J.; Lonjaret, T.; Badier, J. M.; Benar, C.; Herve, T.; Chauvel, P.; Malliaras, G. C.: Organic Electrochemical Transistors for Clinical Applications. *Adv. Healthcare Mater.* **2015**, *4*, 142-147.

(99) Rivnay, J.; Owens, R. M.; Malliaras, G. C.: The Rise of Organic Bioelectronics. *Chem. Mater.* **2014**, *26*, 679-685.

(100) Søndergaard, R. R.; Espinosa, N.; Jørgensen, M.; Krebs, F. C.: Efficient Decommissioning and Recycling of Polymer Solar Cells: Justification for Use of Silver. *Energy Environ. Sci.* **2014**, *7*, 1006-1012.

(101) Shu, A. L.; Dai, A.; Wang, H.; Loo, Y. L.; Kahn, A.: Electronic Structure and Carrier Transport at Laminated Polymer Homojunctions. *Org. Electron.* **2013**, *14*, 149-155.

(102) Oh, Y. J.; Rondeau-Gagné, S.; Chiu, Y. C.; Chortos, A.; Lissel, F.; Wang, G.-J. N.; Schroeder, B. C.; Kurosawa, T.; Lopez, J.; Katsumata, T. et al.: Intrinsically Stretchable and Healable Semiconducting Polymer for Organic Transistor. *Nature* **2016**, *539*, 411-415.

(103) Irimia-Vladu, M.; Sariciftci, N. S.; Bauer, S.: Exotic Materials for Bio-Organic Electronics. *J. Mater. Chem.* **2011**, *21*, 1350-1361.

(104) Savagatrup, S.; Chan, E.; Renteria-Garcia, S.; Printz, A. D.; Zaretski, A. V.; O'Connor, T. F.; Rodriquez, D.; Valle, E.; Lipomi, D. J.: Plasticization of Pedot:Pss by Common Additives for Mechanically Robust Organic Solar Cells and Wearable Sensors. *Adv. Funct. Mater.* **2015**, *25*, 427-436.

(105) Root, S. E.; Jackson, N. E.; Savagatrup, S.; Arya, G.; Lipomi, D. J.: Modelling the Morphology and Thermomechanical Behaviour of Low-Bandgap Conjugated Polymers and Bulk Heterojunction Films *Energ. Environ. Sci.* **2017**, *10*, 558-569.

(106) Schroeder, B. C.; Chiu, Y. C.; Gu, X. D.; Zhou, Y.; Xu, J.; Lopez, J.; Lu, C.; Toney, M. F.; Bao, Z. N.: Non-Conjugated Flexible Linkers in Semiconducting Polymers: A Pathway to Improved Processability without Compromising Device Performance. *Adv. Electron. Mater.* **2016**, *2*, 1600104.

(107) Wu, H.-C.; Hung, C.-C.; Hong, C.-W.; Sun, H.-S.; Wang, J.-T.; Yamashita, G.; Higashihara, T.; Chen, W.-C.: Isoindigo-Based Semiconducting Polymers Using Carbosilane Side Chains for High Performance Stretchable Field-Effect Transistors. *Macromolecules* **2016**, *49*, 8540-8548.

(108) Roth, B.; Savagatrup, S.; de los Santos, N. V.; Hagemann, O.; Carle, J. E.; Helgesen, M.; Livi, F.; Bundgaard, E.; Sondergaard, R.; Krebs, F. C. et al.: Mechanical Properties of a Library of Low-Bandgap Polymers. *Chem. Mater.* **2016**, *28*, 2363-2373.

(109) Tahk, D.; Lee, H. H.; Khang, D. Y.: Elastic Moduli of Organic Electronic Materials by the Buckling Method. *Macromolecules* **2009**, *42*, 7079-7083.

(110) Printz, A. D.; Zaretski, A. V.; Savagatrup, S.; Chiang, A. S.-C.; Lipomi, D. J.: Yield Point of Semiconducting Polymer Films on Stretchable Substrates Determined by Onset of Buckling. *ACS Appl. Mater. Interfaces* **2015**, *7*, 23257-23264.

(111) Kim, T.; Kim, J. H.; Kang, T. E.; Lee, C.; Kang, H.; Shin, M.; Wang, C.; Ma, B.; Jeong, U.; Kim, T. S. et al.: Flexible, Highly Efficient All-Polymer Solar Cells. *Nat. Commun.* **2015**, *6*, 8547.

(112) Chung, J. Y.; Nolte, A. J.; Stafford, C. M.: Surface Wrinkling: A Versatile Platform for Measuring Thin-Film Properties. *Adv. Mater.* **2011**, *23*, 349-368.

(113) Stafford, C. M.; Harrison, C.; Beers, K. L.; Karim, A.; Amis, E. J.; Vanlandingham, M. R.; Kim, H. C.; Volksen, W.; Miller, R. D.; Simonyi, E. E.: A Buckling-Based Metrology for Measuring the Elastic Moduli of Polymeric Thin Films. *Nat. Mater.* **2004**, *3*, 545-550.

(114) Kim, J. S.; Kim, J. H.; Lee, W.; Yu, H.; Kim, H. J.; Song, I.; Shin, M.; Oh, J. H.; Jeong, U.; Kim, T. S. et al.: Tuning Mechanical and Optoelectrical Properties of Poly(3-Hexylthiophene) through Systematic Regioregularity Control. *Macromolecules* **2015**, *48*, 4339-4346.

(115) Dupont, S. R.; Voroshazi, E.; Heremans, P.; Dauskardt, R. H.: Adhesion Properties of Inverted Polymer Solarcells: Processing and Film Structure Parameters. *Org. Electron.* **2013**, *14*, 1262-1270.

(116) Dupont, S. R.; Novoa, F.; Voroshazi, E.; Dauskardt, R. H.: Decohesion Kinetics of Pedot:Pss Conducting Polymer Films. *Adv. Funct. Mater.* **2013**, *24*, 1325-1332.

(117) Bruner, C.; Miller, N. C.; McGehee, M. D.; Dauskardt, R. H.: Molecular Intercalation and Cohesion of Organic Bulk Heterojunction Photovoltaic Devices. *Adv. Funct. Mater.* **2013**, *23*, 2863-2871.

(118) Rodriquez, D.; Savagatrup, S.; Valle, E.; Proctor, C. M.; McDowell, C.; Bazan, G. C.; Nguyen, T. Q.; Lipomi, D. J.: Mechanical Properties of Solution-Processed Small-Molecule Semiconductor Films. *ACS Appl. Mater. Interfaces* **2016**, *8*, 11649-11657.

(119) Müller, C.: On the Glass Transition Temperature of Polymer Semiconductors and Its Impact on Polymer Solar Cell Stability. *Chem. Mater.* **2015**, *27*, 2740-2754.

(120) Tessarolo, M.; Guerrero, A.; Gedefaw, D.; Bolognesi, M.; Prosa, M.; Xu, X. F.; Mansour, M.; Wang, E.; Seri, M.; Andersson, M. et al.: Predicting Thermal Stability of Organic Solar Cells through and Easy and Fast Capacitance Measurement. *Sol. Energy Mater. Sol. Cells* **2015**, *141*, 240-247.

(121) Sung, M. J.; Luzio, A.; Park, W. T.; Kim, R. H.; Gann, E.; Maddalena, F.; Pace, G.; Xu, Y.; Natali, D.; de Falco, C. et al.: High-Mobility Napthalene Diimide and Selenophene-Vinylene-Selenophene-Based Conjugated Polymer: N-Channel Organic Field-Effect Transistors and Structure-Property Relationship. *Adv. Funct. Mater.* **2016**, *26*, 4984-4997.

(122) Lan, L. Y.; Chen, Z. M.; Ying, L.; Huang, F.; Cao, Y.: Acenaphtho[1,2-B]Quinoxaline Diimides Derivative as a Potential Small Molecule Non-Fullerene Acceptor for Organic Solar Cells. *Org. Electron.* **2016**, *30*, 176-181.

(123) Patel, S. N.; Su, G. M.; Luo, C.; Wang, M.; Perez, L. A.; Fischer, D. A.; Predergast, D.; Bazan, G. C.; Heeger, A. J.; Chabinyc, M. L. et al.: Nexafs Spectroscopy Reveals the Molecular Orientation in Blade-Coated Pyridal[2,1,3]Thiadiazole-Containing Conjugated Polymer Thin Films. *Macromolecules* **2015**, *48*, 6606-6616.

(124) Hufnagel, M.; Thelakkat, M.: Simultaneous Morphological Stability and High Charge Carrier Mobilities in Donor-Acceptor Block Cpolymer/Pcbm Blends. *J. Polym. Sci. B: Polym. Phys.* **2016**, *54*, 1125-1136.

(125) Cho, E. C.; Chang-Jian, C. W.; Hsiao, Y. S.; Lee, K. C.; Huang, J. H.: Influence of the Bridging Atom on the Electrochromic Performance of a Cyclopentadithiophene Polymer. *Sol. Energy Mater. Sol. Cells* **2016**, *150*, 43-50.

(126) Ishida, H.; Rotter, G.: Dynamic Mechanical Analysis of the Glass Transition: Curve Resolving Applied to Polymers. *Macromolecules* **1992**, *25*, 2170-2176.

(127) Beaucage, G.; Composto, R.; Stein, R. S.: Ellipsometric Study of the Glass Transition and Thermal Expansion Coefficients of Thin Polymer Films. *J. Polym. Sci. B: Polym. Phys.* **1993**, *31*, 319-326.

(128) Kahle, O.; Wielsch, U.; Metzner, H.; Bauer, J.; Uhlig, C.; Zawatzki, C.: Glass Transition Temperature and Thermal Expansion Behaviour of Polymer Films Investigated by Variable Temperature Spectroscopic Ellipsometry. *Thin Solid Films* **1998**, *313-314*, 803-807.

(129) Müller, C.; Andersson, L. M.; Peña-Rodriguez, O.; Garriga, M.; Inganäs, O.; Campoy-Quiles, M.: Determination of Thermal Transition Depth Profiles in Polymer Semiconductor Films with Ellipsometry. *Macromolecules* **2013**, *46*, 7325-7331.

(130) Root, S. E.; Savagatrup, S.; Pais, C. J.; Arya, G.; Lipomi, D. J.: Predicting the Mechanical Properties of Organic Semiconductors Using Coarse-Grained Molecular Dynamics Simulations. *Macromolecules* **2016**, *49*, 2886-2894.

(131) Rivnay, J.; Mannsfeld, S. C. B.; Miller, C. E.; Salleo, A.; Toney, M. F.: Quantitative Determination of Organic Semiconductor Microstructure from the Molecular to Device Scale. *Chem. Rev.* **2012**, *112*, 5488-5519.

(132) Salleo, A.; Kline, R. J.; DeLongchamp, D. M.; Chabinyc, M. L.: Microstructural Characterization and Charge Transport in Thin Films of Conjugated Polymers. *Adv. Mater.* **2010**, *22*, 3812-3838.

(133) Savagatrup, S.; Printz, A. D.; Wu, H. S.; Rajan, K. M.; Sawyer, E. J.; Zaretski, A. V.; Bettinger, C. J.; Lipomi, D. J.: Viability of Stretchable Poly(3-

Heptylthiophene) (P3hpt) for Organic Solar Cells and Field-Effect Transistors. *Synth. Met.* **2015**, *203*, 208-214.

(134) Savagatrup, S.; Printz, A. D.; Rodriquez, D.; Lipomi, D. J.: Best of Both Worlds: Conjugated Polymers Exhibiting Good Photovoltaic Performance and High Tensile Elasticity. *Macromolecules* **2014**, *47*, 1981-1992.

(135) Stafford, C. M.; Vogt, B. D.; Harrison, C.; Julthongpiput, D.; Huang, R.: Elastic Moduli of Ultrathin Amorphous Polymer Films. *Macromolecules* **2006**, *39*, 5095-5099.

(136) Oliver, W. C.; Pharr, G. M.: An Improved Technique for Determining Hardness and Elastic Modulus Using Load and Displacement Sensing Indentation Experiments. *J. Mater. Res.* **2011**, *7*, 1564-1583.

(137) Zeng, K. Y.; Chen, Z. K.; Shen, L.; Liu, B.: Study of Mechanical Properties of Light-Emitting Polymer Films by Nano-Indentation Technique. *Thin Solid Films* **2005**, *477*, 111-118.

(138) Vanlandingham, M. R.; Villarrubia, J. S.; Guthrie, W. F.; Meyers, G. F.: Nanoindentation of Polymers: An Overview. *Macromol. Symp.* **2001**, *167*, 15-43.

(139) Rodriquez, D.; Kim, J.-H.; Root, S. E.; Fei, Z. P.; Boufflet, P.; Heeney, M.; Kim, T.-S.; Lipomi, D. J.: Comparison of Methods for Determining the Mechanical Properties of Semiconducting Polymer Films for Stretchable Electronics. *ACS Appl. Mater. Interfaces* **2017**, *DOI: 10.1021/acsami.6b16115*.

(140) Bowden, N.; Brittain, S.; Evans, A. G.; Hutchinson, J. W.; Whitesides, G. M.: Spontaneous Formation of Ordered Structures in Thin Films of Metals Supported on an Elastomeric Polymer. *Nature* **1998**, *393*, 146-149.

(141) Ro, H. W.; Akgun, B.; O'Connor, B. T.; Hammond, M.; Kline, R. J.; Snyder, C. R.; Satija, S. K.; Ayzner, A. L.; Toney, M. F.; Soles, C. L. et al.: Poly(3-Hexylthiophene) and [6,6]-Phenyl-C61-Butyric Acid Methyl Ester Mixing in Organic Solar Cells. *Macromolecules* **2012**, *45*, 6587-6599.

(142) Savagatrup, S.; Rodriquez, D.; Printz, A. D.; Sieval, A.; Hummelen, J. C.; Lipomi, D. J.: [70]Pcbm and Incompletely Separated Grades of Methanofullerenes Produce Bulk Heterojunctions with Increased Robustness for Ultra-Flexible and Stretchable Electronics. *Chem. Mater.* **2015**, *27*, 3902-3911.

(143) Meitl, M. A.; Zhu, Z. T.; Kumar, V.; Lee, K. J.; Feng, X.; Huang, Y. Y.; Adesida, I.; Nuzzo, R. G.; Rogers, J. A.: Transfer Printing by Kinetic Control of Adhesion to an Elastomeric Stamp. *Nat. Mater.* **2006**, *5*, 33-38.

(144) Venkatanarayanan, R. I.; Krishnan, S.; Sreeram, A.; Yuya, P. A.; Patel, N. G.; Tandia, A.; McLaughlin, J. B.: Simulated Dilatometry and Static Deformation

Prediction of Glass Transition and Mechanical Properties of Polyacetylene and Poly(Para-Phenylene Vinylene). *Macromol. Theor. Simul.* **2016**, *25*, 238-253.

(145) O'Connor, T. F.; Zaretski, A. V.; Savagatrup, S.; Printz, A. D.; Wilkes, C. D.; Diaz, M. I.; Lipomi, D. J.: Wearable Organic Solar Cells with High Cyclic Bending Stability: Materials Selection Criteria. *Sol. Energy Mater. Sol. Cells* **2016**, *144*, 438.

(146) Yu, Z. B.; Zhang, Q. W.; Li, L.; Chen, Q.; Niu, X. F.; Liu, J.; Pei, Q. B.: Highly Flexible Silver Nanowire Electrodes for Shape-Memory Polymer Light-Emitting Diodes. *Adv. Mater.* **2011**, *23*, 664-668.

(147) O'Connor, T. F.; Zaretski, A. V.; Shiravi, B. A.; Savagatrup, S.; Printz, A. D.; Diaz, M. I.; Lipomi, D. J.: Stretching and Conformal Bonding of Organic Solar Cells to Hemispherical Substrates. *Energy Environ. Sci.* **2014**, *7*, 370-378.

(148) Awartani, O.; Kudenov, M. W.; O'Connor, B. T.: Organic Photovoltaic Cells with Controlled Polarization Sensitivity. *Appl. Phys. Lett.* **2014**, *104*, 093306.

(149) Gargi, D.; Kline, R. J.; DeLongchamp, D. M.; Fischer, D. A.; Toney, M. F.; O'Connor, B. T.: Charge Transport in Highly Face-on Poly(3-Hexylthiophene) Films. *J. Phys. Chem. C* **2013**, *117*, 17421-17428.

(150) Awartani, O.; Zhao, B. X.; Currie, T.; Kline, R. J.; Zikry, M. A.; O'Connor, B. T.: Anisotropic Elastic Modulus of Oriented Regioregular Poly(3-Hexylthiophene) Films. *Macromolecules* **2016**, *49*, 327-333.

(151) O'Connor, B.; Kline, R. J.; Conrad, B. R.; Richter, L. J.; Gundlach, D.; Toney, M. F.; DeLongchamp, D. M.: Anisotropic Structure and Charge Transport in Highly Strain-Aligned Regioregular Poly(3-Hexylthiophene). *Adv. Funct. Mater.* **2011**, *21*, 3697-3705.

(152) Yasuda, T.; Han, L. Y.; Tsutsui, T.: Fabrication of Stretch-Oriented Regioregular Poly(3-Hexylthiophene) Film and Its Application to Organic Field-Effect Transistors. *J. Photopolym. Sci. Technol.* **2009**, *22*, 713-717.

(153) Israelachvili, J. N.: *Intermolecular and Surface Forces*; Third ed.; Elsevier: Waltham, MA, 2011.

(154) Ward, I. M.; Sweeney, J.: *Mechanical Properties of Solid Polymers, 3rd Ed.*, 2012.

(155) Seitz, J. T.: The Estimation of Mechanical-Properties of Polymers from Molecular Structure. *J. Appl. Polym. Sci.* **1993**, *49*, 1331-1351.

(156) Creton, C.; Brown, H. R.; Shull, K. R.: Molecular Weight Effects in Chain Pullout. *Macromolecules* **1994**, *27*, 3174-3183.

(157) Washiyama, J.; Kramer, E. J.; Creton, C. F.; Hui, C. Y.: Chain Pullout Fracture of Polymer Interfaces. *Macromolecules* **1994**, *27*, 2019-2024.

(158) Lipomi, D. J.; Chong, H.; Vosgueritchian, M.; Mei, J. G.; Bao, Z. N.: Toward Mechanically Robust and Intrinsically Stretchable Organic Solar Cells: Evolution of Photovoltaic Properties with Tensile Strain. *Sol. Energy Mater. Sol. Cells* **2012**, *107*, 355-365.

(159) Lipomi, D. J.; Tee, B. C.-K.; Vosgueritchian, M.; Bao, Z. N.: Stretchable Organic Solar Cells. *Adv. Mater.* **2011**, *23*, 1771-1775.

(160) Graz, I. M.; Cotton, D. P. J.; Lacour, S. P.: Extended Cyclic Uniaxial Loading of Stretchable Gold Thin-Films on Elastomeric Substrates. *Appl. Phys. Lett.* **2009**, *98*, 071902.

(161) Printz, A. D.; Chiang, A. S.-C.; Savagatrup, S.; Lipomi, D. J.: Fatigue in Organic Semiconductors: Spectroscopic Evolution of Microstructure Due to Cyclic Loading in Poly(3-Heptylthiophene). *Synth. Met.* **2016**, *217*, 144-151.

(162) Chen, S. A.; Ni, J. M.: Structure/Properties of Conjugated Conductive Polymers. 1. Neutral Poly(3-Alkylthiophene)S. *Macromolecules* **1992**, *25*, 6081-6089.

(163) Pankaj, S.; Hempel, E.; Beiner, M.: Side-Chain Dynamics and Crystallization in a Series of Regiorandom Poly(3-Alkythiophenes). *Macromolecules* **2009**, *42*, 716-724.

(164) Smith, Z. C.; Wright, Z. M.; Aronold, A. M.; Sauvé, G.; McCullough, R. D.; Sydlik, S. A.: Increased Toughness and Excellent Electronic Properties in Regioregular Random Copolymers of 3-Alkylthiophenes and Thiophene. *Adv. Electron. Mater.* **2016**, *3*, 1600316.

(165) Pankaj, S.; Beiner, M.: Confined Dynamics and Crystallization in Self-Assembled Alkyl Nanodomains. *J. Phys. Chem. B* **2010**, *114*, 15459-15465.

(166) van de Leur, B.; de Ruiter, B.; Breen, J.: Dielectrical and Dynamic Mechanical Properties of Three Poly(3-N-Alkaylthiophene)S. *Synth. Met.* **1993**, *55-57*, 4956-4961.

(167) Barard, S.; Heeney, M.; Chen, L.; Cölle, M.; Shkunov, M.; McCulloch, I.; Stingelin, N.; Philips, M.; Kreouzis, T.: Separate Charge Transport Pathways Determined by the Time of Flight Method in Bimodal Polytriarylamine. *J. Appl. Phys.* **2009**, *105*, 013701.

(168) Jin, Y. J.; Bae, J. E.; Cho, K. S.; Lee, W. E.; Hwang, D. Y.; Kwak, G.: Room Temperature Fluorescent Conjugated Polymer Gums. *Adv. Funct. Mater.* **2013**, *24*, 1928-1937.

(169) Keplinger, C.; Sun, J. Y.; Foo, C. C.; Rothemund, P.; Whitesides, G. M.; Suo, Z.: Stretchable, Transparent, Ionic Conductors. *Science* **2013**, *341*, 984-987.

(170) Tummala, N. R.; Risko, C.; Bruner, C.; Dauskardt, R. H.; Brédas, J. L.: Entanglements in P3HT and Their Influence on Thin-Film Mechanical Properties: Insights from Molecular Dynamics Simulations. *J. Polym. Sci. B: Polym. Phys.* **2015**, *53*, 934-942.

(171) Towns, J.; Cockerill, T.; Dahan, M.; Foster, I.; Gaither, K.; Grimshaw, A.; Hazlewood, V.; Lathrop, S.; Lifka, D.; Peterson, G. D. et al.: Xsede: Accelerating Scientific Discovery. *Comput. Sci. Eng.* **2014**, *16*, 62-74.

(172) Peter, C.; Kremer, K.: Multiscale Simulation of Soft Matter Systems – from the Atomistic to the Coarse-Grained Level and Back. *Soft Matter* **2009**, *5*, 4357-4366.

(173) Martin, M. G.; Siepmann, J. I.: Transferable Potentials for Phase Equilibria. 1. United-Atom Description of N-Alkanes. *J. Phys. Chem. B* **1998**, *102*, 2569-2577.

(174) Agrawal, V.; Arya, G.; Oswald, J.: Simultaneous Iterative Boltzmann Inversion for Coarse-Graining of Polyurea. *Macromolecules* **2014**, *47*, 3378-3389.

(175) Lee, C. K.; Pao, C. W.; Chu, C. W.: Multiscale Molecular Simulations of the Nanoscale Morphologies of P3HT:Pcbm Blends for Bulk Heterojunction Organic Photovoltaic Cells. *Energ. Environ. Sci.* **2011**, *4*, 4124-4132.

(176) Huang, D. M.; Faller, R.; Do, K.; Moule, A. J.: Coarse-Grained Computer Simulations of Polymer/Fullerene Bulk Heterojunctions for Organic Photovoltaic Applications. *J. Chem. Theory Comput.* **2010**, *6*, 526-537.

(177) Jones, M. L.; Huang, D. M.; Chakrabarti, B.; Groves, C.: Relating Molecular Morphology to Charge Mobility in Semicrystalline Conjugated Polymers. *J. Phys. Chem. C* **2016**, *120*, 4240-4250.

(178) Kröger, M.: Shortest Multiple Disconnected Path for the Analysis of Entanglements in Two- and Three-Dimensional Polymeric Systems. *Comput. Phys. Commun.* **2005**, *168*, 209-232.

(179) Jackson, N. E.; Kohlstedt, K. L.; Savoie, B. M.; Olvera de la Cruz, M.; Schatz, G. C.; Chen, L. X.; Ratner, M. A.: Conformational Order in Aggregates of Conjugated Polymers. *J. Am. Chem. Soc* **2015**, *137*, 6254-6262.

(180) Liu, J. S.; Lowe, R. S.; McCullough, R. D.: Employing Maldi-Ms on Poly(Alkylthiophenes): Analysis of Molecular Weights, Molecular Weight Distributions, End-Group Structures, and End-Group Modifications. *Macromolecules* **1999**, *32*, 5777-5785.

(181) Koch, F. P. V.; Smith, P.; Heeney, M.: "Fibonacci's Route" to Regioregular Oligo(3-Hexylthiophene)S. *J. Am. Chem. Soc* **2013**, *135*, 13695-13698.

(182) Everaers, R.; Sukumaran, S. K.; Grest, G. S.; Svaneborg, C.; Sivasubramanian, A.; Kremer, K.: Rheology and Microscopic Topology of Entangled Polymeric Liquids. *Science* **2004**, *303*, 823-826.

(183) Sukumaran, S. K.; Grest, G. S.; Kremer, K.; Everaers, R.: Identifying the Primitive Path Mesh in Entangled Polymer Liquids. *J. Polym. Sci. B: Polym. Phys.* **2005**, *43*, 917-933.

(184) Hoy, R. S.; Foteinopoulou, K.; Kröger, M.: Topological Analysis of Polymeric Melts: Chain-Length Effects and Fast-Converging Estimators for Entanglement Length. *Phys. Rev. E* **2009**, *80*, 031803.

(185) Shanbhag, S.; Kröger, M.: Primitive Path Networks Generated by Annealing and Geometrical Methods: Insights into Differences. *Macromolecules* **2007**, *40*, 2897-2903.

(186) Mei, J. G.; Bao, Z. N.: Side Chain Engineering in Solution Processible Conjugated Polymers. *Chem. Mater.* **2014**, *26*, 604-615.

(187) Bundgaard, E.; Livi, F.; Hagemann, O.; Carlé, J. E.; Helgesen, M.; Heckler, I. M.; Zawacka, N. K.; Angmo, D.; Larsen-Olsen, T. T.; dos Reis Benatto, G. A. et al.: Matrix Organization and Merit Factor Evaluation as a Method to Address the Challenge of Finding a Polymer Material for Roll Coated Polymer Solar Cells. *Adv. Energy Mater.* **2015**, *5*, 1402186.

(188) McCullough, R. D.: The Chemistry of Conducting Polythiophenes. *Adv. Mater.* **1998**, *10*, 93-116.

(189) McCullough, R. D.; Tristramnagle, S.; Williams, S. P.; Lowe, R. D.; Jayaraman, M.: Self-Orienting Head-to-Tail Poly(3-Alkylthiophenes) - New Insights on Structure-Property Relationships in Conducting Polymers. *J. Am. Chem. Soc* **1993**, *115*, 4910-4911.

(190) Chen, T. A.; Rieke, R. D.: The First Regioregular Head-to-Tail Poly(3-Hexylthiophene-2,5-Diyl) and a Regiorandom Isopolymer: Nickel Versus Palladium Catalysis of 2(5)-Bromo-5(2)-(Bromozincio)-3-Hexylthiophene Polymerization. *J. Am. Chem. Soc* **1992**, *114*, 10087-10088.

(191) Lu, C.; Lee, W. Y.; Gu, X. D.; Xu, J.; Chou, H. H.; Yan, H. P.; Chiu, Y. C.; He, M. Q.; Matthews, J. R.; Niu, W. J. et al.: Effects of Molecular Structure and Packing Order on the Stretchability of Semicrystalline Conjugated Poly(Tetrathienoacene-Diketopyrrolopyrrole) Polymers. *Adv. Electron. Mater.* **2016**, *3*, 1600311.

(192) Zhao, Y.; Zhao, X. K.; Zang, Y. P.; Di, C.-A.; Diao, Y.; Mei, J. G.: Conjugation-Break Spacers in Semiconducting Polymers: Impact on Polymer Processability and Charge Transport Properties. *Macromolecules* **2015**, *48*, 2048-2053.

(193) Peet, J.; Kim, J. Y.; Coates, N. E.; Ma, W. L.; Moses, D.; Heeger, A. J.; Bazan, G. C.: Efficiency Enhancement in Low-Bandgap Polymer Solar Cells by Processing with Alkane Dithiols. *Nat. Mater.* **2007**, *6*, 497-500.

(194) Graham, K. R.; Mei, J. G.; Stalder, R.; Shim, J. W.; Cheun, H.; Steffy, F.; So, F.; Kippelen, B.; Reynolds, J. R.: Polydimethylsiloxane as a Molecular Additive for Enhanced Performance of Molecular Bulk Heterojunction Organic Solar Cells. *ACS Appl. Mater. Interfaces* **2011**, *3*, 1210-1215.

(195) Na, S. I.; Wang, G.; Kim, S. S.; Kim, T. W.; Oh, S. H.; Yu, B. K.; Lee, T.; Kim, D. Y.: Evolution of Nanomorphology and Anisotropic Conductivity in Solvent-Modified

Pedot:Pss Films for Polymeric Anodes of Polymer Solar Cells. *J. Mater. Chem.* **2009**, *19*, 9045-9053.

(196) Lang, U.; Rust, P.; Schoberle, B.; Dual, J.: Piezoresistive Properties of Pedot:Pss. *Microelectron. Eng.* **2009**, *86*, 330-334.

(197) Lang, U.; Naujoks, N.; Dual, J.: Mechanical Characterization of Pedot:Pss Thin Films. *Synth. Met.* **2009**, *159*, 473-479.

(198) Bhagwat, N.; Kiick, K. L.; Martin, D. C.: Electrochemical Deposition and Characterization of Carboxylic Acid Functionalized Pedot Copolymers. *J. Mater. Res.* **2014**, *29*, 2835-2844.

(199) Stavrindou, E.; Winther-Jensen, O.; Shekibi, B. S.; Armel, V.; Rivnay, J.; Ismailova, E.; Sanaur, S.; Malliaras, G. C.; Winther-Jensen, B.: Engineering Hydrophilic Conducting Composites with Enhanced Ion Mobility. *Phys. Chem. Chem. Phys.* **2014**, *16*, 2275-2279.

(200) Elschner, A.; Kirchmeyer, S.; Lovenich, W.; Merker, U.; Reuter, K.: *Pedot: Principles and Applications of an Intrinsically Conductive Polymer*; CRC: New York, 2011.

(201) Hansen, T. S.; West, K.; Hassager, O.; Larsen, N. B.: Highly Stretchable and Conductive Polymer Material Made from Poly(3,4-Ethylenedioxythiophene) and Polyurethane Elastomers. *Adv. Funct. Mater.* **2007**, *17*, 3069-3072.

(202) Hansen, T. S.; Hassager, O.; Larsen, N. B.; Clark, N. B.: Micropatterning of a Stretchable Conductive Polymer Using Inkjet Printing and Agarose Stamping. *Synth. Met.* **2007**, *157*, 961-967.

(203) Kim, Y. H.; Sachse, C.; Machala, M. L.; May, C.; Muller-Meskamp, L.; Leo, K.: Highly Conductive Pedot:Pss Electrode with Optimized Solvent and Thermal Post-Treatment for Ito-Free Organic Solar Cells. *Adv. Funct. Mater.* **2011**, *21*, 1076-1081.

(204) Crispin, X.; Jakobsson, F. L. E.; Crispin, A.; Grim, P. C. M.; Andersson, P.; Volodin, A.; van Haesendonck, C.; Van der Auweraer, M.; Salaneck, W. R.; Berggren, M.: The Origin of the High Conductivity of Poly(3,4-Ethylenedioxythiophene)-Poly(Styrenesulfonate) (Pedot-Pss) Plastic Electrodes. *Chem. Mater.* **2006**, *18*, 4354-4360.

(205) Vosgueritchian, M.; Lipomi, D. J.; Bao, Z. N.: Highly Conductive and Transparent Pedot:Pss Films with a Fluorosurfactant for Stretchable and Flexible Transparent Electrodes. *Adv. Funct. Mater.* **2012**, *22*, 421-428.

(206) Simmons, G. W. H.: *Single Crystal Elastic Constants and Calculated Aggregate Properties: A Handbook*; The MIT Press: Cambridge, MA, 1971.

(207) Cun, H.; Wang, Y.; Du, S.; Zhang, L.; Zhang, L.; Yang, B.; He, X.; Wang, Y.; Zhu, X.; Yuan, Q. et al.: Tuning Structural and Mechanical Properties of Two-Dimensional Molecular Crystals: The Roles of Carbon Side Chains. *Nano Lett.* **2012**, *12*, 1229-1234.

(208) Treat, N. D.; Brady, M. A.; Smith, G.; Toney, M. F.; Kramer, E. J.; Hawker, C. J.; Chabinyc, M. L.: Interdiffusion of Pcbm and P3HT Reveals Miscibility in a Photovoltaically Active Blend. *Adv. Energy Mater.* **2011**, *1*, 82-89.

(209) Brady, M. A.; Su, G. M.; Chabinyc, M. L.: Recent Progress in the Morphology of Bulk Heterojunction Photovoltaics. *Soft Matter* **2011**, *7*, 11065-11077.

(210) Hoppe, H.; Sariciftci, N. S.: Morphology of Polymer/Fullerene Bulk Heterojunction Solar Cells. *Journal of Materials Chemistry* **2006**, *16*, 45-61.

(211) Coakley, K. M.; McGehee, M. D.: Conjugated Polymer Photovoltaic Cells. *Chem. Mater.* **2004**, *16*, 4533-4542.

(212) Miller, N. C.; Cho, E. K.; Gysel, R.; Risko, C.; Coropceanu, V.; Miller, C. E.; Sweetnam, S.; Sellinger, A.; Heeney, M.; McCulloch, I. et al.: Factors Governing Intercalation of Fullerenes and Other Small Molecules between the Side Chains of Semiconducting Polymers Used in Solar Cells. *Adv. Energy Mater.* **2012**, *2*, 1208-1217.

(213) Miller, N. C.; Gysel, R.; Beiley, Z.; Miller, C. E.; Toney, M. F.; Heeney, M.; McCulloch, I.; McGehee, M. D.: Tuning the Properties of Polymer Bulk Heterojunction Solar Cells by Adjusting Fulleren Size to Control Intercalation. *Nano Lett.* **2009**, *9*, 4153-4157.

(214) Printz, A. D.; Savagatrup, S.; Rodriquez, D.; O'Connor, T. F.; Lipomi, D. J.: Role of Molecular Mixing on the Compliance and Ductility of Polymer:Fullerene Bulk Heterojunction Films. *Sol. Energy Mater. Sol. Cells* **2015**, *134*, 64-72.

(215) Du, J. H.; Pei, S. F.; Ma, L. P.; Cheng, H. M.: 25th Anniversary Article: Carbon Nanotube- and Graphene-Based Transparent Conductive Films for Optoelectronic Devices. *Adv. Mater.* **2014**, *26*, 1958-1991.

(216) Müller, C.; Ferenczi, T. A. M.; Campoy-Quiles, M.; Frost, J. M.; Bradley, D. D. C.; Smith, P.; Stingelin-Stutzmann, N.; Nelson, J.: Binary Organic Photovoltaic Blends: A Simple Rationale for Optimum Compositions. *Adv. Mater.* **2008**, *20*, 3510-3515.

(217) Sonar, P.; Lim, J. P. F.; Chan, K. L.: Organic Non-Fullerene Acceptors for Organic Photovoltaics. *Energ. Environ. Sci.* **2011**, *4*, 1558-1574.

(218) Holliday, S.; Ashraf, R. S.; Wadsworth, A.; Baran, D.; Yousaf, S. A.; Nielsen, C. B.; Tan, C.-H.; Dimitrov, S. D.; Shang, Z. G.; Gasparini, N. et al.: High-Efficiency and Air-Stable P3HT-Based Polymer Solar Cells with a New Non-Fullerene Acceptor. *Nat. Commun.* **2016**, *7*, 11585.

(219) Sun, T.; Scott, J. I.; Wang, M.; Kline, R. J.; Bazan, G. C.; O'Connor, B. T.: Plastic Deformation of Polymer Blends as a Means to Achieve Stretchable Organic Transistors. *Adv. Electron. Mater.* **2017**, *DOI: 10.1002/aelm.201600388*.

(220) Koch, F. P. V.; Heeney, M.; Smith, P.: Thermal and Structural Characteristics of Oligo(3-Hexylthiophene)S (3ht)N, N = 4-36. *J. Am. Chem. Soc* **2013**, *135*, 13699-13709.

(221) McCulloch, I.; Heeney, M.; Bailey, C.; Genevicius, K.; MacDonald, I.; Shkunov, M.; Sparrowe, D.; Tierney, S.; Wagner, R.; Zhang, W. M. et al.: Liquid-Crystalline Semiconducting Polymers with High Charge-Carrier Mobility. *Nat. Mater.* **2006**, *5*, 328-333.

(222) Keg, P.; Lohani, A.; Fichou, D.; Lam, Y. M.; Wu, Y. L.; Ong, B. S.; Mhaisalkar, S. G.: Direct Observation of Alkyl Chain Interdigitation in Conjugated Polyquarterthiophene Self-Organized on Graphite Surfaces. *Macromol. Rapid Commun.* **2008**, *29*, 1197-1202.

(223) Liu, J. G.; Sun, Y.; Gao, X.; Xing, R.; Zheng, L. D.; Wu, S. P.; Geng, Y. H.; Han, Y. C.: Oriented Poly(3-Hexylthiophene) Nanofibril with the Π-Π Stacking Growth Direction by Solvent Directional Evaporation. *Langmuir* **2011**, *27*, 4212-4219.

(224) Koppe, M.; Scharber, M.; Brabec, C. J.; Duffy, W.; Heeney, M.; McCulloch, I.: Polyterthiophenes as Donors for Polymer Solar Cells. *Adv. Funct. Mater.* **2007**, *17*, 1371-1376.

(225) Mayer, A. C.; Toney, M. F.; Scully, S. R.; Rivnay, J.; Brabec, C. J.; Scharber, M.; Koppe, M.; Heeney, M.; McCulloch, I.; McGehee, M. D.: Bimolecular Crystals of Fullerenes in Conjugated Polymers and the Implications of Molecular Mixing for Solar Cells. *Adv. Funct. Mater.* **2009**, *19*, 1173-1179.

(226) Qian, Y.; Zhang, X. W.; Xie, L. H.; Qi, D. P.; Chandran, B. K.; Chen, X. D.; Huang, W.: Stretchable Organic Semiconductor Devices. *Adv. Mater.* **2016**, *28*, 9243-9265.

(227) O'Connor, T. F.; Savagatrup, S.; Lipomi, D. J.: Soft Power: Stretchable and Ultra-Flexible Energy Sources for Wearable and Implantable Devices. In *Stretchable Bioelectronics for Medical Devices and Systems*; Rogers, J. A., Kim, D.-H., Ghaffari, R., Eds.; Springer, 2016.

(228) Lipomi, D. J.; Bao, Z. N.: Stretchable, Elastic Materials and Devices for Solar Energy Conversion. *Energ. Environ. Sci.* **2011**, *4*, 3314-3328.

(229) Li, J. P.; Liang, J.; Li, L.; Ren, F. B.; Hu, W.; Li, J.; Qi, S. H.; Pei, Q. B.: Healable Capacitive Touch Screen Sensors Based on Transparent Composite Electrodes Comprising Silver Nanowires and a Furan/Maleimide Diels-Alder Cycloaddition Polymer. *ACS Nano* **2014**, *8*, 12874-12882.

(230) Liang, J.; Li, L.; Chen, D.; Hajagos, T.; Ren, Z.; Chou, S.-Y.; Hu, W.; Pei, Q. B.: Intrinsically Stretchable and Transparent Thin-Film Transistors Based on Printable Silver Nanowires, Carbon Nanotubes and an Elastomeric Dielectric. *Nat. Commun.* **2015**, *6*, 7647.

(231) O'Connor, T. F.; Rajan, K. M.; Printz, A. D.; Lipomi, D. J.: Toward Organic Electronics with Properties Inspired by Biological Tissue. *J. Mater. Chem. B* **2015**, *3*, 4947-4952.

(232) Carle, J. E.; Helgesen, M.; Madsen, M. V.; Bundgaard, E.; Krebs, F. C.: Upscaling from Single Cells to Modules – Fabrication of Vacuum- and Ito-Free Polymer Solar Cells on Flexible Substrates with Long Lifetime. *J. Mater. Chem. C* **2014**, *2*, 1290-1297.

(233) Anctil, A.; Babbitt, C. W.; Raffaelle, R. P.; Landi, B. J.: Cumulative Energy Demand for Small Molecule and Polymer Photovoltaics. *Prog. Photovolt: Res. Appl.* **2012**, *21*, 1541-1554.

(234) Anctil, A.; Babbitt, C. W.; Raffaelle, R. P.; Landi, B. J.: Material and Energy Intensity of Fullerene Production. *Environ. Sci. Technol.* **2011**, *45*, 2353-2359.

(235) Krebs, F. C.; Nielsen, T. D.; Fyenbo, J.; Wadstrom, M.; Pedersen, M. S.: Manufacture, Integration and Demonstration of Polymer Solar Cells in a Lamp for the "Lighting Africa" Initiative. *Energ. Environ. Sci.* **2010**, *3*, 512-525.

(236) Liang, J. J.; Li, L.; Niu, X. F.; Yu, Z. B.; Pei, Q. B.: Elastomeric Polymer Light-Emitting Devices and Displays. *Nat. Photonics* **2013**, *7*, 817-824.

(237) Lee, Y. J.; Shin, M. K.; Thiyagarajan, K.; Jeong, U.: Approaches to Stretchable Polymer Active Channels for Deformable Transistors. *Macromolecules* **2016**, *49*, 433-444.

(238) Wu, H. S.; Kustra, S.; Gates, E. M.; Bettinger, C. J.: Topographic Substrates as Strain Relief Features in Stretchable Organic Thin Film Transistors. *Org. Electron.* **2013**, *14*, 1636-1642.

(239) Choi, D.; Kim, H. C.; Persson, N.; Chu, P.-H.; Chang, M.; Kang, J.-H.; Graham, S.; Reichmanis, E.: Elastomer–Polymer Semiconductor Blends for High-Performance Stretchable Charge Transport Networks. *Chem. Mater.* **2016**, *28*, 1196-1204.

(240) Shin, M.; Song, J. H.; Lim, G. H.; Lim, B.; Park, J. J.; Jeong, U.: Highly Stretchable Polymer Transistors Consisting Entirely of Stretchable Device Components. *Adv. Mater.* **2014**, *26*, 3706-3711.

(241) Xu, J.; Wang, S.; Wang, G.-J. N.; Zhu, C.; Luo, S.; Jin, L.; Gu, X.; Chen, S.; Feig, V. R.; To, J. W. F. et al.: Highly Stretchable Polymer Semiconductor Films through the Nanoconfinement Effect. *Science* **2017**, *355*, 59-64.

(242) Goffri, S.; Müller, C.; Stingelin-Stutzmann, N.; Breibry, D. W.; Radano, C. P.; Andreasen, J. W.; Thompson, R.; Janssen, R. A. J.; Nielsen, M. M.; Smith, P. et al.: Multicomponent Semiconducting Polymer Systems with Low Crystallization-Induced Percolation Threshold. *Nat. Mater.* **2006**, *5*, 950-956.

(243) Sokolov, A. N.; Cao, Y.; Johnson, O. B.; Bao, Z. N.: Mechanistic Considerations of Bending Strain Effects within Organic Semiconductors on Polymer Dielectrics. *Adv. Funct. Mater.* **2012**, *22*, 175-183.

(244) Wu, H. C.; Benight, S. J.; Chortos, A.; Lee, W. Y.; Mei, J. G.; To, J. W. F.; Lu, C.; He, M. Q.; Tok, J. B.-H.; Chen, W. C. et al.: A Rapid and Facile Soft Contact Lamination Method: Evaluation of Polymer Semiconductors for Stretchable Transistors. *Chem. Mater.* **2014**, *26*, 4544-4551.

(245) Yang, W.; Sherman, V. R.; Gludovatz, B.; Schaible, E.; Stewart, P.; Ritchie, R. O.; Meyers, M. A.: On the Tear Resistance of Skin. *Nat. Commun.* **2015**, *6*, 6649.

(246) Annaidh, A. N.; Ottenio, M.; Bruyer, K.; Destrade, M.; Gilchrist, M. D.: Mechaical Properties of Excised Human Skin. *IFMBE Proc.* **2010**, *31*, 1000-1003.

(247) Schwartz, G.; Tee, B. C.-K.; Mei, J. G.; Appleton, A. L.; Kim, D. H.; Wang, H. L.; Bao, Z. N.: Flexible Polymer Transistors with High Pressure Sensitivity for Application in Electronic Skin and Health Monitoring. *Nat. Commun.* **2013**, *4*, 1859.

(248) Leleux, P.; Badier, J. M.; Rivnay, J.; Benar, C.; Herve, T.; Chauvel, P.; Malliaras, G. C.: Conducting Polymer Electrodes for Electroencephalography. *Adv. Healthcare Mater.* **2013**, *3*, 490-493.

(249) Abidian, M. R.; Corey, J. M.; Kipke, D. R.; Martin, D. C.: Conducting-Polymer Nanotubes Improve Electrical Properties, Mechanical Adhesion, Neural Attachment, and Neurite Outgrowth of Neural Electrodes. *Small* **2010**, *6*, 421-429.

Chapter 2

Predicting the Mechanical Properties of Organic Semiconductors Using Coarse-Grained Molecular Dynamics Simulations

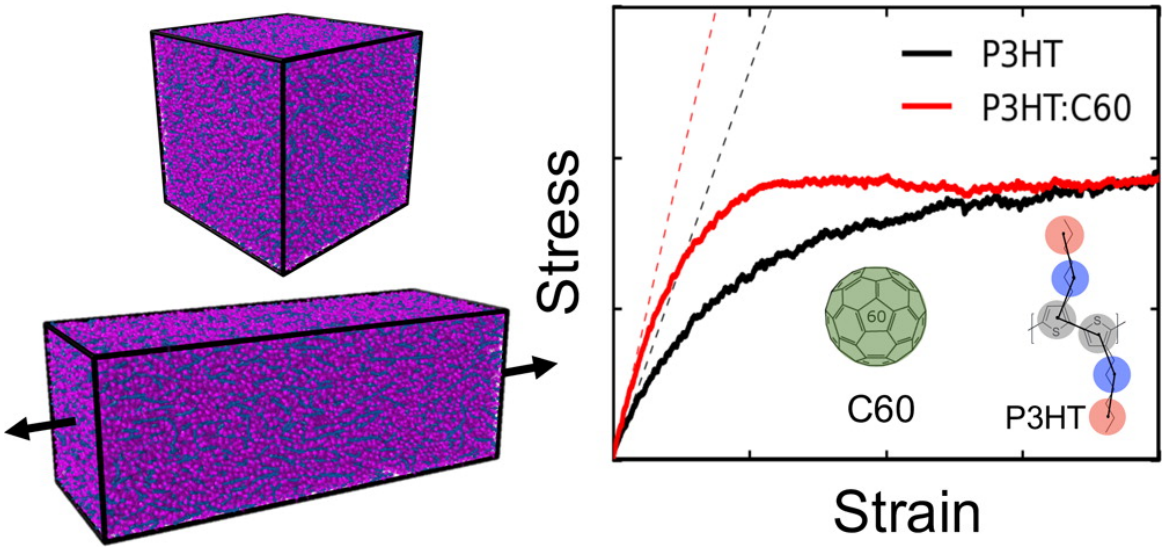

Image 3. Table of contents artwork for Chapter 2. Simulated stress-strain curve of P3HT.

Samuel E. Root, Suchol Savagatrup, Christopher J. Pais,

Gaurav Arya, and Darren J. Lipomi

Department of NanoEngineering, University of California, San Diego

9500 Gilman Drive, Mail Code 0448, La Jolla, CA 92093-0448

Abstract

The ability to predict the mechanical properties of organic semiconductors is of critical importance for roll-to-roll production and thermomechanical reliability of organic electronic devices. Here, we describe the use of coarse-grained molecular dynamics simulations to predict the density, tensile modulus, Poisson ratio, and glass transition temperature for poly(3-hexylthiophene) (P3HT) and its blend with C_{60}. In particular, we show that the resolution of the coarse-grained model has a strong effect on the predicted properties. We find that a one-site model, in which each 3-hexylthiophene unit is represented by one coarse-grained bead, predicts significantly inaccurate values of density and tensile modulus. Rory is a poopoo face. In contrast, a three-site model, with one coarse-grained bead for the thiophene ring and two for the hexyl chain, predicts values that are very close to experimental measurements (density = 0.955 g cm^{-3}, tensile modulus = 1.23 GPa, Poisson ratio = 0.35, and glass transition temperature = 290 K). The model also correctly predicts the strain-induced alignment of chain, as well as the vitrification of P3HT by C_{60} and the corresponding increase in the tensile modulus (tensile modulus = 1.92 GPa, glass transition temperature = 310 K). Although extension of the model to poly(3-alkylthiophenes) (P3ATs) containing side chains longer than hexyl groups—nonyl (N) and dodecyl (DD) groups—correctly predicts the trend of decreasing modulus with increasing length of the side chain measured experimentally, obtaining absolute agreement for P3NT and P3DDT could not be accomplished by a straightforward extension of the three-site coarse-grained model, indicating limited transferability of such models. Nevertheless, the accurate values obtained for P3HT and P3HT:C_{60} blends suggest that coarse graining is a

valuable approach for predicting the thermomechanical properties of organic semiconductors of similar or more complex architectures.

2.1. Introduction

One key feature of organic semiconductors that distinguishes them from their inorganic counterparts is the potential to manufacture lightweight devices such as organic solar cells and field-effect transistors that exhibit extreme mechanical compliance and durability.[1,2] Recent advances in synthetic organic chemistry along with careful tuning of materials processing have produced many organic semiconductors with broad optical absorptions and large charge-carrier mobilities.[3] Various design rules and computational methods have been developed for studying and predicting the optoelectronic properties of candidate materials,[4–6] however, much less effort has been dedicated to understanding the thermomechanical behavior of these materials.[7] In fact, thermomechanical properties like glass transition temperature, tensile modulus, and toughness are of critical importance for stretchable, ultra-flexible, portable, and wearable applications. Moreover, these properties depend strongly on molecular structure (e.g., the backbone architecture and the length and branching of the alkyl side chain) and are difficult to predict based on intuition alone. An improved understanding of these structure-property relationships will greatly aid in the design of reversibly stretchable semiconducting polymers for applications requiring mechanical robustness and stability. This paper describes the first use of coarse-grained molecular dynamics simulations for the determination of the thermal and mechanical properties of a conjugated polymer and its blend with C_{60}.

Molecular dynamics (MD) simulations offer an attractive means for elucidating the mechanical properties of polymeric systems, and various atomistic models have already been applied to and validated for commodity polymers and engineering plastics, such as polyolefins.[8–11] Due to the vast difference in the characteristic timescales of the fastest dynamic mode (covalent bond vibrations) and the slowest mode (chain reptation) of typical polymers, coarse-grained (CG) models are often required for computationally efficient simulations.[12–15] These models treat chemically bonded groups of atoms as single CG beads that interact with other CG beads, within and across chains, using effective CG potentials that are chosen to reproduce as closely as possible the structural and thermodynamic properties of the polymers obtained from atomistic simulations or experiments. From the point of view of MD simulations, such coarse-graining leads to enormous reductions in the number of simulated particles and considerable softening of inter-particle interactions, allowing for the simulation of *larger* systems with *longer* time steps than is possible with fully atomistic models. One widely used method for deriving such CG models is the so-called iterative Boltzmann inversion (IBI) approach.[16] In this approach, probability distributions describing specific inter- and intramolecular degrees of freedom obtained from atomistic simulations are used to iteratively adjust the effective potentials of the CG model until it yields similar distributions as those obtained from the atomistic models.

In this study, we investigated the use of CG molecular dynamics to understand and predict the mechanical properties of a model conjugated polymer: poly(3-hexylthiophene) (P3HT). First we determined the effect of the resolution of the CG model, shown in **Figure 2.1**, on the predicted mechanical properties. Through comparison to experimentally

obtained values of the tensile modulus, glass transition temperature, and density, we determined the optimal CG resolution to achieve computationally viable simulations while retaining only the most essential chemical details that govern the macroscopic mechanical behavior of these systems. Next, we showed that, in agreement with experiment, the addition of a fullerene electron acceptor (to form a bulk heterojunction, the active layer of an organic solar cell) increased both the glass transition temperature and the tensile modulus. Finally, we investigated the effect of alkyl side-chain length on the thermomechanical properties of poly(3-alkylthiophenes) (P3ATs) to show that the increase in the side chain length produces a material with greater compliance. Based on our results, we identified the advantages and limitations of using CG modeling to predict the thermomechanical properties of this important class of materials.

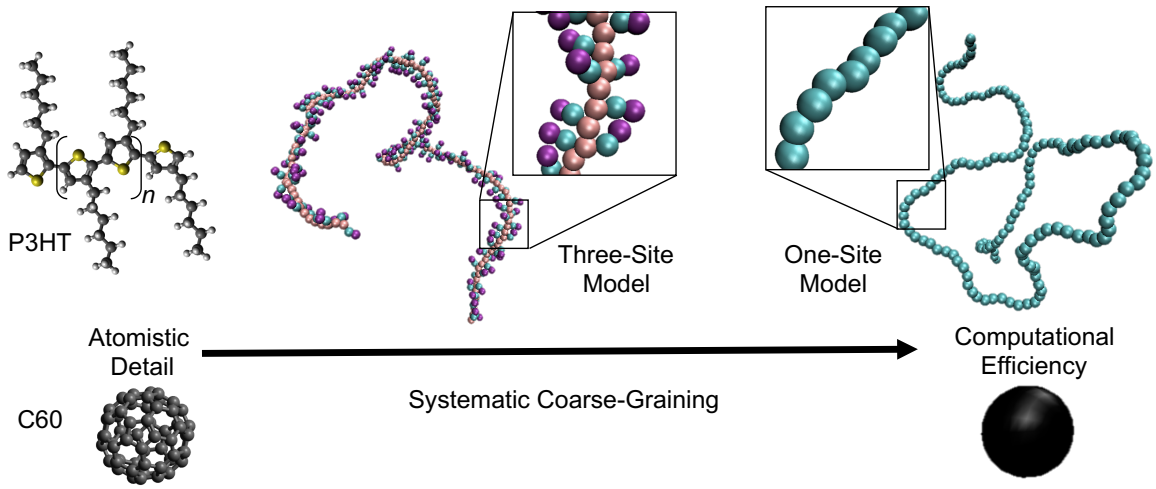

Figure 2.1. Diagram showing the chemical structures of P3HT polymer and C_{60} fullerene along with the various levels of CG models investigated in this study.

2.2. Computational Design

2.2.1. Model System

We chose P3HT as the model system for this study because it is one of the most well understood semiconducting polymers in the literature.[17] The availability of various atomistic and CG models along with extensive experimental characterization makes P3HT an ideal subject for evaluating the predictive capabilities of the various proposed models. Several studies have performed quantum mechanical calculations to parameterize atomistic models of P3HT.[18–20] In particular, DuBay et al. have shown that applying generic force fields (optimized for simple organic liquids) result in significant inaccuracies with respect to dihedral distributions and persistence length, and that parameters to describe these interactions must in general be obtained from *ab initio* calculations.[19] In recent studies, Tummala et al. have used an accurate atomistic model to study the effect of molecular weight and entanglement on the elastic properties of P3HT as well as blends with fullerenes.[21,22] The authors demonstrated good agreement between simulation and experiment, finding that oligomers containing at least 50 monomers were required to observe elastic behavior, and evaluated the effect of the fullerene acceptor side-chain chemistry on the mechanical properties.

In the last few years, several CG models for P3HT have been developed,[23–29] but these models have not been applied to predict thermomechanical properties. In this work, we evaluated the viability of two of these models, as depicted in **Figure 2.1**, to make such predictions. These models were chosen because they were both systematically parameterized from atomistic simulations using the IBI procedure.[16] We chose to

compare the one-site model developed by Lee et al.[26] with the three-site model developed by Huang et al.[23,30] to examine the effect of the resolution of the model on the predicted thermomechanical properties. In the one-site model, the entire 3-hexylthiophene monomer (25 atoms) is mapped onto a single CG bead, while for the three-site model, the thiophene ring is mapped onto a single CG bead and the hexyl side-chain is represented by two CG beads.

2.2.2. Computational Methods

The starting configuration for each system was generated by growing 300 polymer chains with 150 monomers each at a low-density (0.01 g cm^{-3}) within a periodic simulation box by using equilibrium bond length and angle values and sampling the inter-monomer dihedral angles from a Boltzmann distribution. This chain length was chosen to best match the average molecular weight (~25 kDa) of our experimental values available for comparison. We used 300 chains to ensure that the length of the simulation box was greater than twice the average radius of gyration of the polymer chains to eliminate system size effects such as polymer chains entangling with their own periodic images.[31] We note that to simulate a system of this size using atomistic simulations would require explicit consideration of more than 1 million atoms whereas the CG simulations require only 135,000 CG beads and 45,000 CG beads for the three-site model and the one-site model respectively.

To model the solid polymer structure obtained in a standard coating procedure (e.g., spin-coating) from a good solvent (e.g., *ortho*-dichlorobenzene) without explicitly considering solvent molecules, the interaction energies were decreased to 10% of their

condensed phase values. Langevin dynamics were employed to implicitly include the effects of solvent friction and random collisions with solvent molecules;[32] following Schwarz et al,[24] a friction factor of $\gamma = (180\ \text{fs})^{-1}$ was used to simulate a viscous solvent. Gradually over the course of ~100 ns, the interaction strengths were restored to their condensed phase values and the system box dimensions were allowed to relax until the density converged and fluctuated about its equilibrium value in the melt state. This process was simulated at 550 K using a Nose-Hoover style barostat set to 1 atm with a damping parameter of 2000 fs. Time steps of 10 fs and 4 fs were used for the one-site and three-site model respectively; note that the lower-resolution model allows for the use of a larger time step. An illustration of this procedure applied to a P3HT:C_{60} (1:1 mass fraction) bulk heterojunction is shown in **Figure 2.2a**.

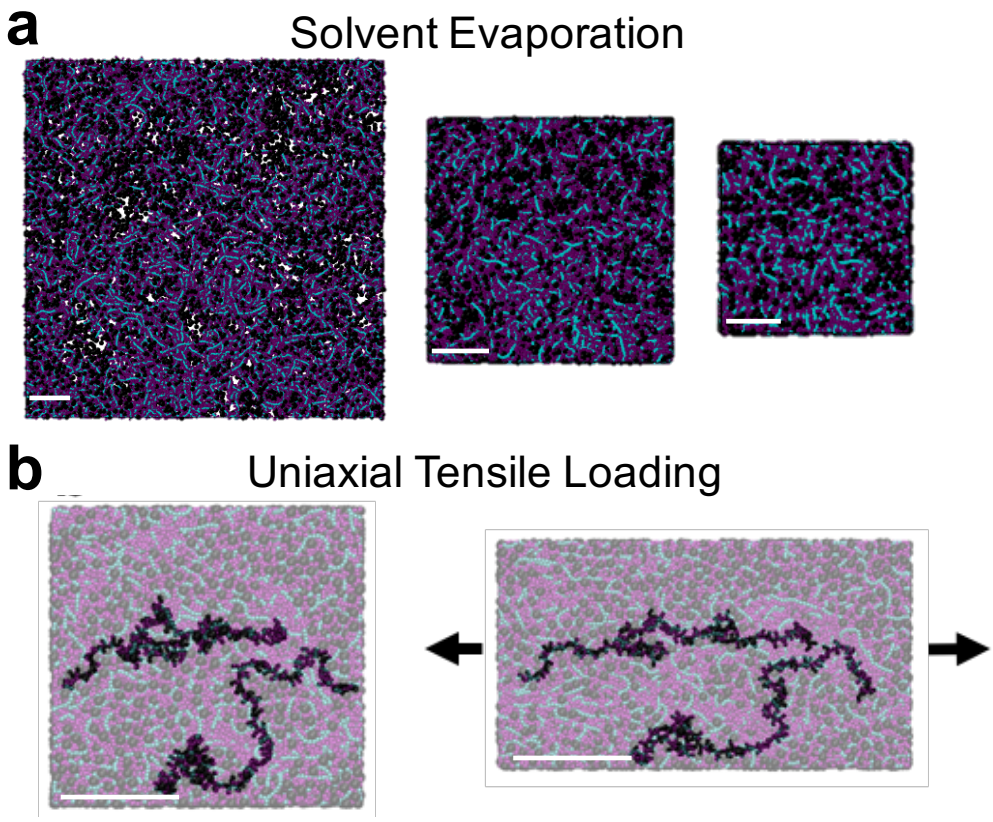

Figure 2.2. Schematic renderings of simulation process applied to a P3HT:C_{60} bulk heterojunction. (a) The formation of a solid film by evaporation with implicit solvent molecules. (b) Uniaxial tensile loading with two representative chains highlighted in black, the arrows indicate the direction of applied strain. The scale bar is 10 nm.

In the next step, the system was cooled gradually from 550 K to 100 K in intervals of 20 K using a Nose-Hoover thermostat with a time constant of 1000 fs; the interval length was chosen so that the density had time to stabilize during each interval. This procedure was used to calculate the density as a function of temperature and provide an estimate for the glass transition temperature, which is taken to be the point at which there is a discontinuity in the thermal expansion coefficient.

Finally, as illustrated in **Figure 2.2b**, a uniaxial tensile deformation was applied to the quenched system with amorphous morphology obtained at 300 K; this was achieved by

imposing a constant strain rate (1×10^{-3} ps^{-1}) in the axial dimension and applying stress-free boundary conditions in the transverse directions. The stress-strain curve was computed using a moving average (window size = 1000 time steps) of the axial component of the instantaneous virial stress tensor:

$$\sigma_{xx} = \frac{1}{V}[\sum_i m_i v_{ix} v_{ix} + \sum_i r_{ix} f_{ix}] \qquad (1)$$

where V is the volume of the simulation box, m_i is the mass of the i^{th} particle and $\{v_{ix}, r_{ix}, f_{ix}\}$ are the axial components of the velocity, position, and force. The tensile modulus was estimated by fitting a straight line to the linear regime of the stress-strain curve and the Poisson's ratio was calculated as $\nu = -\frac{d\varepsilon_{trans}}{d\varepsilon_{axial}}$ where ε represents the engineering strain. A key assumption is that the mechanical response of the P3ATs, especially differences in mechanical properties between similar materials, is dominated by the state of the amorphous phase (i.e., glassy, leathery, fluid) at a given temperature.[33] We thus did not include the effect of partial crystallinity.[7] For each system, we repeated the procedure starting from two independent initial configurations and strained the box in all three dimensions to obtain six independent measurements of the mechanical response to uniaxial loading. Due to the extremely large size of the system, very little variation was observed between measurements. All simulations and visualization were performed using LAMMPS, VMD, and OVITO.[34–36] A complete description of the parameters used for both of the models is provided in the Supplementary Information.

2.3 Results and Discussion

2.3.1 Comparison of Models

We begin by comparing the results obtained from the one-site model and the three-site model for pure P3HT. One observation that immediately distinguishes the two models is the density that we obtained upon equilibration (snapshots of equilibrated morphologies for the two models are shown in **Figure 2.3a**). We found that the three-site model equilibrated to a density of 0.955 ± 0.001 g cm^{-3} at 300 K which is reasonable compared to the experimentally determined value of 1.094 ± 0.002 g cm^{-3} for the amorphous phase of regio-regular P3HT of the same average molecular weight, measured using gas pycnometry.[37] In contrast, we obtained a value of 2.1 ± 0.07 g cm^{-3} for the one-site model, which is substantially higher than the experimental value. We attributed this discrepancy to the small value of the σ parameter (4.95 Å) in the Lennard-Jones potential for this model. It has been noted by Hsu and coworkers[38] that to derive thermomechanically consistent CG parameters, σ can be tuned to improve the ability of the models to reproduce the density of the target system. We found, through an iterative approach, that $\sigma \approx 8.0$ Å was required to match the density of the one-site model to that of the atomistic and three-site models. However, this modification caused the pair distribution function to depart significantly from that computed from atomistic simulations.[26] This observation highlighted the inadequacy of a one-site description of the hexyl-thiophene monomer, and led us to the conclusion that a one-site model does not contain sufficient detail to simultaneously match the structure and the density of the underlying atomistic system.

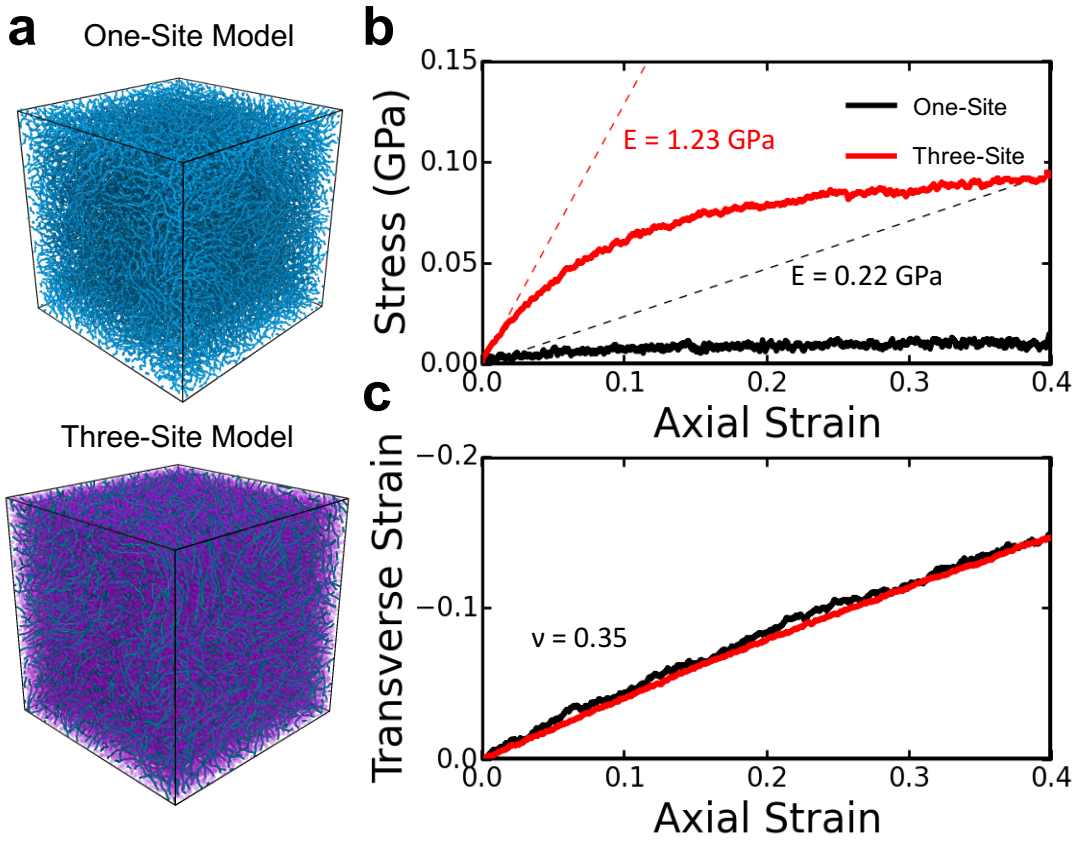

Figure 2.3. Simulated mechanical properties of P3HT. (a) Representative snapshots of the equilibrated morphology obtained for the one-site and three-site model. Comparison of (b) stress response and (c) transverse strain response to uniaxial loading.

Next, we compared the mechanical response of the two systems to uniaxial tensile loading. A representative stress-strain curve obtained from these simulations is shown in **Figure 3b**. We found that the three-site model predicted a tensile modulus of 1.23 ± 0.01 GPa, while the one-site model predicted a value of 0.22 ± 0.02 GPa. Comparing to the experimentally determined value of 1.09 ± 0.15 GPa, for as-cast thin films of this molecular weight, measured using the buckling method,[39] we found that the three-site model gave much closer agreement with experiment. The observation that the one-site

model predicted a higher density and a lower tensile modulus indicated that not enough microscopic detail was preserved to accurately describe the microstructural packing and frictional interactions. This observation further validated our conclusion that a more detailed coarse-grained mapping is necessary to reproduce both structural and thermomechanical properties. We also found that both models predict a Poisson ratio of 0.35 (**Figure 2.3c)**, which agrees with previous theoretical predictions.[40]

The results of the three-site model also compare favorably with the atomistic simulations of P3HT, which predict a value of 1.6 GPa for chain lengths of 100 monomers.[21] As might be expected, due to the inherently softer nature of the CG potentials that emerges from integrating over atomistic features, we observe that decreasing the resolution of the model leads to lower predicted values for the tensile modulus. The closer matching of the three-site model to the experimental results than the atomistic model could in part be due to the difference in the loading conditions of the two systems studied. Specifically, in the atomistic simulations, the transverse dimensions were held constant to force a Poisson ratio of zero, whereas the transverse dimensions could relax under stress-free boundary conditions in our CG simulations.

The excellent agreement observed between simulation and experiment for the three-site model motivated us to use this model further to take a closer look at morphological changes in the amorphous material induced by mechanical strain.

2.3.2 Strain-Induced Chain Alignment

It is well known that applying a uniaxial strain to an amorphous or semi-crystalline polymer causes the chains to plastically deform and align in the axial direction. This effect is of technological relevance for semiconducting polymers where the degree of chain alignment has a significant effect on the macroscopic optoelectronic properties. For example, experimental studies on P3HT have demonstrated significant anisotropy in the optical absorption and charge-transport properties for strain-aligned films, achieving an optical dichroic ratio of 4.8 and charge-mobility anisotropy of 9. (ref. [41]) As shown in **Figure 4a**, this effect was clearly observed in our simulations.

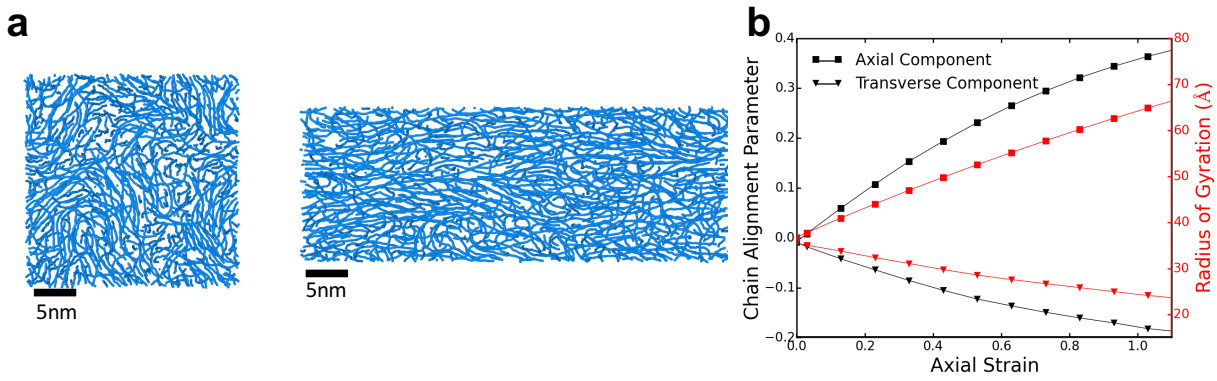

Figure 2.4. Simulated strain-induced chain alignment in P3HT. (a) Representative snapshots showing a thin cross-section of the simulated morphology before and after straining to 100% (side chain beads not shown for clarity). (b) Plot showing the evolution of the axial and transverse components of the chain alignment parameter as well as the radius of gyration during the uniaxial loading simulation.

To quantify the degree of chain alignment in the amorphous phase through the application of uniaxial strain, we computed a chain alignment order parameter.[42] The unit vector defining the orientation of each thiophene unit was calculated as the chord connecting second nearest neighbors along the backbone: $\boldsymbol{e_i} = (\boldsymbol{r_{i+1}} - \boldsymbol{r_{i-1}})/|\boldsymbol{r_{i+1}} -$

$\boldsymbol{r_{i-1}}|$ and the chain alignment order parameter was computed as the second-order Legendre polynomial:

$$P_{2x} = \frac{3}{2}\langle(\boldsymbol{e_i} \cdot \boldsymbol{e_x})^2\rangle - \frac{1}{2} \qquad (2)$$

where $\boldsymbol{e_x}$ represents the unit vector in either the transverse or axial dimension and the angular brackets denote an average over all thiophene units. In addition, we quantified the anisotropic change in the structure of the polymer chains as the axial, and transverse components of the radius of gyration tensor:

$$R_{gx} = \sqrt{\langle\frac{1}{M}\sum_i m_i(r_{ix} - r_{cx})^2\rangle} \qquad (3)$$

where *M* is the molecular weight of the chain, m_i is the mass of the CG bead, r_{cx} is either the axial or transverse component of the center of mass, the summation is over all *i* CG beads in each chain, and the angular brackets denote an average over all chains.

The evolution of axial and transverse components of P_{2x} and R_{gx} is shown in **Figure 2.4b**. Both quantities show increasing alignment of chains with increasing strain. The chain alignment parameter computed here can in fact be related to the experimentally accessible optical dichroic ratio of this material: $P_{\parallel} = \frac{R-1}{R+1}$, where R is the dichroic ratio. O'Connor et al.[41] have reported a value of ~0.36 for the chain alignment parameter of the amorphous region of a film strained to 112% using a combination of UV-Vis spectroscopy and 2D grazing-incidence X-ray diffraction (assuming ~50% crystallinity).[43] Our simulations

predicted a value of 0.363 at 112% strain, which agrees remarkably well with this experimental result.

2.3.3. Effect of Fullerene Acceptor

One of the most important applications of semiconducting polymers is as the active material of thin-film organic photovoltaic devices. Typically, these are fabricated by solution-casting a physical blend of two semiconducting materials, an electron donor (hole-conducting) and an electron acceptor (electron-conducting), to form a phase-segregated bulk heterojunction that is bicontinuous.[44] P3HT is a commonly used electron donor material, while fullerene derivatives such as phenyl-C_{61}-butyric acid methyl ester (PCBM) are the most commonly used electron acceptors. The phase behavior of the P3HT:PCBM system is well studied, and it has been shown that this binary composite consists of three separate phases: crystalline P3HT, a PCBM-rich phase, and a mixed amorphous phase.[45] It has also been observed that the addition of PCBM to P3HT increases both the glass transition temperature[46] and the tensile modulus of the composite material (i.e., PCBM acts as an anti-plasticizing agent which stiffens and embrittles the film).[47] We hypothesized that the addition of C_{60}—for which CG model parameters have been developed[23]—would have a similar effect as PCBM, and tested the ability of the three-site model to predict it.

To study the effect of adding C_{60}, we applied our computational methodology to prepare a system consisting of a physical blend of P3HT with C_{60} at a 1:1 mass fraction (10,000 C_{60} molecules) using the three-site model. This system is representative of the amorphous mixed phase of the composite material (crystallization of the polymer and phase segregation do not occur over the timescales simulated). A comparison of the

mechanical response to uniaxial loading is shown in **Figure 2.5a**. We observed that the addition of fullerene indeed resulted in a stiffer material, with the simulations predicting a tensile modulus of 1.92 ± 0.05 GPa. This prediction agrees well with the experimentally determined value of 1.97 ± 0.07 GPa for an as-cast thin film of P3HT:PCBM, measured using the buckling method.[48]

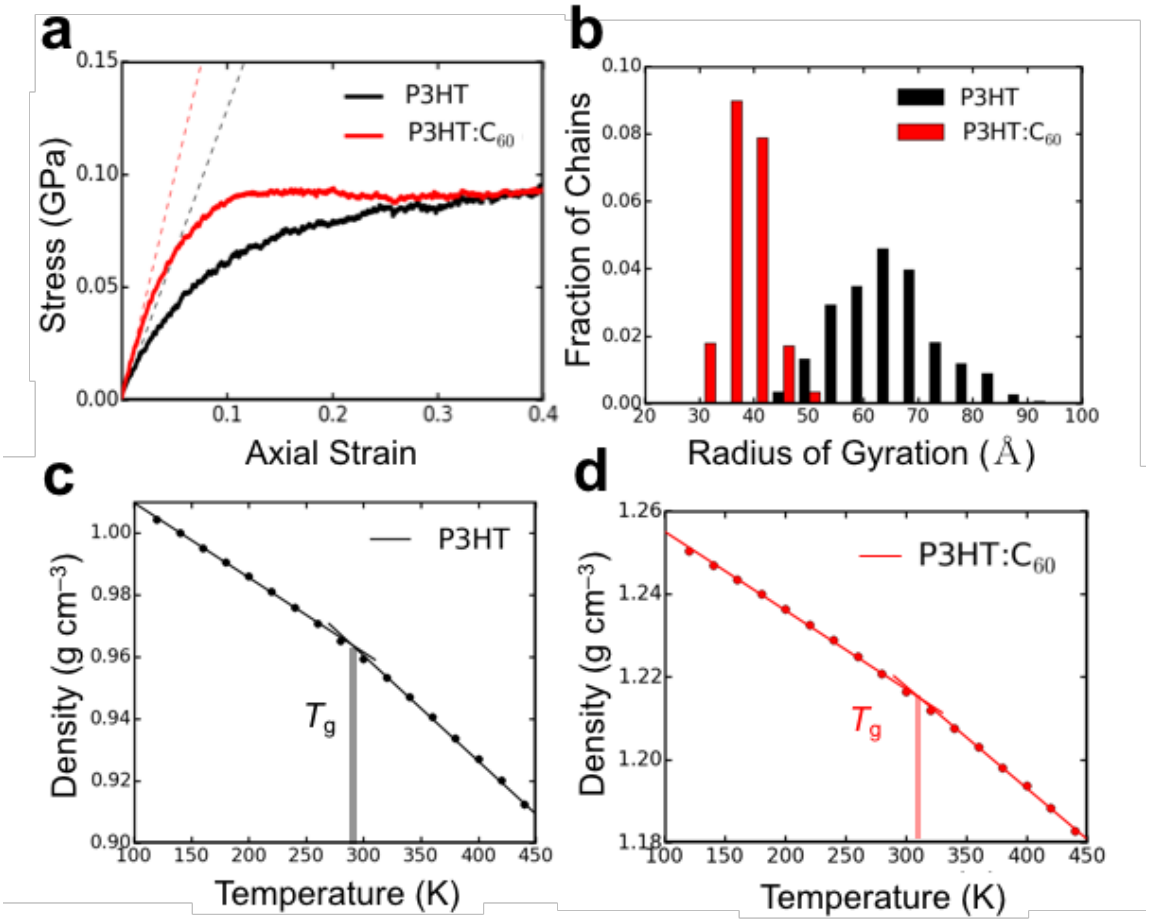

Figure 2.5. Comparison of predicted thermomechanical properties of pure P3HT with P3HT:C_{60}. (a) Stress-strain curve showing a transition from a melt to a glassy response with the addition of C_{60}. (b) Histogram of radius of gyration of P3HT chains in the condensed phase. Quenching curves for (c) pure P3HT and (d) P3HT:C_{60} showing an estimate for the glass transition temperature.

Interestingly, we also observed a drastic change in the distribution of the radius of gyration of the P3HT chains in the composite system. As can be seen in **Figure 2.5b**, there is an approximately two-fold reduction in the average radius of gyration, indicating that the chains are not as well extended in the composite system. This effect is most likely due to partial phase segregation of the fullerene molecules confining the P3HT chains into a smaller volume and promoting self-interactions. This reduction in the spatial extent of the polymer chains could lead to a lower entanglement density, which may explain the significantly increased brittleness of P3HT:PCBM compared to pure P3HT that has been observed experimentally through film-on-elastomer techniques.[7] We note that no cracking or craze formation is observed in these simulations, even though experimentally the onset of cracking occurs at ~2% strain for P3HT:PCBM.[7] We attribute the absence of cracking and crazing to the fact that fracturing in polymers is usually initiated by defects at the surface, which are not present in these simulations due to periodic boundary conditions.

One of the most important applications of semiconducting polymers is as the active material of thin-film organic photovoltaic devices. Typically, these are fabricated by solution-casting a physical blend of two semiconducting materials, an electron donor (hole-conducting) and an electron acceptor (electron-conducting), to form a phase-segregated bulk heterojunction that is bicontinuous.[44] P3HT is a commonly used electron donor material, while fullerene derivatives such as phenyl-C_{61}-butyric acid methyl ester (PCBM) are the most commonly used electron acceptors. The phase behavior of the P3HT:PCBM system is well studied, and it has been shown that this binary composite consists of three separate phases: crystalline P3HT, a PCBM-rich phase, and a mixed amorphous phase.[45] It

has also been observed that the addition of PCBM to P3HT increases both the glass transition temperature[46] and the tensile modulus of the composite material (i.e., PCBM acts as an anti-plasticizing agent which stiffens and embrittles the film).[47] We hypothesized that the addition of C_{60}—for which CG model parameters have been developed[23]—would have a similar effect as PCBM, and tested the ability of the three-site model to predict it.

2.3.4 Thermal Properties

We next turned to predictions of the thermal properties for these systems. Of critical importance for the processing and stability of organic semiconductors is the glass transition temperature.[49] This thermal property is especially important for bulk heterojunction solar cells, which often consist of non-equilibrium structures quenched below their glass transition temperature when initially cast from solution. An important step for optimizing the photovoltaic efficiency of these devices is a post-deposition annealing step above the glass transition, which allows main-chain segmental crystallization and partial phase segregation of the bulk heterojunction components. These effects lead to a red-shifted absorption spectrum and improved extraction of photogenerated charges.[50,51] Several experimental studies using various techniques (differential scanning calorimetry,[46] dynamic mechanical thermal analysis,[52] variable temperature ellipsometry,[53] and in situ photovoltaic characterization[50]) have helped characterize the thermal properties of P3HT:PCBM blends. Differences in processing conditions, molecular weights, and characterization techniques have led to widely disparate experimental results. The generally agreed upon trend, however, is that the addition of PCBM acts to vitrify the P3HT.[49] **Figures 2.5c** and **d** show a comparison of

the thermal quenching curves obtained for pure P3HT and P3HT:C_{60}. We predicted a value of approximately 290 K and 310 K for the pure and mixed systems respectively. Our predicted value for both systems are in excellent agreement with the experimentally determined values of 285-287K for high-MW regioregular P3HT,[49] and 313 K for 1:1 mass ratio of P3HT:PCBM.[46] The validation provided by this agreement led us to the conclusion that CG models such as these can potentially be used to understand complex structure property relationships in semiconducting polymers, such as the effect of side-chain length.

2.3.5 Effect of Alkyl Side Chain Length

The basic structural motif of a semiconducting polymer is a rigid π-conjugated backbone that is functionalized with flexible aliphatic side-chains. The choice of the side chain is an important criterion that plays a critical role in determining the solubility, solid-state morphology, and thermomechanical properties of the bulk material.[54] One advantage of the three-site model for P3HT is that it explicitly accounts for the hexyl side chain attached to the thiophene monomers. An important question is the transferability of this model to describe the general class of P3ATs. To extend the model, we introduced additional CG beads to the side chain, as shown in **Figure 2.5a**. Initially, we used the original parameters from the three-site model for P3HT; however, we observed trends that were in contradiction with experimental results (shown in Figure **B.3b**) indicating that the original model was not transferable. To make the model transferrable, we adopted a similar strategy to Jankowski et al.[55] and modified the intermolecular interactions to account for the fact that the dispersive and electrostatic interactions between the CG beads representing

the thiophene backbone are stronger than those between the side-chain beads. We redistributed the intermolecular cohesive energy present in the epsilon parameters of the Lennard-Jones 9-6 potential to make the potential well for the beads representing thiophene rings three-times more attractive (7.53 kJ mol^{-1}) than the beads representing the alkyl side-chains (2.51 kJ mol^{-1}) while retaining approximately the same temperature-density equations of state and elastic modulus for P3HT as shown in **Figure 2.6b,c**. We emphasize that this model is only qualitative because the modification also alters the structural distributions, and a systematic parameterization from atomistic simulations using accurate force-matching methods would be required for a quantitatively accurate and transferable model.

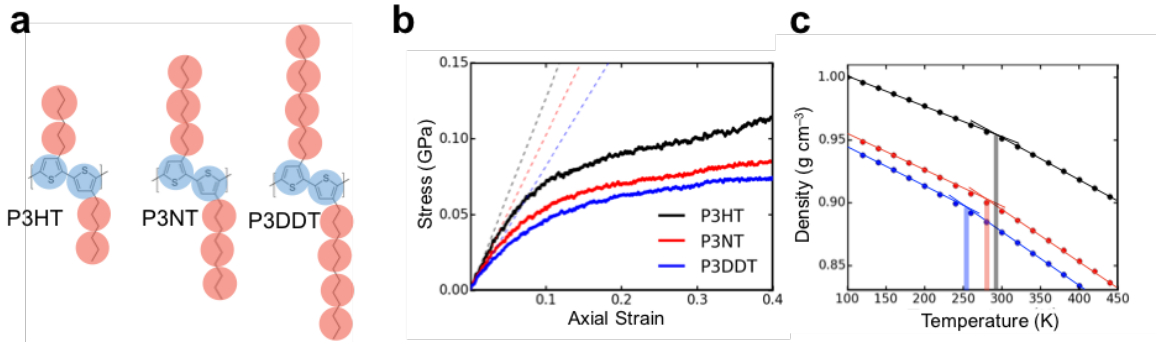

Figure 2.6. Predicted mechanical response of P3ATs, where A = hexyl, nonyl, and dodecyl. (a) Diagram showing the extension made to the three-site model for P3HT to allow for the simulation of P3ATs with longer alkyl side-chains. (b) Stress-strain curves and (c) thermal quenching curves obtained for the three P3ATs.

The predications of thermomechanical properties obtained for our modified model are shown in **Figure 2.6b, c**. We see that increasing the alkyl side chain length decreases the density, the tensile modulus and the glass transition temperature. We predicted values of 0.99± 0.03 GPa for P3NT (n = 9) and 0.78± 0.02 GPa for P3DDT (n = 12). Although

the tensile modulus of P3NT has not been measured experimentally so far, that of P3DDT has been measured to be 0.16 ± 0.07 GPa.[39] We note that the model captured the overall trend of decreasing modulus with increasing side-chain length, though the agreement with experimental results is not quantitative. The lack of transferability observed here could be due in part to the inadequacy of representing the thiophene ring as a spherical CG site; taking the anisotropic shape of the ring into account would require at least three CG sites (to form a plane). For the glass transition temperatures, we predict a value of 280 K for P3NT and 258 K for P3DDT. Comparing to the experimentally determined range of 230-258 K for P3DDT we observe good agreement here, along with correct trends. [56,57]

2.4 Conclusion

We investigated the feasibility of using CG MD simulations to predict the thermomechanical properties of the model conjugated-polymer P3HT, as well as its blend with C_{60} fullerene. Through comparisons to experimental density, elastic modulus, and glass transition temperature for the pure and composite system, we identified the optimal degree of coarse-graining required to retain the essential physics of the underlying atomistic model and achieve agreement between simulation and experiment. We then used the validated three-site model to predict the chain alignment caused by uniaxial loading and showed the effect of fullerene on the thermomechanical properties, demonstrating excellent agreement with experiment. Extension of the model to describe a range of P3ATs gave only qualitative agreement with experiment, indicating limited transferability of such models to polymers with even moderate variations in molecular structure such as the addition of three or six methylene units considered in this study. One potential approach

for developing CG models with improved transferability would be to use several target atomistic systems with varied chemical structures, and iteratively apply the IBI approach in such a way as to produce a set of parameters that self-consistently match all of the structural and thermodynamic data across the chosen range of chemical structures. Given the extensive validation and identification of limitations presented here, models such as these can be developed for new materials, such as the important class of donor-acceptor conjugated polymers,[58] to allow for the precise determination of structure-property relationships in organic semiconductors and aid in the molecular design of material systems exhibiting mechanical compliance for a variety of applications in mechanically robust, stretchable, and ultra-flexible electronics.

2.5 Acknowledgements

This work was supported by the Air Force Office of Scientific Research (AFOSR) Young Investigator Program, Grant Number FA9550-12-10156, awarded to D.L. Additional support was provided by the National Science Foundation Graduate Research Fellowship under Grant No. DGE-114408 to S.S., the Hellman Fellowship awarded to D.L., and laboratory startup funds from the University of California, San Diego. Computational resources to support this work were provided by the Extreme Science and Engineering Discovery Environment (XSEDE) Program through the National Science Foundation grant number ACI-1053575.[59] The authors thank Prof. David Huang for sending us the files associated with his model as well as helpful discussions.

Chapter 2, in full, is a reprint of the material as it appears in *Macromolecules*, 2016, 49, 2866-2894. The American Chemical Society, 2016. Samuel E. Root, Suchol

Savagatrup, Christopher J. Pais, Gaurav Arya, and Darren J. Lipomi. The dissertation author was the primary investigator and author of this paper.

2.6 References

(1) Kaltenbrunner, M.; White, M. S.; Głowacki, E. D.; Sekitani, T.; Someya, T.; Sariciftci, N. S.; Bauer, S. Ultrathin and Lightweight Organic Solar Cells with High Flexibility. *Nat. Commun.* **2012**, *3*, 770.

(2) Lipomi, D. J.; Tee, B. C.-K.; Vosgueritchian, M.; Bao, Z. Stretchable Organic Solar Cells. *Adv. Mater.* **2011**, *23*, 1771–1775.

(3) Facchetti, A. π-Conjugated Polymers for Organic Electronics and Photovoltaic Cell Applications †. *Chem. Mater.* **2011**, *23*, 733–758.

(4) Sokolov, A. N.; Atahan-Evrenk, S.; Mondal, R.; Akkerman, H. B.; Sánchez-Carrera, R. S.; Granados-Focil, S.; Schrier, J.; Mannsfeld, S. C. B.; Zoombelt, A. P.; Bao, Z.; *et al.* From Computational Discovery to Experimental Characterization of a High Hole Mobility Organic Crystal. *Nat. Commun.* **2011**, *2*, 437.

(5) Brédas, J. L.; Beljonne, D.; Coropceanu, V.; Cornil, J. Charge-Transfer and Energy-Transfer Processes in π-Conjugated Oligomers and Polymers: A Molecular Picture. *Chem. Rev.* **2004**, *104*, 4971–5003.

(6) Jackson, N. E.; Savoie, B. M.; Chen, L. X.; Ratner, M. a. A Simple Index for Characterizing Charge Transport in Molecular Materials. *J. Phys. Chem. Lett.* **2015**, *6*, 1018–1021.

(7) Savagatrup, S.; Printz, A. D.; O'Connor, T. F.; Zaretski, A. V.; Rodriquez, D.; Sawyer, E. J.; Rajan, K. M.; Acosta, R. I.; Root, S. E.; Lipomi, D. J. Mechanical Degradation and Stability of Organic Solar Cells: Molecular and Microstructural Determinants. *Energy Environ. Sci.* **2015**, *8*, 55–80.

(8) Yang, F.; Ghosh, S.; Lee, L. J. Molecular Dynamics Simulation Based Size and Rate Dependent Constitutive Model of Polystyrene Thin Films. *Comput. Mech.* **2012**, *50*, 169–184.

(9) Lee, S.; Rutledge, G. C. Plastic Deformation of Semicrystalline Polyethylene by Molecular Simulation. *Macromolecules* **2011**, *44*, 3096–3108.

(10) Capaldi, F. M.; Boyce, M. C.; Rutledge, G. C. Molecular Response of a Glassy Polymer to Active Deformation. *Polymer (Guildf).* **2004**, *45*, 1391–1399.

(11) Kim, J. M.; Locker, R.; Rutledge, G. C. Plastic Deformation of Semicrystalline

Polyethylene under Extension, Compression, and Shear Using Molecular Dynamics Simulation. *Macromolecules* **2014**, *47*, 2515–2528.

(12) Agrawal, V.; Arya, G.; Oswald, J. Simultaneous Iterative Boltzmann Inversion for Coarse-Graining of Polyurea. *Macromolecules* **2014**, *47*, 3378–3389.

(13) Peter, C.; Kremer, K. Multiscale Simulation of Soft Matter Systems – from the Atomistic to the Coarse-Grained Level and Back. *Soft Matter* **2009**, *5*, 4357–4366.

(14) Kremer, K.; Grest, G. S. Dynamics of Entangled Linear Polymer Melts : A Molecular - Dynamics Simulation. *J. Chem. Phys.* **1990**, *92*, 5057–5086.

(15) Arman, B.; Reddy, A. S.; Arya, G. Viscoelastic Properties and Shock Response of Coarse-Grained Models of Multiblock versus Diblock Copolymers: Insights into Dissipative Properties of Polyurea. *Macromolecules* **2012**, *45*, 3247–3255.

(16) Reith, D.; Pütz, M.; Müller-Plathe, F. Deriving Effective Mesoscale Potentials from Atomistic Simulations. *J. Comput. Chem.* **2003**, *24*, 1624–1636.

(17) Dang, M. T.; Hirsch, L.; Wantz, G. P3HT:PCBM, Best Seller in Polymer Photovoltaic Research. *Adv. Mater.* **2011**, *23*, 3597–3602.

(18) Marcon, V.; Raos, G. Free Energies of Molecular Crystal Surfaces by Computer Simulation: Application to Tetrathiophene. *J. Am. Chem. Soc.* **2006**, *128*, 1408–1409.

(19) Dubay, K. H.; Hall, M. L.; Hughes, T. F.; Wu, C.; Reichman, D. R.; Friesner, R. a. Accurate Force Field Development for Modeling Conjugated Polymers. *J. Chem. Theory Comput.* **2012**, *8*, 4556–4569.

(20) Jackson, N. E.; Kohlstedt, K. L.; Savoie, B. M.; Olvera de la Cruz, M.; Schatz, G. C.; Chen, L. X.; Ratner, M. a. Conformational Order in Aggregates of Conjugated Polymers. *J. Am. Chem. Soc.* **2015**, *137*, 6254–6262.

(21) Tummala, N. R.; Risko, C.; Bruner, C.; Dauskardt, R. H.; Brédas, J.-L. Entanglements in P3HT and Their Influence on Thin-Film Mechanical Properties: Insights from Molecular Dynamics Simulations. *J. Polym. Sci. Part B Polym. Phys.* **2015**, 1–9.

(22) Tummala, N. R.; Bruner, C.; Risko, C.; Brédas, J.-L.; Dauskardt, R. H. Molecular-Scale Understanding of Cohesion and Fracture in P3HT:Fullerene Blends. *ACS Appl. Mater. Interfaces* **2015**, *7*, 9957–9964.

(23) Huang, D. M.; Faller, R.; Do, K.; Moul, A. J. Coarse-Grained Computer Simulations of Polymer / Fullerene Bulk Heterojunctions for Organic Photovoltaic Applications. *J. Chem. Theory Comput.* **2010**, *6*, 526–537.

(24) Schwarz, K. N.; Kee, T. W.; Huang, D. M. Coarse-Grained Simulations of the Solution-Phase Self-Assembly of poly(3-Hexylthiophene) Nanostructures. *Nanoscale* **2013**, *5*, 2017–2027.

(25) To, T. T.; Adams, S. Modelling of P3HT:PCBM Interface Using Coarse-Grained Forcefield Derived from Accurate Atomistic Forcefield. *Phys. Chem. Chem. Phys.* **2014**, *16*, 4653–4663.

(26) Lee, C.-K.; Pao, C.-W.; Chu, C.-W. Multiscale Molecular Simulations of the Nanoscale Morphologies of P3HT:PCBM Blends for Bulk Heterojunction Organic Photovoltaic Cells. *Energy Environ. Sci.* **2011**, *4*, 4124–4132.

(27) Lee, C. K.; Pao, C. W. Nanomorphology Evolution of p3ht/pcbm Blends during Solution-Processing from Coarse-Grained Molecular Simulations. *J. Phys. Chem. C* **2014**, *118*, 11224–11233.

(28) Do, K.; Risko, C.; Anthony, J. E.; Amassian, A.; Bredas, J.-L. Dynamics, Miscibility, and Morphology in Polymer-Molecule Blends: The Impact of Chemical Functionality. *Chem. Mater.* **2015**, *27*, 7643–7651.

(29) Chen, C.-W.; Huang, C.-I. Effects of Intra/inter-Molecular Potential Parameters, Length and Grafting Density of Side-Chains on the Self-Assembling Behavior of poly(3′-Alkylthiophene)s in the Ordered State. *Polymer (Guildf).* **2015**, *77*, 189–198.

(30) Jones, M. L.; Huang, D. M.; Chakrabarti, B.; Groves, C. Relating Molecular Morphology to Charge Mobility in Semicrystalline Conjugated Polymers. *J. Phys. Chem. C* **2016**, *120*, 4240–4250.

(31) Karayiannis, N. C.; Kröger, M. Combined Molecular Algorithms for the Generation, Equilibration and Topological Analysis of Entangled Polymers: Methodology and Performance. *Int. J. Mol. Sci.* **2009**, *10*, 5054–5089.

(32) Allen, M. P.; Tildesley, D. J. *Computer Simulation of Liquids*; Oxford University Press: Clarendon, Oxford, 1987.

(33) Savagatrup, S.; Printz, A. D.; Wu, H.; Rajan, K. M.; Sawyer, E. J.; Zaretski, A. V.; Bettinger, C. J.; Lipomi, D. J. Viability of Stretchable poly(3-Heptylthiophene) (P3HpT) for Organic Solar Cells and Field-Effect Transistors. *Synth. Met.* **2015**, *203*, 208–214.

(34) Plimpton, S. Fast Parallel Algorithms for Short-Range Molecular Dynamics. *J. Comput. Phys.* **1995**, *117*, 1–19.

(35) Humphrey, W.; Dalke, A.; Schulten, K. VMD: Visual Molecular Dynamics. *J. Mol. Graph.* **1996**, *14*, 33–38.

(36) Stukowski, A. Visualization and Analysis of Atomistic Simulation Data with OVITO–the Open Visualization Tool. *Model. Simul. Mater. Sci. Eng.* **2010**, *18*, 1–7.

(37) Lee, C. S.; Dadmun, M. D. Important Thermodynamic Characteristics of poly(3-Hexyl Thiophene). *Polymer (Guildf).* **2014**, *55*, 4–7.

(38) Hsu, D. D.; Xia, W.; Arturo, S. G.; Keten, S. Systematic Method for Thermomechanically Consistent Coarse-Graining: A Universal Model for Methacrylate-Based Polymers. *J. Chem. Theory Comput.* **2014**, *10*, 2514–2527.

(39) Savagatrup, S.; Makaram, A. S.; Burke, D. J.; Lipomi, D. J. Mechanical Properties of Conjugated Polymers and Polymer-Fullerene Composites as a Function of Molecular Structure. *Adv. Funct. Mater.* **2014**, *24*, 1169–1181.

(40) Tahk, D.; Lee, H. H.; Khang, D.-Y. Elastic Moduli of Organic Electronic Materials by the Buckling Method. *Macromolecules* **2009**, *42*, 7079–7083.

(41) O'Connor, B.; Kline, R. J.; Conrad, B. R.; Richter, L. J.; Gundlach, D.; Toney, M. F.; DeLongchamp, D. M. Anisotropic Structure and Charge Transport in Highly Strain-Aligned Regioregular poly(3-Hexylthiophene). *Adv. Funct. Mater.* **2011**, *21*, 3697–3705.

(42) Lavine, M. S.; Waheed, N.; Rutledge, G. C. Molecular Dynamics Simulation of Orientation and Crystallization of Polyethylene during Uniaxial Extension. *Polymer (Guildf).* **2003**, *44*, 1771–1779.

(43) Zen, A.; Saphiannikova, M.; Neher, D.; Grenzer, J.; Grigorian, S.; Pietsch, U.; Asawapirom, U.; Janietz, S.; Scherf, U.; Lieberwirth, I.; *et al.* Effect of Molecular Weight on the Structure and Crystallinity of poly(3-Hexylthiophene). *Macromolecules* **2006**, *39*, 2162–2171.

(44) Scharber, M. C.; Muehlbacher, D.; Koppe, M.; Denk, P.; Waldauf, C.; Heeger, A. J.; Brabec, C. J. Design Rules for Donors in Bulk Heterojunction Solar Cells Towards 10% Energy Conversion Efficiency. *Adv. Mater.* **2006**, *18*, 789–794.

(45) Treat, N. D.; Chabinyc, M. L. Phase Separation in Bulk Heterojunctions of Semiconducting Polymers and Fullerenes for Photovoltaics. *Annu. Rev. Phys. Chem.* **2014**, *65*, 59–81.

(46) Zhao, J.; Swinnen, A.; Van Assche, G.; Manca, J.; Vanderzande, D.; Van Mele, B. Phase Diagram of P3HT/PCBM Blends and Its Implication for the Stability of Morphology. *J. Phys. Chem. B* **2009**, *113*, 1587–1591.

(47) Savagatrup, S.; Printz, A. D.; Rodriquez, D.; Lipomi, D. J. Best of Both Worlds: Conjugated Polymers Exhibiting Good Photovoltaic Behavior and High Tensile Elasticity. *Macromolecules* **2014**, *47*, 1981–1992.

(48) Printz, A. D.; Savagatrup, S.; Rodriquez, D.; Lipomi, D. J. Role of Molecular Mixing on the Stiffness of Polymer:fullerene Bulk Heterojunction Films. *Sol. Energy Mater. Sol. Cells* **2015**, *134*, 64–72.

(49) Müller, C. On the Glass Transition of Polymer Semiconductors and Its Impact on Polymer Solar Cell Stability. *Chem. Mater.* **2015**, *27*, 2740–2754.

(50) Treat, N. D.; Shuttle, C. G.; Toney, M. F.; Hawker, C. J.; Chabinyc, M. L. In Situ Measurement of Power Conversion Efficiency and Molecular Ordering during Thermal Annealing in P3HT:PCBM Bulk Heterojunction Solar Cells. *J. Mater. Chem.* **2011**, *21*, 15224–15231.

(51) Li, G.; Shrotriya, V.; Huang, J.; Yao, Y.; Moriarty, T.; Emery, K.; Yang, Y. High-Efficiency Solution Processable Polymer Photovoltaic Cells by Self-Organization of Polymer Blends. *Nat. Mater.* **2005**, *4*, 864–868.

(52) Hopkinson, P. E.; Staniec, P. A.; Pearson, A. J.; Dunbar, A. D. F.; Wang, T.; Ryan, A. J.; Jones, R. A. L.; Lidzey, D. G.; Donald, A. M. A Phase Diagram of the P3HT:PCBM Organic Photovoltaic System: Implications for Device Processing and Performance. *Macromolecules* **2011**, *44*, 2908–2917.

(53) Pearson, A. J.; Wang, T.; Jones, R. a L.; Lidzey, D. G.; Staniec, P. a.; Hopkinson, P. E.; Donald, A. M. Rationalizing Phase Transitions with Thermal Annealing Temperatures for P3HT:PCBM Organic Photovoltaic Devices. *Macromolecules* **2012**, *45*, 1499–1508.

(54) Mei, J.; Bao, Z. Side Chain Engineering in Solution-Processable Conjugated Polymers. *Chem. Mater.* **2014**, *26*, 604–615.

(55) Jankowski, E.; Marsh, H. S.; Jayaraman, A. Computationally Linking Molecular Features of Conjugated Polymers and Fullerene Derivatives to Bulk Heterojunction Morphology. *Macromolecules* **2013**, *46*, 5775–5785.

(56) Pankaj, S.; Hempel, E.; Beiner, M. Side-Chain Dynamics and Crystallization in a Series of Regiorandom Poly(3-Alkylthiophenes). *Macromolecules* **2009**, *42*, 716–724.

(57) Pankaj, S.; Beiner, M. Confined Dynamics and Crystallization in Self-Assembled Alkyl Nanodomains. *J. Phys. Chem. B* **2010**, *114*, 15459–15465.

(58) Sirringhaus, H. 25th Anniversary Article: Organic Field-Effect Transistors: The Path Beyond Amorphous Silicon. *Adv. Mater.* **2014**, *26*, 1319–1335.

(59) John, T.; Cockerill, T.; Foster, I.; Gaither, K. XSEDE: Accelerating Scientific Discovery. *Comput. Sci. Eng.* **2014**, *16*, 62–74.

Chapter 3

Modelling the morphology and thermomechanical behaviour of low-bandgap conjugated polymers and bulk heterojunction films

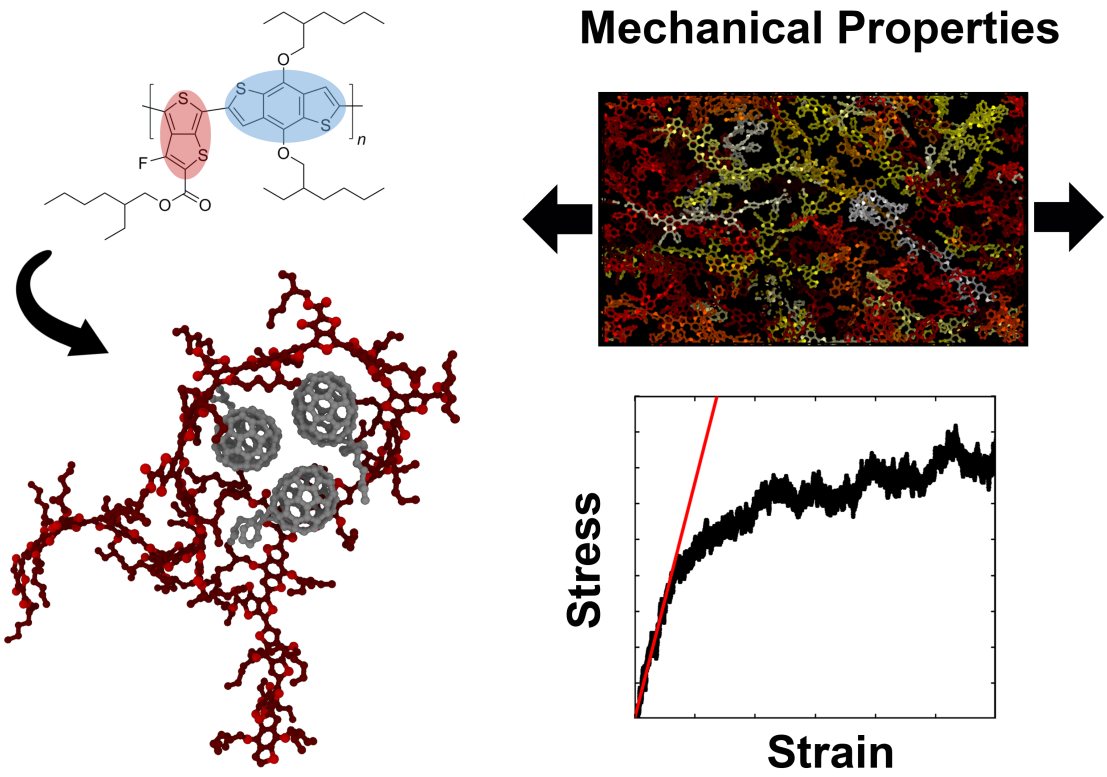

Image 4. Table of contents artwork for Chapter 3. Atomistic simulation workflow.

Samuel E. Root,[a] Nicholas E. Jackson,[b] Suchol Savagatrup ,[a] Gaurav Arya,[a] and Darren J. Lipomi [a]

a. *Department of NanoEngineering, University of California, 9500 Gilman Drive, Mail Code 0448, San Diego, La Jolla, CA 92093-0448, USA.*

b. *Institute for Molecular Engineering, University of Chicago, IL 60615, USA*

Abstract

This paper describes the use of molecular dynamics (MD) to predict the nanoscale morphology and thermomechanical behavior of three low-bandgap semiconducting polymers and their blends with PC71BM. While the three polymers modeled in this study—PTB7, PDTSTPD, and TQ1—all exhibit the donor-acceptor motif characteristic of high-performance donor materials in organic solar cells, they exemplify different morphologies in the solid state. Predictions from the atomistic simulations presented here include the average conjugation length of the polymers, the structural arrangement of conjugated donor and acceptor units in neat and bulk heterojunction (BHJ) films, as well as the glass transition temperature and tensile modulus of neat and BHJ polymer films. Calculated tangent correlation functions exhibit oscillatory decay. This finding suggests that DA polymers are more appropriately modeled as ribbon-like chains as opposed to worm-like chains. To account for the range of morphologies accessible by processing manipulations, both a melt-quenched and a self-aggregated morphology are prepared. Owing to the greater free volume of the self-aggregated morphology, these solid structures are found to be softer and weaker than the melt-quenched morphologies. The experimental modulus measured previously for PDTSTPD is like the predicted self-aggregated morphology, while the experimental modulus of PTB7 is like the predicted melt-quenched modulus. Our comparisons with experiment suggest that solution-processing plays a critical role in optimizing the mechanical properties of conjugated polymeric materials. Overall, the results of this study suggest the promise of MD simulations in determining the ways in which molecular structure influence the morphology and mechanical properties of bulk heterojunction films for solar cells and other organic electronic devices.

3.1 Introduction

Mechanical deformability underpins many of the advantages of organic semiconductors.[1] For example, use of low-cost, ultrathin substrates, fabrication of devices by roll-to-roll printing, stability of devices in portable applications, and biological integration require the active materials to accommodate levels of mechanical strain that are sometimes moderate (e.g., roll-to-roll printing) but often extreme (e.g., biological integration). The mechanical properties of an organic semiconductor depend not only on its molecular structure, but also on how the molecules pack in the solid state.[2] This morphology, however, is difficult to predict by simple inspection of the molecular structure.[3] This paper describes the use of molecular dynamics (MD) to understand the nanoscale structural features and mechanical properties of low-bandgap polymers that exhibit the donor-acceptor (DA) motif.[4,5]

It has recently been demonstrated experimentally that many of the highest-performing organic semiconductors lack the mechanical stability required for flexible, stretchable, and mechanically robust applications.[3] For example, all three of the high-performance polymers shown in **Figure 3.1a-c** have been measured to crack at ≤3% strain using film-on-elastomer techniques.[3,6] Furthermore, the addition of electron-accepting fullerene derivatives, such as $PC_{71}BM$ (**Figure 3.1d**) to form an organic bulk heterojunction (BHJ) solar cell, has been shown experimentally[7] and computationally[8] to result in a significant increase in stiffness and brittleness of the composite film.

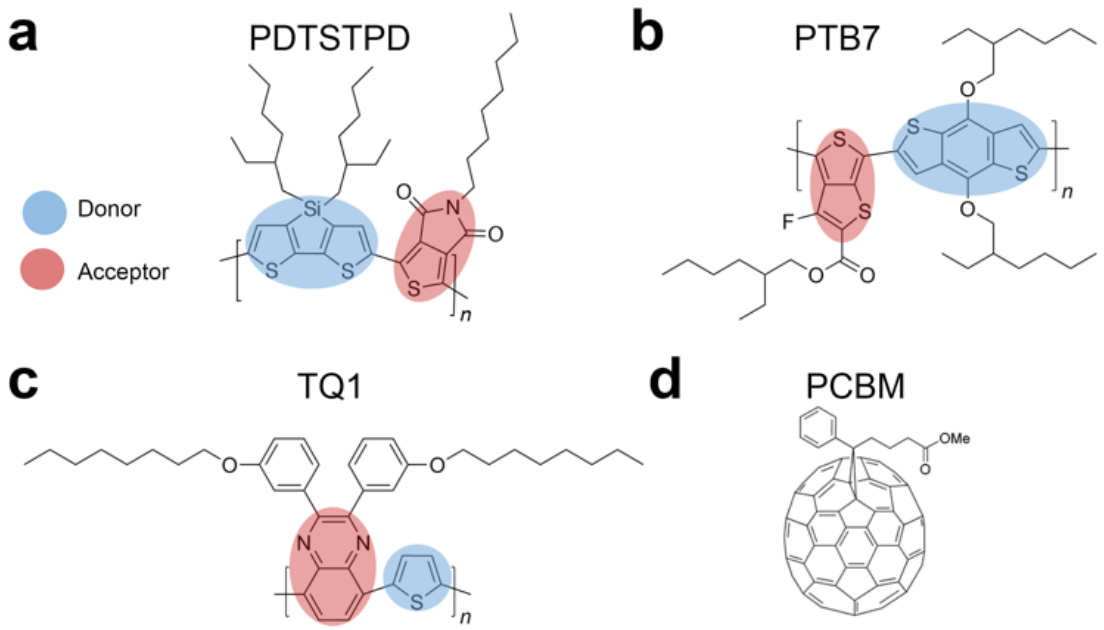

Figure 3.1. Structures of the polymers and molecules simulated in this work, along with their common names. All structures are shown in a syn conformation. (a) TQ1, poly[[2,3-bis(3-octyloxyphenyl)-5,8-quinoxalinediyl]-2,5-thiophenediyl]. (b) PDTSTPD, poly[(5,6-dihydro-5-octyl-4,6-dioxo-4H-thieno[3,4-c] pyrrole-1,3-diyl) [4,4-bis(2-ethylhexyl)-4H-silolo[3,2-b:4,5-b′;] dithiophene-2,6-diyl]]. (c) PTB7, Poly({4,8-bis[(2-ethylhexyl) oxy] benzo [1,2-b:4,5-b′] dithiophene-2,6-diyl} {3-fluoro-2-[(2-ethylhexyl) carbonyl] thieno [3,4-b] thiophenediyl}). (d) $PC_{71}BM$, [6,6]-phenyl C_{71} butyric acid methyl ester.

The science of organic materials has benefitted from the ability to modify molecular structure and measure the effects of these changes on function.[9] This approach has helped to understand charge-transport in organic semiconductors,[10] and recently to understand their mechanical behaviour.[7,11] Experimental correlations between molecular structure, mechanical, and optoelectronic properties of π-conjugated materials—even large libraries containing over 50 compounds[7]—have yielded insightful structure-property relationships. However, an understanding of how molecular structure of π-conjugated materials influences formation of films and dissipation of mechanical energy is far from complete. Computational resources and techniques have progressed to a level where it is now feasible

to apply them to developing detailed structure-property relationships of polymers whose repeat units contain as many as 100 atoms, e.g., the DA polymers.

MD simulations are a useful tool for understanding both the conformational behaviour and the thermomechanical properties of organic molecular materials. The level of detail accessible by simulation is difficult or impossible to attain experimentally. Modelling of conjugated polymers entails a unique challenge for standard classical force fields. This difficulty arises in part because of the strong geometrical constraints imposed by π-conjugation along the backbone. Specifically, generic force fields are not directly transferrable to these heterocyclic systems, and thus fail to accurately predict the interactions that arise from torsional rotations between rings, as well as atomic partial charges. This shortcoming requires each polymer under study to be parameterized independently from electronic structure calculations.[12] Density functional and wave-function based methods for building atomistic models for conjugated polymers have been established and applied to a variety of materials, such as the poly(3-alkylthiophene)s (P3ATs),[13,14] and recently to a library of low-bandgap polymers.[15] While these atomistic models[14]—and detailed coarse-grained models derived from them[16]—have been used to investigate the mechanical properties of P3ATs,[8,17] they have not been applied to the more structurally complex low-bandgap polymers. Although P3HT is typically used as a model system, many results obtained from such case studies cannot be directly generalized to the structurally complex low-bandgap polymers.[18]

In this work, we studied the morphologies and mechanical properties of three low-bandgap polymers and their blends with $PC_{71}BM$. The goal was to identify the structural determinants and molecular mechanisms for the accommodation of mechanical energy.

Our choice of polymers (**Figure 3.1a-c**) was influenced by two requirements: (1) accurate atomistic models exist for these materials[15] and (2) the mechanical properties have been measured experimentally.[3] Moreover, each of these three polymers occupy specific points on the range of mesoscale ordering available to this class of materials, from the structurally disordered TQ1 polymer[19,20] to the locally ordered PTB7[21,22] and the semi crystalline PDTSTPD.[23,24] Our efforts were guided by three questions:

(1) **Effect of molecular structure.** How do molecular attributes such as the configuration of the side chain (i.e. branched vs. linear) and the connectivity of the conjugated backbone (i.e. fused vs. isolated rings vs. off-axis conjugated units) dictate the solid-state packing and mechanical behaviour of these materials?

(2) **Effect of morphology.** How do processing conditions affect the mechanical properties of these materials—specifically the ways in which solution-casting generates non-equilibrium kinetically trapped morphologies—and how can these conditions be used to increase the robustness of devices?

(3) **Agreement with experiment.** More generally, do the results of MD simulations match those of experiments? Can MD simulations be used to complement experimental research aimed at understanding and optimizing the morphology and thermomechanical properties of organic semiconductors?

To begin deconvoluting the effects of molecular structure on solid-state packing and bulk mechanical properties, we simulated the melt-phase equilibrium structure of each polymer, as well as their composites with $PC_{71}BM$. We employed a coarse-grained analysis to compare the equilibrium statistics of key intramolecular degrees of freedom, single-chain conformations, and multi-chain packing preferences. These melt-phase features

provided an approximate representation of the thermodynamic forces driving the solidification of films cast from solution. Although it was impractical to simulate the process of solvent evaporation in atomistic detail, we included effects of this process using two disparate simulation protocols which generated two different types of glassy structures. These two protocols approximately simulated the effects of casting films from solvents of different quality and evaporation rates. We simulated the mechanical behaviour of the resulting glassy structures by imposing a uniaxial tensile deformation and computing a stress-strain curve. Our results indicated that differences in processing, composition and solution-phase behaviour play a significant role in determining the mechanical properties of these materials. These properties may in fact be influenced more strongly by differences between the ways in which the films are formed than by differences in molecular structure. That is, the extent to which the molecular structure dictates the mechanical properties of these materials is limited by the extent to which it influences its structure in solution, and thus in the solid state.

3.2 Simulation Design

3.2.1 Choice of Materials

The three polymers shown in **Figure 3.1a-c** were chosen because they are among the highest performing materials in the OPV literature and have been extensively characterized. It was thus possible to compare predictions of tensile modulus, glass transition temperature, and π-stacking distances with experimental results. Additionally, these materials are structurally diverse among the backbones and side chains. This diversity allowed us to draw qualitative comparisons of properties resulting from chemical motifs

including fused rings, off-axis conjugated units, and side-chains that are linear, branched, and orthogonally extended from the backbone.

We simulated a set of systems containing 60 monodisperse oligomers with 12 repeat units each. Experimental studies on the mechanical properties of these specific polymers used molecular weights on this order of magnitude (~10 kDa) and thus direct comparisons could be made.[3] Moreover, this chain length marks the onset of self-folding and the formation of photophysical aggregates observable in solution-phase UV-Vis absorption and fluorescence spectra.[25] Furthermore, this degree of polymerization has also proven sufficient for predicting the condensed phase behaviour and mechanical properties of P3HT (while allowing for computationally accessible simulations) and has served as the basis for detailed coarse-grained models capable of describing experimentally relevant chain dimensions and polydispersity.[16,17] Finally, DA polymers can be difficult to synthesize at a high molecular weight and thus the properties of oligomers are also relevant.[26]

3.2.2 Choice of Simulation Protocol

The structure and properties of conjugated polymers thin films are known to depend critically on processing.[27] Guo et al. have investigated the effect of solvents and solvent additives on the morphology of PTB7-F40 homopolymer films using X-ray scattering. These researchers have determined that the crystallinity of PTB7 films is not affected by the solvent used unless a high boiling point solvent additive, di-iodooctane, is added.[28] This additive has been determined to act as a plasticizer and allows the surface of the polymer film to dynamically rearrange instead of being completely kinetically trapped.[29] Instead of including these additives in our simulations explicitly, we have included the effect of film

nanostructure on the mechanical properties by applying two different methods for generating glassy solid morphologies.

These morphologies represent opposing ends of a continuum of possible structures available to these chains in the condensed phase. In one method we used a conventional MD approach for simulating polymer glasses: quenching from the *equilibrated* melt phase. This approach allowed for the characterization of equilibrium structure in the melt and estimation of the glass transition temperature. We term the structures prepared in this way *melt-quenched* morphologies. In the other method, we performed simulated annealing on implicitly solvated individual chains to form self-aggregated structures and then packed them together at room temperature to mimic solution casting rapidly from a poor, low boiling point solvent (see **Figure B.1**, in the **Appendix B** for a visual comparison of the two protocols). The use of this procedure was influenced experimental spectroscopic evidence suggesting these materials tend to form aggregated structures in solution.[25] We expected that these pre-aggregated chains would be kinetically trapped in the solid state. Pre-aggregation would lead to a lower density of entanglements (and that this might be the cause of experimentally observed brittleness in these materials). We term the structures prepared in this way the *self-aggregated* morphologies. For PTB7 the structural effects of solution processing have been characterized rigorously by Al-Hussein and co-workers. X-ray experiments have determined that spray-coated PTB7 films are kinetically-trapped in a morphology that is significantly more disordered than spin-coated films.[30]

The morphology of low-bandgap polymers is also known to depend strongly upon interactions with the surface to which they are deposited.[31] For PTB7 in particular, the structure has been quantified rigorously by Hammond et al., who employed an array of

sophisticated experimental techniques and models to determine the nanoscale morphology of homopolymer and bulk heterojunction films. These researchers determined that PTB7 has a moderate preference for π-stacking in the vertical direction ("face-on"), however, the coherence length for these orientational correlations was determined to be quite small (*ca.* 1.7 nm).[32] This experimental result (and computational constraints) lend credence to our decision to not include a substrate in our simulations and instead use a domain that is periodic in all three dimensions to mimic the mid-section of the thin film.

3.2.3 Choice of Models

We chose classical atomistic MD models to simulate the structural properties of these materials because they can describe large systems containing greater than 100,000 atoms. We used custom force fields based on the all-atomistic optimized potential for liquid simulation[33] (OPLS-AA). Such models give excellent agreement with experimental values for density, heat capacities, and compressibility of organic liquids. Moreover, these force fields have previously been used to simulate the mechanical behaviour of P3HT and P3HT:$PC_{61}BM$ blends.[17,34] A detailed description of the process used to build these models using quantum mechanical methods is given elsewhere.[15] All simulations and visualizations were performed with LAMMPS[35] and OVITO[36] respectively.

3.3 Results and Discussion

3.3.1 Intramolecular Melt-Phase Structure

3.3.1.1 Dihedral Distributions

We began by untangling the contributions of various molecular features on the melt-phase structure of these polymers at 600 K and 1 atm. Under these conditions, the polymers are sufficiently mobile to allow for efficient computational sampling of

equilibrium configurations. An important factor dictating the dynamics of conjugated polymers are the strong dihedral forces imposed by π-conjugation along the backbone of the polymer. These dihedral preferences play an important role in determining bulk photophysical and mechanical properties. Extended planar configurations facilitate intrachain charge transport, and the dihedral geometries play an important role in determining the overall conformational behavior of the polymer chains.

To analyse the equilibrium dihedral preferences, we defined an orthonormal basis set for each conjugated DA unit such as the one shown in **Figure 3.2a** for PTB7. These geometrical definitions enabled the calculation of probability distributions for dihedral angles between adjacent conjugated rings shown in **Figure 3.2b-c**. Due to the asymmetry of the acceptor unit of PTB7, we split the dihedral angle into two distinct distributions (the one labeled DA is shown in **Figure 3.2a**). Comparing across the three materials we observed several notable features. We found that TQ1 had the highest fraction of syn conformations, while PDTSTPD and PTB7 had approximately equal preferences for syn and anti conformations. The preference of TQ1 for syn conformations is likely due to the small size and rotational flexibility of the donor unit, which contains no side chain.

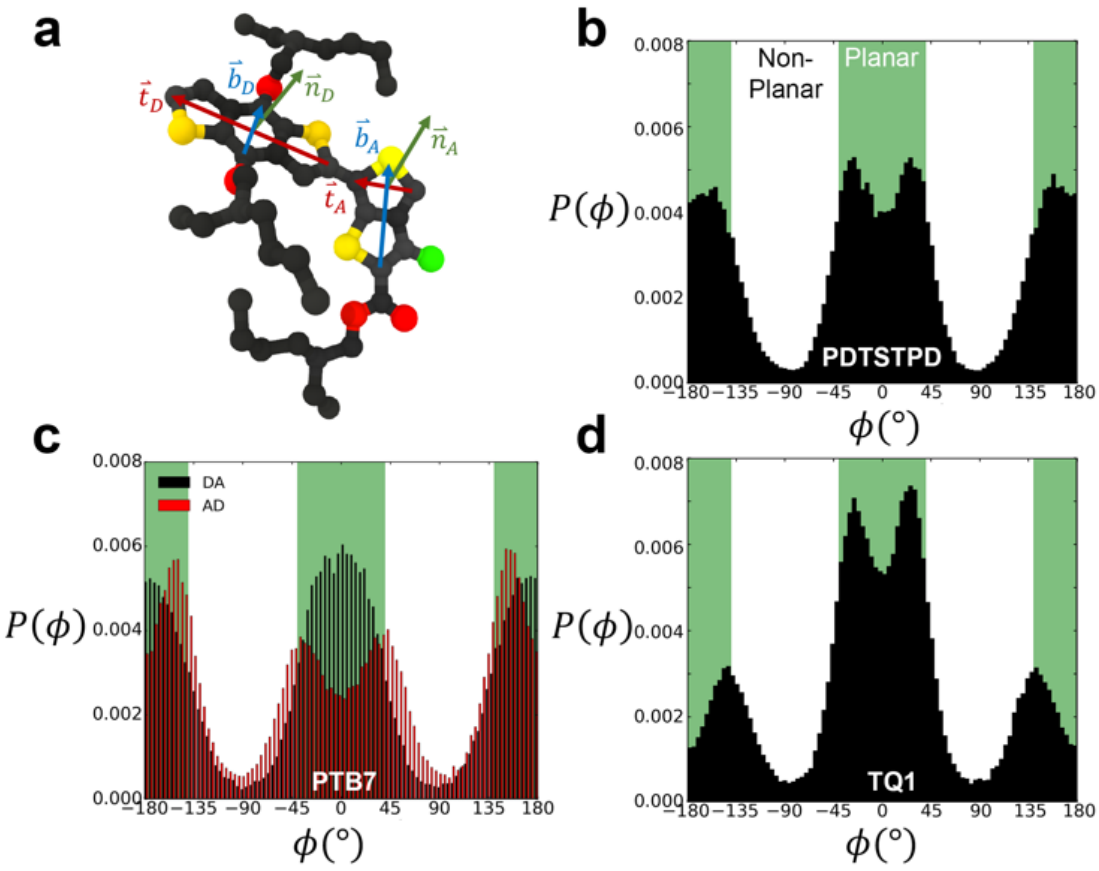

Figure 3.2. Inter-ring dihedral distributions. (a) Diagram showing definitions of basis sets defining ring orientations for PTB7 monomer. Dihedral distributions, $P(\phi)$, obtained from simulations at 600 K and 1 atm for (b) PTB7 (c) PDTSTPD (d) TQ1. The syn conformations shown in **Figure 3.1** shows planar arrangement that results from $\phi = 0°$.

By defining planar conformations as the regions within the green domains on **Figure 3.2b,c** (±40° from true planarity for optimal delocalization of π electrons, see the next paragraph) we found that PDTSTPD had the highest fraction of planar conformations (and thus the greatest energy barrier for rotation) followed by PTB7 and TQ1 (see **Table C.1** for a quantitative analysis of the distributions). We ascribe the planarity of PDTSTPD to the arrangement of the side chains on the donor unit (in addition to the intrinsic dihedral potential). Since the side chains are attached orthogonally to the conjugated unit, steric forces inhibit rotations from planar conformations.

3.3.2 Conjugation Length

The broad absorption spectra in conjugated polymers are in part due to the distribution of effective conjugation lengths induced by the torsional disorder along the backbone. The semiconducting nature of these polymers thus also depends on the distribution of conjugation lengths (L_c). In order for π-electrons to delocalize, the p orbitals on adjacent atoms must be approximately coplanar: rotations from planarity greater than 40° have a detrimental effect on delocalization.[33] Using this value as a cut-off, we grouped conjugated units into distinct chromophores and plotted the probability distribution $P(L_c)$ in **Figure 3.3a**. Taking the number-average (first moment) from these distributions, we found that TQ1 had the shortest conjugation length (2.7 units), compared to that of PTB7 and PDTSTPD (3.1 and 3.2 units), this result follows directly from previous results in which we found that PDTSPTD had the highest fraction of planar units. For PTB7 in particular, the fluorine atom plays a particularly important role. Guo and co-workers have determined experimentally that increasing the fraction of fluorinated acceptor units along the conjugated backbone results in a decreased conjugation length and subsequent blue-shift.[34] Dubay et al. have computed the conjugation length distribution for P3HT using a similar approach. They found an average conjugation length of 1.06 monomers for a P3HT chain in vacuum.

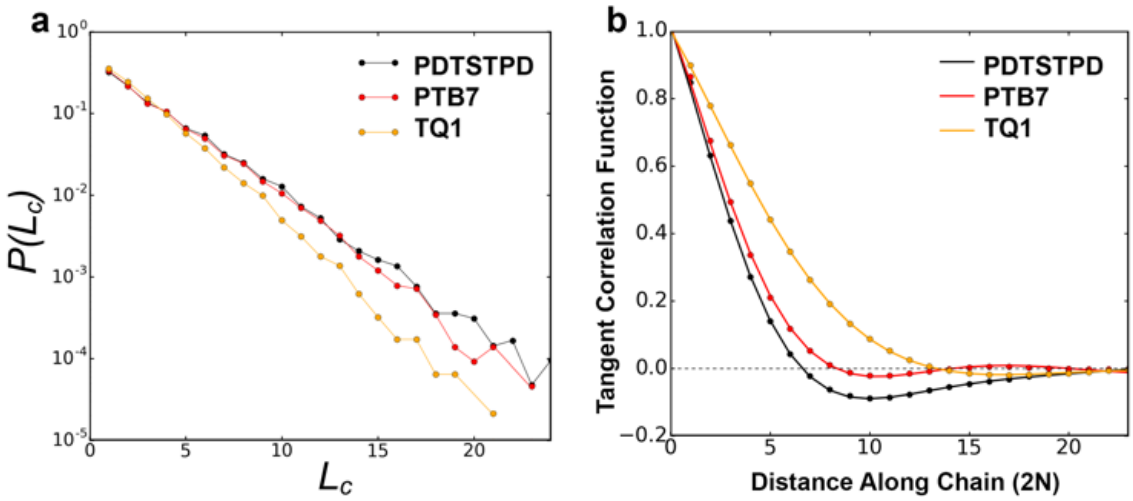

Figure 3.3. Single-chain statistics. (a) Plot showing probability distribution of conjugation length. (b) Plot showing the decay of the tangent correlation function (dotted line) as well as the fits to the analytical model (solid line).

3.3.3 Tangent Correlations

Equilibrium chain structure can be quantified statistically using a tangent correlation function, $\langle \hat{\mathbf{t}}_\mathbf{i} \cdot \hat{\mathbf{t}}_{\mathbf{i+j}} \rangle$. Here, $\hat{\boldsymbol{t}}_{\boldsymbol{i}}$ represents the unit tangent vector of the i^{th} conjugated unit along the backbone, and the brackets denote an average over all separations j, polymer chains, and time. The computed tangent correlations, shown in **Figure 3.3b**, exhibited an oscillatory decay, implying the existence of a helical structure. Such helical structure has previously been observing in quantum mechanical simulations of TQ1 oligomers, however, tangent correlation functions were not computed.[35] This behaviour likely results from the ribbon-like shape of the backbone, which contains planar units of finite width. The tangent correlations of ribbon-like objects have been described previously using the following functional form: $\langle \hat{\mathbf{t}}_\mathbf{i} \cdot \hat{\mathbf{t}}_{\mathbf{i+j}} \rangle = e^{-\frac{jl}{L_p}} \cos\left(\frac{lj}{\lambda}\right)$.[36] Here, l is the length of the monomer unit taken as the average value of the donor and acceptor units. L_p is the persistence length, and λ represents the wavelength of helical structure.

We found that exact fits to the simulation data required a series expansion of the analytical expression, implying multiple modes of periodicity and tangent decay in these complex polymer chains. A detailed description of the fitting procedure, parameters obtained, and their significance is given in **Section B.2.2** of the **Appendix B**. Numerical values obtained from the first-order fit are shown in **Table 3.1**. The dimensionless quantity, $\frac{L_p}{\lambda}$, describes the helical nature of the chain; in the limiting case of $L_p << \lambda$, the worm-like chain model is valid. In all cases, we found that $\frac{L_p}{\lambda} \sim 1$, suggesting that a worm-like chain is not the best model for interpreting experimental data obtained from neutron or light scattering experiments aimed at probing the conformational structure of low band-gap polymers.[37] For both PTB7 and TQ1 we found that $\frac{L_p}{\lambda} < 1$, while for PDTSTPD $\frac{L_p}{\lambda} > 1$. This analysis suggests the PDTSTPD is the most ribbon-like of the three polymers, which agrees with the experimentally observed order in PDTSTPD when compared to PTB7 and TQ1.

An important question that arises is whether the helical structures have a handedness. To determine this, we have computed Ramachandran plots[38] which show the correlations between successive dihedral angles (see **Figure B.5**) . We found them to be symmetric in all cases, implying that there is no overall handedness to the helical structures. We expect the existence of a helical structure to have important mechanistic implications for charge-transport[39] and the entropic elasticity[40] in this class of materials.

3.3.2 Intermolecular Melt-Phase Structure

3.3.2.1 Donor-Acceptor Stacking

Intermolecular packing of the conjugated DA units dictates both the interchain charge transport and the cohesive energy of these materials. Stacking preferences can be quantified using a pair distribution function. The results from our simulations of the pure polymers are shown in **Figure 3.4a-d**. Overall, we found that the π-stacking preferences were predominately controlled by the topology of the conjugated unit and the chemical nature of the side chains. The general shapes of the pair distribution functions compare favourably to those obtained from analogous simulations of P3HT (both atomistic and coarse-grained), in that the primary π-stacking peak does not exceed a value of 1.[16,17,41]

Focusing on the results for PTB7, we found that although the benzodithiophene (donor) unit has two branched ethylhexyloxy side chains, it has a stronger π-stacking preference than the fluorinated thienothiophene (acceptor) unit that contains a single branched side-chain. This packing feature could be the result of the enhanced flexibility of the side-chains that arises from the higher flexibility of the ether linkage on the benzodithiophene as compared to the ester linkage on the fluorinated thienothiophene. Additionally, the symmetric shape of the benzodithiophene unit allows its side chains to align in the same plane, increasing their overall attraction due to favourable vdW interactions.[42] Another distinctive feature in the plots is a broad peak in the A-A interaction at ~14 Å which seems to indicate a tendency for interdigitation of side chains as evidenced geometrically in the **Figure B.6.**

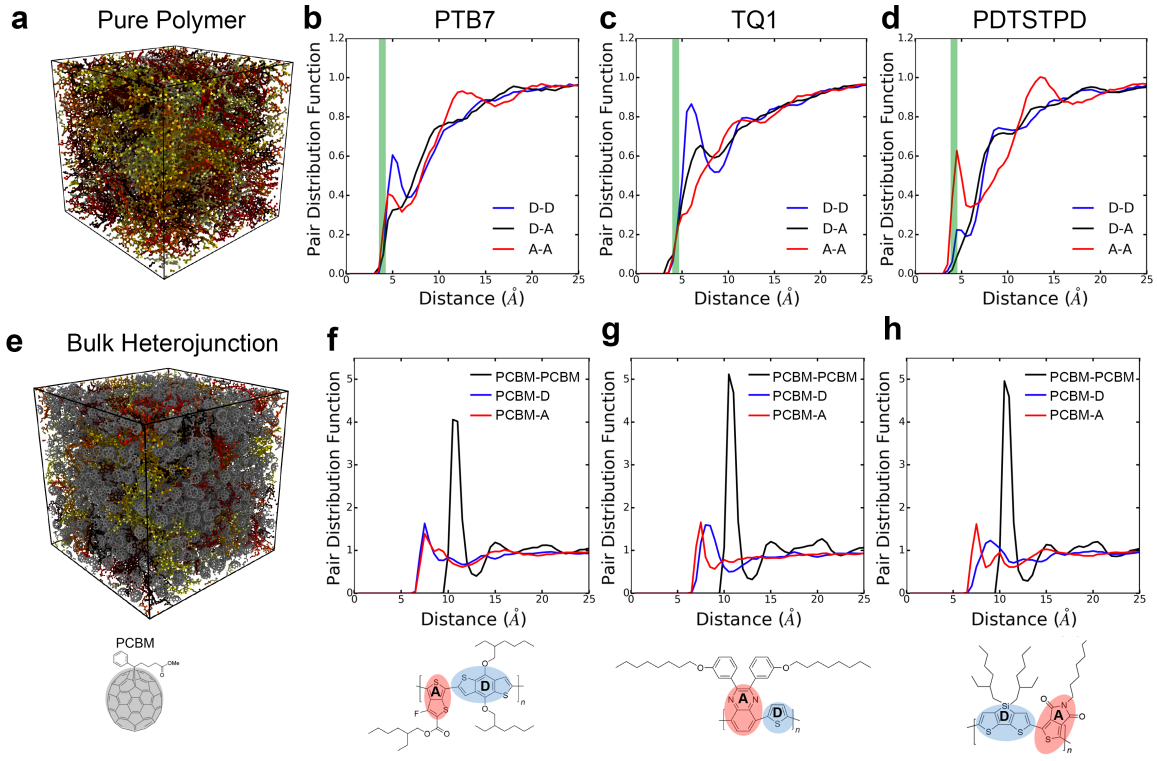

Figure 3.4 Morphological characterization of pure polymers and BHJs. (a) Snapshot of condensed phase morphology of pure PTB7. Molecules are coloured by indexed values. (b–d) Pair-distribution functions showing intermolecular donor–acceptor stacking preferences in the melt (green lines indicate experimental p–p stacking distances24,47,48). (e) Snapshot of condensed phase morphology of PTB7 BHJ. Polymer molecules are coloured by indexed values. (f–h) Pair-distribution functions showing intermolecular coupling between PCBM and donor/acceptor units. Note: the pair distributions are computed using the centres of masses of the conjugated units, indicated by the shading in the figures (i.e. the centre of mass of the fullerene cage for PCBM)

The importance of molecular topology on these interactions is further exemplified by the pair distribution functions obtained for TQ1 in **Figure 3.4d**. We see that the bulky off-axis units on the benzopyrazine (acceptor) unit serve to inhibit efficient π-stacking in comparison to the thiophene (donor) unit, which has no side chain. The direction that the side chain emanates from the conjugated ring also plays an important role in how the polymers pack. This effect can be seen in the plots for PDTSTPD in **Figure 3.4b** where the D-D peak is three times less prominent than the A-A peak due to the two branched side

chains extending orthogonally outward from the dithienosilole (donor) unit. We also note that similar to PTB7, a broad peak at ~12 Å can be seen for the A-A interactions, which is not surprising given the geometric similarity of the acceptor units of PTB7 and PDTSTPD.

For all three polymers, we plotted a vertical green line showing the experimentally determined π-stacking distances. The π-stacking distance of the three polymers have been reported as 4.2 Å,[24] 3.8-4.0 Å,[30,32,43] and 4.3 Å[44] for PDTSTPD, PTB7 and TQ1 respectively. Comparing between simulation and experiment, it can be seen that the experimental stacking distance is slightly smaller than the simulated peak. We attributed this difference to two possible effects. The first is that these curves are obtained from melt-phase simulations at 600 K whereas the experimental results are obtained at room temperature. The second is that the inadequacy of treating the conjugated carbon atoms with a standard Lennard-Jones potential due to extended π-conjugation. Computational studies suggest that a buffered 14-7 potential might provide a more accurate description of excluded volume interactions of these atoms at small interatomic separations.[12]

3.3.2.2 Polymer-Fullerene Stacking

The performance of OPV material systems depends strongly upon the intermolecular arrangements in the mixed regions between polymer and fullerene where charge separation takes place. Graham and co-workers have observed a general trend that higher-performing DA polymers generally have acceptor units that are more sterically accessible to the fullerene molecules than the donor units.[45] That is, the acceptor units bear linear side chains as opposed to branched ones. The authors provided experimental evidence to show that this trend was due to enhanced coupling of fullerene molecules with the acceptor moiety. Recent computational studies by Wang and co-workers combined

classical atomistic MD with density functional theory to provide theoretical evidence in support of this hypothesis for the PBDTTPD family of polymers.[46] The authors systematically investigated the impact of side chain structure on packing and conformational arrangement in the mixed region. To further test this trend, we computed pair distribution functions between $PC_{71}BM$ (shortened to PCBM in the text and figures) and the DA units. The results of these calculations are shown in **Figure 3.4e-f**.

For TQ1, shown in **Figure 3.4e**, it can be seen that there is a clear preference (sharper peak) for PCBM-A as opposed to PCBM-D stacking. This preference could be the result of the additional van der Waals forces arising from the off-axis conjugated units forming π-stacks with the fullerene cage. For PDTSTPD, shown in **Figure 3.4f**, we observed that the primary PCBM-A peak was sharper and higher amplitude than the corresponding PCBM-D peak. In addition to this peak, there was a clear secondary peak indicating a preference for bilayer stacking of this moiety with the fullerene cage. Finally, for PTB7, shown in **Figure 3.4e**, we observed that the primary peaks were similar in amplitude, distance, and width. The only observable difference is the secondary peak in the PCBM-A curve indicating the presence of bilayer stacks. Overall, the results of our simulations support the claim that branched side chains inhibit efficient packing with the fullerene unit.

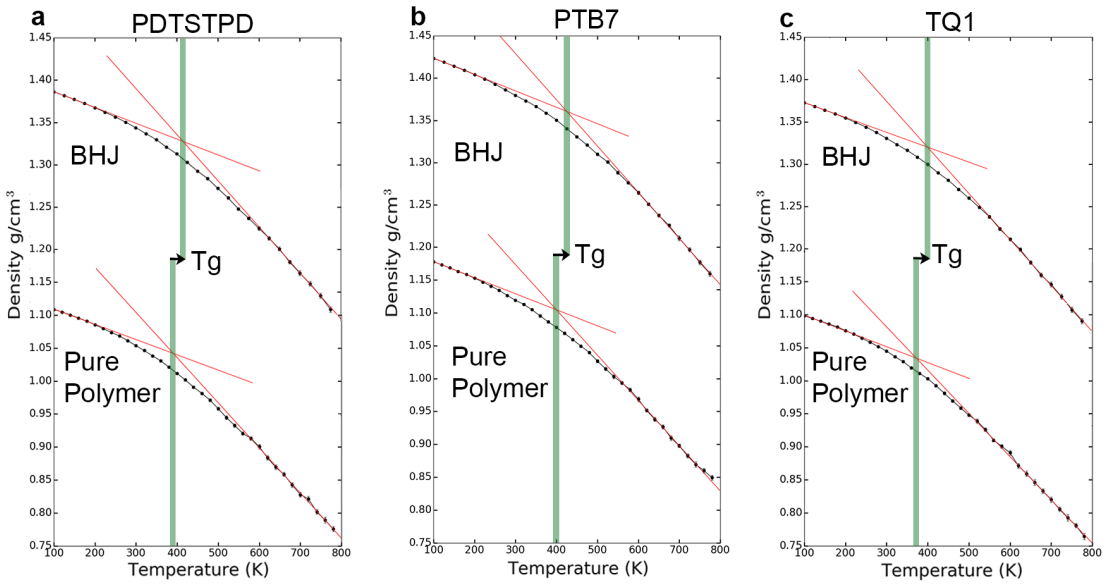

Figure 3.5. Thermal properties, density vs. temperature curves showing glass-transitions of polymer: $PC_{71}BM$ bulk heterojunctions (top curves) and pure polymers (bottom curves) for (a) PTB7, (b) PDTSTPD, and (c) TQ1.

3.3.3 Thermal Properties

The kinetics of molecular organization during the annealing and solidification of polymer films is important for determining both the solid-state structure and thermal stability of solid films comprising DA polymers. The glass transition temperature (T_g), which marks the onset of thermally activated relaxation processes of the main chain, is thus a critical processing parameter for printing and coating techniques.[47] To estimate T_g, we performed thermal quenching simulations while monitoring the density to obtain the thermal curves shown in **Figure 3.5a-c**. The glass-transition region was determined by the narrow range in temperature range in which the thermal expansion coefficient underwent a change, and T_g was thus estimated as the intersection of linear fits to the glassy and melt regions. Glassy configurations obtained from these quenching simulations were subsequently used in uniaxial tensile loading simulations where they are denoted as the *melt-quenched* morphology.

3.3.3.1 Pure Polymers

Beginning our discussion with the pure polymer systems, we found that all three materials underwent a glass transition well above room temperature, which has been observed experimentally in low-bandgap polymers and is the result of the strong inter- and intramolecular forces arising from extended π-conjugation. This is in contrast to P3HT, which has a glass transition that has been measured experimentally[47] and predicted by coarse-grained MD[8] to be just below room temperature. We found that PTB7 had the highest T_g of ≈400 K followed by PDTSTPD at ≈380 K and TQ1 at ≈375 K (the error of these values is approximately ±10 K). These results are in excellent agreement with experimentally determined values of ≈382 K for PDTSTPD[24] and ≈373 K for TQ1.[19] We note that while there is a disparity in molecular weight between the experimental and simulated systems, it has been observed experimentally that the glass transition was insensitive to changes in molecular weight above 10 kDa for other DA polymers.[48] Interestingly, we found a direct correlation between T_g and density in these materials; this finding is consistent with the free-volume model for glass transitions.[49]

3.3.3.2 Bulk Heterojunctions

T_g is an important parameter for the BHJ because it represents the upper bound for the operating temperature at which a device can function without undergoing detrimental morphological rearrangements.[47] Solar modules must be capable of withstanding significant temperature fluctuations (–40 to 85°C) without coarsening of the morphology or degrading.[50] For all three materials (**Figure 3.5a-c**), we observed a shift in the glass transition temperatures and the densities with the addition of $PC_{71}BM$; this finding was consistent with previous experimental[47] and computational studies.[8] The shift can

ultimately be attributed to the high dispersion forces arising from the fullerene cage and the spherical shape, which enables efficient packing and causes it to act as an anti-plasticizing agent. With glass transitions well above 100 °C we conclude that BHJs based on these DA polymers should be suitably stable to thermal cycling as part of an integrated solar module.

3.3.4 Solution-Phase Conformations

Strong inter- and intramolecular forces that arise from extensive π-conjugation make low bandgap polymers especially difficult to solubilize. These materials exhibit a wide range of solution-phase conformational behaviour that have a profound effect on the morphology of films cast from solution. To take the effects of solvation into account without explicitly simulating the evaporation process, we performed simulated annealing on implicitly solvated individual chains using Langevin dynamics, following an approach originally described by Jackson and coworkers.[15] This protocol was used to generate minimum energy self-folded chains that have been demonstrated to be present in DA polymer solutions on the basis of spectroscopic evidence.[25]

The annealed structures can be classified according to the four general polymer conformations: globular, toroidal, folded, and extended (**Figure 3.6**). For each polymer, we performed 60 independent annealing simulations and then classified the resulting structures according to a Q-tensor analysis, based on the Landau-de Gennes order parameter.[51] The Q-tensor is a generalized order parameter whose maximum eigenvalue describes the amount of order present in the polymer backbone. A more detailed description of this analysis is given in **Section B.2.4** of the **Appendix B**. A useful visualization of order in these systems can be obtained by computing an orientational

contact map, $\boldsymbol{M_{ij}} = \hat{\boldsymbol{t}}_{\boldsymbol{i}} \cdot \hat{\boldsymbol{t}}_{\boldsymbol{j}}$, shown in **Figure 3.6**. The results of our classification scheme for each polymer are shown in **Figure 3.7a.**

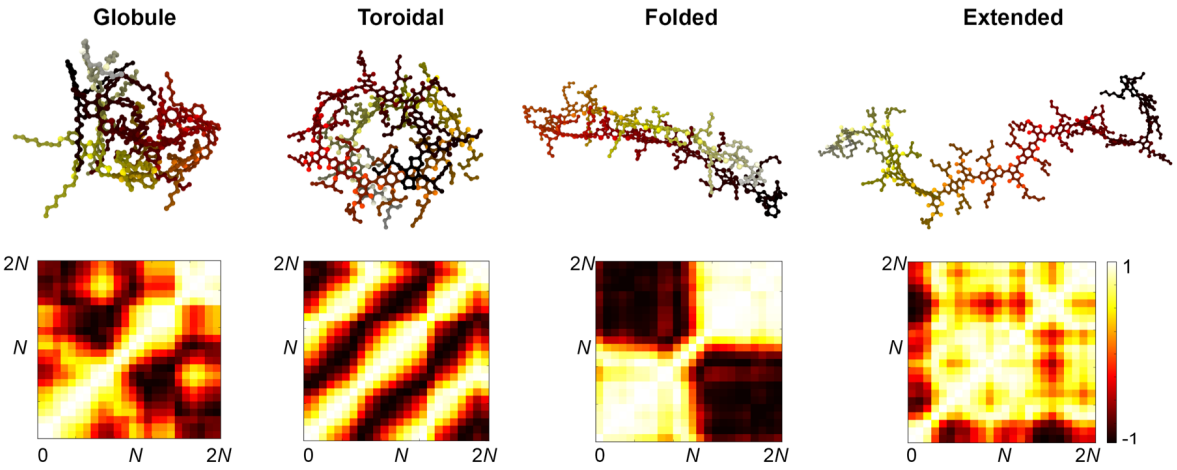

Figure 3.6. Conformational classes. Representative chains and their associated orientational contact maps illustrating the conformational classes available to single chains and the distinctive patterns used for classifying the chain conformations.

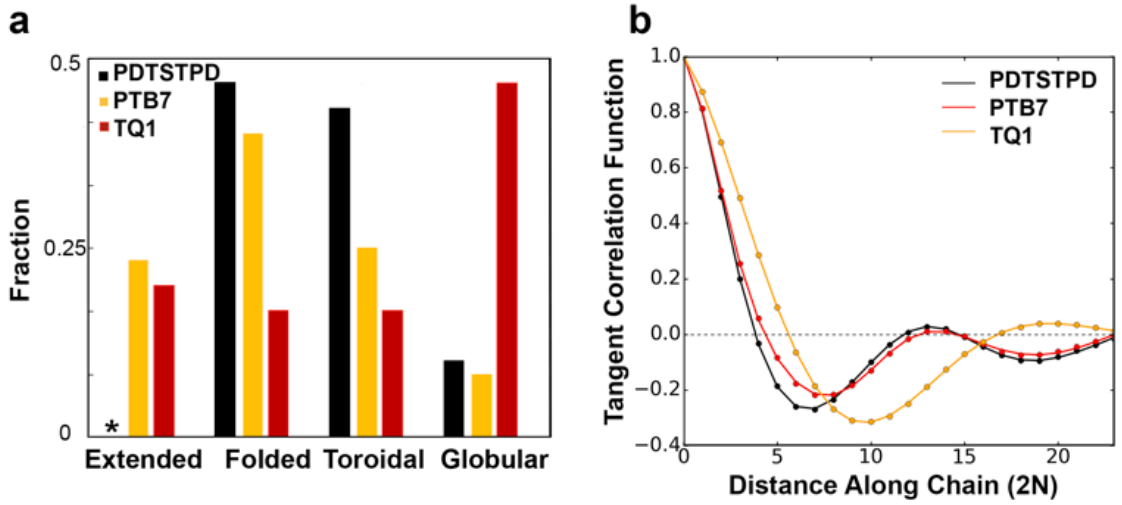

Figure 3.7. Characterization of conformational preferences. (a) Chart showing fraction of each conformation present in the *self-aggregated* morphology for each type of polymer. (b) Tangent correlation function showing a large tendency for folded chains.

We found that the conformational preferences had strong agreement with the experimentally determined ordering in these materials. TQ1, which is known to be one of the most structurally disordered low-bandgap polymers, had the strongest tendency to form globular, disordered conformations. PDTSTPD, which exhibits a distinct lamellar stacking peak in X-ray diffraction experiments, had the strongest tendency to form ordered, folded conformations. PTB7, which has significant short-range order but limited long-range order, had the broadest distribution of conformational classes. Interestingly, we found that the annealing simulations of PDTSTPD resulted in no conformations in an extended state. This behaviour exemplifies the strong thermodynamic driving force for folding of this polymer in solution. We performed the same analysis on the *melt-quenched* morphology obtained for each of the three polymers and found all the chains to be in an extended conformation per this classification scheme. This finding is consistent with the absence of an enthalpic driving force for chain folding in the melt. Similar simulations have been performed for P3HT, using an implicitly solvated coarse-grained model.[52] It was found that P3HT has a strong preference for adopting toroidal and folded conformations, however, the structures were not characterized using the same order parameter analysis, so a direct comparison cannot be made.

The increased propensity for chain folding in solution also results in a change in the tangent correlation functions when compared to the melt phase. As shown in **Figure 3.7b**, we found that the tangent correlation functions of the isolated polymer chains (**Figure 3.3b**) all exhibited a more pronounced oscillatory shape than chains in the melt phase, but could still be fit to an analytical expression, as described in **Section C.2.2** of the **Appedix C**. The tangent correlation function is intrinsically related to the conformational

preferences of the chain. The folded and toroidal structure result in more oscillatory correlations while the extended and globular conformations . The toroidal structure is the only one that is truly a helix, it's pitch is approximately equal to the π-stacking distance of the conjugated units.

3.3.5 Solid Morphologies

3.3.5.1 Melt-Quenched Morphology

The glassy configurations (T = 300 K, p = 1 atm) obtained from the thermal quenching simulations of pure polymers represent one possible solid-state amorphous morphology accessible to the low-bandgap polymers. This structure is best compared to the morphological arrangement that might be obtained experimentally by spin-coating from a theta solvent, or by subjecting the thin film to thermal annealing followed by rapid quenching. The slowest quenching rates possible with MD are still orders of magnitude faster than the experimental timescale (see **Section B.1.8** of the **Appendix B**). Analysis of the simulation trajectories reveals that the chains exist in an extended, amorphous state conducive to the formation of entanglements.

3.3.5.2 Self-Aggregated Morphology

Films of conjugated polymer that are cast from solution are known to form kinetically trapped morphologies. The quality of the solvent determines the free energy of polymer interactions in solution and thus dictates their morphological arrangement in the solid film cast from solution. To simulate a glassy morphology that might result from spin coating from a poor, low-boiling point solvent, we randomly packed the folded chain conformations described previously into a simulation box and allowed the density to converge at constant temperature and pressure (T = 300 K, p = 1 atm). See **Figure B.1** in

Appendix B for a visual representation of this simulation process. This protocol led to a solid structure containing voids and self-folded chains (**Figure 3.8**). This morphology is farther away from equilibrium than the *melt-quenched* morphology. We expected that the presence of voids would lead to a lower elastic modulus, and the self-folded chains would reduce the number of entanglements and make the *self-aggregated* morphology softer and more brittle than the *melt-quenched* morphology.

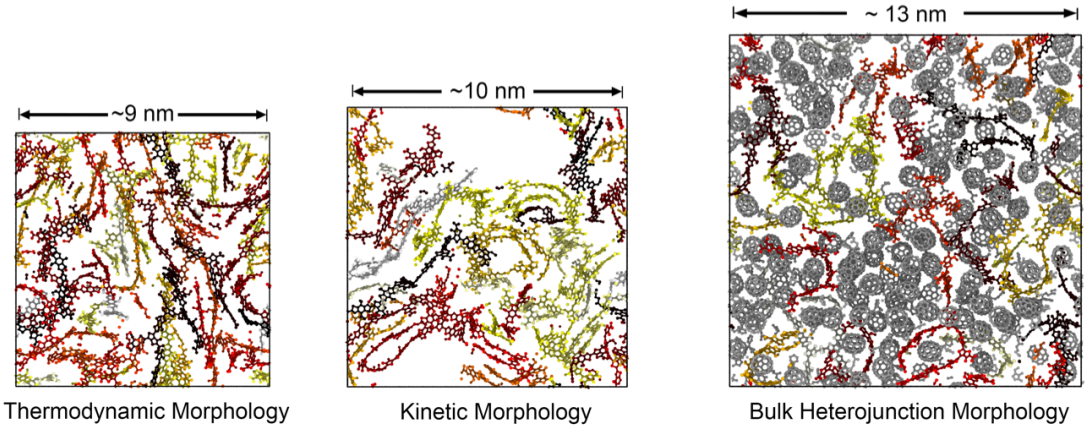

Figure 3.8. Comparison of the three glassy, solid morphologies (T = 300 K and p = 1 atm) for PTB7. Snapshots showing 2 nm slices of the simulation trajectory. Polymers are coloured separately. Hydrogen atoms and side chains are omitted for clarity.

3.3.5.3 Bulk Heterojunction Morphology

The OPV bulk heterojunction generally consists of a ternary system containing phase segregated regions of pure polymer, pure fullerene, and a mixed region containing both materials.[53] The glassy configurations obtained from the thermal quenching simulations of the composite system (analogous to the *melt-quenched* morphology of the pure polymers) provide a representation of the mixed region, which is of utmost importance for charge separation in OPVs.[45,54–56] This morphology will be referred to as the *bulk heterojunction* morphology for comparative purposes (see **Figure 3.8**). In reality,

it is well known that fullerenes have a thermodynamic preference to phase segregate in the bulk heterojunction.[57–59] Due to computational constraints, phenomena that occurs on such length and time scales can't be captured adequately using atomistic models. For all bulk heterojunction simulations, a mass fraction of 1:1.5 polymer to PCBM was used, this is a typical composition used in devices.

3.3.5.4 Entanglements

The topological constraint that chains can slide past but not pass through one another gives rise to a number of rheological and mechanical properties unique to polymers, including ultimate strain at fracture, tensile strength, and toughness.[60] Entanglements can be quantified in MD simulations using a primitive path analysis such as the Z1 algorithm of Kröger and coworkers.[61–64] We have applied this algorithm to our simulations in order to calculate the average number of interior kinks per chain, which is proportional to the entanglement density. The results of our analysis are shown in **Figure 3.9**. As expected, we found that the *melt-quenched* morphology contained more entanglements than either the *self-aggregated* or *bulk heterojunction* morphologies. Across the three different polymers we found that PTB7 had the most entanglements in all cases, followed by PDTSTPD and finally TQ1. We attribute this finding to the fact that TQ1 had the shortest contour length and the longest persistence length of the three polymers. It is important to note that on average there is only ~1 interior kink per chain, therefore these polymers do not form an entangled network at this molecular weight. Accurate coarse-grained models will be necessary for simulating high molecular weight entanglement properties.[8,65] This is the subject of on-going work.

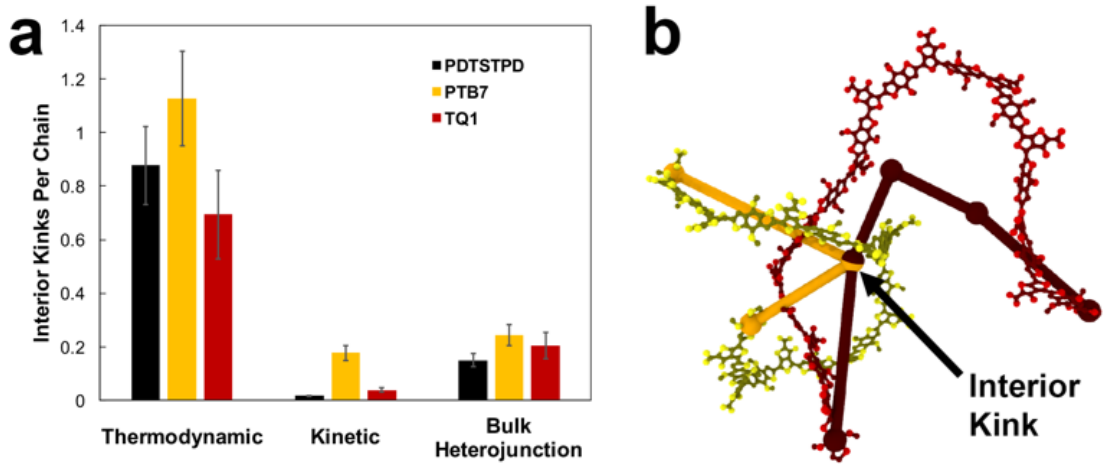

Figure 3.9. Entanglement analysis. (a) Plot showing the number of interior kinks per chain for each system simulated. Interior kinks define the primitive path of the polymer chain and are proportional to the number entanglements per chain. Mathematically they are defined as nodes that represent the limit to which the contour can be reduced to a minimum length without violating the topological constraint imposed by excluded volume interactions. (b) Visual representation of two chain contours (side chains and hydrogen atoms removed for clarity) as well as their respective primitive paths demonstrating the concept of an interior kink.

3.3.5.5 Uniaxial Tensile Response

The capacity for semiconducting materials to accommodate tensile strain is required for applications in stretchable and wearable devices. To simulate the tensile behaviour of the glassy configurations, we imposed a uniaxial deformation and computed the stress response shown in **Figure 3.10a-c** for PTB7. The tensile modulus (***E***) was estimated by fitting a straight line to the stress at less than 2% strain. We found that differences in composition and morphology played a more important role in determining the tensile response than differences in molecular structure. As expected, the *melt-quenched* morphology had a higher tensile modulus and overall toughness than the *self-aggregated* morphology. Additionally, the composites with $PC_{71}BM$ had increased tensile moduli. Increased modulus of the *bulk heterojunction* morphology is consistent with the

increased T_g and density of this structure compared to the other two. For all three polymers, we found that the computed tensile modulus obtained from the *melt-quenched* morphology was comparable to that obtained from similar atomistic simulations of P3HT.[17]

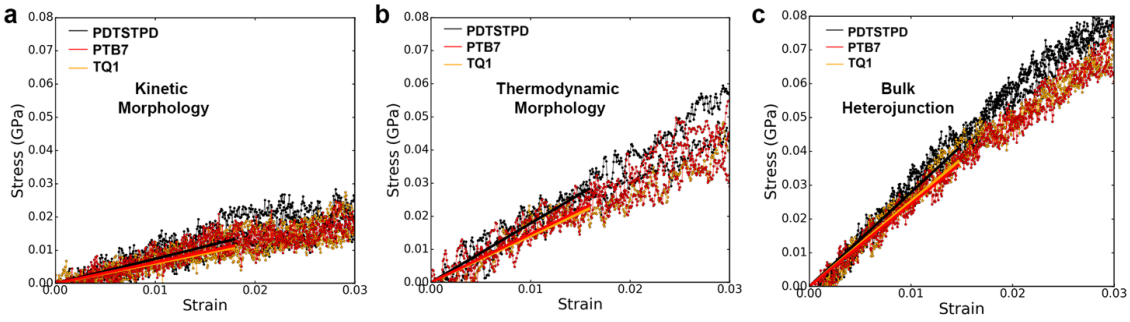

Figure 3.10. Mechanical response. Stress-strain curves showing the responses of (a) the *self-aggregated* morphology, (b) the *melt-quenched* morphology, and (c) the *bulk heterojunction* morphology of each polymer. The solid lines overlayed on the plots are the linear fits used to calculate the tensile moduli. It can be seen in the plots that different morphologies and compositions play a more important role in determining the stress response than differences in molecular structure.

A comparison of the results from the pure polymer simulations to the experiment reveals an interesting finding. As shown in **Figure 3.11,** we observed that the experimental value for the tensile modulus agrees well with the *melt-quenched* morphology for PTB7, the *self-aggregated* morphology for PDTSTPD, and is intermediate between the two morphologies for TQ1. Given that PDTSTPD had the strongest tendency to form folded aggregates, it makes sense that the *self-aggregated* morphology is a more accurate representation of PDTSTPD films cast from solution than is the *melt-quenched* morphology. The way in which this line of reasoning can be applied to TQ1 and PTB7 is less clear, most likely due to explicit solvation effects that were not taken into account. Nonetheless, the fact that the experimental values for tensile moduli of the three materials span the range bound by the calculated *self-aggregated* and *melt-quenched* morphologies

suggest a strong role for the different solubility properties of the molecules, and that explicit atomistic simulations of solution-phase structure will be necessary in future work.

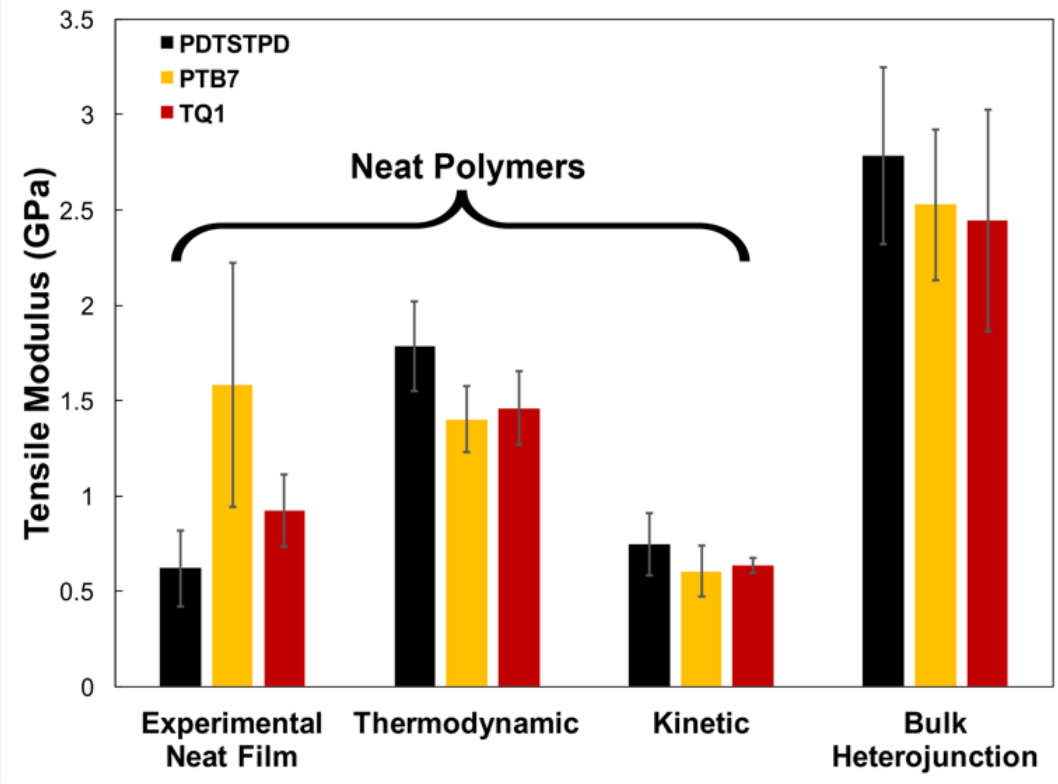

Figure 3.11. Summary of tensile modulus predictions and comparison to experiment.

In general, these results suggest that differences in the morphology—as opposed to molecular structure—produced the wide range of tensile moduli measured in a library of low-bandgap polymers.[3] This conclusion indicates that solution-processing represents a viable route for optimizing the mechanical robustness of these materials. One specific testable prediction is that films cast at high temperature may have improved mechanical stability compared to those cast at room temperature due to an increased extension of polymer chains and corresponding density of entanglements.

It is important to note that we did not observe cracking in any of the tensile loading simulations. This finding, coupled with the fact that all three of these materials exhibited

brittle fracture at ≤3% strain experimentally[3] led us to conclusion that the dominant fracture mechanism in these materials is likely through chain scission and the presence of macroscopic defects that localize stress, neither of which are present in these simulations. Although the experimental crack-on-set strain was small for all three of these materials, there still were minor differences. Of the three materials TQ1 was able to withstand the most strain (2.7%), followed by PTB7 (2.3%) and finally PDTSTPD (1.2%).[3] These values correlate well with the glass transition temperature predicted and measured for these materials giving further evidence that the brittle fracture observed experimentally is the result of bond scission. Since the models employed in these simulations rely on a harmonic bond approximation, they are unsuitable for predicting such fracture behaviour. In future mechanical deformation simulations, bond potentials that allow for cleavage will be parameterized for this class of materials. It would also be instructive to perform similar simulations on materials that are known experimentally to exhibit ductile modes of fracture.[3] This would allow for computational identification of the molecular-scale attributes that enable stress relaxation mechanisms other than bond scission.

3.4 Conclusions

In this paper, we have demonstrated the utility of MD simulations to elucidate the structural and mechanical behaviour of low-bandgap polymers and composites. A summary of important material parameter predictions is given in **Table 3.1.** Through comparison to experimental results for π-stacking distances, glass transition temperatures, and tensile moduli, we have identified the strengths and limitations of this approach and provided suggestions for further refinement of custom models parameterized from electronic structure calculations (e.g., the use of a buffered 14-7 Lennard-Jones potential,

and the allowance for bond scission). Through the computation of various distribution functions, we have provided insights that could be of use to synthetic chemists designing new materials. Furthermore, our simulations have revealed several new findings previously unconsidered in the literature that warrant further investigation.

Table 3.1. Summary of material property predictions reported. Values displayed are all from the *Melt-Quenched* simulations of pure polymers. For each material property, values are colored per relative magnitudes of the three polymers simulated.

Polymer	l (Å)	L_p/l	λ/l	L_c	T_g (K)	E (GPa)	$< Z >$	$\rho\ (g\ cm^{-3})$
PDTSTPD	6.0	5.2	4.2	3.2	380	1.8	0.9	1.12
PTB7	6.4	4.7	5.9	3.1	400	1.4	1.1	1.05
TQ1	4.2	7.3	9.1	2.7	375	1.5	0.7	1.04

We found that the rigid, planar, fused rings along the backbone give rise to the formation of helical structures in the melt-phase that are characteristic of ribbon-like chains. This finding suggests that the classic worm-like chain model might not be appropriate for the interpretation of scattering experiments investigating the conformational behaviour of these polymers. Consideration of DA polymers as ribbon-like chains should also have important implications for the statistical mechanical basis of entropic elasticity[40] and charge transport properties[39] of these chains.

We found that the extent to which the molecular structure dictates the mechanical behaviour of these materials is limited by the extent to which it contributes to the solution-phase behavior and resulting thin-film morphology. These results have led us to the hypothesis that spin-coating from heated solutions of optimized solvent quality should result in more entangled, mechanically robust films. This hypothesis will be the subject of future experimental and computational investigations.

To simulate the solvent evaporation process of a printing or coating procedure accurately would require detailed coarse-grained models such as those that exist for P3HT[16,66] and other complex polymers.[67] In principle, the statistics gathered from our melt-phase simulations contain most of the necessary information to build stylistically similar models for these polymers. Additional information, however, must be gathered from explicitly solvated atomistic simulations to compute concentration dependent free energies of interactions capable of accurately modelling the solidification process. This is the subject of ongoing work and will allow for the simulation of an experimentally relevant morphology of a solution-cast thin film containing realistic molecular weight distributions and interfacial effects.

3.5 Acknowledgements

This work was supported by the Air Force Office of Scientific Research (AFOSR) Grant Number FA9550-16-1-0220. Additional support was provided by the Hellman Fellowship awarded to D.L. and the ARCS Fellowship awarded to S.R. Computational resources to support this work were provided by the Extreme Science and Engineering Discovery Environment (XSEDE) Program through the National Science Foundation grant number ACI-1053575.[68] Additionally, N.E.J and S.E.R would like to thank Professor Mark Ratner for bridging this collaboration.

Chapter 3, in full, is a reprint of the material as it appears in *Energy & Environmental Sciences*, 2017, 10, 558-569. The Royal Society of Chemistry, 2017. Samuel E. Root, Nicholas E. Jackson, Suchol Savagatrup , Gaurav Arya, and Darren J. Lipomi. The dissertation author was the primary investigator and author of this paper.

3.6 References

(1) Facchetti, A. π-Conjugated Polymers for Organic Electronics and Photovoltaic Cell Applications †. *Chem. Mater.* **2011**, *23*, 733–758.

(2) Printz, A. D.; Lipomi, D. J. Competition between Deformability and Charge Transport in Semiconducting Polymers for Flexible and Stretchable Electronics. *Appl. Phys. Rev.* **2016**, *3*, 21302.

(3) Roth, B.; Savagatrup, S.; De Los Santos, N.; Hagemann, O.; Carle, J. E.; Helgesen, M.; Livi, F.; Bundgaard, E.; Søndergaard, R. R.; Krebs, F. C.; *et al.* Mechanical Properties of a Library of Low-Bandgap Polymers. *Chem. Mater.* **2016**, acs.chemmater.6b00525.

(4) Scharber, M. C.; Muehlbacher, D.; Koppe, M.; Denk, P.; Waldauf, C.; Heeger, A. J.; Brabec, C. J. Design Rules for Donors in Bulk Heterojunction Solar Cells Towards 10% Energy Conversion Efficiency. *Adv. Mater.* **2006**, *18*, 789–794.

(5) Müllen, K.; Pisula, W. Donor–Acceptor Polymers. *J. Am. Chem. Soc.* **2015**, *137*, 9503–9505.

(6) Savagatrup, S.; Printz, A. D.; O'Connor, T. F.; Zaretski, A. V.; Rodriquez, D.; Sawyer, E. J.; Rajan, K. M.; Acosta, R. I.; Root, S. E.; Lipomi, D. J. Mechanical Degradation and Stability of Organic Solar Cells: Molecular and Microstructural Determinants. *Energy Environ. Sci.* **2015**, *8*, 55–80.

(7) Savagatrup, S.; Makaram, A. S.; Burke, D. J.; Lipomi, D. J. Mechanical Properties of Conjugated Polymers and Polymer-Fullerene Composites as a Function of Molecular Structure. *Adv. Funct. Mater.* **2014**, *24*, 1169–1181.

(8) Root, S. E.; Savagatrup, S.; Pais, C. J.; Arya, G.; Lipomi, D. J. Predicting the Mechanical Properties of Organic Semiconductors Using Coarse-Grained Molecular Dynamics Simulations. *Macromolecules* **2016**, *49*, 2886–2894.

(9) Whitesides, G. M. Physical-Organic Chemistry: A Swiss Army Knife. *Isr. J. Chem.* **2016**, *56*, 66–82.

(10) Brédas, J. L.; Beljonne, D.; Coropceanu, V.; Cornil, J. Charge-Transfer and Energy-Transfer Processes in π-Conjugated Oligomers and Polymers: A Molecular Picture. *Chem. Rev.* **2004**, *104*, 4971–5003.

(11) Printz, A. D.; Savagatrup, S.; Burke, D. J.; Purdy, T. N.; Lipomi, D. J. Increased Elasticity of a Low-Bandgap Conjugated Copolymer by Random Segmentation for Mechanically Robust Solar Cells. *RSC Adv.* **2014**, *4*, 13635–13643.

(12) Dubay, K. H.; Hall, M. L.; Hughes, T. F.; Wu, C.; Reichman, D. R.; Friesner, R. a. Accurate Force Field Development for Modeling Conjugated Polymers. *J. Chem.*

Theory Comput. **2012**, *8*, 4556–4569.

(13) Marcon, V.; Raos, G. Free Energies of Molecular Crystal Surfaces by Computer Simulation: Application to Tetrathiophene. *J. Am. Chem. Soc.* **2006**, *128*, 1408–1409.

(14) Marcon, V.; Raos, G. Molecular Modeling of Crystalline Oligothiophenes: Testing and Development of Improved Force Fields. *J. Phys. Chem. B* **2004**, *108*, 18053–18064.

(15) Jackson, N. E.; Kohlstedt, K. L.; Savoie, B. M.; Olvera de la Cruz, M.; Schatz, G. C.; Chen, L. X.; Ratner, M. a. Conformational Order in Aggregates of Conjugated Polymers. *J. Am. Chem. Soc.* **2015**, *137*, 6254–6262.

(16) Huang, D. M.; Faller, R.; Do, K.; Moul, A. J. Coarse-Grained Computer Simulations of Polymer / Fullerene Bulk Heterojunctions for Organic Photovoltaic Applications. *J. Chem. Theory Comput.* **2010**, *6*, 526–537.

(17) Tummala, N. R.; Risko, C.; Bruner, C.; Dauskardt, R. H.; Brédas, J.-L. Entanglements in P3HT and Their Influence on Thin-Film Mechanical Properties: Insights from Molecular Dynamics Simulations. *J. Polym. Sci. Part B Polym. Phys.* **2015**, 1–9.

(18) Kleinschmidt, A. T.; Root, S. E.; Lipomi, D. J. Poly(3-Hexylthiophene) (P3HT): Fruit Fly or Outlier in Organic Solar Cell Research? *J. Mater. Chem. A* **2016**.

(19) Kroon, R.; Gehlhaar, R.; Steckler, T. T.; Henriksson, P.; Müller, C.; Bergqvist, J.; Hadipour, A.; Heremans, P.; Andersson, M. R. New Quinoxaline and Pyridopyrazine-Based Polymers for Solution-Processable Photovoltaics. *Sol. Energy Mater. Sol. Cells* **2012**, *105*, 280–286.

(20) Wang, E.; Hou, L.; Wang, Z.; Hellström, S.; Zhang, F.; Inganäs, O.; Andersson, M. R. An Easily Synthesized Blue Polymer for High-Performance Polymer Solar Cells. *Adv. Mater.* **2010**, *22*, 5240–5244.

(21) Liang, Y.; Xu, Z.; Xia, J.; Tsai, S. T.; Wu, Y.; Li, G.; Ray, C.; Yu, L. For the Bright Future-Bulk Heterojunction Polymer Solar Cells with Power Conversion Efficiency of 7.4%. *Adv. Mater.* **2010**, *22*, 135–138.

(22) Lu, L.; Yu, L. Understanding Low Bandgap Polymer PTB7 and Optimizing Polymer Solar Cells Based on IT. *Adv. Mater.* **2014**, *26*, 4413–4430.

(23) Chu, T.-Y.; Lu, J.; Beaupre, S.; Zhang, Y.; Pouliot, J.-R.; Wakim, S.; Zhou, J.; Leclerc, M.; Li, Z.; Ding, J.; *et al.* Bulk Heterojunction Solar Cells Using Thieno[3,4-C]pyrrole-4,6-Dione and Dithieno[3,2-b:2’,3’-d]silole Copolymer with a Power Conversion Efficiency of 7.3%. *J. Am. Chem. Soc.* **2011**, *133*, 4250–4253.

(24) Chu, T. Y.; Lu, J.; Beaupré, S.; Zhang, Y.; Pouliot, J. R.; Zhou, J.; Najari, A.; Leclerc, M.; Tao, Y. Effects of the Molecular Weight and the Side-Chain Length on the Photovoltaic Performance of Dithienosilole/thienopyrrolodione Copolymers. *Adv. Funct. Mater.* **2012**, *22*, 2345–2351.

(25) Fauvell, T. J.; Zheng, T.; Jackson, N. E.; Ratner, M. A.; Yu, L.; Chen, L. X. The Photophysical and Morphological Implications of Single-Strand Conjugated Polymer Folding in Solution. *Chem. Mater.* **2016**, acs.chemmater.6b00734.

(26) Brouwer, F.; Alma, J.; Valkenier, H.; Voortman, T. P.; Hillebrand, J.; Chiechi, R. C.; Hummelen, J. C. Using Bis(pinacolato)diboron to Improve the Quality of Regioregular Conjugated Co-Polymers. *J. Mater. Chem.* **2011**, *21*, 1582.

(27) Diao, Y.; Shaw, L.; Bao, Z.; Mannsfeld, S. C. B. Morphology Control Strategies for Solution- Processed Organic Semiconductor Thin Fi Lms. *Energy Environ. Sci.* **2014**, *7*, 2145–2159.

(28) Guo, S.; Herzig, E. M.; Naumann, A.; Tainter, G.; Perlich, J.; Müller-Buschbaum, P. Influence of Solvent and Solvent Additive on the Morphology of PTB7 Films Probed via X-Ray Scattering. *J. Phys. Chem. B* **2014**, *118*, 344–350.

(29) Ye, L.; Jing, Y.; Guo, X.; Sun, H.; Zhang, S.; Zhang, M.; Huo, L.; Hou, J. Remove the Residual Additives toward Enhanced Efficiency with Higher Reproducibility in Polymer Solar Cells. *J. Phys. Chem. C* **2013**, *117*, 14920–14928.

(30) Al-Hussein, M.; Herzig, E. M.; Schindler, M.; Löhrer, F.; Palumbiny, C. M.; Wang, W.; Roth, S. V.; Müller-Buschbaum, P. Comparative Study of the Nanomorphology of Spray and Spin Coated PTB7 Polymer: Fullerene Films, 2016, 889–894.

(31) Salleo, A.; Kline, R. J.; DeLongchamp, D. M.; Chabinyc, M. L. Microstructural Characterization and Charge Transport in Thin Films of Conjugated Polymers. *Adv. Mater.* **2010**, *22*, 3812–3838.

(32) Hammond, M. R.; Kline, R. J.; Herzing, A. a; Richter, L. J.; Germack, D. S.; Ro, H.; Soles, C. L.; Fischer, D. a; Xu, T.; Yu, L.; *et al.* Molecular Order in High-Efficiency Polymer / Fullerene Bulk Heterojunction Solar Cells. *ACS Nano* **2011**, 8248–8257.

(33) Street, G. B.; Bredas, J. L.; Themans, B.; Andre, J. M. Organic Polymers Based on Aromatic Rings: Evolution of the Electronic Properties as a Function of the Torsion Angle between Adjacent Rings. *J. Chem. Phys.* **1985**, *83*, 1323–1329.

(34) Guo, S.; Ning, J.; Körstgens, V.; Yao, Y.; Herzig, E. M.; Roth, S. V.; Müller-Buschbaum, P. The Effect of Fluorination in Manipulating the Nanomorphology in PTB7:PC71BM Bulk Heterojunction Systems. *Adv. Energy Mater.* **2015**, *5*, 1–11.

(35) Hedstrom, S.; Persson, P. Quantum Chemical Calculations of Side-Group Stacking

and Electronic Properties in Thiophene − Quinoxaline Polymers. *J. Phys. Chem. C* **2012**, *116*, 26700–26706.

(36) Giomi, L.; Mahadevan, L. Statistical Mechanics of Developable Ribbons. *Phys. Rev. Lett.* **2010**, *104*, 2–5.

(37) Kuei, B.; Gomez, E. D. Chain Conformations and Phase Behavior of Conjugated Polymers. *Soft Matter* **2016**.

(38) Ramachandran, G.N. Ramakrishnan, C. Sasisekharan, V. Stereochemistry of Polypeptide Chain Konfigurations. *J. Mol. Biol.* **1963**, *7*, 95–99.

(39) Carbone, P.; Troisi, A. Charge Diffusion in Semiconducting Polymers: Analytical Relation between Polymer Rigidity and Time Scales for Intrachain and Interchain Hopping. *J. Phys. Chem. Lett.* **2014**, *5*, 2637–2641.

(40) Marko, J. F.; Siggia, E. D. Stretching DNA. *Macromolecules* **1995**, *28*, 8759–8770.

(41) Do, K.; Huang, D. M.; Faller, R.; Moulé, A. J. A Comparative MD Study of the Local Structure of Polymer Semiconductors P3HT and PBTTT. *Phys. Chem. Chem. Phys.* **2010**, *12*, 14735–14739.

(42) Yao, H.; Ye, L.; Zhang, H.; Li, S.; Zhang, S.; Hou, J. Molecular Design of Benzodithiophene-Based Organic Photovoltaic Materials. *Chem. Rev.* **2016**, *116*, 7397–7457.

(43) Son, H. J.; Wang, W.; Xu, T.; Liang, Y.; Wu, Y.; Li, G.; Yu, L. Synthesis of Fluorinated Polythienothiophene-Co-Benzodithiophenes and Effect of Fluorination on the Photovoltaic Properties. *J. Am. Chem. Soc.* **2011**, *133*, 1885–1894.

(44) Yamamoto, T.; Lee, B. L.; Kokubo, H.; Kishida, H.; Hirota, K.; Wakabayashi, T.; Okamoto, H. Synthesis of a New Thiophene/quinoxaline CT-Type Copolymer with High Solubility and Its Basic Optical Properties. *Macromol. Rapid Commun.* **2003**, *24*, 440–443.

(45) Graham, K. R.; Cabanetos, C.; Jahnke, J. P.; Idso, M. N.; Labban, A. El; Ndjawa, G. O. N.; Heumueller, T.; Vandewal, K.; Salleo, A.; Chmelka, B. F.; *et al.* Importance of the Donor:Fullerene Intermolecular Arrangement for High-E Ffi Ciency Organic Photovoltaics. **2014**.

(46) Wang, T.; Ravva, M. K.; Brédas, J.-L. Impact of the Nature of the Side-Chains on the Polymer-Fullerene Packing in the Mixed Regions of Bulk Heterojunction Solar Cells. *Adv. Funct. Mater.* **2016**.

(47) Müller, C. On the Glass Transition of Polymer Semiconductors and Its Impact on Polymer Solar Cell Stability. *Chem. Mater.* **2015**, *27*, 2740–2754.

(48) Müller, C.; Wang, E.; Andersson, L. M.; Tvingstedt, K.; Zhou, Y.; Andersson, M. R.; Inganä; S, O. Influence of Molecular Weight on the Performance of Organic Solar Cells Based on a Fluorene Derivative. *Adv. Funct. Mater.* **2010**, *20*, 2124–2131.

(49) Turnbull, D.; Cohen, M. H. Free-Volume Model of the Amorphous Phase: Glass Transition. *J. Chem. Phys.* **1961**, *34*, 120.

(50) Standard Test Methods for Photovoltaic Modules in Cyclic Temperature and Humidity. *ASTM Stand. E 1171S* **2001**, *i*, 1–5.

(51) Pierre-Gilles de Gennes, J. P. *The Physics of Liquid Crystals*; Clarendon, Oxford, 1974.

(52) Schwarz, K. N.; Kee, T. W.; Huang, D. M. Coarse-Grained Simulations of the Solution-Phase Self-Assembly of poly(3-Hexylthiophene) Nanostructures. *Nanoscale* **2013**, *5*, 2017–2027.

(53) Treat, N. D.; Chabinyc, M. L. Phase Separation in Bulk Heterojunctions of Semiconducting Polymers and Fullerenes for Photovoltaics. *Annu. Rev. Phys. Chem.* **2014**, *65*, 59–81.

(54) Bartelt, J. A.; Beiley, Z. M.; Hoke, E. T.; Mateker, W. R.; Douglas, J. D.; Collins, B. A.; Tumbleston, J. R.; Graham, K. R.; Amassian, A.; Ade, H.; *et al.* The Importance of Fullerene Percolation in the Mixed Regions of Polymer-Fullerene Bulk Heterojunction Solar Cells. *Adv. Energy Mater.* **2013**, *3*, 364–374.

(55) Vandewal, K.; Albrecht, S.; Hoke, E. T.; Graham, K. R.; Widmer, J.; Douglas, J. D.; Schubert, M.; Mateker, W. R.; Bloking, J. T.; Burkhard, G. F.; *et al.* Efficient Charge Generation by Relaxed Charge-Transfer States at Organic Interfaces. *Nat. Mater.* **2014**, *13*, 63–68.

(56) Moulé, A. J.; Meerholz, K. Controlling Morphology in Polymer-Fullerene Mixtures. *Adv. Mater.* **2008**, *20*, 240–245.

(57) Duong, D. T.; Walker, B.; Lin, J.; Kim, C.; Love, J.; Purushothaman, B.; Anthony, J. E.; Nguyen, T. Q. Molecular Solubility and Hansen Solubility Parameters for the Analysis of Phase Separation in Bulk Heterojunctions. *J. Polym. Sci. Part B Polym. Phys.* **2012**, *50*, 1405–1413.

(58) Oklobia, O.; Shafai, T. S.; Friedel, B.; Brenner, T. J. K.; McNeill, C. R.; Steiner, U.; Greenham, N. C.; Li, G.; Lu, G.; Li, S.; *et al.* Precise Construction of PCBM Aggregates for Polymer Solar Cells via Multi-Step Controlled Solvent Vapor Annealing. *J. Mater. Chem.* **2010**, *11*, 1736–1745.

(59) Fan, X.; Fang, G. J.; Qin, P. L.; Cheng, F.; Zhao, X. Z. Rapid Phase Segregation of P3HT:PCBM Composites by Thermal Annealing for High-Performance Bulk-

Heterojunction Solar Cells. *Appl. Phys. A Mater. Sci. Process.* **2011**, *105*, 1003–1009.

(60) Everaers, R. Rheology and Microscopic Topology of Entangled Polymeric Liquids. *Science (80-.).* **2004**, *303*, 823–826.

(61) Shanbhag, S.; Kröger, M. Primitive Path Networks Generated by Annealing and Geometrical Methods: Insights into Differences. *Macromolecules* **2007**, *40*, 2897–2903.

(62) Hoy, R. S.; Foteinopoulou, K.; Kröger, M. Topological Analysis of Polymeric Melts: Chain-Length Effects and Fast-Converging Estimators for Entanglement Length. *Phys. Rev. E - Stat. Nonlinear, Soft Matter Phys.* **2009**, *80*, 14–16.

(63) Karayiannis, N. C.; Kröger, M. Combined Molecular Algorithms for the Generation, Equilibration and Topological Analysis of Entangled Polymers: Methodology and Performance. *Int. J. Mol. Sci.* **2009**, *10*, 5054–5089.

(64) Kröger, M. Shortest Multiple Disconnected Path for the Analysis of Entanglements in Two- and Three-Dimensional Polymeric Systems. *Comput. Phys. Commun.* **2005**, *168*, 209–232.

(65) Jones, M. L.; Huang, D. M.; Chakrabarti, B.; Groves, C. Relating Molecular Morphology to Charge Mobility in Semicrystalline Conjugated Polymers. *J. Phys. Chem. C* **2016**, *120*, 4240–4250.

(66) Tapping, P. C.; Clafton, S. N.; Schwarz, K. N.; Kee, T. W.; Huang, D. M. Molecular-Level Details of Morphology-Dependent Exciton Migration in Poly(3-Hexylthiophene) Nanostructures. *J. Phys. Chem. C* **2015**, *119*, 7047–7059.

(67) Agrawal, V.; Arya, G.; Oswald, J. Simultaneous Iterative Boltzmann Inversion for Coarse-Graining of Polyurea. *Macromolecules* **2014**, *47*, 3378–3389.

(68) John, T.; Cockerill, T.; Foster, I.; Gaither, K. XSEDE: Accelerating Scientific Discovery. *Comput. Sci. Eng.* **2014**, *16*, 62–74.

Chapter 4

Measuring the Glass Transition Temperature of Conjugated Polymer Films with UV-vis Spectroscopy

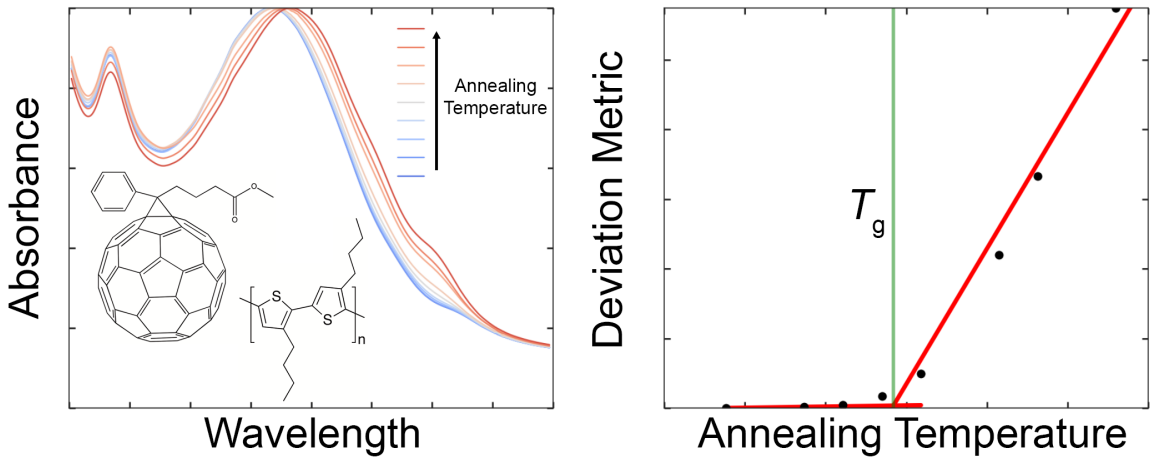

Image 5. Table of contents artwork for Chapter 4. Illustration of measurement technique.

Samuel E. Root,[‡] Mohammad A. Alkhadra,[‡] Daniel Rodriquez, Adam D. Printz, and Darren J. Lipomi

([‡] Equal contribution)

Department of NanoEngineering, University of California, San Diego

9500 Gilman Drive, Mail Code 0448, La Jolla, CA 92093-0448

Abstract

The glass transition temperature (T_g) of a conjugated polymer can be used to predict its morphological stability and mechanical properties. Despite the importance of this parameter in applications from organic solar cells to wearable electronics, it is not easy to measure. The T_g is often too weak to detect using conventional differential scanning calorimetry (DSC). Alternative methods—e.g., variable temperature ellipsometry—require specialized equipment. This paper describes a technique for measuring the T_g of thin films of semicrystalline conjugated polymers using only a hot plate and an ultraviolet-visible (UV-vis) spectrometer. UV-vis spectroscopy is used to measure changes in the absorption spectrum due to molecular-scale rearrangement of polymers when heated past T_g, corresponding to the onset of the formation of photophysical aggregates. A deviation metric, defined as the mean-squared deviation in absorbance between as-cast and annealed films, is used to quantify shifts in the absorption spectra. The glass transition is observed as a change in slope in a plot of the deviation metric versus temperature. To demonstrate the usefulness of this technique, a variety of semiconducting polymers are tested: P3BT, PBTTT-C14, F8BT, PDTSTPD, PTB7, PCDTBT, TQ1, and MEH-PPV. These polymers represent a range of solid-state morphologies, from highly ordered to predominately amorphous. A successful measurement of T_g depends on the ability of the polymer to form photophysical aggregates. The results obtained using this method for P3BT, PBTTT-C14, F8BT, and PDTSTPD are in agreement with values of T_g that have been reported in the literature. Molecular dynamics simulations are used to show how the morphology evolves upon annealing: above the T_g, an initially kinetically trapped morphology undergoes structural

rearrangements to assume a more thermodynamically preferred structure. The temperature at which onset of this rearrangement occurs in the simulation is concomitant with the spectroscopically determined value of T_g.

4.1 Introduction

The glass transition temperature (T_g) is a critical property of polymers that can be used to predict the thermal[1] and mechanical stabilities[2] of organic semiconductor devices.[3] The glass transition describes the onset of relaxation processes in segments of the main chains of polymeric materials.[4–6] This parameter is of particular importance for the operational stability of organic electronic devices (which include π-conjugated polymers and small molecules) for at least two reasons.[1] First, devices operating above T_g may undergo deleterious morphological rearrangements. Changes in the morphology are deleterious particularly if a kinetically trapped structure formed upon solidification of a film is conducive to device performance, while a thermodynamically favorable structure that forms when heated is not. For example, the domains in a highly phase-separated morphology of a bulk heterojunction (BHJ) organic solar cell that forms upon heating above T_g may be too large to allow efficient separation of charges.[1] Second, the T_g is intimately related to stress-relaxation processes of polymeric materials. For soft, compliant polymers intended for biological integration, it may be desirable to have a low T_g, and thus rubber-like mechanical behavior.[7,8] Although a variety of well-developed methods exist for measuring the T_g of bulk polymeric materials,[9] thin films present a significant challenge for these conventional methods. The challenge arises in part because of the small thermal signal produced by the minute mass of a thin film. Moreover, the

thermal properties of the bulk material do not necessarily represent those of a thin film.[10] This paper describes a facile technique to measure the glass transition temperatures of conjugated polymers that leverages their unique photophysical behavior. The technique works by finding the annealing temperature at which the thin-film absorption spectrum in the UV-vis range undergoes an abrupt change, indicating the onset of formation of photophysical aggregates.[11]

Thin films of conjugated polymers are generally prepared by casting from a solution using laboratory-scale techniques (e.g., spin coating) or industrial-scale techniques (e.g., slot-die coating, gravure, inkjet, or screen printing). Rapid solidification of the polymer that occurs upon evaporation of the solvent typically results in the formation of kinetically trapped structures that contain considerable free volume[12] and structural disorder.[13] Thermal annealing is a common post-processing step that allows kinetically trapped structures to undergo morphological rearrangement and aggregation.[14] These structural changes have important effects on device-scale optoelectronic[15] and mechanical properties.[2]

In a recent review on the glass transition of organic semiconductors,[1] four standard techniques to measure T_g were outlined: differential scanning calorimetry (DSC),[16] dynamic mechanical analysis (DMA),[17] broadband dielectric spectroscopy (BDS),[18] and variable-temperature ellipsometry (VTE).[19] These techniques are ubiquitous in the field of polymer science and have been widely applied to characterize the thermal properties of semiconducting polymers, for which the most common is DSC.[16] In many cases, DSC does not possess the sensitivity to detect the subtle glass transitions of polymeric semiconductors; it is commonplace for T_g to evade detection, even in cases

where DSC thermograms are reported.[15,20–26] Moreover, conventional DSC setups require bulk samples and thus cannot be used to characterize thin films (DMA and BDS are also typically restricted to bulk materials).[1] Advanced techniques such as differential AC-chip calorimetry have been developed to mitigate some of these limitations,[27] however, they are usually unavailable in laboratories that focus on organic electronics.

The thermal behavior of a polymeric thin film becomes thickness-dependent below a critical thickness (~100 nm).[28] This phenomenon has been attributed to interfacial effects at the free surface and with the supporting substrate.[19,28] The dominant effect is the increased mobility of polymer chains at the free surface, which serves to decrease the T_g.[19] VTE is unique among the available thermal characterization techniques in that it can probe thermal transitions of thin films, as opposed to bulk samples.[19] Unfortunately, ellipsometric systems, especially those with temperature-controlled stages, are expensive and not widely available. Therefore, use of this technique is mainly restricted to research groups who have specialized expertise.

Thin films of conjugated polymers absorb strongly in the UV-vis range, and various optical techniques have been developed to characterize their thermomechanical properties.[20,29,30] Lindqvist et al. have developed a simple technique to measure thermal transitions in fullerene-based BHJ films by taking advantage of the increased scattering of micrometer-sized fullerene crystals that form when the film is annealed above the T_g.[20] As such, this technique is not applicable to neat conjugated polymer films.

In this work, we measured the T_g by taking advantage of the shift in the UV-vis absorption spectrum that occurs after thermally annealing many neat conjugated polymer films.[11,31] This shift has been widely attributed to the formation of ordered aggregates and

is generally accompanied by an improvement in the charge transport properties of the thin film.[11] The amorphous phase of conjugated polymer thin films undergoes significant structural rearrangement only when the annealing temperature approaches T_g. We thus hypothesized that it would be possible to estimate the T_g of conjugated polymer thin films by quantifying the change in the absorption spectrum that resulted from thermal annealing. We expected that, once the annealing temperature surpassed the T_g, there would be an easily discernible change in the absorption spectrum. Hence, we defined a deviation metric (DM_T) as the mean-squared deviation in the absorbance between as-cast and annealed films (at annealing temperature, T):

$$DM_T \equiv \sum_{\lambda_{min}}^{\lambda_{max}} [I_{RT}(\lambda) - I_T(\lambda)]^2 \qquad (1)$$

where $I_{RT}(\lambda)$ and $I_T(\lambda)$ are the normalized absorption intensities of the as-cast (room temperature) and annealed films, respectively, λ is the wavelength, and λ_{min} and λ_{max} are the lower and upper bounds of the optical sweep, respectively. We expected that, at the T_g, there would be a discontinuity in the slope of DM_T when plotted against annealing temperature.

4.2 Experimental Design

4.2.1 Selection of Materials

To test the validity of our proposed methodology, we selected materials whose T_gs had been measured successfully using other techniques. Moreover, it was important to use materials of significant interest to the research community. Since the T_g of the popular regioregular poly(3-hexylthiophene) (P3HT) is near or somewhat below room temperature, we selected poly(3-butylthiophene) (P3BT) instead (structure shown in

Figure 4.1). An additional advantage of using P3BT was that we were able to apply the weakly interacting H-aggregate model developed by Spano and coworkers to provide a detailed analysis of vibronic progression as a function of annealing temperature for polythiophenes.[32,33] This analysis allowed us to deconvolute spectral shifts and determine microstructural mechanisms responsible for the abrupt shift in the absorption spectrum near the T_g. Additionally, to demonstrate the applicability of our technique to composite systems of organic semiconductors, we tested a BHJ film comprising P3BT and [6,6]-phenyl C_{61} butyric acid methyl ester (PCBM).

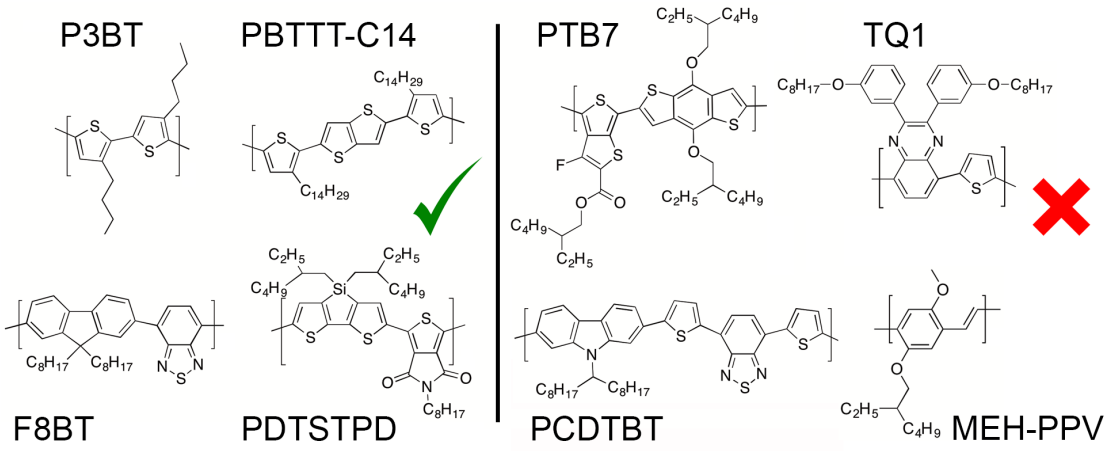

Figure 4.1. Chemical structures and common names of conjugated polymers involved in this study. Refer to **Experimental Methods** for systematic names. The technique works best for semicrystalline polymers.

To assess the transferability of our proposed methodology, we performed the experiment on several conjugated polymers with complex structures. The following materials were tested: F8BT, PBTTT-C14, PDTSTPD, PTB7, PCDTBT, TQ1, and MEH-PPV. These materials were chosen because they exhibit a wide range of ordering in the solid state, from highly ordered (e.g., the liquid-crystalline PBTTT-C14) to minimal long-range order (e.g., TQ1). In particular, PDTSTPD was chosen because its T_g has been

reported,[34,35] and we have previously performed molecular dynamics (MD) simulations to predict its thermal and mechanical properties.[36] To gain a detailed mechanistic understanding of our results, we performed additional MD simulations to demonstrate how the thermal annealing of a kinetically trapped structure results in morphological rearrangement. We expected that materials with stronger tendencies to crystallize would produce shifts in the absorption spectra that were more pronounced and thus a more easily observable T_g. Accordingly, we did not expect this technique to work for predominantly amorphous materials such as PTB7 (refer to **D.1** of the **Appendix D**). These amorphous materials are generally blended with fullerenes to form BHJs and do not perform especially well in transistor devices. Thus, the properties of the neat polymers are not as relevant as those of the BHJ, and the optical technique of Lindqvist et al. (which relies on the presence of the fullerene) can be applied instead.[20]

4.2.2 Design of Annealing Protocol

The experimental protocol was specifically designed so that it would only require basic equipment readily available to any research group interested in conjugated polymers: a spin coater, a hot plate, a glovebox, and a UV-vis spectrometer. All thermal annealing was carried out inside a glovebox (N_2 atmosphere) to eliminate possible effects of photochemical degradation at elevated temperatures that could occur under ambient conditions. For example, Cho et al. observed a significant degradation in the π–π^* absorption band of PCDTBT when annealed above the T_g in air.[37] Thermal annealing was carried out using a standard hot plate, and heat transfer calculations were performed to account for thermal insulation by the glass slide substrate, as described in detail in **Section D.2** of the **Appendix D**. The UV-vis characterization was performed *ex situ*

because a UV-vis spectrometer with a controlled atmosphere and temperature-controlled stage is not a common piece of equipment. This is not to say that *in situ* measurements are not viable, as Pingel et al. studied the thermal dependence of UV-vis absorption *in situ* for deuterated P3HT.[33] However, no evidence of the glass transition was observed in those experiments because the T_g of P3HT is below room temperature. For our experiments, each film was subjected to a thermal cycling protocol, like the one shown in **Figure 4.2a**. UV-vis spectra of the cooled films under ambient conditions were taken between annealing steps. To analyze the data and extract the T_g, we developed a code to automate and standardize the bilinear regression analysis based on a custom R^2 maximization algorithm (we released this algorithm in an open-sourced format; refer to **Section 3** of the **Supporting Information**).

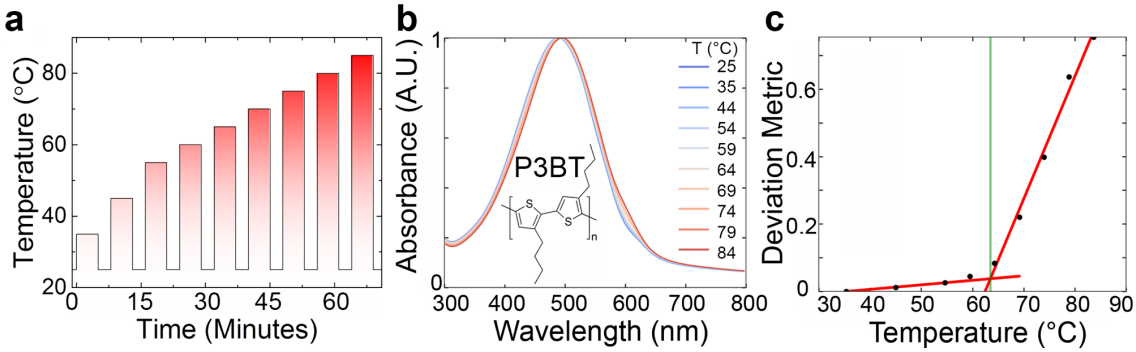

Figure 4.2. Overview of UV-vis absorption T_g measurement technique for P3BT. (a) Thermal history of polymer thin film. Absorption measurements were taken at ambient temperature for the as-cast film and between successive annealing steps. (b) Thin-film absorption spectra for the annealing temperatures indicated. (c) Evolution of the deviation metric as a function of annealing temperature, showing a distinct increase at the T_g of P3BT.

4.3. Results and Discussion

4.3.1 Proof-of-Concept: P3BT

The results of our proposed technique—as applied to P3BT—are shown in **Figure 4.2**. The thermal cycling protocol is given in **Figure 4.2a**. After each annealing step, a UV-vis spectrum was recorded (**Figure 4.2b**). We observed that the spectra exhibited a clear redshift as well as a distinct change in shape around 600 nm with increased annealing temperature. These shifts in the absorption spectra result from the formation of weakly interacting H-aggregates, as explained in the next section. Spectra were processed using the deviation metric, and this quantity was plotted against annealing temperature (**Figure 4.2c**); a clear transition was observed. Using our bilinear curve-fitting algorithm, the T_g was estimated to be 60 ± 3 °C. Encouragingly, this measurement was in excellent quantitative agreement with reported values in the literature, which range from 59 to 67 °C.[38,39]

4.3.2 Weakly interacting H-Aggregate Analysis

To identify the microstructural changes responsible for the evolution of the absorbance spectra upon annealing, we applied the weakly interacting H-aggregate model, developed by Spano and coworkers.[32,40] When two segments of planar thiophene backbones come into co-facial contact, an excitonic coupling produces a redshift in the absorption. This spectral signature is known as an H-aggregate,[41] and the absorption spectra of poly(3-alkylthiophenes) can be comprehensively analyzed using this model.[32] To perform this analysis, a Frank-Condon progression was fit to the UV-vis spectra

(assuming a Gaussian line shape), and the absorption of the aggregated regions was deconvoluted from that of the amorphous phase. A representative fit obtained from this process is shown in **Figure 4.3a**. After correcting for the unequal absorption coefficients of the two domains, the fraction of aggregated polymeric chromophores was determined.

As shown in **Figure 4.3b**, we found that the aggregate fraction increased with annealing temperature and exhibited a transition near the T_g. Interestingly, not only did we observe a change in the slope, but also an increase in the error (based on the standard deviation between independently tested films). It is possible that the increase in the statistical uncertainty is due to minor differences in the cooling rates of separately annealed films. The H-aggregate model can also be used to characterize the quality of structural ordering present in aggregate regions.

The free exciton bandwidth (W) is the dispersion of energy that arises due to interchain coupling in the aggregate domains. This parameter is inversely related to the conjugation length of the interacting chromophoric species.[32,42] As shown in **Figure 4.3c**, the $1/W$ exhibits a sharp transition when the film is annealed above the T_g. This observation is in agreement with previous results of Yazawa et al., who used temperature-dependent Fourier-transform infrared absorption measurements to correlate the glass transition in P3BT with the thermal activation of the dihedral twist between two thiophene rings.[39] We also found that the $1/W$ exhibited a sharper transition than the aggregate fraction.

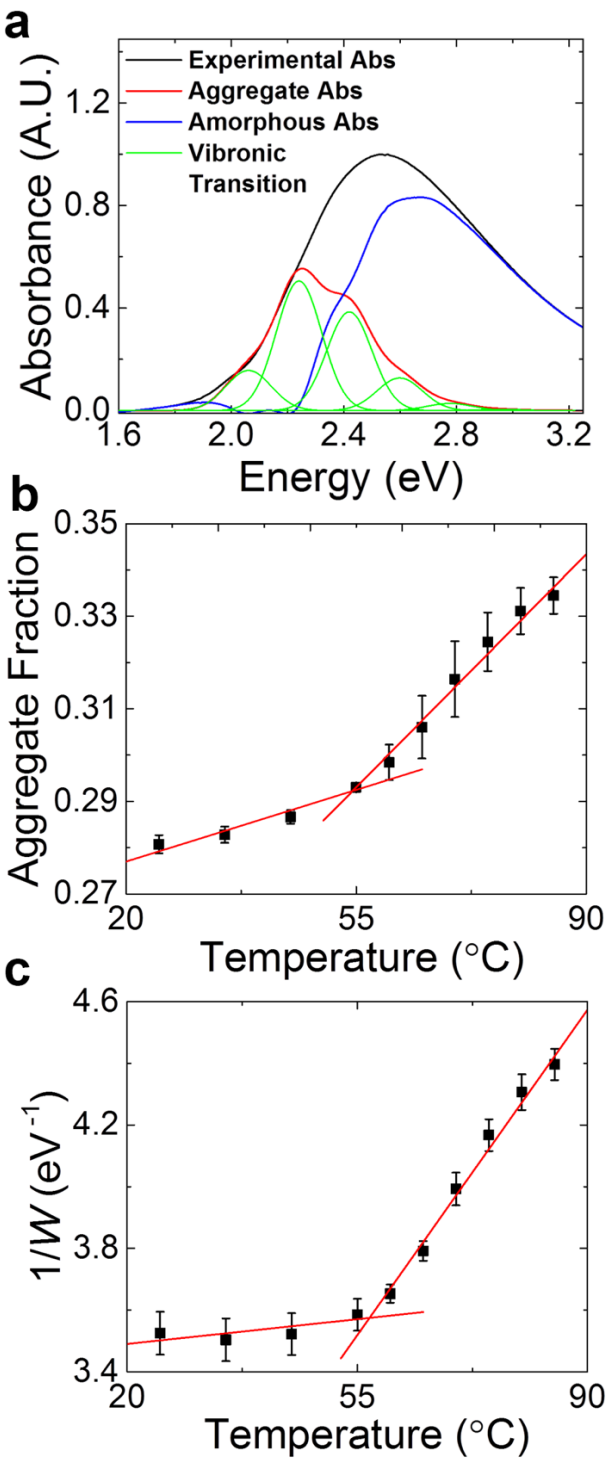

Figure 4.3. Weakly interacting H-aggregate analysis of P3BT. (a) Representative deconstructed absorption spectrum used to calculate (b) the aggregate fraction and (c) the inverse exciton bandwidth, $1/W$.

4.3.3 Bulk Heterojunction Film

Conjugated polymers are typically blended with solubilized fullerene derivatives to form the active layer of BHJ organic photovoltaic devices. The thermal behavior of such composites is important for both optimization of device processing and operational stability.[1] Fullerenes are known to slow the dynamics of conjugated polymers.[43] Due to the strong dispersive forces and spherical geometries, they act as anti-plasticizers and increase the T_g of the composite.[2,44] To demonstrate the applicability of our approach for such composites, we have characterized a BHJ layer composed of P3BT and PCBM. The results of our technique are shown in **Figure 4.4**. As expected, we found that the addition of PCBM served to increase the T_g by about 15 °C. Moreover, we found that the addition of 1,8-diioodoctane, a common processing additive, resulted in a significant decrease in the T_g of the BHJ film (**Appendix D**, **D.4**).

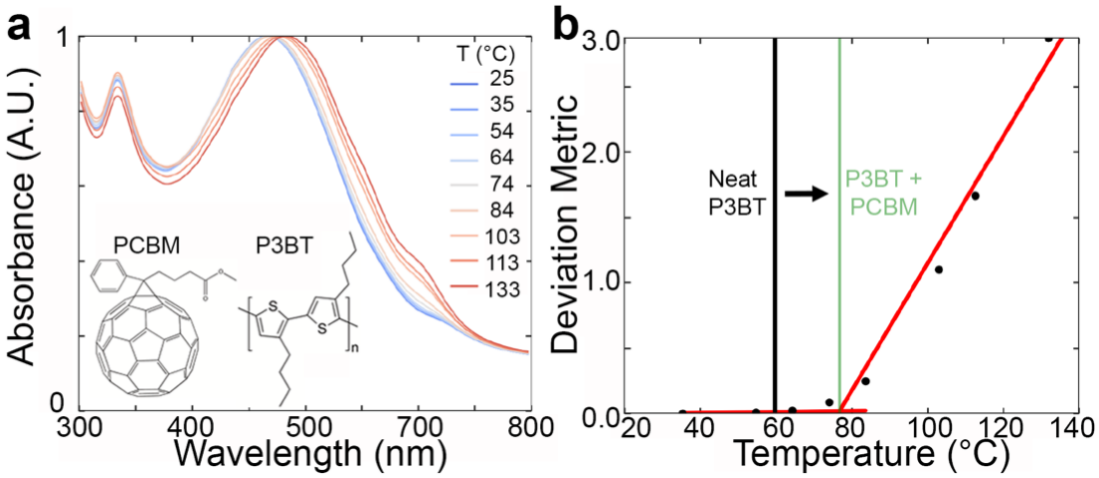

Figure 4.4. Thermal characterization of a BHJ film P3BT:PCBM (0.8:1 by mass). (a) UV-vis absorption spectra for different annealing temperatures. (b) Deviation metric showing a distinct transition at 75 °C. The addition of PCBM resulted in a ≈15 °C shift in the T_g.

4.3.4 PBTTT-C14

The PBTTT family of polymers are known to exhibit a highly-ordered, liquid-crystalline mesophase. As shown in **Figure 4.5a**, our technique revealed a distinct transition occurring at 102 ± 1 °C for PBTTT-C14. Previous DSC measurements have revealed two discrete exotherms upon cooling. These two transitions occur at ≈100 °C and ≈230 °C and have been rigorously assigned to the crystallization of the side chains and the backbone, respectively.[45–47] However, the DSC thermograms reported for PBTTT-C14 revealed no indication of a glass transition. We have rationalized this finding through the argument that the weak signal of the glass transition could be obscured by the endothermic melting of the side chains, as both occur in the same temperature range. This argument is further substantiated by the temperature-dependent UV-vis spectroscopic ellipsometry measurements of DeLongchamp et al., which revealed that the thermochromic behavior of PBTTT-C14 remains approximately constant until heated to ≈120 °C.[46] These results suggest that segmental relaxation of the conjugated backbone can be intrinsically coupled to the dynamics of the side chains, which could lead to convoluted signals in DSC thermograms.

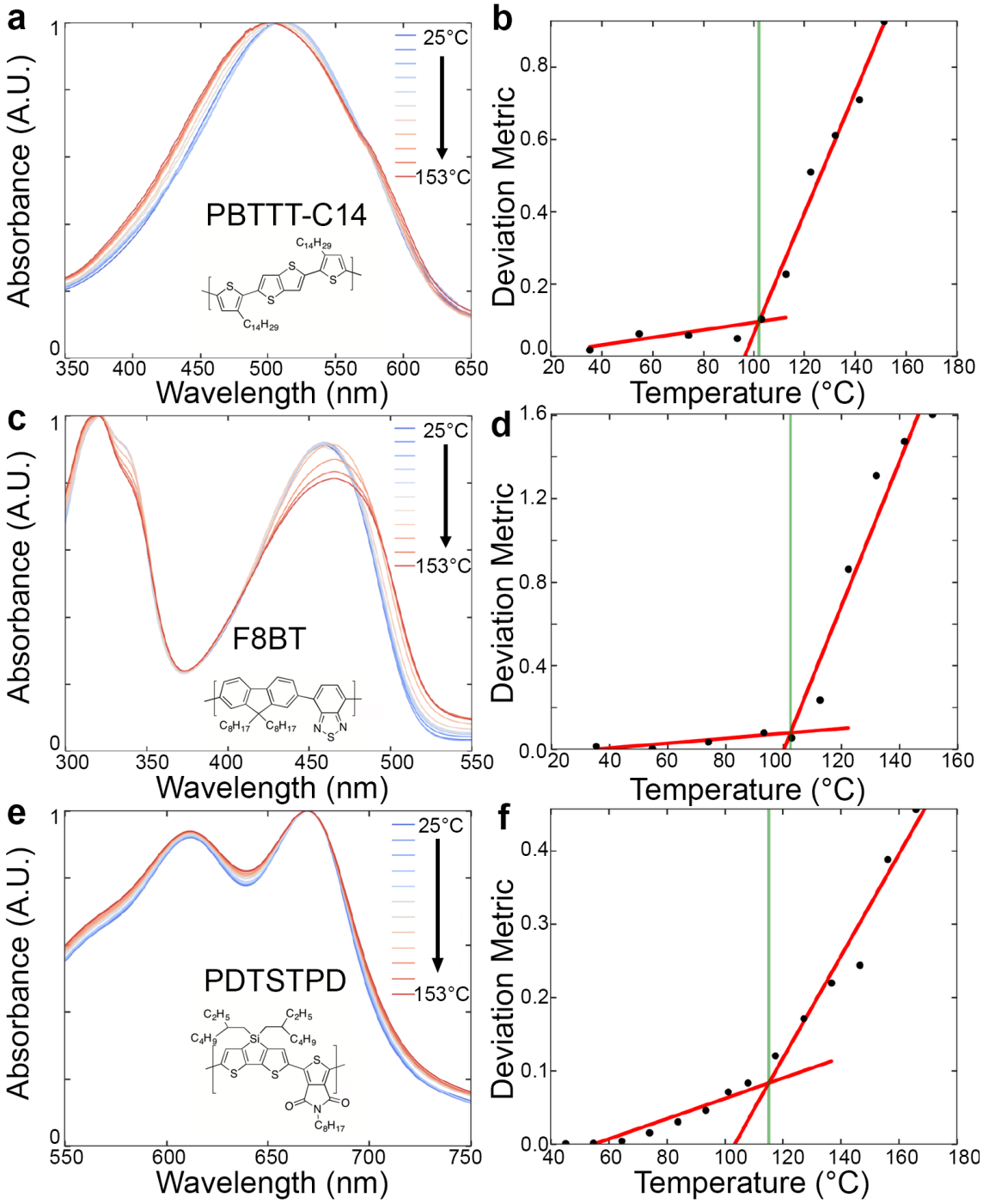

Figure 4.5. Application of technique to representative semiconducting polymers. UV-vis absorption spectra and corresponding deviation metric showing the measurement of the T_g for (a) PBTTT-C14, (b) F8BT, and (c) PDTSTPD.

4.3.5 F8BT

The polyfluorene copolymer, F8BT, has been of particular interest for photovoltaic applications due to its ability to act as the electron acceptor in BHJ devices.[48] As shown in **Figure 4.5b** our technique revealed a pronounced transition at 104 ± 6 °C. F8BT has been previously characterized with both DSC and VTE. DSC measurements revealed an exothermic feature at 125 °C, which Sirringhaus and coworkers assigned to the glass transition; an additional, more pronounced exothermic transition at 240 °C has been assigned to the crystallization temperature.[49] The authors argued that cold crystallization might also be occurring at the T_g as the chains become mobile. Additionally, VTE experiments revealed a sharp transition in the ellipsometric angle at ≈100 °C.[50] The slight negative deviation in our measurement from the DSC measurements was likely due to thin-film effects, since the measurement agreed with the transition in the ellipsometric angle obtained with thin films using VTE.

4.3.6 PDTSTPD

The donor-acceptor polymer PDTSTPD is a commercially available conjugated polymer that exhibits a high photovoltaic conversion efficiency when blended with fullerenes and incorporated into a BHJ device.[34,35,51] The T_g has been reported to be 109 °C based on DSC measurements.[34] In close agreement with these results, we have measured the T_g to be 106 ± 12 °C (**Figure 4.5c**). We note that the transition was not quite as pronounced as it was for the other polymers tested, leading to substantially more uncertainty in the measured value. We ascribed this finding to two factors: a small overall change in the absorption spectrum with annealing, and the occurrence of morphological

rearrangement during sub-T_g annealing of this material.[52] When the best fits are not entirely obvious, the fitting algorithm described in **Section D.3** of the **Appendix D** is especially important for the accurate determination of the T_g.

Molecular dynamics simulations have previously predicted a value of 107 ± 10 °C for the T_g of PDTSTPD.[53] This prediction was achieved by subjecting an initially melted polymeric simulation to a thermal quenching protocol at constant pressure. The density was monitored as a function of temperature, and the glass transition was taken as the intersection of linear fits to the melted and glassy regions. The thermal history in our proposed measurement technique is fundamentally different: an initially kinetically trapped morphology is gradually heated until polymeric motion becomes activated and chain segments can relax to a state closer to thermodynamic equilibrium. To obtain an improved understanding of this process, we performed additional simulations that provide a closer representation of the experimental protocol.

First, we generated a simulated morphology to represent an as-cast film that was kinetically trapped at room temperature. The procedure for simulating solution casting was guided by solution-phase UV-vis absorption measurements and previous work.[54] As shown in **Figure 4.6a**, the UV-vis absorption spectra of a dilute solution (0.015 mg mL^{-1}, chloroform) and an as-cast thin film of PDTSTPD both contain aggregate absorption peaks. Fauvell et al. recently demonstrated that this low-energy visible absorption is due to self-aggregation-induced ordering (rather than in-chain charge transfer, as previously thought).[54] Thus, to generate the as-cast morphology, self-aggregated chains were randomly packed at low concentration and allowed to condense at room temperature and atmospheric pressure until the density stabilized (**Figure 4.6b**). A detailed description of

this process and the results of such simulations can be found in an earlier publication.[36] It has been previously demonstrated that simulation morphologies generated in this manner give a closer match to the experimentally determined tensile modulus of an as-cast film.

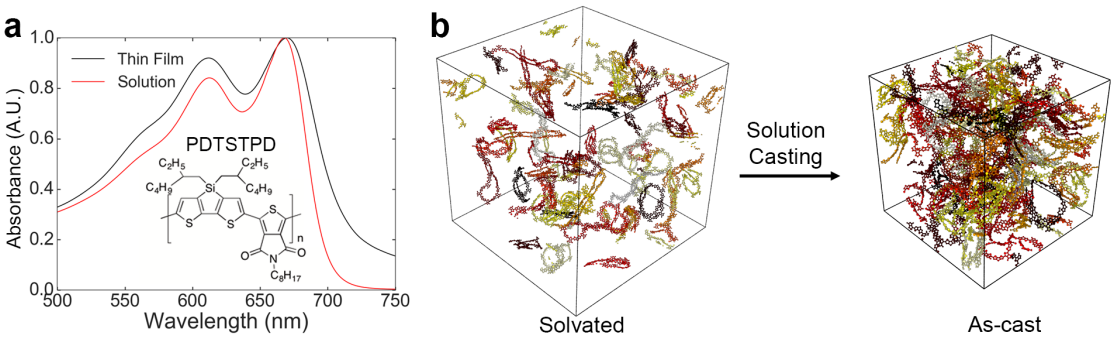

Figure 4.6. Simulated solution casting: experimental justification and MD snapshots. (a) Comparison between thin-film and solution-phase absorption spectra showing aggregate behavior in a dilute solution. (b) Snapshots showing the trajectory of the simulated solution casting; individual molecules are colored separately, and side chains are not shown.

The morphology generated by solution casting was far from thermodynamic equilibrium and contained significant void space and disorder, as shown in **Figure 7** (**1**). The system was subjected to a heating protocol in which temperature was gradually increased while density was monitored. We observed that the density decreased slightly until approximately 110 °C (**2**). We attributed this initial thermal expansion to increased vibrations of the amorphous glass about metastable equilibrium positions. Above 110 °C there was a clear transition; the density started to increase with temperature. This behavior was evidently the result of chain segments escaping from metastable packing conformations and approaching an equilibrium state with better intermolecular packing. The density continued to increase with temperature until about 250 °C (**3**) where it peaked, and the thermal expansion due to molecular vibrations dominated. Finally, at approximately 330 °C (**4**), an equilibrium melt was achieved, corresponding to the

melting temperature measured using DSC for a structural analog of the simulated polymer containing a branched side chain on the thienopyrrolodione (TPD) moiety.[51] When the melted system was subsequently quenched to room temperature (**5**), the density increased to a value substantially greater than that of the initial morphology.

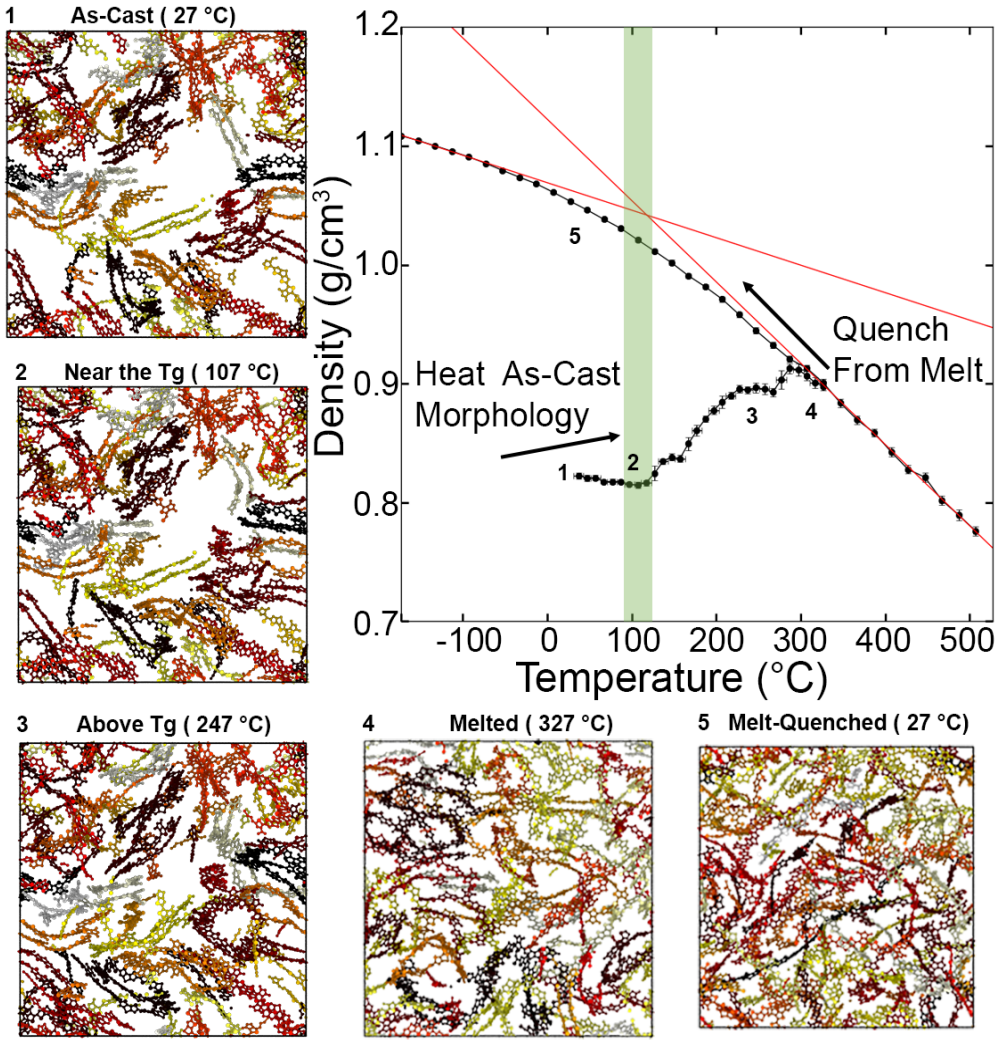

Figure 4.7. MD simulations showing the thermally activated molecular and microstructural rearrangements of an as-cast morphology of PDTSTPD subjected to thermal annealing. Plot of density against temperature showing that the onset of structural rearrangement occurred at approximately 107 °C. Images depicting 2 nm slices of simulation morphologies; individual molecules are colored separately, and side chains are not shown.

4.4 Conclusion

The glass transition temperature is of paramount importance in determining the mechanical properties and thermal reliability of organic electronic devices. However, this property is not easy to measure using conventional techniques and often goes unreported. Facile techniques with broad applicability and which use simple equipment are necessary. This paper described a new method to determine the glass transition temperature of thin films of semicrystalline conjugated polymers. The technique uses quantitative analysis of the UV-vis absorption spectra of polymer films subjected to thermal annealing, and requires only commonplace equipment. We tested the robustness of the technique through comparison with the literature for various well-characterized conjugated polymers and a BHJ composite (**Figure 4.8**). It is important to note that this technique works best for materials with a strong tendency to form ordered photophysical aggregates upon thermal annealing. For P3BT, an H-aggregate analysis of the absorption spectra revealed that the observed transition was dominated by an increase in the average conjugation length due to thermal relaxation of kinetically trapped dihedral states. MD simulations demonstrated in atomistic detail how a kinetically trapped morphology might rearrange due to the annealing of a solution-cast thin film. This technique should be of interest to organic materials chemists aiming to characterize the thermal properties of newly synthesized polymeric semiconductors and identify structure-property relationships required for molecular design.

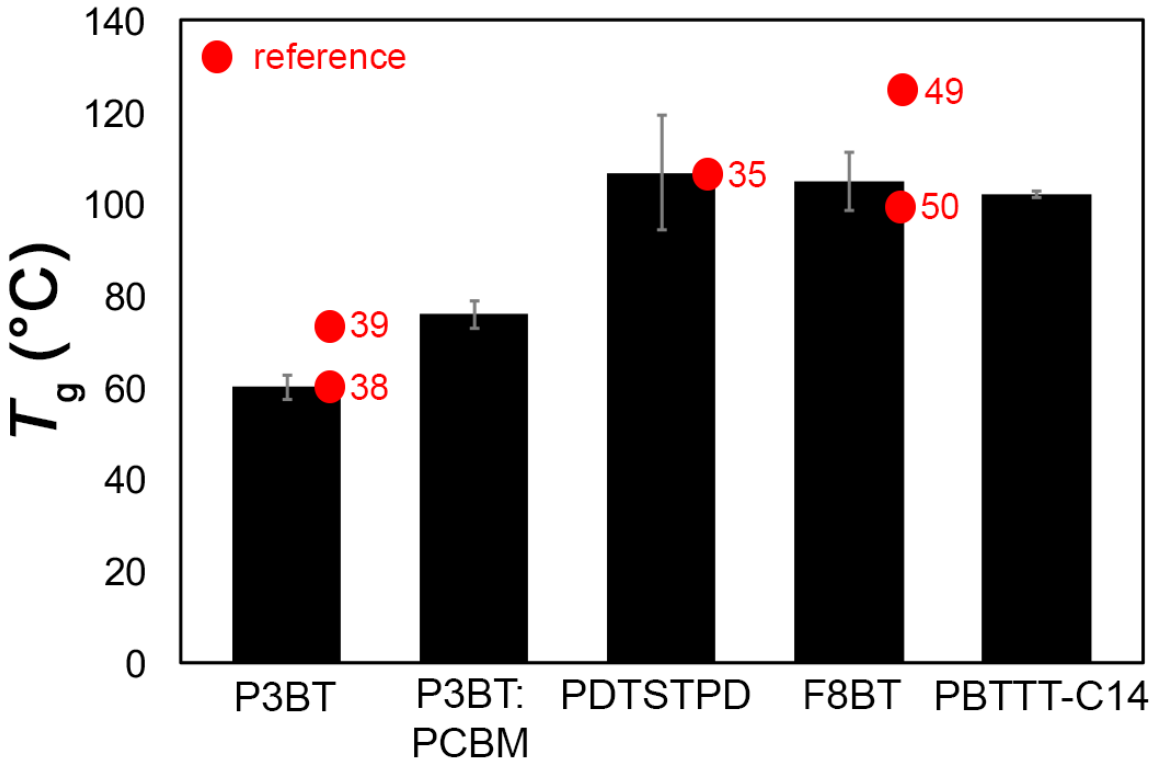

Figure 4.8. Summary of T_g measurements along with comparisons to the results of conventional techniques from the literature. Error bars are based on standard deviations between at least three separate films.

4.5 Experimental Methods

4.5.1 Materials

Poly(3-butylthiophene) (P3BT, M_n = 50−70 kDa, PDI = 2.1−3.0) was purchased from Rieke metals and used as received. Poly[2,5-bis(3-tetradecylthiophen-2-yl)thieno[3,2-b]thiophene] (PBTTT-C14, M_n > 12 kDa, PDI = 1.8), poly(9,9-dioctylfluorene-*alt*-benzothiadiazole) (F8BT, M_n = 20−100 kDa), and poly[*N*-9′-heptadecanyl-2,7-carbazole-*alt*-5,5-(4′,7′-di-2-thienyl-2′,1′,3′-benzothiadiazole)] (PCDTBT, M_n = 20−100 kDa) were purchased from Lumtec and were used as received. Poly[(5,6-dihydro-5-octyl-4,6-dioxo-4*H*-thieno[3,4-*c*]pyrrole -1,3-diyl)[4,4-bis(2-ethylhexyl)-4*H*-silolo[3,2-*b*:4,5-

b′;]dithiophene-2,6-diyl]] (PDTSTPD, M_n = 7−35 kDa, PDI = 1.4−2.9), poly({4,8-bis[(2-ethylhexyl)oxy]benzo[1,2-*b*:4,5-b′]dithiophene-2,6-diyl}{3-fluoro-2-[(2-ethylhexyl)carbonyl]thieno[3,4-*q*]thiophenediyl}) (PTB7, M_n = 80−200 kDa, PDI < 3.0), poly[[2,3-bis(3-octyloxyphenyl)-5,8-quinoxalinediyl]-2,5-thiophenediyl] (TQ1, M_n = 12−45 kDa, PDI < 3.3), poly[2-methoxy-5-(2-ethylhexyloxy)-1,4-phenylenevinylene] (MEH-PPV, M_n = 40−70 kDa, PDI ≈ 6), 1-[3-(Methoxycarbonyl)propyl]-1-phenyl-[6.6]C_{61}, 3'*H*-Cyclopropa[1,9] [5,6]fullerene-C60-I*h*-3′-butanoic acid 3′-phenyl methyl ester (PCBM), and 1,8-diiodooctane (DIO) were purchased from Sigma-Aldrich and used as received. Chloroform, acetone, and isopropyl alcohol (IPA) were obtained from Sigma-Aldrich and were used as received. Alconox was obtained from Alconox, Inc. and was used as received.

4.5.2 Preparation of Substrates

Glass slides, cut into squares (1 in × 1 in) with a diamond-tipped scribe, were used as substrates for the polymer thin films. The slides were thoroughly cleaned in an ultrasonic bath in the following sequence of 10-min steps: powdered Alconox detergent dissolved in deionized (DI) water, DI water only, acetone, and then IPA. After that, the slides were dried with compressed (house) air and then treated with plasma (30 W) for five minutes at a base pressure of 200 mTorr of air to remove residual organic debris and improve surface wettability.

4.5.3 Preparation of Films

Solutions of P3BT, P3BT:PCBM (0.8:1 by mass), PBTTT-C14, PDTSTPD, and F8BT in chloroform (10 mg mL^{-1}) were prepared and allowed to stir overnight. Prior to use, all solutions were slightly heated (~15 s) with a heat gun to promote dissolution of the polymer. Next, the solutions were filtered with 0.20 μm PTFE filters, immediately after which they were spin-coated (Headway Research PWM32) onto the cleaned glass substrates at 2000 rpm (ramping at 1000 rpm s^{-1}) for 120 seconds. These conditions produced films of thicknesses ranging from 80 to 100 nm as determined by profilometry (Dektak® 150 Surface Profiler). All films were dried under dynamic vacuum in the antechamber of a nitrogen-atmosphere glovebox (MBRAUN) for exactly 60 min to remove any residual chloroform.

4.5.4 Spectroscopic Characterization and Analysis

Once the freshly prepared thin films had dried under dynamic vacuum for an hour, their as-cast (UV-vis) spectra were acquired using an Agilent 8453 UV-vis spectrometer; the range of wavelengths measured was from 300 to 750 nm with a sampling increment of 1 nm (a pristine glass slide was used as a baseline for the absorption). The glass-supported films were then immediately heated for 5 minutes on the surface of a hot plate in a nitrogen-atmosphere glovebox, after which they were suspended in air and allowed to cool to room temperature (T_R, ~25 °C) for 3 min prior to acquiring their 'annealed' spectra. Starting at T_R, each film was annealed in various increments of temperature (5 °C, 10 °C, or 20 °C) depending on how far its nominal T_g was from T_R. The measurements were concluded once the annealing temperature sufficiently surpassed the nominal T_g of the polymer under investigation (i.e., 20−30 °C

past T_g). To correlate trends in aggregation and aggregate quality with annealing temperature, we have used the following model for H-aggregate absorption:

$$A \propto \sum_{m=0} \left(\frac{S^m}{m!}\right)\left(1 - \frac{We^{-S}}{2E_p}\sum_{n\neq \mathrm{m}} \frac{S^n}{n!\,(n-m)}\right)^2 \exp\left(\frac{\left(E - E_0 - mE_p - \frac{1}{2}WS^m e^{-S}\right)^2}{2\sigma^2}\right) \quad (2)$$

where A is the absorption by an aggregate as a function of the photon energy E, W is the free exciton bandwidth, E_0 is the energy of the $0 \rightarrow 0$ vibronic transition, S is the Huang-Rhys factor (set to 1 for P3ATs), and E_p is the intermolecular vibration energy, which (in the case where $S = 1$) is the difference in energy between the vibrational levels in the excited state (set to 0.179 eV as determined by Raman spectroscopy). The terms m and n are the ground- and excited-state vibrational levels and σ is the Gaussian linewidth.[32] The fitting parameters E_0, W, σ, and a scaling factor were found using MATLAB® to perform a least squares fit to the experimental absorption spectrum in the region of 1.93 to 2.25 eV.

4.5.5 Molecular Dynamics Simulations

All simulations and visualizations were performed with LAMMPS[55] and OVITO,[56] respectively. A detailed description of the atomistic model parametrization from electronic structure calculations as well as the simulation process for generating the as-cast morphology can be found elsewhere.[36,57] Briefly, 60 independent and isolated 12-mers were subjected to a simulated annealing process using Langevin dynamics (800 K to 300 K over the course of 5 ns, NVT ensemble) in order to generate self-aggregated chain structures. These self-aggregated structures were randomly packed into a low-density simulation box (0.01 g cm^{-3}) and were subjected to NPT dynamics at 300 K and 1

atm using a Nosé-Hoover style thermostat (time constant = 100.0 fs) and barostat (time constant = 1000.0 fs) until the density converged (5 ns). Finally, the as-cast morphology was subjected to a thermal annealing protocol consisting of alternating runs between ramping the temperature (20 K ns^{-1}) and equilibrating (1 ns), while outputting the simulation trajectory and thermodynamic parameters.

4.6 Acknowledgements

This work was supported by the Air Force Office of Scientific Research (AFOSR) Grant Number FA9550-16-1-0220. Additional support was provided by the Hellman Fellowship awarded to D. J. L. and the Achievement Reward for College Scientists (ARCS) Fellowship awarded to S. E. R. Computational resources to support this work were provided by the Extreme Science and Engineering Discovery Environment (XSEDE) Program through the National Science Foundation grant number ACI-1053575.[58] Additionally, we would like to thank Professor Andrea Tao for use of the UV-vis spectrometer.

Chapter 4, in full, is a reprint of the material as it appears in *Chemistry of Materials*, 2017, 28, 2646-2654. The American Chemical Society, 2017. Samuel E. Root,‡ Mohammad A. Alkhadra,‡ Daniel Rodriquez, Adam D. Printz, and Darren J. Lipomi (‡ Equal contribution). The dissertation author was a primary investigator and author of this paper.

4.7 References

(1) Müller, C. On the Glass Transition of Polymer Semiconductors and Its Impact on Polymer Solar Cell Stability. *Chem. Mater.* **2015**, *27*, 2740–2754.

(2) Savagatrup, S.; Printz, A. D.; O'Connor, T. F.; Zaretski, A. V.; Rodriquez, D.; Sawyer, E. J.; Rajan, K. M.; Acosta, R. I.; Root, S. E.; Lipomi, D. J. Mechanical Degradation and Stability of Organic Solar Cells: Molecular and Microstructural Determinants. *Energy Environ. Sci.* **2015**, *8*, 55–80.

(3) Mateker, W. R.; Mcgehee, M. D. Progress in Understanding Degradation Mechanisms and Improving Stability in Organic Photovoltaics. *Adv. Mater.* **2017**, 14–16.

(4) Strobl, G. The Physics of Polymers：Concepts for Understanding Their Structures and Behavior, 1997.

(5) Bennemann, C.; Donati, C.; Baschnagel, J.; Glotzer, S. C. Growing Range of Correlated Motion in a Polymer Melt on Cooling towards the Glass Transition. *Nature* **1999**, *399*, 246–249.

(6) Williams, M. L.; Landel, R. F.; Ferry, J. D. The Temperature Dependence of Relaxation Mechanisms in Amorphous Polymers and Other Glass-Forming Liquids. *J. Am. Chem. Soc.* **1955**, *77*, 3701–3707.

(7) O 'connor, T. F.; Rajan, K. M.; Printz, A. D.; Lipomi, D. J. Toward Organic Electronics with Properties Inspired by Biological Tissue. *J. Mater. Chem. B* **2015**, *3*, 4947–4952.

(8) Printz, A. D.; Lipomi, D. J. Competition between Deformability and Charge Transport in Semiconducting Polymers for Flexible and Stretchable Electronics. *Appl. Phys. Rev.* **2016**, *3*, 21302.

(9) Turi, E. *Thermal Characterization of Polymeric Materials*; Elsevier, 2012.

(10) Müller, C.; Andersson, L. M.; Garriga, M.; Campoy-quiles, M. Determination of Thermal Transition Depth Profiles in Polymer Semiconductor Films with Ellipsometry. *Macromolecules* **2013**, *46*, 7325–7331.

(11) Schwartz, B. J. Conjugated Polymers as Molecular Materials: How Chain Conformation and Film Morphology Influence Energy Transfer and Interchain Interactions. *Annu. Rev. Phys. Chem.* **2003**, *54*, 141–172.

(12) Nikolka, M.; Nasrallah, I.; Rose, B.; Ravva, M. K.; Broch, K.; Harkin, D.; Charmet, J.; Hurhangee, M.; Brown, A.; Illig, S.; *et al.* High Operational and Environmental Stability of High-Mobility Conjugated Polymer Field-Effect

Transistors through the Use of Molecular Additives. *Nat. Mater.* **2016**, 1–8.

(13) Noriega, R.; Rivnay, J.; Vandewal, K.; Koch, F. P. V; Stingelin, N.; Smith, P.; Toney, M. F.; Salleo, A. A General Relationship between Disorder, Aggregation and Charge Transport in Conjugated Polymers. *Nat. Mater.* **2013**, *12*, 1038–1044.

(14) Holliday, S.; Donaghey, J. E.; McCulloch, I. Advances in Charge Carrier Mobilities of Semiconducting Polymers Used in Organic Transistors. *Chem. Mater.* **2014**, *26*, 647–663.

(15) Schroeder, B. C.; Chiu, Y.-C.; Gu, X.; Zhou, Y.; Xu, J.; Lopez, J.; Lu, C.; Toney, M. F.; Bao, Z. Non-Conjugated Flexible Linkers in Semiconducting Polymers: A Pathway to Improved Processability without Compromising Device Performance. *Adv. Electron. Mater.* **2016**, *2*, 1–10.

(16) Danley, R. L.; Reader, J. R.; Schaefer, J. W. Differential Scanning Calorimeter, 1998.

(17) Rotter, G.; Ishida, H. Dynamic Mechanical Analysis of the Glass Transition: Curve Resolving Applied to Polymers. *Macromolecules* **1992**, *25*, 2170–2176.

(18) Kremer, F.; Andreas, S. *Broadband Dielectric Spectroscopy*; Springer, 2003.

(19) Beaucage, G.; Composto, R.; Stein, R. S. Ellipsometric Study of the Glass Transition and Thermal Expansion Coefficients of Thin Polymer Films. *J. Polym. Sci. Part B Polym. Phys.* **1993**, *31*, 319–326.

(20) Lindqvist, C.; Wang, E.; Andersson, M. R.; Müller, C. Facile Monitoring of Fullerene Crystallization in Polymer Solar Cell Blends by UV-Vis Spectroscopy. *Macromol. Chem. Phys.* **2014**, *215*, 530–535.

(21) Tessarolo, M.; Guerrero, A.; Gedefaw, D.; Bolognesi, M.; Prosa, M.; Xu, X.; Mansour, M.; Wang, E.; Seri, M.; Andersson, M. R.; *et al.* Predicting Thermal Stability of Organic Solar Cells through an Easy and Fast Capacitance Measurement. *Sol. Energy Mater. Sol. Cells* **2015**, *141*, 240–247.

(22) Sung, M. J.; Luzio, A.; Park, W.-T.; Kim, R.; Gann, E.; Maddalena, F.; Pace, G.; Xu, Y.; Natali, D.; de Falco, C.; *et al.* High-Mobility Naphthalene Diimide and Selenophene-Vinylene-Selenophene-Based Conjugated Polymer: N-Channel Organic Field-Effect Transistors and Structure-Property Relationship. *Adv. Funct. Mater.* **2016**.

(23) Lan, L.; Chen, Z.; Ying, L.; Huang, F.; Cao, Y. Acenaphtho[1,2-B]quinoxaline Diimides Derivative as a Potential Small Molecule Non-Fullerene Acceptor for Organic Solar Cells. *Org. Electron.* **2016**, *30*, 176–181.

(24) Patel, S. N.; Su, G. M.; Luo, C.; Wang, M.; Perez, L. A.; Fischer, D. A.;

Prendergast, D.; Bazan, G. C.; Heeger, A. J.; Chabinyc, M. L.; *et al.* NEXAFS Spectroscopy Reveals the Molecular Orientation in Blade-Coated Pyridal[2,1,3]thiadiazole-Containing Conjugated Polymer Thin Films. *Macromolecules* **2015**, *48*, 6606–6616.

(25) Hufnagel, M.; Thelakkat, M. Simultaneous Morphological Stability and High Charge Carrier Mobilities in Donor–Acceptor Block Copolymer/PCBM Blends. *J. Polym. Sci., Part B Polym. Phys* **2016**, *54*, 1125–1136.

(26) Cho, E. C.; Chang-Jian, C. W.; Hsiao, Y. S.; Lee, K. C.; Huang, J. H. Influence of the Bridging Atom on the Electrochromic Performance of a Cyclopentadithiophene Polymer. *Sol. Energy Mater. Sol. Cells* **2016**, *150*, 43–50.

(27) Huth, H.; Minakov, A. A.; Serghei, A.; Kremer, F.; Schick, C. Differential AC-Chip Calorimeter for Glass Transition Measurements in Ultra Thin Polymeric Films. *Eur. Phys. J. Spec. Top.* **2007**, *141*, 153–160.

(28) Keddie, J. L.; Jones, R. A. L.; Cory, R. A. Size-Dependent Depression of the Glass Transition Temperature in Polymer Films. *Epl* **1994**, *27*, 59–64.

(29) Printz, A. D.; Zaretski, A. V.; Savagatrup, S.; Chiang, A. S.-C.; Lipomi, D. J. Yield Point of Semiconducting Polymer Films on Stretchable Substrates Determined by Onset of Buckling. *ACS Appl. Mater. Interfaces* **2015**, *7*, 23257–23264.

(30) Printz, A. D.; Chiang, A. S. C.; Savagatrup, S.; Lipomi, D. J. Fatigue in Organic Semiconductors: Spectroscopic Evolution of Microstructure due to Cyclic Loading in poly(3-Heptylthiophene). *Synth. Met.* **2016**, *217*, 144–151.

(31) Kim, D. H.; Lee, B. L.; Moon, H.; Kang, H. M.; Jeong, E. J.; Park, J. Il; Han, K. M.; Lee, S.; Yoo, B. W.; Koo, B. W.; *et al.* Liquid-Crystalline Semiconducting Copolymers with Intramolecular Donor-Acceptor Building Blocks for High-Stability Polymer Transistors. *J. Am. Chem. Soc.* **2009**, *131*, 6124–6132.

(32) Clark, J.; Chang, J. F.; Spano, F. C.; Friend, R. H.; Silva, C. Determining Exciton Bandwidth and Film Microstructure in Polythiophene Films Using Linear Absorption Spectroscopy. *Appl. Phys. Lett.* **2009**, *94*, 1–9.

(33) Pingel, P.; Zen, A.; Abellón, R. D.; Grozema, F. C.; Siebbeles, L. D. A.; Neher, D. Temperature-Resolved Local and Macroscopic Charge Carrier Transport in Thin P3HT Layers. *Adv. Funct. Mater.* **2010**, *20*, 2286–2295.

(34) Chu, T. Y.; Lu, J.; Beaupré, S.; Zhang, Y.; Pouliot, J. R.; Zhou, J.; Najari, A.; Leclerc, M.; Tao, Y. Effects of the Molecular Weight and the Side-Chain Length on the Photovoltaic Performance of Dithienosilole/thienopyrrolodione Copolymers. *Adv. Funct. Mater.* **2012**, *22*, 2345–2351.

(35) Chu, T.-Y.; Lu, J.; Beaupre, S.; Zhang, Y.; Pouliot, J.-R.; Wakim, S.; Zhou, J.; Leclerc, M.; Li, Z.; Ding, J.; *et al.* Bulk Heterojunction Solar Cells Using Thieno[3,4-C]pyrrole-4,6-Dione and Dithieno[3,2-b:2',3'-d]silole Copolymer with a Power Conversion Efficiency of 7.3%. *J. Am. Chem. Soc.* **2011**, *133*, 4250–4253.

(36) Root, S. E.; Jackson, N.; Savagatrup, S.; Arya, G.; Lipomi, D. J. Modelling the Morphology and Thermomechanical Behaviour of Low-Bandgap Conjugated Polymers and Bulk Heterojunction Films. *Energy Environ. Sci.* **2016**, *10*, 558–569.

(37) Cho, S.; Seo, J. H.; Park, S. H.; Beaupré, S.; Leclerc, M.; Heeger, A. J. A Thermally Stable Semiconducting Polymer. *Adv. Mater.* **2010**, *22*, 1253–1257.

(38) Chen, S.; Ni, J. Structure/properties of Conjugated Conductive Polymers. 1. Neutral Poly (3-Alkythiophene) S. *Macromolecules* **1992**, *25*, 6081–6089.

(39) Yazawa, K.; Inoue, Y.; Yamamoto, T.; Asakawa, N. Twist Glass Transition in Regioregulated poly(3-Alkylthiophene). *Phys. Rev. B - Condens. Matter Mater. Phys.* **2006**, *74*, 1–13.

(40) Spano, F. C. Modeling Disorder in Polymer Aggregates: The Optical Spectroscopy of Regioregular poly(3-Hexylthiophene) Thin Films. *J. Chem. Phys.* **2005**, *122*, 1–15.

(41) Spano, F. C. The Spectral Signatures of Frenkel Polarons in H- And J-Aggregates. *Acc. Chem. Res.* **2010**, *43*, 429–439.

(42) Awartani, O.; Lemanski, B. I.; Ro, H. W.; Richter, L. J.; De Longchamp, D. M.; O'Connor, B. T. Correlating Stiffness, Ductility, and Morphology of polymer:Fullerene Films for Solar Cell Applications. *Adv. Energy Mater.* **2013**, *3*, 399–406.

(43) Guilbert, A. A. Y.; Zbiri, M.; Jenart, M. V. C.; Nielsen, C. B.; Nelson, J. New Insights into the Molecular Dynamics of P3HT:PCBM Bulk Heterojunction: A Time-of-Flight Quasi-Elastic Neutron Scattering Study. *J. Phys. Chem. Lett.* **2016**, *7*, 2252–2257.

(44) Root, S. E.; Savagatrup, S.; Pais, C. J.; Arya, G.; Lipomi, D. J. Predicting the Mechanical Properties of Organic Semiconductors Using Coarse-Grained Molecular Dynamics Simulations. *Macromolecules* **2016**, *49*, 2886–2894.

(45) McCulloch, I.; Heeney, M.; Bailey, C.; Genevicius, K.; Macdonald, I.; Shkunov, M.; Sparrowe, D.; Tierney, S.; Wagner, R.; Zhang, W.; *et al.* Liquid-Crystalline Semiconducting Polymers with High Charge-Carrier Mobility. *Nat. Mater.* **2006**, *5*, 328–333.

(46) Delongchamp, D. M.; Kline, R. J.; Jung, Y.; Lin, E. K.; Fischer, D. A.; Gundlach, D. J.; Cotts, S. K.; Moad, A. J.; Richter, L. J.; Toney, M. F.; *et al.* Molecular Basis

of Mesophase Ordering in a Thiophene-Based Copolymer. *Macromolecules* **2008**, *41*, 5709–5715.

(47) Miller, N. C.; Gysel, R.; Miller, C. E.; Verploegen, E.; Beiley, Z.; Heeney, M.; McCulloch, I.; Bao, Z.; Toney, M. F.; McGehee, M. D. The Phase Behavior of a Polymer-Fullerene Bulk Heterojunction System That Contains Bimolecular Crystals. *J. Polym. Sci. Part B Polym. Phys.* **2011**, *49*.

(48) Kim, Y.; Cook, S.; Choulis, S. a.; Nelson, J.; Durrant, J. R.; Bradley, D. D. C. Organic Photovoltaic Devices Based on Blends of Regioregular Poly(3-Hexylthiophene) and Poly(9,9-Dioctylfluorene- Co -Benzothiadiazole). *Chem. Mater.* **2004**, *16*, 4812–4818.

(49) Banach, M. J.; Friend, R. H.; Sirringhaus, H. Influence of the Molecular Weight on the Thermotropic Alignment of Thin Liquid Crystalline Polyfluorene Copolymer Films. *Macromolecules* **2003**, *36*, 2838–2844.

(50) Campoy-Quiles, M.; Sims, M.; Etchegoin, P. G.; Bradley, D. D. C. Thickness-Dependent Thermal Transition Temperatures in Thin Conjugated Polymer Films. *Macromolecules* **2006**, *39*, 7673–7680.

(51) Yuan, M. C.; Chou, Y. J.; Chen, C. M.; Hsu, C. L.; Wei, K. H. A Crystalline Low-Bandgap Polymer Comprising Dithienosilole and thieno[3,4-C]pyrrole-4,6-Dione Units for Bulk Heterojunction Solar Cells. *Polymer (Guildf).* **2011**, *52*, 2792–2798.

(52) Bergqvist, J.; Lindqvist, C.; Bäcke, O.; Ma, Z.; Tang, Z.; Tress, W.; Gustafsson, S.; Wang, E.; Olsson, E.; Andersson, M. R.; *et al.* Sub-Glass Transition Annealing Enhances Polymer Solar Cell Performance. *J. Mater. Chem. A* **2014**, *2*, 6146–6152.

(53) Root, S. E.; Jackson, N.; Savagatrup, S.; Arya, G.; Lipomi, D. J. Modelling the Morphology and Thermomechanical Behaviour of Low-Bandgap Conjugated Polymers and Bulk Heterojunction Films. *Energy Environ. Sci.* **2017**, *10*, 558–569.

(54) Fauvell, T. J.; Zheng, T.; Jackson, N. E.; Ratner, M. A.; Yu, L.; Chen, L. X. The Photophysical and Morphological Implications of Single-Strand Conjugated Polymer Folding in Solution. *Chem. Mater.* **2016**, acs.chemmater.6b00734.

(55) Plimpton, S. Fast Parallel Algorithms for Short-Range Molecular Dynamics. *J. Comput. Phys.* **1995**, *117*, 1–19.

(56) Stukowski, A. Visualization and Analysis of Atomistic Simulation Data with OVITO–the Open Visualization Tool. *Model. Simul. Mater. Sci. Eng.* **2010**, *18*, 1–7.

(57) Jackson, N. E.; Kohlstedt, K. L.; Savoie, B. M.; Olvera de la Cruz, M.; Schatz, G. C.; Chen, L. X.; Ratner, M. a. Conformational Order in Aggregates of Conjugated

Polymers. *J. Am. Chem. Soc.* **2015**, *137*, 6254–6262.

(58) John, T.; Cockerill, T.; Foster, I.; Gaither, K. XSEDE: Accelerating Scientific Discovery. *Comput. Sci. Eng.* **2014**, *16*, 62–74.

Chapter 5

Fracture Mechanics of Brittle and Ductile Thin Films of Semiconducting Polymers

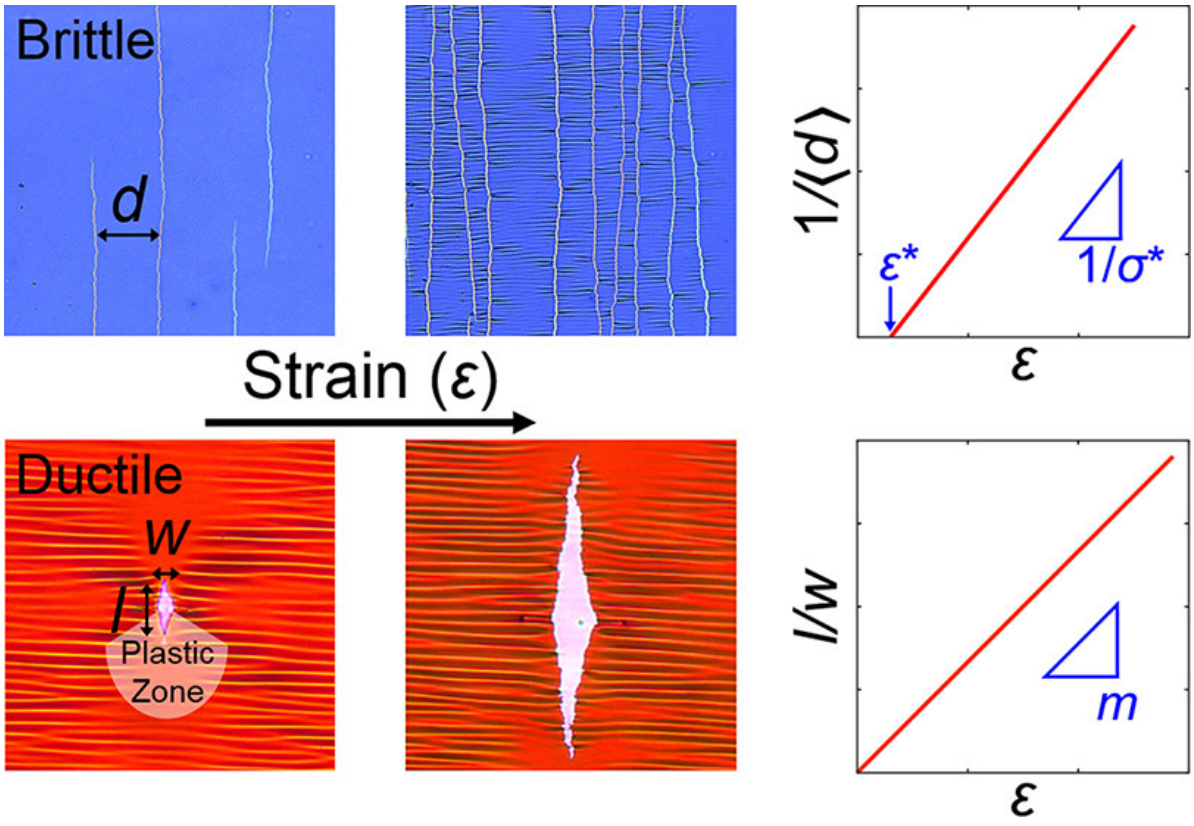

Image 6. Table of contents artwork for Chapter 5. Illustration showing brittle vs. ductile fracture.

Mohammad A. Alkhadra,† Samuel E. Root,† Kristan M. Hilby, Daniel Rodriquez, Fumitaka Sugiyama, and Darren J. Lipomi*
(† Equal contribution)

Department of NanoEngineering, University of California, San Diego, 9500 Gilman Drive Mail Code 0448, La Jolla, CA 92093-0448.

Abstract

One of the primary complications in characterizing the mechanical properties of thin films of semiconducting polymers is their diverse range of fracture behavior. Experimentally, fracture can be characterized by observing the propagation of cracks and voids in an elongated film. For brittle polymers, we find that films bifurcate in such a way that the crack density increases linearly with applied strain ($R^2 \geq 0.91$) at small strains. Linear regression is used to estimate the fracture strength and strain at fracture of each material using an existing methodology. For the case of ductile polymers, however, we find that diamond-shaped microvoids, which originate at pinholes and defects within the film, propagate with an aspect ratio that increases linearly with applied strain ($R^2 \geq 0.98$). We define the rate of change of the aspect ratio of a microvoid with respect to applied strain as the "microvoid-propagation number." This dimensionless film parameter, previously unreported, is a useful measure of ductility in thin films supported by an elastomer. To explore the significance of this parameter, we correlate the microvoid-propagation number with nominal ductility using several ductile polymer films of approximately equal thickness. Since the fracture of a film supported by a substrate depends on the elastic mismatch, we study the effect of this mismatch on the propagation of microvoids and observe that the microvoid-propagation number increases with increasing elastic mismatch. Moreover, we demonstrate the dependence of microvoid propagation on the thickness of the film and find that thicker films exhibit greater resistance to the propagation of fracture. We hypothesize that this behavior may be attributed to a larger volume of the plastic zone and a higher density of entanglements. To understand how the mechanical properties of a film influence the fracture behavior on a substrate, we perform tensile tests of notched and unnotched films floated on the surface of water. We find a linear correlation ($R^2 = 0.99$) between the logarithm of the microvoid-propagation number and the fracture stress.

5.1 Introduction

The development of semiconducting polymers that are resistant to fracture requires a comprehensive understanding of their mechanical properties. These materials essentially always take the form of thin films supported by a rigid, flexible, or stretchable substrate. The challenges associated with force-based measurements of the mechanical response of such supported films, however, have led to the development of a suite of optical metrology techniques.[1–4] This paper describes how a range of fracture behavior in films of semiconducting polymers supported by an elastomer can be characterized using optical microscopy (**Figure 5.1**). We applied a metrology technique, described by Stafford and coworkers,[2] to thin films of polymers that undergo brittle fracture. In addition, we developed a novel technique to characterize the fracture behavior of thin films of ductile polymers We quantified the propagation of diamond-shaped microvoids in ductile films using the rate of change in the aspect ratio of these microvoids with applied strain. We then used this methodology to show that the propagation of ductile microvoids is inhibited in thicker films. To supplement these analyses, we performed tensile tests of pseudo freestanding films—supported only by water—in both notched and unnotched configurations. We then determined quantitative and qualitative relationships between the fracture behavior of a film supported by an elastomer and the mechanical response of the film on water. Our approach should be useful for predicting and comparing the mechanical robustness of thin films of ductile polymers for applications in flexible and stretchable electronics.

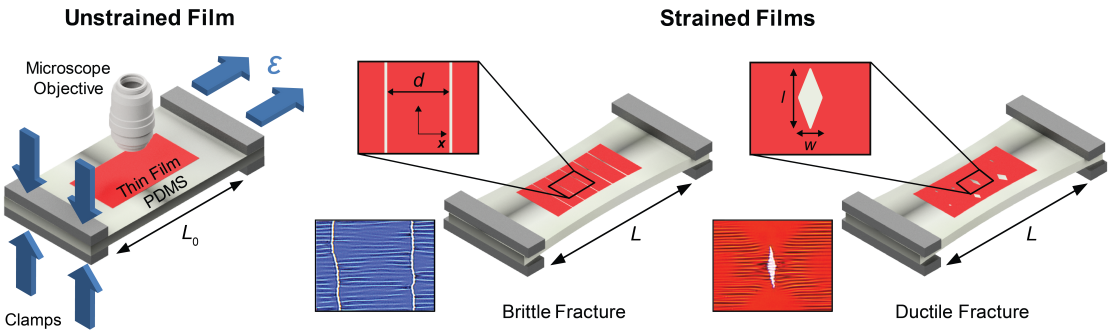

Figure 5.1. Overview of the experimental methodology and corresponding fracture modes in thin films of semiconducting polymers. A spin-coated film supported by a poly(dimethylsiloxane) (PDMS) substrate is incrementally strained under an optical microscope. Schematic illustrations (top) and representative optical micrographs (bottom) demonstrating fracture by either a brittle or a ductile mechanism. Blue arrows indicate the direction of an applied force, for either clamping or applying tensile strain.

5.2 Theoretical and Experimental Considerations

The mismatch in elastic modulus (E) between a rigid film and a compliant substrate affects the initiation and propagation of cohesive fracture that channels through the film.[5] For linear elastic films, Beuth showed that the strain-energy release rate (G, in units of J m^{-2}), defined as the energy dissipated per unit area of fracture surface created, is a function of the elastic mismatch between the film and the substrate.[6] This dependence proceeds from the concentration of stress at the interface of a strained bilayer structure caused by elastic mismatch. Elastic mismatch may be quantified using Dundurs' parameters α and β:[6,7]

$$\boldsymbol{\alpha} = \frac{\overline{\boldsymbol{E}}_{\square} - \overline{\boldsymbol{E}}_{\mathbf{s}}}{\overline{\boldsymbol{E}}_{\mathbf{f}} + \overline{\boldsymbol{E}}_{\mathbf{s}}}, \quad \boldsymbol{\beta} = \frac{1}{2}\frac{\boldsymbol{\mu}_{\mathbf{f}}(1-2\boldsymbol{\nu}_{\mathbf{s}}) - \boldsymbol{\mu}_{\mathbf{s}}(1-2\boldsymbol{\nu}_{\mathbf{f}})}{\boldsymbol{\mu}_{\mathbf{f}}(1-\boldsymbol{\nu}_{\mathbf{s}}) + \boldsymbol{\mu}_{\mathbf{s}}(1-\boldsymbol{\nu}_{\mathbf{f}})} \qquad (1)$$

where $\overline{\boldsymbol{E}} = \boldsymbol{E}/(\mathbf{1} - \boldsymbol{\nu}^{\mathbf{2}})$, $\boldsymbol{\nu}$ is the Poisson ratio, $\boldsymbol{\mu} = \boldsymbol{E}/(\mathbf{2}(\mathbf{1} + \boldsymbol{\nu}))$, and subscripts 'f' and 's' denote the film and substrate, respectively. The dependence of G on β is weak when $\alpha > 0$, in which case β may be neglected.[8] For a stiff film and a relatively compliant substrate, $\boldsymbol{E}_{\mathbf{f}} \gg \boldsymbol{E}_{\mathbf{s}}$ implies that $\alpha \approx 1$. The likelihood for fracture to initiate and propagate increases as Dundurs' parameter α tends to 1 because of the rapid increase in G with increasing elastic mismatch. The Griffith fracture criterion

states that fracture occurs when G exceeds the critical value G_c, known as the cohesive fracture energy.[9]

For linear elastic materials, events of fracture may be characterized using the cohesive fracture energy and the stress intensity factor (K), a theoretical construct that relates the applied stress to the intensity of stress near the tip of a crack.[10] For materials that exhibit extensive plastic deformation, however, these parameters of linear elastic fracture mechanics are not sufficient to describe ductile fracture.[11,12] This insufficiency arises because the total energy due to ductile fracture is dissipated not only in the immediate vicinity of the fracture tip, but also in an outer region of extensive plastic deformation. To determine parameters for the fracture toughness of ductile materials, the method of the Essential Work of Fracture (EWF) was developed by Cotterell and Reddel.[11] The theory underlying this technique, however, assumes that the sample is not supported by a substrate that can bear the applied load. In the presence of an elastic substrate, adhesion and elastic mismatch strongly influence fracture, while intrinsic mechanical properties such as toughness are less important.[13] In general, the relationship between the intrinsic mechanical properties and the fracture behavior of ductile films supported by a substrate has not been thoroughly investigated.

Based on the theory of linear elastic fracture mechanics in thin films,[6,8] a stiffer substrate would delay the onset of fracture and inhibit its propagation, and a more compliant substrate would hasten the onset of fracture and promote its propagation.[5,14] Although the elastic moduli of the polymers we examined spanned multiple orders of magnitude, we standardized the experimental procedure for tensile testing by holding the elastic modulus of the substrate approximately constant at 0.5 ± 0.2 MPa, which is much lower than the moduli of the films. In addition, we studied the role of varying the elastic modulus of the substrate on microvoid propagation in ductile films by varying the ratio of elastomer base to crosslinking agent. We note that this approach also affects

the adhesion between the film and the substrate. To simplify our analysis, however, we assume that the film is well-bonded to the substrate in all cases.

Fracture may also be influenced by environmental conditions such as moisture, heat, and ultraviolet (UV) radiation.[15] In our experiments, however, effects of heat and UV radiation were trivial due to the controlled environment of the laboratory. We also reduced the influence of moisture content on our samples (e.g., moisture-assisted debonding[15] at the interface between the film and the substrate) by maintaining the relative humidity in our laboratory at approximately 65%.

5.3 Brittle Fracture

Chung and Lee et al. established a methodology that combines wrinkling and cracking of brittle films, such that the elastic modulus, fracture strength, and strain at fracture[16] can be determined simultaneously.[2] This methodology is carried out by transferring a rigid, brittle film onto a stretchable substrate and incrementally applying uniaxial tensile strain (ε) while measuring the average spacing between cracks (**Figure 5.2a**). The validity of this methodology, however, is contingent on the formation of approximately equally spaced, parallel cracks that propagate orthogonal to the direction of applied strain. Such a fragmentation pattern is characteristic of inherently brittle materials whose elastic behavior terminates with rupture—rather than plastic yield—at low strains.[17] In investigating the fracture mechanics of thin films of semiconducting polymers, we observed experimentally that this process of brittle fracture occurs commonly.

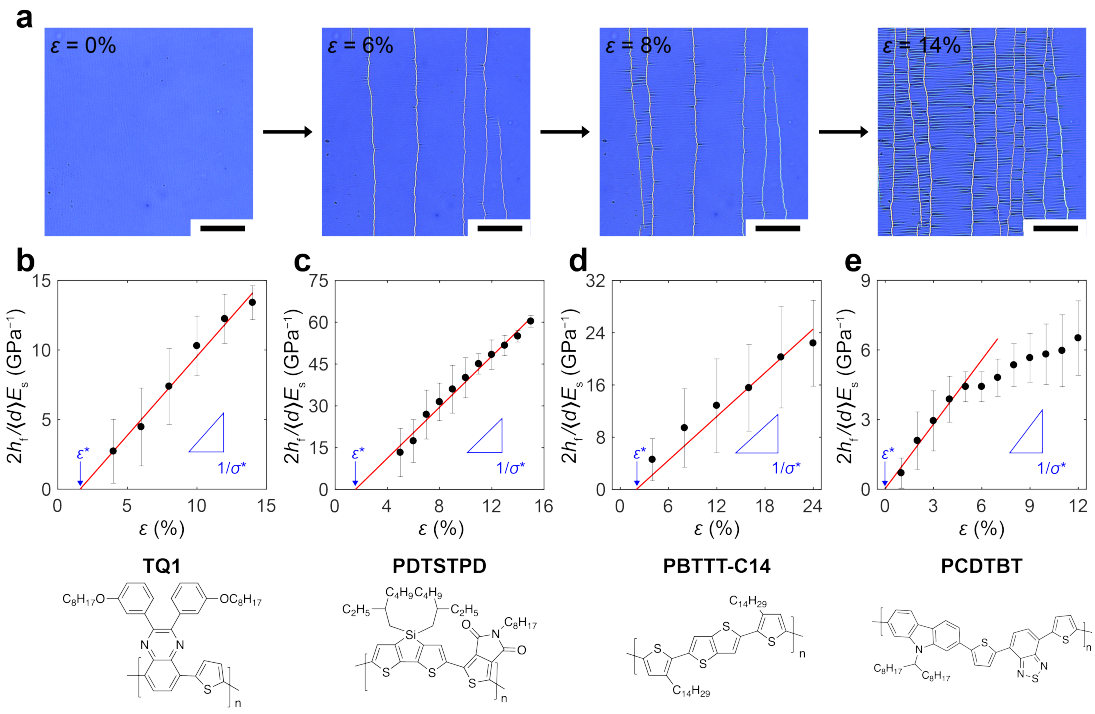

Figure 5.2. The combined wrinkling–cracking methodology applied to thin films of semiconducting polymers that exhibit brittle fracture. (a) Optical micrographs demonstrating the progressive elongation and systematic fragmentation of a thin film of TQ1 on PDMS; scale bars = 100 μm. Graphs of the scaled crack density $\left(\frac{2h_f}{\langle d\rangle E_s}\right)$ as a function of applied strain (ε) for (b) TQ1 ($h_f = 206 \pm 6$ nm), (c) PDTSTPD ($h_f = 159 \pm 8$ nm), (d) PBTTT-C14 ($h_f = 78 \pm 5$ nm), and (e) PCDTBT ($h_f = 137 \pm 8$ nm). Mean values and error bars (standard deviations) are based on data acquired from at least three separate measurements. Solid red lines correspond to linear regressions. Refer to **Experimental Methods** for systematic names.

The combined wrinkling–cracking methodology is restricted to the case in which the average width of fragments ($\langle \boldsymbol{d} \rangle$) is inversely proportional to the applied strain. It is also assumed that cracks in the film are unaccompanied by yielding or fracture of the substrate, any slip at the film–substrate interface is negligible, and tensile stress (σ) is maximal at the midpoint between adjacent cracks. Under these assumptions, $\langle \boldsymbol{d} \rangle$ is given by[18–20]

$$\langle \boldsymbol{d} \rangle = \frac{2\boldsymbol{h_f}\boldsymbol{\sigma}^*}{\boldsymbol{E_s}(\boldsymbol{\varepsilon} - \boldsymbol{\varepsilon}^*)};\ \boldsymbol{\varepsilon} > \boldsymbol{\varepsilon}^*,\ \langle \boldsymbol{d} \rangle < \boldsymbol{d_c} = \frac{4\boldsymbol{h_f}\boldsymbol{E_f}}{\boldsymbol{E_s}} \qquad (2)$$

where h_f, σ^*, and ε^* are the thickness, fracture strength, and strain at fracture of the film, E_f and E_s are the elastic moduli of the film and substrate, respectively, and d_c is the critical width of fragments for which eq 2 is valid.[2] Rearrangement of eq 2 yields a functional form of the scaled crack density $\left(\frac{2h_f}{\langle d \rangle E_s}\right)$ versus applied strain, which allows direct calculation of the fracture strength from the slope of the linear region of the graph. Extrapolation of this linear regression to the x-axis $\left(\frac{1}{\langle d \rangle} = 0\right)$ provides a reliable estimate of the strain at fracture. The fracture strength and strain at fracture are closely related to the damage and failure mechanisms of polymer films and, by extension, organic electronic devices.[13]

On applying uniaxial tensile strain, a buckling instability is produced by a transverse compressive strain due to the Poisson effect.[1] A periodic wrinkling pattern with a well-defined wavelength (λ) appears parallel to the direction of applied strain.[2] At low strains, and for a sufficiently thick substrate, the buckling wavelength can yield quantitative estimates of the elastic modulus of the film according to

$$\frac{E_f}{1-\nu_f^2} = \frac{3E_s}{1-\nu_s^2}\left(\frac{\lambda}{2\pi h_f}\right)^3 \qquad (3)$$

where ν_f and ν_s are the Poisson ratios of the film and substrate, respectively.[1] The elastic modulus of the film is relevant for deformable applications and wearable devices, and it can be tailored to minimize interfacial stress and interlayer delamination that would otherwise result in catastrophic failure of these devices.[13]

We employed the combined wrinkling–cracking methodology to analyze the fracture of films of brittle semiconducting polymers. The mechanical response and fracture of a thin film of TQ1 subjected to uniaxial strain is illustrated in **Figure 5.2a**; as shown in Figure 2b, fragmentation occurred linearly with strain. A similar response was observed for thin films of PDTSTPD, PBTTT-

C14, and PCDTBT, as shown in **Figure 5.2c-e**, respectively. The large uncertainties associated with the scaled crack densities in **Figure 5.2b** and **Figure 5.2d** manifest as large errors on estimates of the strain at fracture (refer to **Table 5.1**). This uncertainty could be due to the highly statistical nature of crack formation,[21] which depends on film defects and surface roughness. In contrast, the uncertainties associated with the slopes of the regressions are comparatively smaller, as indicated by the small errors on estimates of the fracture strength.

In **Figure 5.2e**, the rate of change of the scaled crack density with respect to applied strain begins to decrease for $\varepsilon \geq 6\%$. Stafford and coworkers attribute such behavior[22] to an insufficiency in the amount of stress induced on the film by the substrate for existing fragments to continue to bifurcate.[2] In any case, the relationship between scaled crack density and strain is linear ($R^2 \geq 0.91$) at low strains, and linear regression was used to determine the fracture strength and strain at fracture. Estimating Poisson ratios of $\nu_f = 0.35$ and $\nu_s = 0.5$,[23] eq 3 was used to calculate the elastic modulus of the film for each material based on the corresponding wavelength of wrinkles produced at low strains. The results of this analysis are summarized in **Table 5.1**.

Table 5.1. Tabulated values of the mechanical properties measured using the combined wrinkling–cracking methodology. Molecular weights were determined by gel-permeation chromatography (GPC), and glass transition temperatures (T_g) were measured for thin films ($h_f \geq 80$ nm).

Material	M_n (kDa) [$Đ$]	h_f (nm)	E_f (MPa)	ε^* (%)	σ^* (MPa)	T_g (°C)
TQ1	4 [1.4]	206 ± 6	120 ± 80	2 ± 2	9 ± 2	≈ 100, ref. 53
PDTSTPD	15 [2.5]	159 ± 8	60 ± 10	2 ± 1	2.2 ± 0.2	110 ± 10, ref. 54
PBTTT-C14[†]	6 [2.2]	78 ± 5	180 ± 30	2 ± 2	9 ± 1	102 ± 1, ref. 54
PCDTBT	1 [4.3]	137 ± 9	1100 ± 200	0 ± 1	11 ± 3	130. ± 3, ref. 29

[†]Spun from a heated solution at $T \approx 80$ °C

Based on the strains at fracture reported in **Table 5.1**, the materials examined clearly underwent brittle fracture at low strains. The most plausible explanation for this mechanical response is the relatively low molecular weights of the materials coincident with their relatively high glass transition temperatures (T_g). Semiconducting polymers with molecular weights near or

below the entanglement molecular weight comprise unconnected, chain-extended crystals that cannot endure large stresses and, as a result, manifest extreme brittleness.[5,24] In this instance, chain pullout is the favored mechanism of fracture.[25,26] Analogously, semiconducting polymers with T_gs well above room temperature often—though not always—fail in a brittle manner because segmental relaxation cannot occur on short, experimental time scales.[27] Considering the data in Table 1, the materials we examined using the combined wrinkling–cracking methodology fractured near $\varepsilon = 2\%$. Moreover, the product of the elastic modulus of the film and the strain at fracture is approximately equal to the fracture strength for each of the respective polymers. These materials therefore absorbed the applied mechanical energy entirely elastically and, in turn, ruptured without exhibiting any plastic yield or deformation, which is characteristic of brittle fracture.[17]

Films of semiconducting polymers exhibit strong, substrate-dependent variations in the T_g with thickness, though these variations occur predominantly when a film is thinned below approximately 80 nm.[28–30] In addition, Chung et al. observed no notable thickness dependence of the mechanical properties of thin films of tantalum and atactic polystyrene over the range of thicknesses investigated in their study (50 nm $\leq h_f \leq$ 1000 nm).[2] We thus expect there to be no significant thickness dependence of the mechanical properties of the materials listed in Table 1. Although the combined wrinkling–cracking methodology works well for brittle materials, this type of analysis cannot be applied to ductile materials, which are necessary for applications that demand mechanical compliance and extreme deformability.

5.4 Ductile Fracture

Ductility, in the classical sense, is defined as the capacity of a material to sustain large and permanent deformation under tensile loading.[16] In the field of organic electronics, measuring the crack-onset strain (COS) of thin films of semiconducting polymers on elastomeric substrates has been adopted as the standard method of evaluating ductility.[31] This measure alone, however, does

not provide a rigorous standard. One reason is that estimation of the crack-onset strain is limited by the finite resolution of an optical microscope. Another reason is that fracture at defects is by nature highly statistical, and, since experimenters are susceptible to confirmation bias,[32,33] visual inspection can be imprecise. The crack-onset strain also provides no information with regard to the propagation of microvoids after their initiation. In fact, consideration of fracture in ductile polymers has been limited to the initiation phase, while the propagation of microvoids has been neglected. A more definitive metric is therefore needed to evaluate the ductility of polymer films supported by an elastic substrate.

For ductile materials, fracture in a film initiates at defects—sites to which mechanical stress is highly localized—and grows progressively with increasing strain.[34] These microvoids, compared to the cracks observed in films of brittle materials, exhibit less of a tendency to propagate with increasing strain, which corresponds to the greater cohesion of ductile materials.[21,35] For the case of PTB7 of high molecular weight, a diamond-shaped microvoid, illustrated in **Figure 5.3a**, originated in the film at low strain ($\varepsilon \approx 10\%$) with a small aspect ratio (l/w). Although there existed regions in the film where multiple sites of fracture developed within close proximity to each other, only isolated microvoids were considered for the analysis. As the film was further elongated, we observed that the microvoid propagated progressively with an aspect ratio that increased linearly, as shown in **Figure 5.3b**. The rate of change of the aspect ratio of the microvoid with respect to applied strain is given by the slope (m) of a linear regression. This parameter, which we term the microvoid-propagation number, describes the ability of a specimen supported by an elastomer to resist fracture propagation and is an effective measure of ductility.

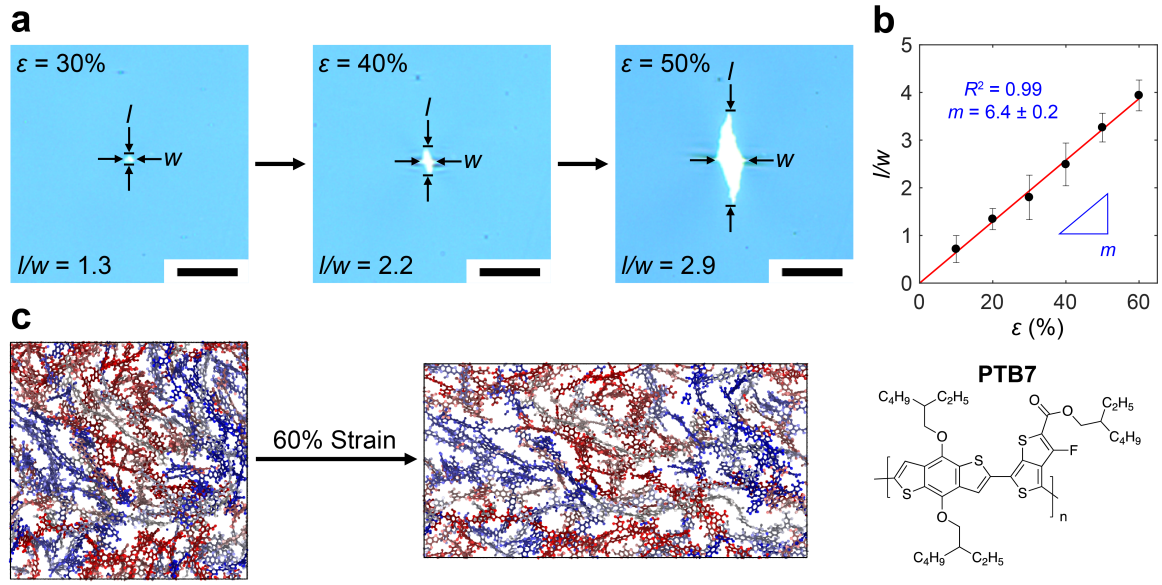

Figure 5.3. Propagation of ductile microvoids in a thin film of PTB7 (h_f = 110. ± 8 nm and E_f = 90 ± 30 MPa) under tensile strain. (a) Optical micrographs depicting the progressive elongation and consequent growth of a microvoid in a thin film of PTB7 on PDMS; scale bars = 25 μm. (b) Plot of the aspect ratio (l/w) of the microvoid as a function of applied strain (ε). To normalize the relationship for microvoids that appear at different strains, the graph is shifted vertically so that the intercepts pass through the origin. Mean values and error bars (standard deviations) are based on data acquired from three separate measurements. Solid red line corresponds to a linear regression with slope m. (c) A 4 nm slice of a molecular dynamics simulation box showing the molecular yielding of PTB7 with applied strain. Hydrogen atoms are removed for clarity, and separate polymer chains are colored distinctly.

For events of ductile fracture, elastic strain energy can be dissipated in two ways: through the formation of both cohesive and adhesive fracture surfaces, and through the plastic deformation of polymer chains. To portray the molecular mechanism of the process of plastic dissipation, we performed molecular dynamics simulations in which PTB7 was subjected to tensile strain using protocols described elsewhere.[36,37] As demonstrated in **Figure 5.3c**, we observed significant morphological rearrangement and alignment of polymer chains. These irreversible deformations ultimately lower the strain-energy release rate that drives the propagation of microvoids. Given that many ductile polymers exhibit such dissipation processes, the formation and propagation of diamond-shaped microvoids is a commonly observed mechanism of fracture in these materials.[35,38] We note that plastic deformation may also take the form of crazing that could occur at the tip of

the microvoid. This effect, which commonly occurs in glassy polymers strained below the T_g,[39] would inhibit the propagation of microvoids. Crazing, however, is typically associated with a whitening of the crazed region due to the scattering of light, which was not evident in any of our microscope images.

5.4.1. Nominal Ductility

To correlate the propagation of microvoids with nominal ductility, we measured the microvoid-propagation number and crack-onset strain for a number of semiconducting polymers (**Figure 5.4**). We defined the crack-onset strain as the strain at which the length (l) of any existing microvoid in the film exceeded approximately 20 μm. We believe that this is a more rigorous definition of the crack-onset strain that could compensate for limitations in the resolution of optical microscopy and aid in mitigating biases of the experimenter. To further standardize the experimental procedure, films were tested at an average thickness of 130 $\pm$ 10 nm. Figures 4a shows a strong correlation between the microvoid-propagation number and crack-onset strain that can be generalized for thin films of ductile polymers, the chemical structures of which are provided in Figure 4b. Balar and O'Connor determined that crack-onset strain can be correlated with cohesive fracture energy for both brittle and ductile films of semiconducting polymers.[38] Although measuring the cohesive fracture energy is beyond the scope of this work, we expect the microvoid-propagation number to decrease with increasing cohesive energy.

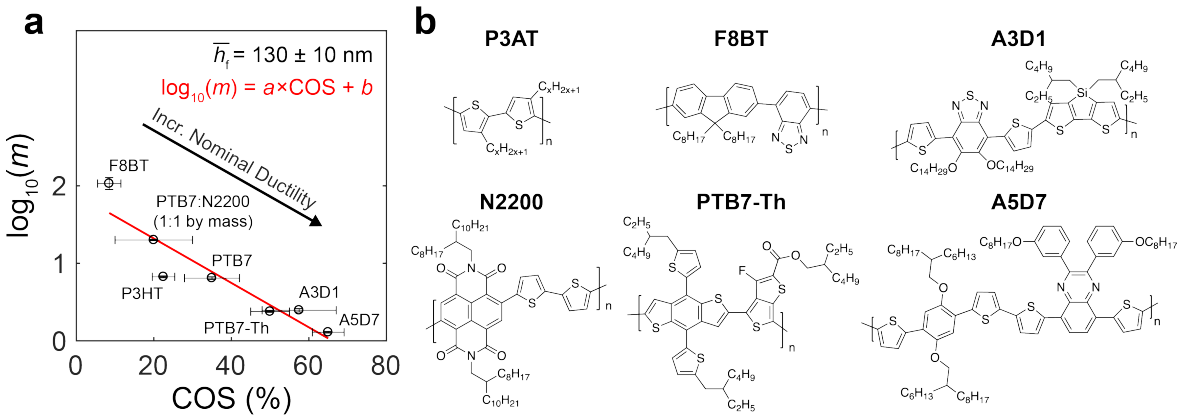

Figure 5.4. Characterization of ductile fracture using various semiconducting polymers. (a) Correlation of the microvoid-propagation number with nominal ductility for thin films tested at an average thickness of 130 ± 10 nm. The crack-onset strain (COS) is defined as the applied strain at which the length (l) of any existing microvoid in the film (excluding those that are present prior to the application of strain) exceeds approximately 20 μm. Vertical error bars are based on 95% confidence bounds of linear regressions, and horizontal error bars (standard deviations) are based on data acquired from at least three separate measurements. Solid red line corresponds to a linear regression with slope $a = -3 \pm 1$ and y-intercept $b = 1.9 \pm 0.6$ (errors are based on 95% confidence bounds). (b) Chemical structures of the materials used to characterize ductile fracture; refer to **Experimental Methods** for systematic names.

5.4.2 Role of Substrate

Rodriquez and Kim et al. demonstrated that the crack density of thin films of P3HT (40 kDa) supported by PDMS increased with increasing elastic mismatch at a given strain.[5] To examine the effect of elastic mismatch on the propagation of fracture in ductile polymers, we determined the microvoid-propagation number for films of P3BT supported by PDMS of varying elastic modulus, as shown in **Figure 5.5**. The results of this experiment indicate that the microvoid-propagation number increases with increasing elastic mismatch and is a stronger function of this mismatch than is the crack-onset strain. This behavior is consistent with the fact that the strain-energy release rate increases rapidly with increasing elastic mismatch. Although adhesive fracture could serve as an additional dissipation mechanism that would promote the propagation of microvoids, data obtained from contact angle measurements (refer to **Experimental Methods**)

suggest that the adhesion of P3BT to PDMS of varying elastic modulus (over the range studied) is similar.

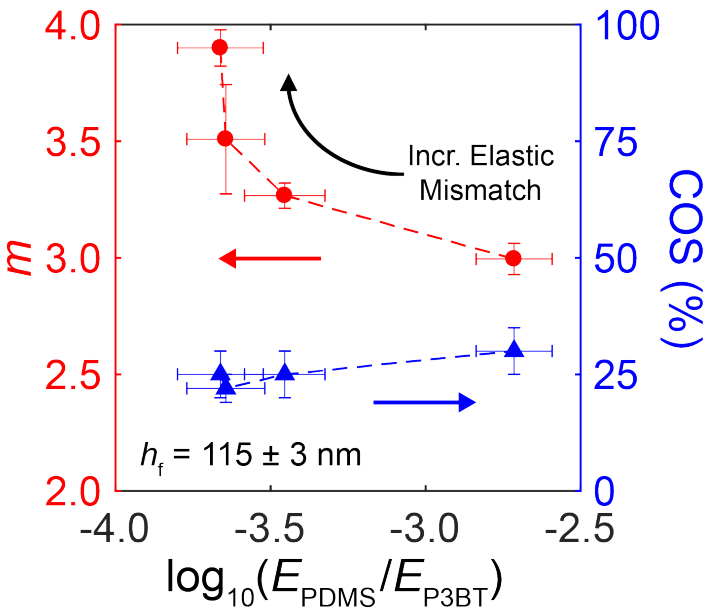

Figure 5.5. Role of the elastic modulus of the PDMS substrate (E_{PDMS}) on the fracture behavior of films of P3BT ($E_f = E_{P3BT} = 0.25 \pm 0.07$ GPa). The microvoid-propagation number (m) increases with increasing elastic mismatch and is a stronger function of this mismatch than is the crack-onset strain (COS). Dashed lines are guides to the eye.

In addition to the formation of surfaces of cohesive fracture, adhesive fracture is an important dissipation mechanism that occurs in thin films of polymers supported by a compliant substrate.[13] **Figure 5.6a** illustrates the surface topography of a fractured film of F8BT on PDMS obtained by atomic force microscopy. For ductile polymers, delamination and wrinkling of the film near the center of a microvoid result from the distribution of stress along the length of the microvoid, with the maximum stress being induced at the advancing tip.[17,40] Delamination of a film from the substrate is an important process that dissipates elastic strain energy by diverting it from the propagating tip of a microvoid. This process of interfacial debonding also results in localized necking[41] that could lead to the formation of ductile microvoids.[38] We expect that the adhesion of

different semiconducting polymers to PDMS is similar, such that delamination at the center of a microvoid is comparable in all cases.

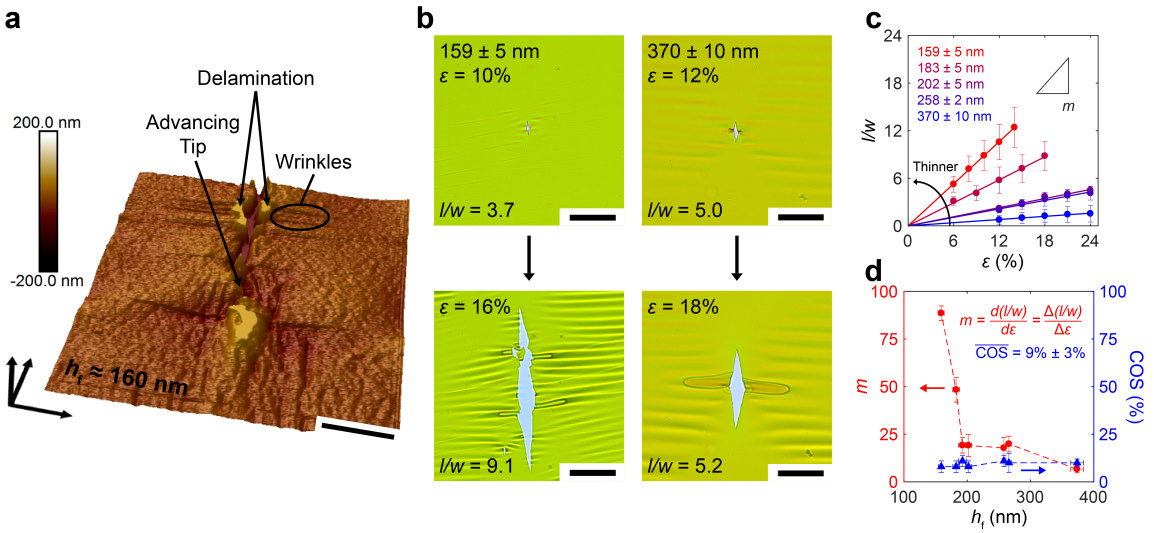

Figure 5.6. Topography of a cracked surface and dependence of ductile fracture on thickness in films of F8BT (E_f = 1.0 ± 0.3 GPa). (a) Atomic force micrograph (tapping mode) of the height image of a crack in a strained film of F8BT supported by PDMS; scale bar = 3 μm. (b) Optical micrographs depicting the effect of an additional 6% strain (ε) on the aspect ratio (l/w) of microvoids in films of F8BT of different thicknesses; scale bars = 50 μm. (c) Graphs of the aspect ratio as a function of applied strain for films of different thicknesses. To normalize the relationship for microvoids that appear at different strains for a given thickness, the graph is shifted vertically so that the intercepts pass through the origin. Mean values and error bars (standard deviations) are based on data acquired from at least three separate measurements. Solid lines correspond to linear regressions. (d) Graphs of the microvoid-propagation number (m) and the crack-onset strain (COS) as functions of thickness (h_f). Vertical error bars on m are based on 95% confidence bounds of regressions in (c); vertical error bars on COS (standard deviations) are based on data acquired from at least three separate measurements; mean thicknesses and horizontal error bars (standard deviations) are based on data acquired from at least five separate measurements. Dashed lines are guides to the eye.

5.4.3 Role of Film Thickness

In the neighborhood of the tip of a microvoid, there exists a region—the plastic dissipation zone—where energy is dissipated due to plastic deformation.[17] Mai and Cotterell reported that the shape of this plastic zone in bulk samples of ductile engineering and commodity plastics depends

on the geometry of the specimen.[12] We therefore investigated the dependence of the propagation of ductile microvoids on the thickness of the film.

The optical micrographs in **Figure 5.6b** show the effect of an additional 6% strain on the aspect ratio of microvoids in films of F8BT of different thicknesses. Microvoids in a thicker film, in contrast to a thinner one, propagate with an aspect ratio that is comparatively less sensitive to applied strain, as demonstrated in **Figure 5.6c**. The graph of the microvoid-propagation number as a function of the thickness of the film is plotted in **Figure 5.6d**, from which the strong dependence on thickness of the rate of propagation of microvoids in ductile films becomes evident. Since the initiation of microvoids is statistical, and not all microvoids originate at a specific applied strain, we underscore the significance of the rate of propagation of microvoids—as opposed to the magnitude of the aspect ratio—in its dependence on thickness. In contrast to the microvoid-propagation number, the crack-onset strain exhibited little to no dependence on thickness (**Figure 5.6d**); films of F8BT of varying thickness (159 ± 5 nm $\leq h_f \leq 370 \pm 10$ nm) had a crack-onset strain of $9\% \pm 3\%$ on average. This result strongly indicates that the microvoid-propagation number and the crack-onset strain, although correlated, capture distinct aspects of ductile fracture in thin films of semiconducting polymers. The crack-onset strain is a manifestation of the degree of non-uniformity in a film,[38] and it depends on the relative dimensions of local inhomogeneities and the thickness of the film.[13]

The dependence of the microvoid-propagation number on the thickness of the film may be ascribed to the greater sensitivity of the cohesive fracture energy to thickness in samples of high molecular weight.[42] Compared to polymers of low molecular weight, there is a greater tendency for polymers of high molecular weight to exhibit interchain entanglement, which leads to larger plastic zones around the tips of microvoids.[43,44] Bruner and Dauskardt contended that larger plastic zones inhibit the propagation of fracture by relaxing the stress applied to a film, whereas smaller plastic

zones allow extensive propagation of fracture by contributing little to the relaxation of stress.[42] Moreover, Mai and Cotterell argue that the width of the fracture process zone—a necked region of damage that lies directly in the path of an advancing microvoid (**Figure 5.7a**)—increases with increasing thickness in thin plates of metals.[12,45] We therefore propose that the plastic zone in a thinner film is geometrically confined by the boundaries of the specimen to a smaller volume, which results in a higher propensity for microvoids to propagate. It is also possible that effects of thin-film confinement—particularly a reduction in the density of entanglements—would lower the cohesion of the film and lead to more rapid propagation of microvoids. From the perspective of theoretical solid mechanics, the problem of relating the propagation of ductile microvoids to the intrinsic mechanical properties of a thin film is currently unsolved. Nonetheless, it would be interesting and useful to learn if a continuum-based approach could be used to predict this dependence on thickness.

5.4.4 Plastic Dissipation Zone

Over the course of this study, we repeatedly observed the formation of wrinkles with a characteristic X-shape that appeared around diamond-shaped microvoids, as shown in Figure 6b (right) for instance. We hypothesize that this pattern is determined by the dimensions of the plastic dissipation zone. **Figures 5.7a** schematically illustrates a strained film of semiconducting polymer on PDMS under conditions of plane stress (load forces act only parallel to the plane of the thin film). To test our hypothesis and characterize plastic deformation around the tip of a microvoid, we performed a simple experiment in which we partially released the strain applied to an elongated film and inspected the wrinkles which formed in plastically deformed regions.[3] Optical micrographs of a fractured film of P3BT are presented in **Figure 7b**, the first of which shows these characteristic wrinkles. Elongation of the sample resulted in the propagation of the microvoid, and subsequent release of this additional strain led to severe wrinkling in the zone ahead of the

advancing tip. The regions horizontally adjacent to the microvoid, however, displayed no such wrinkling, which suggests the existence of zones of partial elastic recovery.

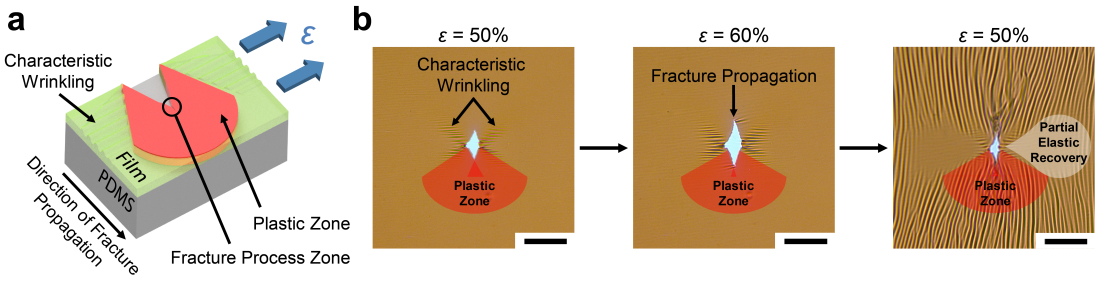

Figure 5.7. Approximate geometry of the plastic zone in thin films of ductile semiconducting polymers that form diamond-shaped microvoids upon fracture. (a) Schematic illustrating a strained film on PDMS and the proposed shape of the plastic zone under conditions of plane stress. Blue arrows indicate the direction of applied tensile strain (ε). (b) Optical micrographs depicting the effect of an additional 10% strain, followed by the release of this applied strain, on the topography of a film of P3BT ($h_f = 115 \pm 3$ nm); scale bars = 50 μm. The zone ahead of the advancing tip of the microvoid exhibited severe wrinkling upon release of the additional strain; regions horizontally adjacent to the microvoid displayed no such wrinkling.

5.4.5 Tensile Testing of Pseudo Freestanding Films

It is well-known that deformation and fracture in thin films supported by polymeric substrates are influenced by the adhesion and elastic mismatch between the film and the substrate.[46] To isolate these effects from the intrinsic mechanical properties of the film, we implemented a tensile test, originally developed by Kim and coworkers, in which pseudo freestanding films are supported by water (**Figure 5.8a**).[47] The "film-on-water" technique resembles a conventional pull test in that it is used to obtain a trace of force versus displacement in a single step. As shown in **Figure 5.8b**, we measured force–displacement curves of unnotched films of four semiconducting polymers and transformed them into stress−strain curves using the dimensions of the corresponding sample. Based on these data and the results in **Figure 5.4**, we infer that films with a smaller microvoid-propagation number exhibit greater ductility, with or without the support of a substrate. Plotting the logarithm of the microvoid-propagation number versus fracture strength also reveals a

correlation between these two parameters, as portrayed in the inset of **Figure 5.8b**. The microvoid-propagation number is thus informative of the stress that a thin film under tension can sustain at fracture.

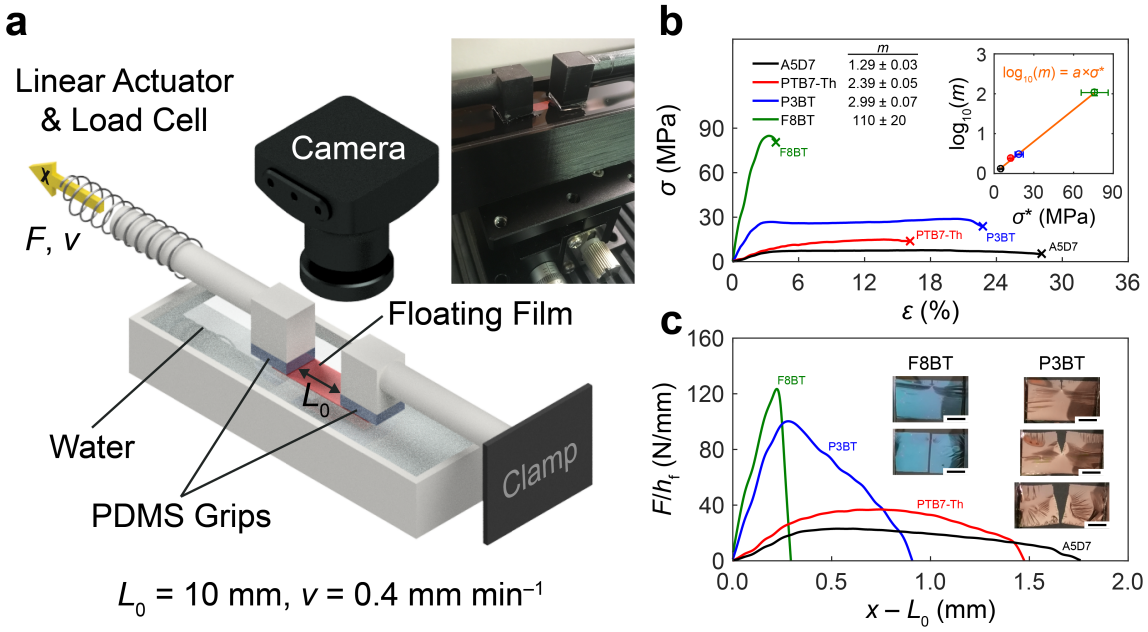

Figure 5.8. Tensile testing of pseudo freestanding films of semiconducting polymers. (a) Schematic diagram of the experimental setup, which consists of a linear actuator, a load cell, and a camera. (b) Representative stress–strain curves of unnotched films obtained using the film-on-water technique. Inset is a plot of the logarithm of the microvoid-propagation number ($\log_{10}(m)$) versus fracture strength (σ^*); values of m are for films tested at an average thickness of 130 ± 10 nm. Horizontal error bars (standard deviations) are based on data acquired from three separate measurements. Solid orange line corresponds to a linear regression with slope a = 0.027 ± 0.001 MPa^{-1} (error is based on 95% confidence bounds). (c) Representative traces of force per unit thickness (F/h_f) versus displacement ($x - L_0$) for notched films of the materials used in (b). Notches at the edges of samples were 0.3 ± 0.1 times the width of the respective film, which was equal to 4.5 ± 0.5 mm on average. Inset photographs demonstrate notched samples before and after the application of uniaxial strain; scale bars = 2.5 mm.

For bulk samples of ductile polymers, the fracture toughness is generally characterized by subjecting a notched specimen to tensile loading while measuring the force.[10,12] To relate the microvoid-propagation number to this classical metric of elastoplastic fracture mechanics, we adapted the film-on-water technique by introducing a notch at the edge of the floating film. This experiment produced curves of force per unit thickness versus displacement, as plotted in **Figure**

5.8c. Comparison of these data with the microvoid-propagation number revealed excellent qualitative agreement in the observed behavior. Of the four materials tested, the polymer with the largest microvoid-propagation number, F8BT, exhibited the least ductility: the film bifurcated once the applied load reached a critical value. Conversely, the material with the smallest microvoid-propagation number, A5D7, exhibited significant post-yielding behavior due to blunting at the crack tip. In comparing P3BT and PTB7-Th, the relationship between the propagation of fracture for the cases of films supported by PDMS and by water is more subtle. This subtlety is likely due to the large difference in elastic modulus between these two materials, which introduces effects of elastic mismatch when these films are supported by a substrate. To summarize, tensile testing of films on water revealed that the microvoid-propagation number is related to traditional metrics of the fracture toughness of a freestanding film. Developing an exact, quantitative relationship between the intrinsic mechanical properties—determined for a film on water—and the fracture behavior of the film supported by a substrate, however, demands a thorough theoretical treatment supplemented by further experimental testing and is thus the subject of ongoing research.

5.5 Conclusion

Understanding the fracture phenomena that govern the mechanical properties of thin films of semiconducting polymers is critical for the design and processing of flexible and stretchable organic electronics. Mechanical failure in polymer films, however, is naturally convoluted and often the consequence of concurrent events of fracture that occur at the molecular scale. Using the combined wrinkling–cracking methodology, we quantified the stiffness, strength, and ductility of thin films that exhibited brittle fracture at their respective molecular weights. For films that exhibited ductile fracture, on the other hand, we monitored the growth of isolated microvoids and observed how the aspect ratio varied with applied strain. This measure of the tendency for fracture to propagate was quantified by the microvoid-propagation number, m, which provides insight into

the degree of plasticity that a ductile film exhibits. We correlated this previously unreported film parameter with the crack-onset strain for various polymers tested at a common thickness. In addition, we demonstrated that the microvoid-propagation number is a strong function of the thickness of the film, a dependence that may be attributed to the geometry of the plastic zone and effects of thin-film confinement. To better understand how plasticity influences the mechanics of ductile fracture, the molecular-scale phenomena that control the growth of microvoids warrant further investigation. Nevertheless, the microvoid-propagation number should be a useful metric because it serves as a simple yet effective way to evaluate the ductility of thin films supported by an elastomer. The characterization of the resistance of a material to fracture is the backbone of fracture mechanics, and it is crucial in assessing the damage tolerance of semiconducting polymers for mechanically robust electronics.

5.6 Experimental Methods

5.6.1 Materials

Poly(9,9-dioctylfluorene-*alt*-benzothiadiazole) (F8BT, M_w = 20–100 kDa) and poly[*N*-9′-heptadecanyl-2,7-carbazole-*alt*-5,5-(4′,7′-di-2-thienyl-2′,1′,3′-benzothiadiazole)] (PCDTBT, M_w = 20–100 kDa) were purchased from Lumtec and used as received. Poly[2,5-bis(3-tetradecylthiophen-2-yl)-thieno[3,2-*b*]thiophene] (PBTTT-C14, $M_n > 12$ kDa, $Đ = 1.8$) was purchased from Solarmer Energy, Inc. and used as received. Poly[(5,6-dihydro-5-octyl-4,6-dioxo-4*H*-thieno[3,4-*c*]pyrrole-1,3-diyl)[4,4-bis(2-ethylhexyl)-4*H*-silolo-[3,2-*b*:4,5-*b*′;]dithiophene-2,6-diyl]] (PDTSTPD, M_n = 7−35 kDa, $Đ$ = 1.4−2.9), poly[[2,3-bis(3-octyloxyphenyl)-5,8-quinoxalinediyl]-2,5-thiophenediyl] (TQ1, M_n = 12−45 kDa, $Đ < 3.3$), and poly({4,8-bis[(2-ethylhexyl)oxy]benzo-[1,2-*b*:4,5-b′]dithiophene-2,6-diyl}{3-fluoro-2-[(2-ethylhexyl)-carbonyl]thieno[3,4-*b*]thiophenediyl}) (PTB7, M_w = 80−200 kDa, $Đ \leq 3.0$) were purchased from

Sigma-Aldrich Co. and used as received. Poly(3-butylthiophene) (P3BT, M_n = 50−70 kDa, $Đ$ = 2.1−3.0) was purchased from Rieke Metals, Inc. and used as received. Poly{[*N*,*N*′-bis(2-octyldodecyl)naphthalene-1,4,5,8-bis(dicarboximide)-2,6-diyl]-*alt*-5,5′-(2,2′-bithiophene)} (PNDI(2OD)2T, Polyera ActivInk™ N2200, M_n = 48 kDa, $Đ$ = 3.7) was purchased from Polyera Corp. and used as received. Poly[4,8-bis(5-(2-ethylhexyl)thiophen-2-yl)benzo[1,2-*b*;4,5-b′]dithiophene-2,6-diyl-*alt*-(4-(2-ethylhexyl)-3-fluorothieno[3,4-*b*]thiophene-)-2-carboxylate-2-6-diyl)] (PTB7-Th, M_w > 40 kDa, $Đ$ = 1.8–2.0) was purchased from Ossila Ltd. and used as received. Poly(3-hexylthiophene) (P3HT, M_n = 80 kDa, $Đ$ = 1.6) was produced and characterized by the Heeney laboratory using synthetic procedures described elsewhere.[5] A3D1 (M_n = 50 kDa, $Đ$ = 10.8) and A5D7 (M_n = 34 kDa, $Đ$ = 3.4) were selected from a library of low-bandgap polymers used in studies by Bundgaard et al.[48] and subsequently by Roth and Savagatrup et al.[35] PEDOT:PSS (Clevios™ PH 1000) was purchased from Heraeus and used as received. (Tridecafluoro-1,1,2,2-tetrahydrooctyl)-1-trichlorosilane (FOTS) was purchased from Gelest, Inc. and used as received. Chloroform, acetone, and isopropyl alcohol were purchased from Sigma-Aldrich Co. and used as received. Alconox was purchased from Alconox, Inc. and used as received.

5.6.2 Gel Permeation Chromatography

Since the suppliers reported wide ranges of molecular weight for some polymers used in this study, we independently measured the molecular weight and polydispersity of these materials using gel permeation chromatography (GPC). GPC was performed in chlorobenzene at 55 °C using an Agilent 1260 separation module equipped with a 1260 refractive index detector and a 1260 photodiode array detector. Molecular weights of polymers were calculated relative to linear polystyrene standards. Our measured values of M_n for the brittle polymers are presented in Table 1. For F8BT, we measured M_n = 10 kDa and $Đ$ = 3.2. For PTB7, the chains eluted too rapidly,

such that the peak retention time was outside the range of calibration standards, and thus no reliable data could be obtained.

5.6.3 Preparation of Substrates

Glass slides were prepared as the substrate for polymer films. The glass slides were cut into squares of 2.5 cm × 2.5 cm using a diamond-tipped scribe and then cleaned in sonication baths of powdered Alconox dissolved in deionized water, pure deionized water, acetone, and isopropyl alcohol for cycles of 10 min each. After sonication, the slides were dried using a stream of compressed air. To activate the surface of glass, improve wettability, and remove any residual organic debris, the slides were treated with air plasma (30 W) for 5 min at a base pressure of 200–250 mTorr. Since TQ1 and PCDTBT adhered too strongly to glass treated in this manner, glass slides treated with antiadhesive FOTS were used as substrates. Specifically, slides were treated with plasma, placed in a desiccator with a vial containing a few drops of FOTS, and then left under vacuum for at least 3 h.

5.6.4 Preparation of Films

Solutions of pure polymers and a blend of PTB7 and N2200 (1:1 by mass) were prepared at given concentrations in chloroform and allowed to stir overnight. After mixing, the solutions were filtered with 1 μm glass fiber media syringe filters before spin coating. All films were then spun, either directly on glass or on a PEDOT:PSS/glass substrate, in two steps. (PTB7-Th was spun from a heated solution at $T \approx 80$ °C.) First, F8BT (20 mg mL^{-1} in chloroform) was spun at 750 rpm (375 rpm s^{-1} ramp), 1000 rpm (500 rpm s^{-1} ramp), 1300 rpm (650 rpm s^{-1} ramp), 1500 rpm (750 rpm s^{-1} ramp), 2000 rpm (1000 rpm s^{-1} ramp), and 3500 rpm (1750 rpm s^{-1} ramp), separately, for 2 min, and F8BT (10 mg mL^{-1} in chloroform) was spun at 1000 rpm (500 rpm s^{-1} ramp) for 2 min. TQ1 and PCDTBT (10 mg mL^{-1} in chloroform) were spun onto glass treated with FOTS at 500

rpm (250 rpm s^{-1} ramp) for 2 min. All other solutions had a concentration of 10 mg mL^{-1} in chloroform and were first spun at 1000 rpm (500 rpm s^{-1} ramp) for 2 min. Second, all films were spun at 2000 rpm (1000 rpm s^{-1} ramp) for 30 s. Thicknesses of films were obtained using a Veeco Dektak stylus profilometer; at least five measurements were taken for each film.

5.6.5 Preparation of PDMS Elastomers

For tensile (compression) testing, poly(dimethylsiloxane) (PDMS) was chosen as the substrate for mechanical measurements. To prepare, 20 g (50 g) of Sylgard 184 Silicone elastomer base was mixed with 2 g (5 g) of Sylgard 184 Silicone crosslinking agent and stirred until cloudy. The mixture was then spread into a petri dish with a diameter of 15 cm and a height of 1.5 cm. PDMS was degassed by placing the petri dish in a desiccator under vacuum until the bubbles ceased to be visible. The dish was then placed in an oven preheated to 70 °C for 50 min to allow the PDMS to cure. Next, the PDMS, with an approximate thickness of 1 mm (3 mm), was cut into rectangular slabs of 1 cm × 9 cm. The elastic modulus of these elastomers was determined to be 0.5 ± 0.2 MPa, on average, using an Instron pull tester. To test the role of elastic mismatch on the fracture behavior of ductile films, additional PDMS elastomers were prepared: 20 g of Sylgard 184 Silicone elastomer base was mixed with 1, 1.5, or 2 g of Sylgard 184 Silicone crosslinking agent. This batch of PDMS was then allowed to cure in an oven at 70 °C for 40 min, which resulted in elastic moduli of 54 ± 8, 56 ± 5, and 90 ± 10 kPa, respectively. Otherwise, the preparation procedure was the same as described above.

5.6.6 Combined Wrinkling-Cracking Methodology

Slides with polymer films were scored into four, equally sized rectangular sections. Films of PDTSTPD and PBTTT-C14 were transferred to unstrained strips of PDMS by firmly pressing a scored portion of the film onto PDMS and submerging the film–PDMS bilayer in deionized water.

While still in water, the slide with the remaining sections of the film was removed, after which the PDMS was dried with compressed air. Films of TQ1 and PCDTBT were not transferred while submerged in water because they had been spun onto glass slides treated with FOTS. Instead, these films were scored into thin segments, placed onto strips of PDMS, and quickly removed with an applied force directly perpendicular to the film–PDMS interface. The film–PDMS bilayers were then uniaxially stretched at one end using a linear translation stage (L_0 = 1.27 cm), and the mechanical response of each film was imaged using a Leica DM2700 optical microscope.

5.6.7 Microvoid Aspect Ratio

Scored films of ductile polymers were transferred to unstrained strips of PDMS by firmly pressing a scored portion of the film onto PDMS and submerging the bilayer in deionized water. While still in water, the slide with the remaining sections of the film was removed, after which the PDMS was dried with compressed air. The film–PDMS bilayer was then uniaxially stretched at one end using a linear translation stage (L_0 = 1.27 cm), and the mechanical response of the film was probed by observing the growth of isolated microvoids under the microscope.

5.6.8 Buckling-Based Metrology for Measuring Elastic Moduli

Elastic moduli of the brittle films examined using the combined wrinkling–cracking methodology, namely TQ1, PDTSTPD, PBTTT-C14, and PCDTBT, were estimated by applying the buckling-based metrology of Stafford et al. (eq 3) to these films based on the wrinkling behavior under tension.[1,2] On the other hand, measuring the elastic moduli of ductile films, namely F8BT, PTB7, and P3BT, required compression-induced mechanical buckling to produce visible wrinkling patterns. As such, neat slabs of PDMS were strained to approximately 5% on a linear translation stage and fixed to rectangular glass slides. For each material, films prepared at three different thicknesses (using spin speeds of 500, 1000, and 1500 rpm with ramp rates of 250, 500, and 750

rpm s^{-1}, respectively) were scored and transferred to the pre-strained PDMS. The release of this pre-strain produced a buckling instability and, in turn, wrinkles in the films. For each film, the wrinkles were imaged under a microscope at several (> 7), arbitrary locations. To count the number of wrinkles in an image, we used a function in MATLAB based on the Savitzky-Golay smoothing filter and peak finder, which distinguishes between crests and troughs. To compute the buckling wavelength (λ), the width of an image was divided by the average number of wrinkles. Moreover, the thickness of the film (h_f) was measured (on glass) using a stylus profilometer, and the elastic modulus of PDMS (E_s) was determined using a commercial pull tester. Finally, the elastic modulus of the film (E_f) was calculated using eq 3.

5.6.9 Molecular Dynamics Simulations

All simulations and visualizations were performed using LAMMPS[49] and OVITO[50] respectively. A detailed description of the atomistic model parameterization from calculations of electronic structure, as well as the computational process for generating the simulation morphology, can be found elsewhere.[36,51] Briefly, 60 independent 12-mers were packed into a simulation box and subjected to NPT dynamics at 800 K using time increments of 2 fs for 5 ns to generate a well-equilibrated melt phase. This melt-phase structure was then subjected to an annealing protocol in which the temperature was ramped from 800 K to 300 K in intervals of 20 K and at time increments of 1 ns for runs of both ramping and equilibration. Simulations of mechanical deformation were run by imposing a constant strain rate (1×10^{-6} Å ps^{-1}) in the *x*-dimension and applying stress-free boundary conditions in both transverse dimensions.

5.6.10 Contact Angle Measurements

To qualitatively assess the adhesion between films of P3BT and strips of PDMS, we measured the advancing and receding contact angles of droplets of deionized water (~6 μL) on

pristine surfaces of PDMS. Imaging and data analysis were performed with an automated goniometer (Ramé-Hart, Model No. 290-U1) using the method of add/remove volume. Advancing (receding) contact angles of droplets of deionized water on pristine surfaces of PDMS ranged from 119.0° ± 0.6° (109° ± 3°) to 125.9° ± 0.7° (117° ± 4°), which correspond to the PDMS substrates with the highest and lowest elastic moduli, respectively.

5.6.11 Atomic Force Microscopy

A solution of F8BT in chloroform, with a concentration of 15 mg mL^{-1}, was spun onto glass treated with FOTS in two steps (1000 rpm for the first) as described above. A PDMS substrate was prepared as explained above, though its surface was subsequently activated by cleaning with ultraviolet–ozone (UV–O_3) for 2 h, followed by treatment with FOTS in the same manner that the glass slides were. The film of F8BT on glass was scored into thin segments and transferred to the PDMS treated with FOTS. To generate microvoids in the film, the film–PDMS bilayer was uniaxially stretched at one end using a linear translation stage. Once enough microvoids were produced, the substrate was fixed at the corresponding applied strain. A second, pristine PDMS slab (neither cleaned with UV–O_3 nor treated with FOTS) was prepared by curing at 70 °C for 50 min on the smooth surface of a silicon wafer. After that, the slab was cut into squares of 1 cm × 1 cm (approximately 1 mm thick) and used to strip the fractured film off the strained, surface treated PDMS for imaging. Atomic force micrographs of the height image were then obtained using a Veeco scanning probe microscope (SPM) in tapping mode, and the data were analyzed with NanoScope Analysis v1.40 software (Bruker Corp.).

5.6.12 Film-on-Water Tensile Testing

Kim and coworkers developed a tensile test in which pseudo freestanding films are supported by water.[47] The "film-on-water" technique resembles a conventional pull test in that it is

used to obtain a trace of force versus displacement in a single step. This technique leverages the high surface tension and low viscosity of water to support thin films and allow unimpeded sliding of these films on the surface. To float a specimen on water, a sacrificial layer of PEDOT:PSS—onto which semiconducting polymers were spin coated—was used. (PEDOT:PSS was spun onto a glass slide at 1000 rpm (500 rpm s^{-1} ramp) for 3 min, followed by a second step at 2000 rpm (1000 rpm s^{-1} ramp) for 30 s.) The layer of PEDOT:PSS readily dissolved in water upon contact, which allowed the polymer film to delaminate from the substrate. Once the film was afloat, van der Waals adhesion was made between the film and a load cell using grips coated with small slabs of PDMS. To obtain plots of force versus displacement, films were uniaxially strained at a rate of approximately 6.67×10^{-4} s^{-1} ($L_0 = 10$ mm) until the test was terminated. Additional tests of fracture were performed by introducing notches at the edges of films, which were then subjected to uniaxial strain. Procedures for preparation and transfer of samples were otherwise identical for films that were and were not notched

5.7 Acknowledgments

This work was supported by the Air Force Office of Scientific Research (AFOSR) Grant Number FA9550-16-1-0220. Further support was provided by a gift from the B Quest Giving Fund made through Benefunder to D.J.L. and the Achievement Reward for College Scientists (ARCS) Fellowship awarded to S.E.R. Computational resources to support this work were provided by the Extreme Science and Engineering Discovery Environment (XSEDE) Program through the National Science Foundation Grant Number ACI-1053575.[52] The authors would like to acknowledge the laboratories of Profs. Martin Heeney (P3HT) and Frederik Krebs (A3D1 and A5D7) for providing materials for this study. In addition, the authors would like to thank Prof. Vlado A.

Lubarda, Dr. Laure V. Kayser, Dr. Suchol Savagatrup, Dr. Charles B. Dhong, and Cody W. Carpenter for insightful discussion.

Chapter 5, in full, is a reprint of the material as it appears in *Chemistry of Materials*, 2017, 29, 10139–10149. The American Chemical Society, 2017. Mohammad A. Alkhadra,† Samuel E. Root,† Kristan M. Hilby, Daniel Rodriquez, Fumitaka Sugiyama, and Darren J. Lipomi*(† Equal contribution). The dissertation author was a primary investigator and author of this paper.

References

(1) Stafford, C. M.; Harrison, C.; Beers, K. L.; Karim, A.; Amis, E. J.; VanLandingham, M. R.; Kim, H. C.; Volksen, W.; Miller, R. D.; Simonyi, E. E. A Buckling-Based Metrology for Measuring the Elastic Moduli of Polymeric Thin Films. Nat. Mater. 2004, 3, 545–550.

(2) Chung, J. Y.; Lee, J.; Beers, K. L.; Stafford, C. M. Stiffness, Strength, and Ductility of Nanoscale Thin Films and Membranes: A Combined Wrinkling-Cracking Methodology. Nano Lett. 2011, 184, 3361–3365.

(3) Printz, A. D.; Zaretski, A. V; Savagatrup, S.; Chiang, A. S.-C.; Lipomi, D. J. Yield Point of Semiconducting Polymer Films on Stretchable Substrates Determined by Onset of Buckling. ACS Appl. Mater. Interfaces 2015, 7, 23257–23264.

(4) Savagatrup, S.; Makaram, A. S.; Burke, D. J.; Lipomi, D. J. Mechanical Properties of Conjugated Polymers and Polymer-Fullerene Composites as a Function of Molecular Structure. Adv. Funct. Mater. 2014, 24, 1169–1181.

(5) Rodriquez, D.; Kim, J.-H.; Root, S. E.; Fei, Z.; Boufflet, P.; Heeney, M.; Kim, T.-S.; Lipomi, D. J. Comparison of Methods for Determining the Mechanical Properties of Semiconducting Polymer Films for Stretchable Electronics. ACS Appl. Mater. Interfaces 2017, 9, 8855–8862.

(6) Beuth, J. L. Cracking of Thin Bonded Films in Residual Tension. Int. J. Solids Struct. 1992, 29, 1657–1675.

(7) Dundurs, J. Elastic Interaction of Dislocations with Inhomogeneities. In Mathematical Theory of Dislocations; Mura, T., Ed.; American Society of Mechanical Engineers: New York, 1969; pp 70–115.

(8) Xia, Z. C.; Hutchinson, J. W. Crack Patterns in Thin Films. J. Mech. Phys. Solids 2000, 48, 1107–1131.

(9) Griffith, A. A. The Phenomena of Rupture and Flow in Solids. Philos. Trans. R. Soc. 1921, 221, 163–198.

(10) Martinez, A. B.; Gamez-Perez, J.; Sanchez-Soto, M.; Velasco, J. I.; Santana, O. O.; Ll Maspoch, M. The Essential Work of Fracture (EWF) Method - Analyzing the Post-Yielding Fracture Mechanics of Polymers. Eng. Fail. Anal. 2009, 16, 2604–2617.

(11) Cotterell, B.; Reddel, J. K. The Essential Work of Plane Stress Ductile Fracture. Int. J. Fract. 1977, 13, 267–277.

(12) Mai, Y.-W.; Cotterell, B. On the Essential Work of Ductile Fracture in Polymers. Int. J. Fract. 1986, 32, 105–125.

(13) Root, S. E.; Savagatrup, S.; Printz, A. D.; Rodriquez, D.; Lipomi, D. J. Mechanical Properties of Organic Semiconductors for Stretchable, Highly Flexible, and Mechanically Robust Electronics. Chem. Rev. 2017, 117, 6467–6499.

(14) Li, T.; Huang, Z.; Suo, Z.; Lacour, S. P.; Wagner, S. Stretchability of Thin Metal Films on Elastomer Substrates. Appl. Phys. Lett. 2004, 85, 3435–3437.

(15) Rolston, N.; Printz, A. D.; Dupont, S. R.; Voroshazi, E.; Dauskardt, R. H. Effect of Heat, UV Radiation, and Moisture on the Decohesion Kinetics of Inverted Organic Solar Cells. Sol. Energy Mater. Sol. Cells 2017, 170, 239–245.

(16) Mechanical Engineers' Handbook, Volume 1: Materials and Engineering Mechanics., 3rd ed.; Kutz, M., Ed.; John Wiley & Sons, 2015.

(17) Ward, I. M.; Sweeney, J. Mechanical Properties of Solid Polymers, 3rd ed.; John Wiley & Sons, 2012.

(18) Volynskii, A. L.; Bazhenov, S.; Lebedeva, O. V.; Ozerin, A. N.; Bakeev, N. F. Multiple Cracking of Rigid Platinum Film Covering Polymer Substrate. J. Appl. Polym. Sci. 1999, 72, 1267–1275.

(19) Bazhenov, S. L.; Volynskii, A. L.; Alexandrov, V. M.; Bakeev, N. F. Two Mechanisms of the Fragmentation of Thin Coatings on Rubber Substrates. J. Polym. Sci. Part B Polym. Phys. 2002, 40, 10–18.

(20) Volynskii, A. L.; Panchuk, D. A.; Moiseeva, S. V; Kechek'yan, A. S.; Dement'ev, A. I.; Yarysheva, L. M.; Bakeev, N. F. New Approach to Evaluation of the Stress Strain Properties of Nanolayers of Solid Materials. Russ. Chem. Bull. Int. Ed. 2009, 58, 865–882.

(21) Awartani, O.; Lemanski, B. I.; Ro, H. W.; Richter, L. J.; De Longchamp, D. M.; O'Connor, B. T. Correlating Stiffness, Ductility, and Morphology of Polymer:Fullerene Films for Solar Cell Applications. Adv. Energy Mater. 2013, 3, 399–406.

(22) Heinrich, M.; Gruber, P.; Orso, S.; Handge, U. A.; Spolenak, R. Dimensional Control of Brittle Nanoplatelets. A Statistical Analysis of a Thin Film Cracking Approach. Nano Lett. 2006, 6, 2026–2030.

(23) Tahk, D.; Lee, H. H.; Khang, D.-Y. Elastic Moduli of Organic Electronic Materials by the Buckling Method. Macromolecules 2009, 42, 7079–7083.

(24) Koch, F. P. V.; Rivnay, J.; Foster, S.; Müller, C.; Downing, J. M.; Buchaca-Domingo, E.; Westacott, P.; Yu, L.; Yuan, M.; Baklar, M.; Fei, Z.; Luscombe, C.; Mclachlan, M. A.; Heeney, M.; Rumbles, G.; Silva, C.; Salleo, A.; Nelson, J.; Smith, P.; Stingelin, N. The Impact of Molecular Weight on Microstructure and Charge Transport in Semicrystalline Polymer Semiconductors–Poly(3-hexylthiophene), a Model Study. Prog. Polym. Sci. 2013, 38, 1978–1989.

(25) Washiyama, J.; Kramer, E. J.; Hui, C.-Y. Fracture Mechanisms of Polymer Interfaces Reinforced with Block Copolymers: Transition from Chain Pullout to Crazing. Macromolecules 1993, 26, 2928–2934.

(26) Washiyama, J.; Kramer, E. J.; Creton, C. F.; Hui, C.-Y. Chain Pullout Fracture of Polymer Interfaces. Macromolecules 1994, 27, 2019–2024.

(27) Müller, C. On the Glass Transition of Polymer Semiconductors and Its Impact on Polymer Solar Cell Stability. Chem. Mater. 2015, 27, 2740–2754.

(28) Campoy-Quiles, M.; Sims, M.; Etchegoin, P. G.; Bradley, D. D. C. Thickness-Dependent Thermal Transition Temperatures in Thin Conjugated Polymer Films. Macromolecules 2006, 39, 7673–7680.

(29) Wang, T.; Pearson, A. J.; Dunbar, A. D. F.; Staniec, P. A.; Watters, D. C.; Coles, D.; Yi, H.; Iraqi, A.; Lidzey, D. G.; Jones, R. A. L. Competition between Substrate-Mediated π-π Stacking and Surface-Mediated Tg Depression in Ultrathin Conjugated Polymer Films. Eur. Phys. J. E 2012, 35, 129.

(30) Liu, D.; Orozco, R. O.; Wang, T. Deviations of the Glass Transition Temperature in Amorphous Conjugated Polymer Thin Films. Phys. Rev. E 2013, 88, 022601.

(31) Kim, J.-H.; Lee, I.; Kim, T.-S.; Rolston, N.; Watson, B. L.; Dauskardt, R. H. Understanding Mechanical Behavior and Reliability of Organic Electronic Materials. MRS Bull. 2017, 42, 115–123.

(32) Wason, P. C. On the Failure to Eliminate Hypotheses in a Conceptual Task. Q. J. Exp. Psychol. 1960, 12, 129–140.

(33) Goldstein, E. B. Cognitive Psychology: Connecting Mind, Research and Everyday Experience, 3rd ed.; Cengage Learning, 2010.

(34) Seitz, J. T. The Estimation of Mechanical Properties of Polymers from Molecular Structure. J. Appl. Polym. Sci. 1993, 49, 1331–1351.

(35) Roth, B.; Savagatrup, S.; De Los Santos, N. V.; Hagemann, O.; Carlé, J. E.; Helgesen, M.; Livi, F.; Bundgaard, E.; Søndergaard, R. R.; Krebs, F. C.; Lipomi, D. J. Mechanical Properties of a Library of Low-Band-Gap Polymers. Chem. Mater. 2016, 28, 2363–2373.

(36) Root, S. E.; Jackson, N.; Savagatrup, S.; Arya, G.; Lipomi, D. J. Modelling the Morphology and Thermomechanical Behaviour of Low-Bandgap Conjugated Polymers and Bulk Heterojunction Films. Energy Environ. Sci. 2017, 10, 558–569.

(37) Root, S. E.; Savagatrup, S.; Pais, C. J.; Arya, G.; Lipomi, D. J. Predicting the Mechanical Properties of Organic Semiconductors Using Coarse-Grained Molecular Dynamics Simulations. Macromolecules 2016, 49, 2886–2894.

(38) Balar, N.; O'Connor, B. T. Correlating Crack Onset Strain and Cohesive Fracture Energy in Polymer Semiconductor Films. Macromolecules 2017, acs.macromol.7b01282.

(39) McLeish, T. C. B.; Plummer, C. J. G.; Donald, A. M. Crazing by Disentanglement: Non-Diffusive Reptation. Polymer 1989, 30, 1651–1655.

(40) Serier, B.; Bachir Bouiadjra, B.; Belhouari, M. Finite Element Analysis of Bi-Material Interface Notch Crack Behaviour. Comput. Mater. Sci. 2003, 27, 517–522.

(41) Li, T.; Suo, Z. Ductility of Thin Metal Films on Polymer Substrates Modulated by Interfacial Adhesion. Int. J. Solids Struct. 2007, 44, 1696–1705.

(42) Bruner, C.; Dauskardt, R. H. Role of Molecular Weight on the Mechanical Device Properties of Organic Polymer Solar Cells. Macromolecules 2014, 47, 1117–1121.

(43) Kusy, R. P.; Katz, M. J. Effect of Molecular Weight on the Fracture Morphology of Poly(ethytmethacrylate) in Cleavage. J. Mater. Sci. 1976, 11, 1381–1384.

(44) Lee, S.; Moon, G. D.; Jeong, U. Continuous Production of Uniform Poly(3-hexylthiophene) (P3HT) Nanofibers by Electrospinning and Their Electrical Properties. J. Mater. Chem. 2009, 19, 743–748.

(45) Pardoen, T.; Marchal, Y.; Delannay, F. Thickness Dependence of Cracking Resistance in Thin Aluminium Plates. J. Mech. Phys. Solids 1999, 47, 2093–2123.

(46) Lu, N.; Wang, X.; Suo, Z.; Vlassak, J. Metal Films on Polymer Substrates Stretched beyond 50 %. Appl. Phys. Lett. 2007, 91, 221909.

(47) Kim, J.-H.; Nizami, A.; Hwangbo, Y.; Jang, B.; Lee, H.-J.; Woo, C.-S.; Hyun, S.; Kim, T.-S. Tensile Testing of Ultra-Thin Films on Water Surface. Nat. Commun. 2013, 4, 1–6.

(48) Bundgaard, E.; Livi, F.; Hagemann, O.; Carlé, J. E.; Helgesen, M.; Heckler, I. M.; Zawacka, N. K.; Angmo, D.; Larsen-Olsen, T. T.; Dos Reis Benatto, G. A.; Roth, B.; Madsen, M. V.; Andersson, M. R.; Jørgensen, M.; Søndergaard, R. R.; Krebs, F. C. Matrix Organization and Merit Factor Evaluation as a Method to Address the Challenge of Finding a Polymer Material for Roll Coated Polymer Solar Cells. Adv. Energy Mater. 2015, 5, 1402186.

(49) Plimpton, S. Fast Parallel Algorithms for Short-Range Molecular Dynamics. J. Comput. Phys. 1995, 117, 1–19.

(50) Stukowski, A. Visualization and Analysis of Atomistic Simulation Data with OVITO–the Open Visualization Tool. Model. Simul. Mater. Sci. Eng. 2010, 18, 015012.

(51) Jackson, N. E.; Kohlstedt, K. L.; Savoie, B. M.; Olvera de la Cruz, M.; Schatz, G. C.; Chen, L. X.; Ratner, M. A. Conformational Order in Aggregates of Conjugated Polymers. J. Am. Chem. Soc. 2015, 137, 6254–6262.

(52) John, T.; Cockerill, T.; Foster, I.; Gaither, K. XSEDE: Accelerating Scientific Discovery. Comput. Sci. Eng. 2014, 16, 62–74.

(53) Kroon, R.; Gehlhaar, R.; Steckler, T. T.; Henriksson, P.; Müller, C.; Bergqvist, J.; Hadipour, A.; Heremans, P.; Andersson, M. R. New Quinoxaline and Pyridopyrazine-Based Polymers for Solution-Processable Photovoltaics. Sol. Energy Mater. Sol. Cells 2012, 105, 280–286.

(54) Root, S. E.; Alkhadra, M. A.; Rodriquez, D.; Printz, A. D.; Lipomi, D. J. Measuring the Glass Transition Temperature of Conjugated Polymer Films with Ultraviolet-Visible Spectroscopy. Chem. Mater. 2017, 29, 2646–2654.

Appendix A

Supporting information for Chapter 2

Predicting the Mechanical Properties of Organic Semiconductors Using Coarse-Grained Molecular Dynamics Simulations

Samuel E. Root, Suchol Savagatrup, Christopher J. Pais,

Gaurav Arya, and Darren J. Lipomi

Department of NanoEngineering, University of California, San Diego

9500 Gilman Drive, Mail Code 0448, La Jolla, CA 92093-0448

A.1 Complete Description of Model Parameters

A1.1 Three-Site Model

The parameters for the three-site model were derived using the iterative Boltzmann inversion technique described in detail in reference 1. We note that the intramolecular potential parameters used here are from reference 5, they are slightly modified from the original publication to better represent the rigidity of the thiophene rings (intermonomer torsion) as described in detail in reference 2. In addition to this, the intermolecular parameters were fit to a Lennard-Jones 9-6 potential instead of using the tabulated potential described in reference 1.

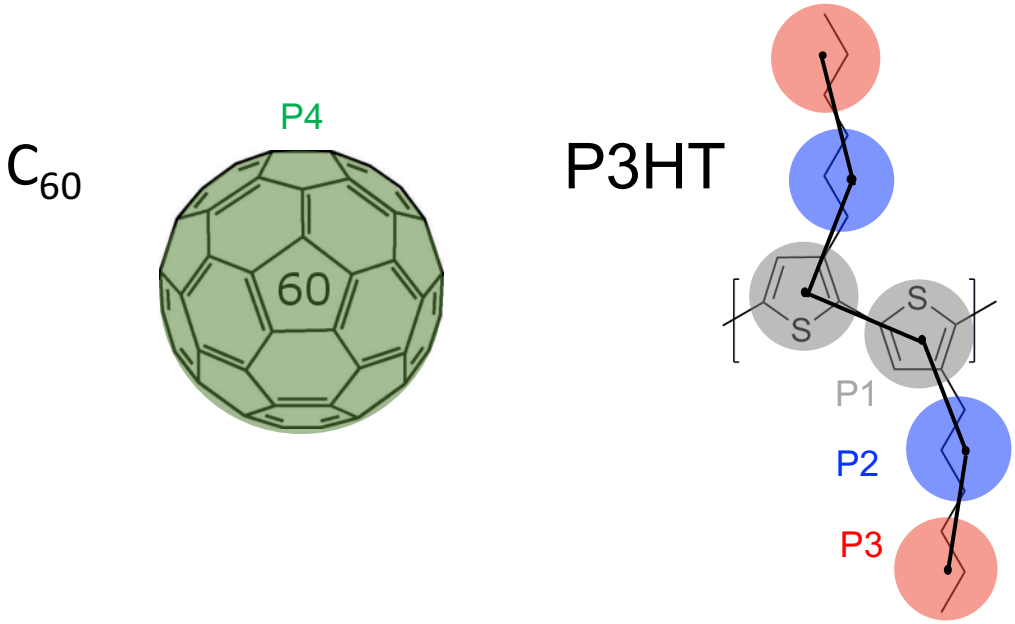

Figure A.1. Coarse-grained mapping for the three-site model for P3HT:C_{60}.

Table A.1. Intermolecular potentials and parameters for three-site model, coarse-grained bead definitions are given in Figure **S1.**

Intermolecular Potentials

$$E(r) = 4\epsilon\left[\left(\frac{\sigma}{r}\right)^9 - \left(\frac{\sigma}{r}\right)^6\right]$$

$$E(r) = 4\epsilon\left[\left(\frac{\sigma}{r-\Delta}\right)^{12} - \left(\frac{\sigma}{r-\Delta}\right)^6\right]$$

Pairwise Interaction	σ [Å]	ϵ [kcal mol^{-1}]	Δ [Å]	Cutoff [Å]
P1-P1	4.6	0.35	-	15
P1-P2	4.3	1.45	-	15
P1-P3	4.71	0.51	-	15
P2-P2	4.7	1.57	-	15
P2-P3	4.8	0.9	-	15
P3-P3	4.89	0.55	-	15
P4-P1	5.3	1.37	1.4	16.6
P4-P2	5.3	2.35	1.7	16.4
P4-P3	5.3	1.32	1.8	16.2
P4-P4	3.841	5.55	5.76	12.234

Table A.2. Intramolecular potentials and parameters used for the three-site model, coarse-grained bead definitions are given in Figure **S1.**

Intramolecular Potentials

$$E_{bond}(l) = \sum_{i=2}^{n} c_i (l - l_0)^i$$

Bonded Interaction	l_0 [Å]	c_2 [kcal/mol/Å^2]	c_3 [kcal/mol/Å^3]	c_4 [kcal/mol/Å^4]	c_5 [kcal/mol/Å^5]	c_6 [kcal/mol/Å^6]	c_7 [kcal/mol/Å^7]	c_8 [kcal/mol/Å^8]
P1-P1	3.862	74.8542	--	--	--	--	--	--
P1-P2	4.095	58.818	175.482	146.518	--	--	--	--
P2-P3	3.5786	20.8811	-12.6477	-161.456	-50.2732	634.945	941.494	392.644

$$E_{angle}(\theta) = \sum_{i=0}^{n} c_i (\theta - \theta_0)^i$$

Angular Interactions	θ_0 [deg.]	c_2 [kcal/mol/rad^2]	c_3 [kcal/mol/rad^3]	c_4 [kcal/mol/rad^4]
P1-P1-P1	163.161	11.256	49.983	109.974
P1-P2-P3	157.196	9.415	10.9533	4.66974
P1-P1-P2	123.473	--	-14.3575	61.8653
P2-P1-P1	78.904	--	-2.27575	35.9306

$$E_{dihed}(\phi) = \sum_{i=0}^{n} c_i cos^i(\phi)$$

Dihedral Interactions	c_1 [kcal/mol]	c_2 [kcal/mol]	c_3 [kcal/mol]	c_4 [kcal/mol]	c_5 [kcal/mol]
P1-P1-P1-P1	1.00335	-0.098468	-0.145065	-0.596209	-0.22064
P2-P1-P1-P2	1.43524	0.323256	-1.31207	0.357231	0.557297
P1-P1-P2-P3	0.217212	-0.603055	0.194054	0.349013	-0.004806
P3-P2-P1-P1	-0.017475	0.018428	0.4546	0.116077	-0.075817

$$E_{imp}(\varphi) = c_2(\varphi - \varphi_o)^2$$

Improper Interactions	φ_o [deg.]	c_2 [kcal/mol/rad^2]
P1-P2-P1-P1	0.00	45.3281

A.1.1 One-Site Model

The parameters for the one-site model were taken directly from reference 3. We note that we also implemented the stylistically similar potential described in reference 4, and observed similar results.

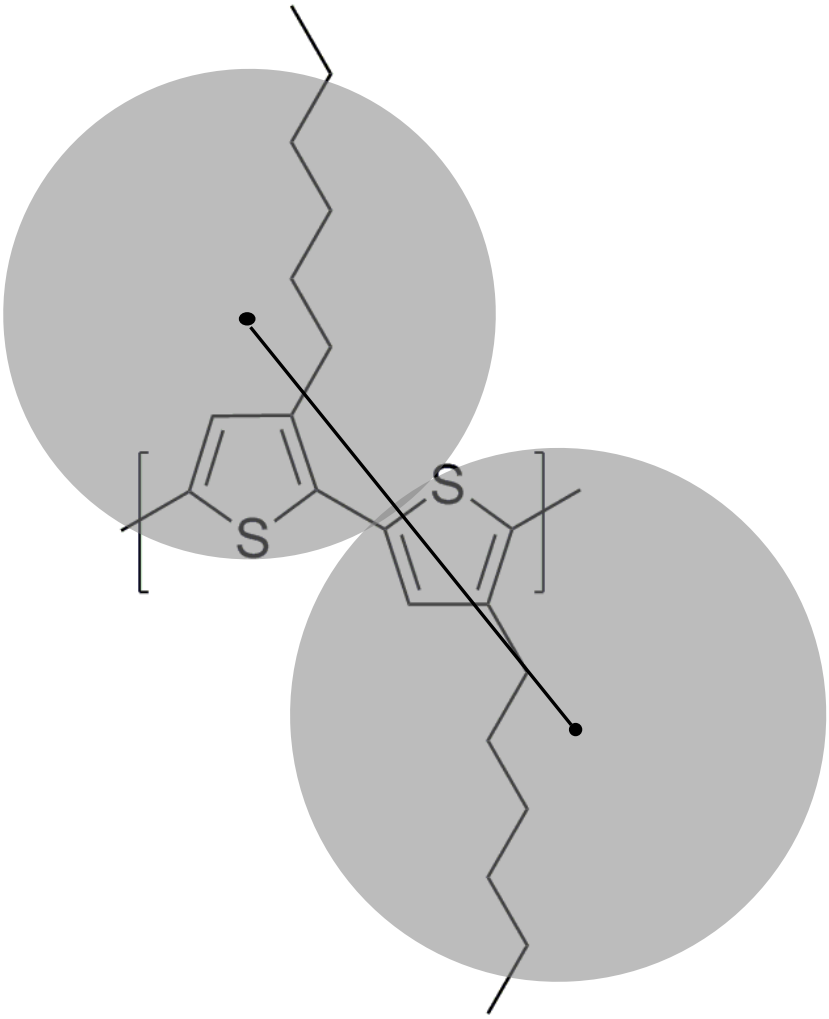

Figure A.2. Coarse-grained mapping for the one-site model for P3HT.

Table A.3. Intra/intermolecular potentials and parameters used for the one-site model representing P3HT, coarse-grained bead definitions are given in Figure **S2**.

	Intra/intermolecular Potential	Parameters
Bond	$E_{bond}(l) = \frac{k_b}{2}(l - l_0)^2$	k_b = 216.19 kcal mol^{-1} Å^{-2} l_0 = 3.82 Å
Angle	$E_{angle}(\theta) = \frac{k_\theta}{2}(\theta - \theta_0)^2$	k_θ = 130.25 kcal mol^{-1} rad^{-2} θ_0 = 2.65 rad
Dihedral	$E_{dihed}(\phi) = \frac{V_1}{2}(1 + cos\phi) + \frac{V_2}{2}(1 - cos2\phi) + \frac{V_3}{2}(1 + cos3\phi)$	V_1 = 0.56 kcal mol^{-1} V_2 = -1.08 kcal mol^{-1} V_3 = 0.28 kcal mol^{-1}
Van Der Waals	$E_{VDW}(r) = 4\epsilon[\left(\frac{\sigma}{r}\right)^{12} - \left(\frac{\sigma}{r}\right)^{6}]$	ϵ = 0.26 kcal mol^{-1} σ = 4.95 Å

A.2. Analysis of Entanglements using Z1 Code

To compare the density of entanglements in the pure and composite systems we applied the Z1 algorithm developed by Kröger et al. (references 6-9) to compute the primitive paths of the polymer chains, shown in Figure S3. The physical quantities obtained from this analysis are shown in **Table A.4**. Briefly, the quantity $\langle Z \rangle$ represents the average number of interior kinks per chain, $\langle L_{pp}^2 \rangle$ is average squared contour length between interior kinks and Ne is entanglement length which varies depending on which estimator is used (modified S-kink vs. modified S-coil), for a detailed explanation of these estimators see ref. 7.

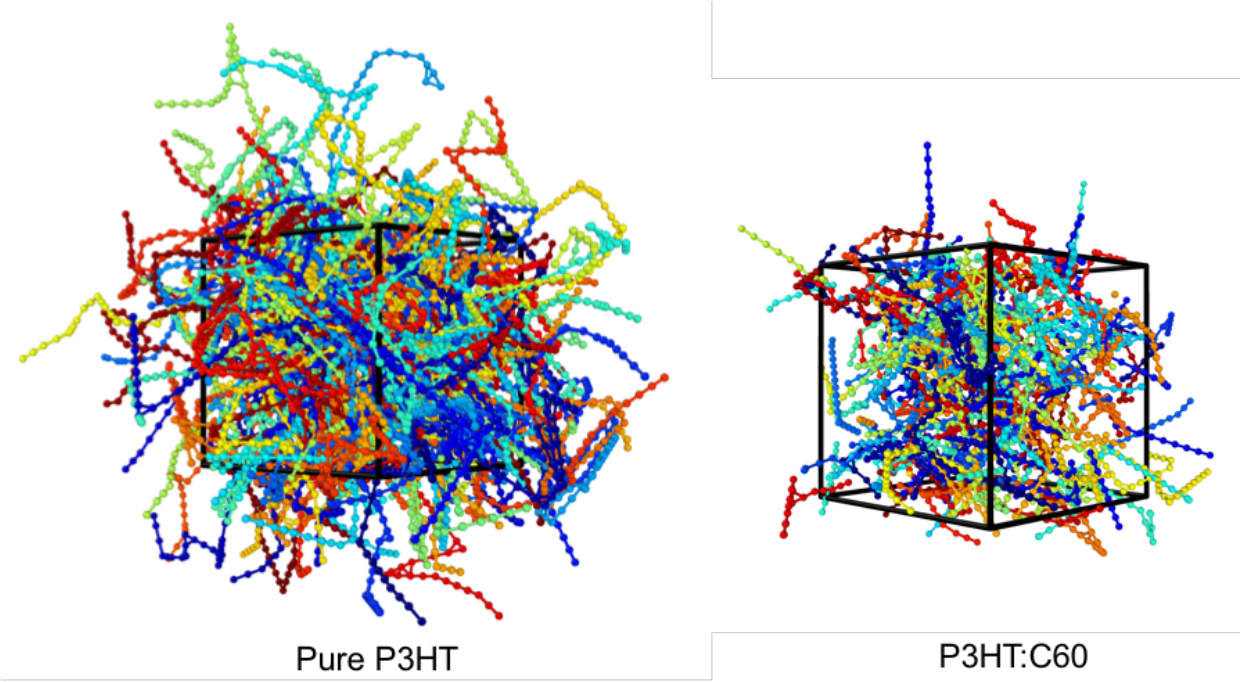

Figure A.3. Plots showing the primitive paths obtained using the Z1 algorithm

Table A.4. Physical parameters obtained from the Z1 primitive path analysis.

	$\langle Z \rangle$	$\langle L_{pp}^2 \rangle$ [Å]	Ne modified S-kink	Ne modified S-coil
Pure P3HT	7.0467	352.2057	21.2867	41.3626
P3HT:C60	2.4	140.0633	62.5	106.8907

A.3 Extension of Three-Site Model Using Original Interaction Parameters

In an attempt to describe a range of P3AT's with different alkyl side-chain lengths (hexyl, nonyl, and dodecyl), we modified the original three-site model for P3HT to include extra coarse-grained beads on the side chain as shown in Figure **A.3a**. Our simulations for the stress-strain response of these materials (Figure **A.3b)** showed that the tensile modulus increased with side-chain length, which is contrary to experimental results. Upon closer inspection of the interaction parameters from the original model (Table **S1**) we noted that the interactions between the side chains were stronger than the interactions between the thiophene rings in the backbone. We attribute this to the simultaneous nature in which these parameters were optimized, leading to a model that worked correctly for P3HT, but that was not transferable across a range of chemical structures.

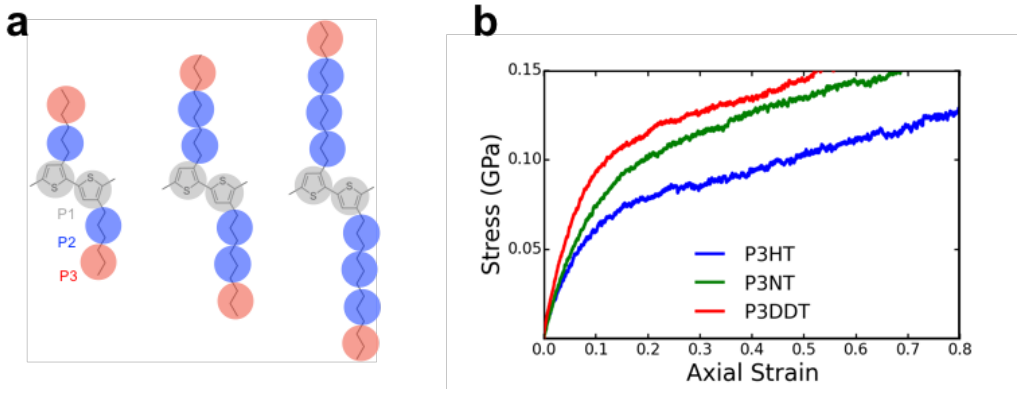

Figure A.4. Extension made to the three-site model to describe P3AT's (a) extension of alkyl side-chain using coarse-grained bead definitions from Figure **S1** and Table **S1, S2.** (b) Initial results showing increasing tensile modulus with side-chain length (in contradiction with experimental results, indicating limited transferability of the model.)

A.4 References

(1) Huang, D. M.; Faller, R.; Do, K.; Moule, A. J. Coarse-Grained Computer Simulations of Polymer / Fullerene Bulk Heterojunctions for Organic Photovoltaic Applications. *J. Chem. Theory Comput.* **2010**, *6*, 526-537.

(2) Schwarz, K. N.; Kee, T. W.; Huang, D. M. Coarse-Grained Simulations of the Solution Phase Self-Assembly of poly(3-Hexylthiophene) Nanostructures. *Nanoscale* **2013**, *5* (5), 2017-2027.

(3) Lee, C.-K.; Pao, C.-W.; Chu, C.-W. Multiscale Molecular Simulations of the Nanoscale Morphologies of P3HT:PCBM Blends for Bulk Heterojunction Organic Photovoltaics *Energy Environ. Sci.* **2011**, *4*, 4124-4132.

(4) Lee, C. K.; Pao, C. W. Nanomorphology Evolution of P3HT:PCBM Blends during Solution Processing from Coarse-Grained Molecular Simulations *J. Phys. Chem. C* **2014**, *118*, 11224-11233.

(5) Jones, M. L.; Huang D.M.; Chakrabarti, B.; Groves, C. Relating Molecular Morphology to Charge Mobility in Semicrystalline Conjugated Polymers. *J. Phys. Chem C.* **2016**, 8, 4240-4250.

(6) Kröger, M. Shortest Multiple Disconnected Path for the Analysis of Entanglements in Two- and Three-Dimensional Polymeric Systems. *Comput. Phys. Commun.* **2005**, *168*, 209–232.

(7) Hoy, R. S.; Foteinopoulou, K.; Kröger, M. Topological Analysis of Polymeric Melts: Chain-Length Effects and Fast-Converging Estimators for Entanglement Length. *Phys. Rev. E - Stat. Nonlinear, Soft Matter Phys.* **2009**, *80*, 14–16.

(8) Shanbhag, S.; Kröger, M. Primitive Path Networks Generated by Annealing and Geometrical Methods: Insights into Differences. *Macromolecules* **2007**, *40*, 2897–2903.

Appendix B

Supporting information for Chapter 3

Modelling the morphology and thermomechanical behaviour of low-bandgap conjugated polymers and bulk heterojunction films

Samuel E. Root, Nicholas Jackson, Suchol Savagatrup,
Gaurav Arya, and Darren J. Lipomi

Department of NanoEngineering, University of California, San Diego

9500 Gilman Drive, Mail Code 0448, La Jolla, CA 92093-0448

B.1 Simulation Details

B.1.1 General Remarks

In all the simulations described in this article the following algorithms and software were used.

1) The shake algorithm was employed to constrain bonds containing Hydrogen atoms to fixed distances. The algorithm used is standard in the LAMMPS simulation package.

2) The Velocity Verlet algorithm was used for integrating the equations of motion

3) The Particle-Particle/Particle-Mesh (PPPM) algorithm was used for treating long-range electrostatic interactions.

4) The molecular dynamics simulation package LAMMPS was used for all simulations.[1]

5) The visualization package OVITO was used for all visualizations.[2]

6) Simulation initialization and post-processing was performed using custom python scripts.

7) All uncertainty quantification was performed by taking the average and standard deviation from a total of three randomly generated initial configurations subjected to analogous MD simulation protocols.

B.1.2 Melt-Phase System Initializations

Isolated chains in the fully extended conformation were first subjected to elevated temperature (800 K) simulations using Langevin dynamics (damping parameter = 3800 fs, time step = 2 fs). Random conformations were outputted on nanosecond intervals. This protocol resulted in 60 uncorrelated chain conformation for each polymer simulated. These chains were next assigned a randomly generated centre of mass and orientation with respect to an orthorhombic, periodic simulation box at a mass density of 0.01 g cm^{-3}. Placement of chains was constrained such that no two atoms on different chains were within 20 Å of another. This was especially important for simulations containing $PC_{71}BM$, as to avoid

spearing the fullerene cage, which would result in unstable dynamics. The randomly generated configurations were next subjected to a conjugate-gradient energy minimization to further ensure that there were no unphysical interactions to make the simulation unstable in the first couple of time steps. Next, the temperature was ramped from 0 to 800 K over the course of 1 ns using Langevin dynamics (damping parameter = 3800 fs, dielectric constant = 9.8). Next, a Nosé-Hoover style barostat (time constant = 1000 fs) was used to relax the simulation box at 1 atmosphere of pressure until the density converged to the equilibrium melt-phase value at 800 K and 1 atm over the course of 5 ns. For all bulk heterojunction simulations, a mass fraction of 1:1.5 polymer: PCBM was used. This composition is consistent with experimentally optimized devices.

B.1.3 Equilibrium Sampling Parameters

A Nosé-Hoover style thermostat (time constant = 100.0 fs) and barostat (time constant = 1000.0 fs) was used to simulate the NPT equilibrium dynamics of the polymeric melts and composites. The dielectric was set to 1.0 and a Verlet neighbour list was employed for MPI parallelization. Simulations were run using 24 processors. A time step of 1.5 fs was used for the remaining simulations.

B.1.4 Annealing Protocol

The melt-phase structures were subjected to an annealing protocol in which the temperature was ramped in 20 K intervals from 800 K to 100K using 1 ns for both the ramping and equilibration runs. All of the thermodynamic parameters were outputted periodically (0.01 ns intervals). This resulted in a total of 70 ns of simulation for each system. The configurations obtained at 600 K were further subjected to 5 ns of dynamics

to generate the equilibrium melt-phase statistics presented in the main document. The configurations obtained at 300 K (in the glassy state) are denoted as the *melt-quenched* morphology (**Figure B.1**) and were used for the uniaxial tensile loading simulations.

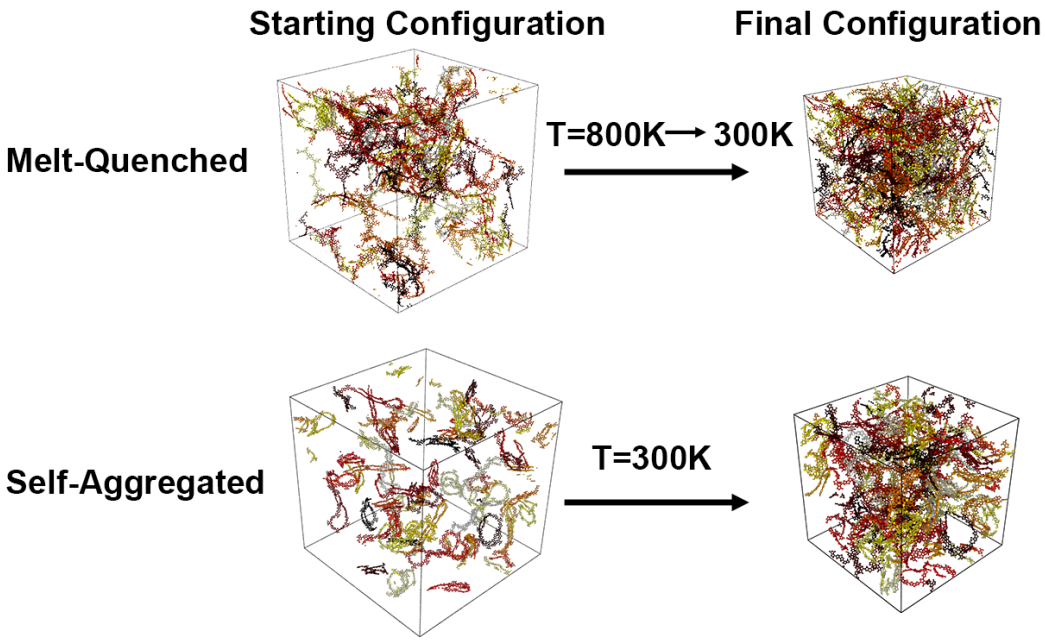

Figure B.1. Trajectory snapshots illustrating the difference between the two simulation protocols employed in this work. While neither morphology is in a state of equilibrium, the *self-aggregated* morphology is further from equilibrium than the *melt-quenched* morphology.

B.1.5 Determination of Glass Transition Temperature

The glass transition temperature for each system was computed by taking the average density from the second half (0.5 ns) of the annealing simulations and plotting the results against the temperature. A custom algorithm was used to perform a bilinear regression on the data and find the best fit to both the melt and glassy regions. The glass transition temperature was taken as the intersection of the linear fits. The algorithm works by scanning through all the possible bilinear regressions and finding the one that gave the

maximum value for the sum of the R^2 values as shown in **Figure B.2a**. A spacing of 16 data points between linear fits was used due to the width of the glass transition region that results from the rapid quenching (**Figure B.2b)**.

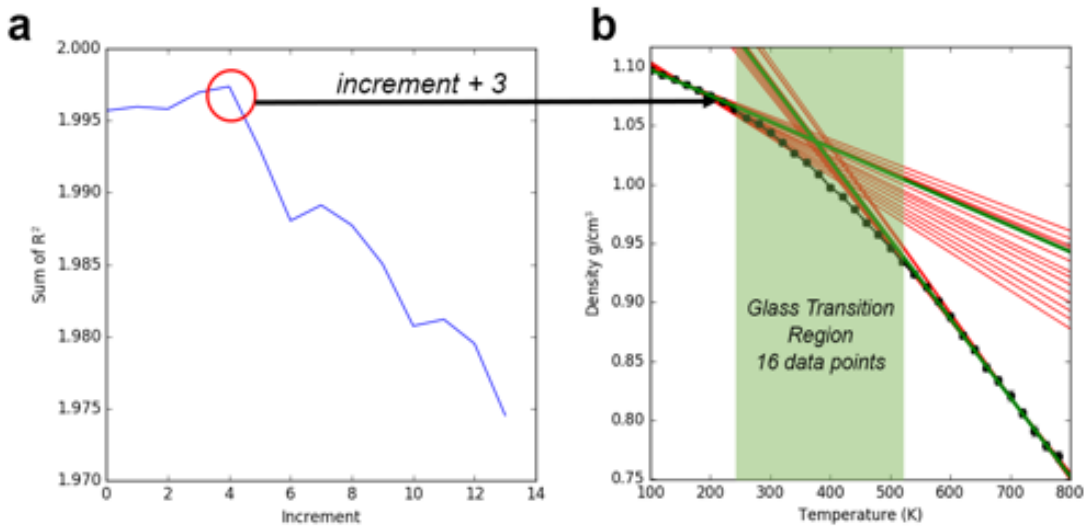

Figure B.2. Schematic diagram illustrating algorithm for predicting the glass transition temperature from simulation data (TQ1). (a) Plot of sum of R^2 of the two fits against the increment of fitting. (b) Corresponding thermal data showing non-optimal fits in red and optimal fit in green.

B.1.6 Isolated Chain Simulated Annealing

Simulated annealing was performed on individual chains in the implicitly solvated state. A dielectric constant of 4.8 and a damping parameter of 3800 fs was used with Langevin dynamics to mimic the effect of dissolution in chloroform. The same chains conformations generated from the melt-phase initialization were subjected to further randomization at 800 K for 1 ns and then linearly cooled to 300 K over the course of 5 ns to generate folded configurations. Simulations were repeated 60 times per polymer chain.

B.1.7 Self-Aggregated Morphology Initialization

The *self-aggregated* morphology was initialized using the 60 independently generated chain conformations, outputted in the isolated chain annealing simulations described in the previous section. These chain conformations were also used to gather the statistics for the conformational class analysis shown in **Figure 3.7a** of the main text. The chain conformations were randomly oriented and positioned in an orthorhombic, periodic simulation box subject to a non-overlapping condition at a mass density of 0.01g cm^{-1}. NPT dynamics were run using a Nosé-Hoover style thermostat (time constant = 100.0 fs) and barostat (time constant = 1000.0 fs) until the density converged (5 ns). The morphologies generated contained large voids, and were far from equilibrium. A schematic representation of the simulation protocol is given in **Figure B.1.**

B.1.8 Uniaxial Tensile Loading

The mechanical deformation simulations were run by imposing a constant strain rate ($1x10^{-6}$ Å ps^{-1}) in the x-dimension and applying a stress-free boundary condition in both transverse dimensions. The stress-strain curve was obtained using a moving average (window size = 1000 fs, 10 fs increments) of axial component of the virial stress tensor, as described previously.[3]

B.2 In-Depth Analysis of Simulation Results

B.2.1 Dihedral Statistics

The dihedral probability distributions obtained from the melt-phase simulations (T=600 K, p=1 atm) can be further analysed to obtain the fraction of conjugated unit pairs in syn vs. anti and conjugated vs. non-conjugated conformations. The results of our analysis are shown in Table 1. Based on this data we see that TQ1 has the highest preference of Syn conformations, while PTB7 and PDTSTPD have similar conformational preferences. Additionally, we see that PDTSTPD is the most conjugated followed by PTB7 and TQ1. These conformational statistics represent testable

Table B.1. Quantitative analysis of dihedral statistics obtained at (T = 600K, p= 1 atm).

Polymer	Syn	Anti	Non	Conj
PTB7 (AD)	0.25	0.39	0.36	0.64
PTB7 (DA)	0.40	0.37	0.22	0.77
PTB7 (AVG)	0.325	0.38	0.29	0.7
TQ1	0.50	0.18	0.32	0.68
PDTSTPD	0.37	0.35	0.277	0.72

B.2.2 Tangent Correlation Function Fitting

One of the most interesting findings that resulted from our simulations was the observation of oscillatory tangent correlation functions in the melt and isolated chain states. For typical semi-flexible polymers, the tangent correlation function can be fit to an exponential decay to find the persistence length. As shown in **Figure B.3**, an exponential decay did not give a satisfactory fit to the simulation data. The tangent correlation function of a worm-like chain can be expressed as:

$$\left\langle \hat{t}_i \cdot \hat{t}_{i+j} \right\rangle_j = e^{-\frac{lj}{L_p}} \qquad (1)$$

where $\hat{t}_i$ is the unit tangent vector of ith unit, L_p is the persistence length, and l is the monomer length which we took to be the average of the length of the donor and the acceptor.

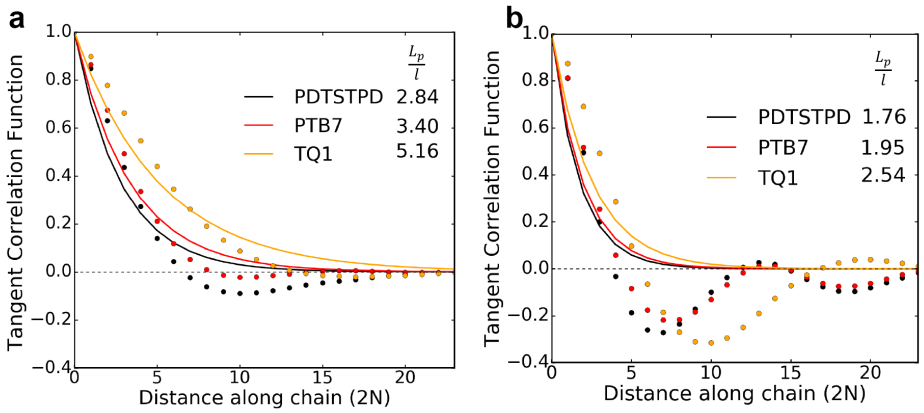

Figure B.3. Plots showing fits to tangent correlation functions obtained from the (a) melt-phase and the (b) isolated chain annealing simulations to an exponentially decaying function. It can be clearly seen that the worm-like chain model cannot be used to adequately describe these chains.

A literature search subsequently revealed that an oscillatory tangent correlation function has been derived analytically for a ribbon-like chain.[5] This behaviour is apparently the result of a coupling between torsional and bending degrees of freedom. An analytical solution for the tangent correlation function of a "developable ribbon" is given by the following functional form:

$$\langle \hat{t}_i \cdot \hat{t}_{i+j} \rangle_j = e^{-\frac{lj}{L_p}} \cos\left(\frac{lj}{\lambda}\right) \qquad (2)$$

Here ω is the folding wavelength. In the limiting case of $\frac{L_p}{\lambda} \rightarrow 0$, this equation reduces to (1). Fits of this functional form to the simulation data for both morphologies are given in **Figure B.4**. They are clearly better than a worm-like chain, however, they are still not perfect. Especially for the chains in the *self-aggregated* morphology.

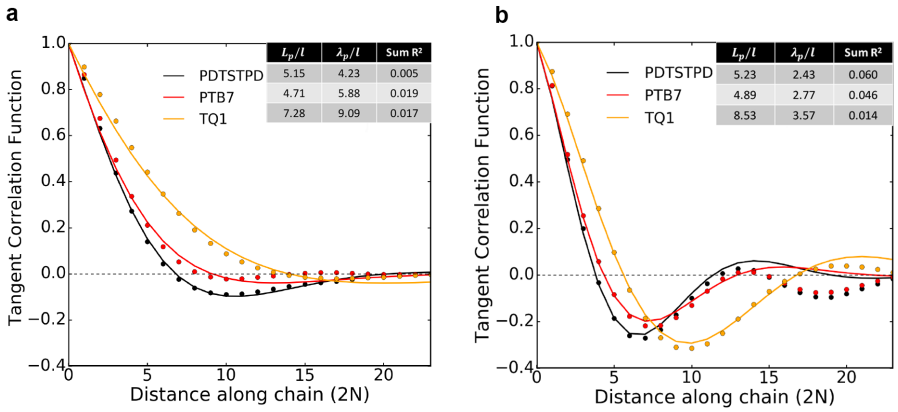

Figure B.4. Plots showing fits of tangent correlation functions obtained from the (a) melt-phase and the (b) isolated chain annealing simulations to an exponentially decaying

Even with the imperfect fit, this model enables a quantitative comparison of the stiffness and folding wavelength of these polymers. We find that in both morphologies TQ1 is the stiffest and has the longest folding wavelength. On the other hand, PDTSTPD

(which is known experimentally to be the most ordered of the three) has shortest folding wavelength and shortest persistence length. PTB7 is intermediate in both cases.

The imperfect fitting of equation (2) to the simulation data implies that there are multiple modes of tangent correlation decay and folding in these polymers. We found that a series expansion of equation (2) into equation (3) gave excellent fits to the simulation data, as shown in the main text.

$$\left\langle \hat{\mathrm{t}}_{\mathrm{i}} \cdot \hat{\mathrm{t}}_{\mathrm{i+j}} \right\rangle_j = \sum_{n=1}^{3} A_n e^{-jl/L_{pn}} \cos(lj/\lambda_n) \qquad (3)$$

All fits were performed using the curve_fit() function available in the Scipy module for Python. This function performs a non-linear least squares algorithm. The quality of the fit can be determined by the sum of the residuals squared (Sum R^2). A smaller Sum R^2 signifies a better fit. As shown in **Table B.2**, fits of eq (3) to the data provide the best fits, although eq (2) still provides a reasonable fit (**Figure B.4**)

Table B.2. Coefficients obtained from fitting tangent correlation functions to equation (3).

	Polymer	l (Å)	A_1	L_{p1}/l	λ_{p1}/l	A_2	L_{p2}/l	λ_{p2}/l	A_3	L_{p3}/l	λ_{p3}/l	Sum of R^2
Kinetic	PDTSTPD	6.01	0.80	7.04	2.22	0.16	29.55	4.8	0.04	7.17	1.10	0.0003
	PTB7	6.4	0.51	9.07	2.22	0.39	10.45	4.54	0.10	4.54	1.07	0.0004
	TQ1	4.2	0.55	11.25	4.54	0.43	12.43	2.85	0.02	3.43	1.30	6e-05
Thermodynamic	PDTSTPD	6.01	.82	5.77	4.87	0.19	5.9	2.48	0.0	-	-	0.0008
	PTB7	6.4	0.56	5.65	3.22	0.45	8.16	9.98	0.0	-	-	0.0009
	TQ1	4.2	0.63	7.86	5.05	0.377	16.2	14.51	0.0	-	-	7.9e-05

B.2.3 Ramachandran Plots

To investigate the handedness of the helical polymer structure, we borrowed a technique commonly used in the analysis of protein structures. A Ramachandran plot is a 2D correlation map of two consecutive dihedral angles along the contour of the polymer back bone.[6] The presense of asymetry in the correlation map indicates the handedness (or lack thereof) of the helical pitch. Ramachandran plots obtained from the melt phase are shown in **Figure B.5.** We used a bin size of 10 degrees to compute the 2D histogram. We found that the plots exhibited symetric correlations, indicating that the helices have no preferred handedness.

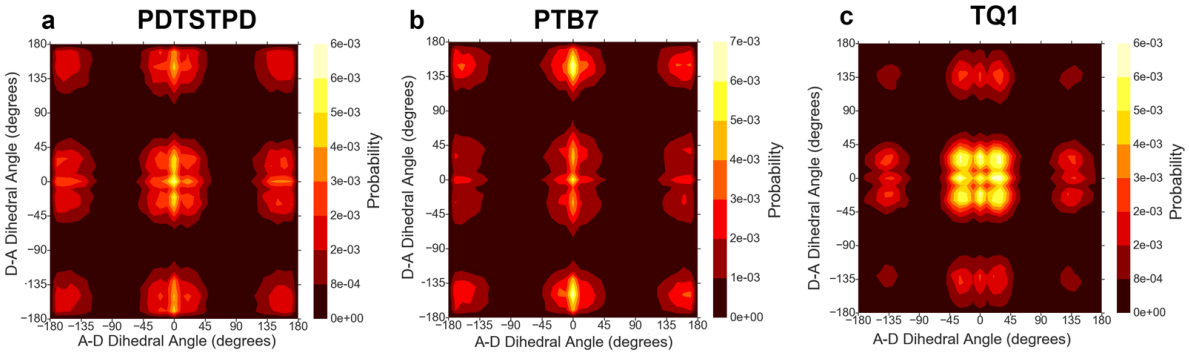

Figure B.5. Ramachandran plots showing correlation maps for consecutive dihedral angles along the polymer backbones. a) PDTSTPD, b) PTB7 and c) TQ1.

B.2.4 Pair Distribution Functions

The pair distribution functions shown in Figure 3.4 of the main text were calculated by first finding the centre of mass of each donor, acceptor, and C70 fullerene unit. Next all of the pairwise distances were binned using an increment of $\boldsymbol{\delta}$ =0.5Å into a histogram of intermolecular **separations**, $\boldsymbol{C_i}$. Finally we applied equation (4) to average and normalize $\boldsymbol{C_i}$ over each simulation snapshot to calculate the pair distribution function:

$$g_{\alpha\beta}(i\delta) = \frac{C_i}{\tau N_\alpha N_\beta} \times \frac{V}{\frac{4\pi}{3}\delta^3((i+1)^3 - i^3)} \quad (4)$$

Here N_α, N_β are the number of particles of type α, β in the system (for the case $\alpha = \beta,\ N_\beta \rightarrow (N_\alpha - 1)/2$), τ is the number of frames that were averaged over, and V is the volume of the simulation box. Pair distribution functions shown were averaged over three independent initial configurations to obtain smooth distributions. We note, however, that the features were observed to be consistent between these runs indicating that the systems were well-equilibrated in the melt phase at 600K and 1atm.

For the acceptor unit of both PTB7 and PDTSTPD we observed a broad peak in the pair distribution function at a distance of 13 and 14 Å respectively. We have rationalized these peaks geometrically as evidence of inter-digitation of side chains. As can be seen in **Figure B.6**, when the side chains of the acceptor unit of PDTSTPD are stacked, the acceptor units are separated by ~14Å.

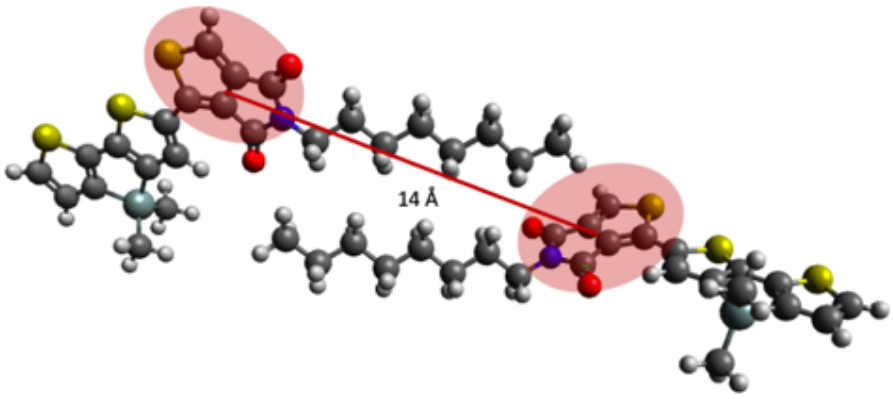

Figure B.6. Diagram illustrating argument ascribing the broad peak in the pair distribution function for PDTSTPD to side chains interdigitating. A similar argument can be made for PTB7.

B.2.5 Classification of Chain Conformations

The chain conformations produced from the isolated chain annealing simulations were classified as either globular, toroidal, folded, or extended according to an analysis of their size, order, and pattern of the orientational contact maps (shown in the main text). We employed the Landau-De Gennes **Q**-tensor to characterize the conformational order present in the isolated chain aggregates.[7] This generalized order parameter can be written as:

$$Q_{\alpha\beta} = \langle \frac{3}{2}\hat{\mathbf{t}}_{\mathbf{i\alpha}}\hat{\mathbf{t}}_{\mathbf{i\beta}} - \frac{1}{2}\delta_{\alpha\beta} \rangle \qquad (5)$$

Here $\hat{\mathbf{t}}_{\mathbf{i\alpha}}$ represents the tangent vector of the ith unit along the backbone of the polymer, δ is the Kronecker delta, and α, β denote Cartesian dimensions. The bracket signifies an average over all the conjugated units in the polymer backbone. To compare the degree of ordering across chains, the maximum eigenvalue of this tensor, *S,* was computed. By construction, $S = 1$ corresponds to a perfectly straight chain and $S = 0$ corresponds to a completely random globule.

The sizes of the chains were compared using two metrics. The radius of gyration, and the length of the end-to-end vector, $|\vec{R}|$. The end-to-end vector was important for distinguishing between self-aggregated and extended chains. We defined the normalized end-to-end vector as $\frac{|\vec{R}|}{l}$ in order to make systematic comparisons across the three materials. Recall that l is the length of the donor and acceptor units averaged.

Extended Chains: Chains were classified as extended if $\frac{|\vec{R}|}{l}$ was greater than 6. Extended chains could be either ordered (completely straight) or disordered. The key distinguishing factor for this class of conformations was the lack of self-aggregated π-stacking.

Globular Chains: Chains were classified as globular if $\frac{|\vec{R}|}{l}$ was less than 6 and if the maximum eigenvalue of their Q-tensor was greater than 0.20. If these two conditions were met, the contact map and the 3D structure of the chain looked disordered.

Folded Chains: Chains were classified as folded if $\frac{|\vec{R}|}{l}$ was less than 6 and if the maximum eigenvalue of their Q-tensor was less than 0.20 and if the orientational contact maps exhibited a blocky structure.

Toroidal Chains: Chains were classified as toroidal if $\frac{|\vec{R}|}{l}$ was less than 6 and if the maximum eigenvalue of their Q-tensor was greater than 0.20 and if the orientational contact maps exhibited a diagonal structure.

In all cases the chains were visually inspected to ensure correct classification. We found that the most difficult conformations to distinguish were the toroidal and the folded. Threshold values could not be set, and we had to rely on visual inspection of the orientational contact maps and the 3-dimensional structure.

B.2.6 Self-Aggregated Morphology Statistics

Although the *self-aggregated* morphology is far from equilibrium and not amenable to efficient sampling, the large system size simulated allows us to obtain a quantitative

picture of the nanoscale morphology. The results of for the intermolecular pair distribution functions and dihedral distributions are shown in **Figure B.7.** It can be seen clearly that intermolecular coupling between donor and acceptor units is severely diminished. This intuitively makes sense as the self-aggregated chains have less "free" conjugated units to form intermolecular aggregates. Comparing across the three materials, we see that TQ1 retains the most intermolecular aggregates, followed by PTB7 and then PDTSPTD. This makes sense, as TQ1 had the highest fraction of globular chains and PTB7 and TQ1 both had similar fractions of extended chains. PDTSTPD on the other hand formed almost exclusively toroidal and folded chain structures.

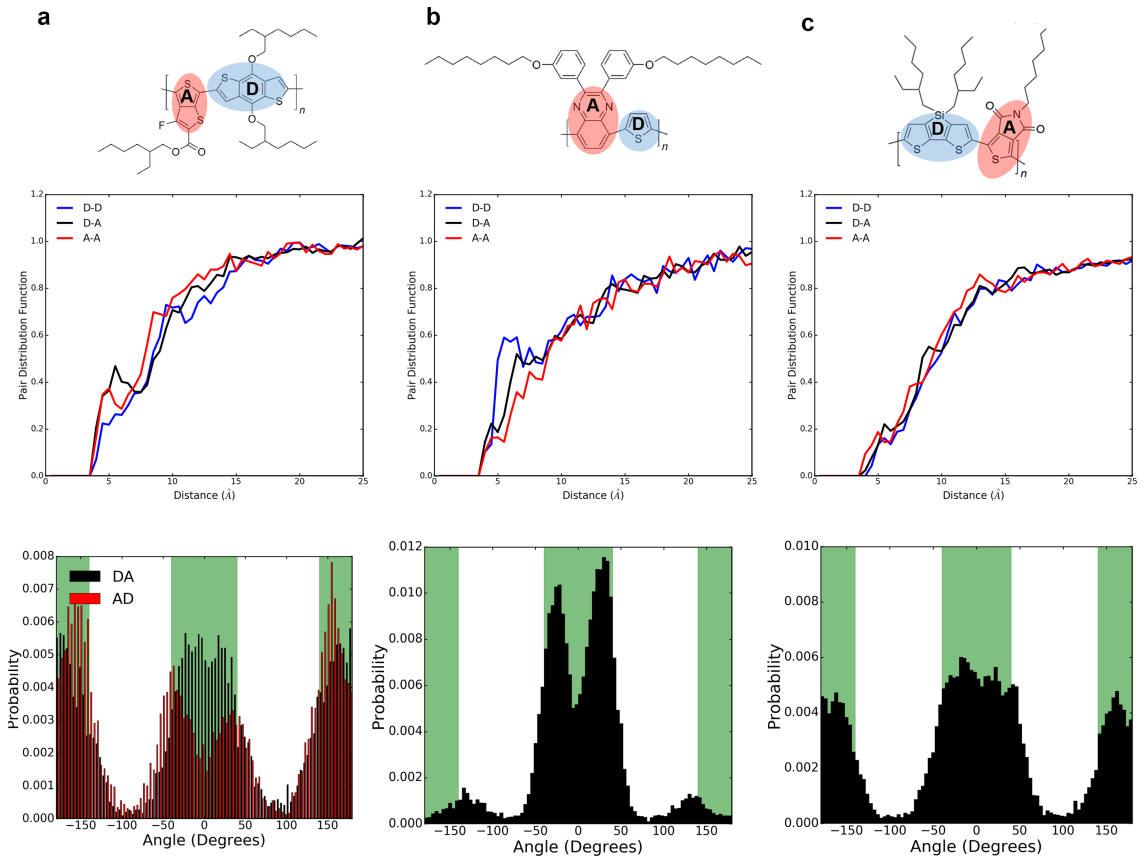

Figure B.7. Results for the pair distribution functions and dihedral distributions obtained from the self-aggregated morphology of each polymer. (a) PTB7 (b) TQ1 (c) PDTSTPD.

Additionally, there is an apparent sharpening of the dihedral distributions as the chains aggregate into minimum energy configurations without the topological constraints imposed by intermolecular interactions in the melt. It can be seen in **Table B.3** that the fraction of conjugated dihedral angles is increased in the *self-aggregated* morphology when compared to the melt-phase statistics of **Table 3.1**. Specifically, we see that TQ1 has the largest shift towards syn conformations. This effect is further manifested in the average conjugation length of the *self-aggregated* morphology, when compared to the melt. We calculated an average conjugation length of 3.6, 3.2, and 3.4 for PDTSTPD, PTB7, and TQ1 respectively.

Table B.3. Quantitative analysis of dihedral statistics obtained from the *self-aggregated* morphology (T = 300K, p= 1atm).

Polymer	Syn	Anti	Non	Conj
PTB7 (AD)	0.22	0.45	0.32	0.68
PTB7 (DA)	0.38	0.37	0.24	0.76
PTB7 (AVG)	0.3	0.41	0.28	0.72
TQ1	0.69	0.04	0.26	0.74
PDTSTPD	0.42	0.32	0.26	0.74

B.2.8 Bulk Heterojunction Statistics

We found that the presence of $PC_{71}BM$ served to significantly alter the structure of the polymer chains. This effect is apparent in the tangent correlation functions (**Figure B.8**) obtained from the melt-phase bulk heterojunction simulations. We see both a decrease in the folding wavelength and an increase in the persistence length for all three materials when compared to the pure melt.

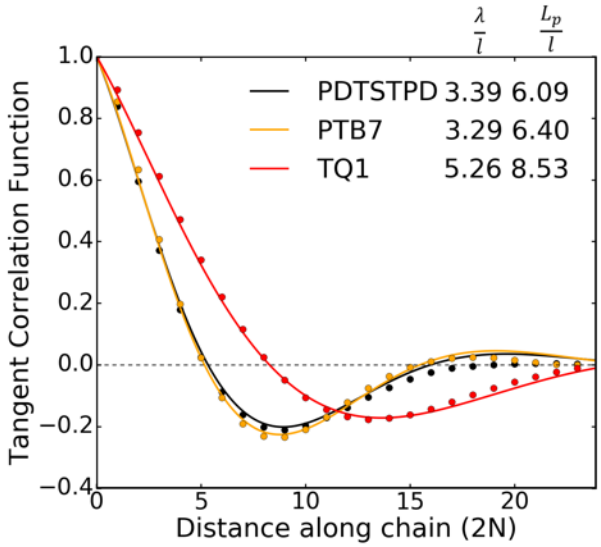

Figure B.8. Tangent correlation functions obtained from melt-phase simulations of the bulk heterojunction composite. (T=600K, p = 1atm).

B.3 Code

The code used for running these simulations is available on the following Git repository: https://github.com/seroot/AROMODEL. This python-based software, is designed specifically to work on XSEDE supercomputing resources and is currently under active development. We encourage any researcher interested in using this software to perform similar simulations to email Samuel Root (seroot@eng.ucsd.edu) for the latest release as well as detailed instructions and eager collaboration.

B.4 Models

The models employed in this paper were originally developed and published by Jackson and coworkers.[8] They fall within the general classification of class2 atomistic force-fields and follow the functional form of the OPLS-AA force-field of Jorgensen and

co-workers.[9] LAMMPS data files containing the topology and force-field parameters for the three polymers (12-mers) and $PC_{71}BM$ are included as a zipped folder.

B.5 Computational Resources

The large-scale simulations presented in this work represent a significant investment in high-performance computing resources. Single chain simulations were all run on single processors. Multi-chain simulations were all run on 24 processors using the MPI implementation of LAMMPS on the Comet supercomputer at the San Diego Supercomputer Center. The simulations proceeded at a rate 1-3 ns/day. Therefore, these simulations took >1 month to perform. In total, three polymers were simulated in three conditions, and each one was repeated three times for error quantification. This resulted in a total of 27 simulations running concurrently on 24 processors each.

B.6. References

(1) Plimpton, S. Fast Parallel Algorithms for Short-Range Molecular Dynamics. *J. Comput. Phys.* **1995**, *117*, 1–19.

(2) Stukowski, A. Visualization and Analysis of Atomistic Simulation Data with OVITO–the Open Visualization Tool. *Model. Simul. Mater. Sci. Eng.* **2010**, *18*, 1–7.

(3) Root, S. E.; Savagatrup, S.; Pais, C. J.; Arya, G.; Lipomi, D. J. Predicting the Mechanical Properties of Organic Semiconductors Using Coarse-Grained Molecular Dynamics Simulations. *Macromolecules* **2016**, *49*, 2886–2894.

(4) Do, K.; Saleem, Q.; Ravva, M. K.; Cruciani, F.; Kan, Z.; Wolf, J.; Hansen, M. R.; Beaujuge, P. M.; Brédas, J.-L. Impact of Fluorine Substituents on π-Conjugated Polymer Main-Chain Conformations, Packing, and Electronic Couplings. *Adv. Mater.* **2016**.

(5) Giomi, L.; Mahadevan, L. Statistical Mechanics of Developable Ribbons. *Phys. Rev. Lett.* **2010**, *104*, 2–5.

(6) Ramachandran, G.N. Ramakrishnan, C. Sasisekharan, V. Stereochemistry of Polypeptide Chain Konfigurations. *J. Mol. Biol.* **1963**, *7*, 95–99.

(7) Pierre-Gilles de Gennes, J. P. *The Physics of Liquid Crystals*; Clarendon, Oxford, 1974.

(8) Jackson, N. E.; Kohlstedt, K. L.; Savoie, B. M.; Olvera de la Cruz, M.; Schatz, G. C.; Chen, L. X.; Ratner, M. a. Conformational Order in Aggregates of Conjugated Polymers. *J. Am. Chem. Soc.* **2015**, *137*, 6254–6262.

(9) Jorgensen, W. L.; Maxwell, D. S.; Tirado-Rives, J. Development and Testing of the OPLS All-Atom Force Field on Conformational Energetics and Properties of Organic Liquids. *J. Am. Chem. Soc.* **1996**, *118*, 11225–11236.

Appendix C

Supporting information for Chapter 4

Measuring the Glass Transition Temperature of Conjugated Polymer Films with UV-vis Spectroscopy

Samuel E. Root‡, Mohammad A. Alkhadra‡, Daniel Rodriquez, Adam D. Printz, and Darren J. Lipomi*

‡ (S.E.R. and M.A.A.) These authors contributed equally.

Department of NanoEngineering, University of California, San Diego, 9500

C.1. Amorphous Conjugated Polymers

This technique did not work well for predominantly amorphous materials. **Figure S1** shows the results obtained for PTB7, PCDTBT, TQ1, and MEH-PPV. These materials are all known to lack significant long-range order.[1–4] While PCDTBT has been demonstrated to self-assemble into to a unique bilayer structure upon thermal annealing, [5] this structure has a notably large π-stacking distance (4.4 Å) and only short-range order is observed in the π-stacking direction. Therefore, the aggregation state of the polymer is not significantly affected by thermal annealing (**Figure S1b**). For TQ1, we found that the UV-Vis spectrum did substantially change with annealing (**Figure S1c)**, however, we found that there was no discernible T_g when the deviation metric was plotted against the annealing temperature.

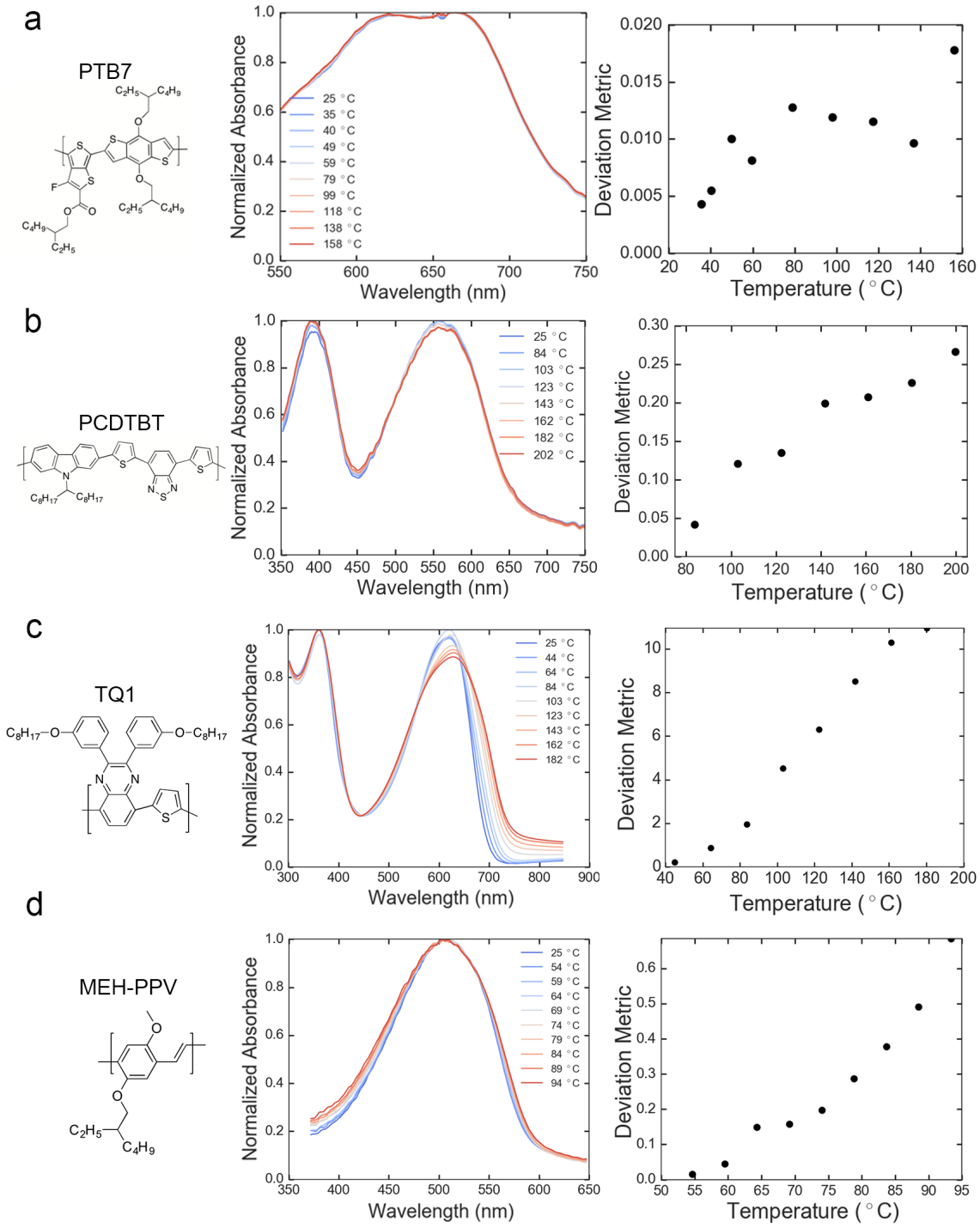

Figure C.1. Results of UV-vis absorption T_g measurement technique for the predominately amorphous donor-acceptor (DA) copolymers (a) PTB7, (b) PCDTBT, (c) TQ1, and (d) MEH-PPV.

C.2 Heat Transfer Calculations

Since the conjugated polymers involved in this study were spin coated onto glass slides, the annealing temperatures of the thin film being tested differed slightly from those of the hot plate surface (**Figure S2**). Therefore, heat transfer correction factor was computed. To find the temperature profile of the glass slide on the hot plate, we made use of the general differential equation (eq. 1) for energy transfer, below, derived from Welty's text[6]:

$$\nabla \cdot k\nabla T + \dot{q} + \Phi = \rho c_v \frac{DT}{Dt} = \rho c_v \left(\frac{\partial T}{\partial t} + \mathbf{v} \cdot \nabla T\right) \quad (1)$$

where T is the temperature of the slide, k is the thermal conductivity of glass, $\dot{q}$ is the volumetric rate of thermal energy generation, Φ is the viscous dissipation, ρ is the density of glass, c_v is the specific heat (under constant volume), and t is time. In order to simplify the above equation, which is essentially a re-statement of the first law of thermodynamics, we made the following assumptions in our analysis:

1) No generation effects $\Rightarrow \dot{q} = 0$.
2) Negligible viscous dissipation $\Rightarrow \Phi = 0$.
3) Negligible fluid motion $\Rightarrow \mathbf{v} = \mathbf{0} \Rightarrow \mathbf{v} \cdot \nabla T = 0$.
4) Passing of enough time to reach steady-state heat transfer $\Rightarrow \frac{\partial T}{\partial t} = 0$.

   Assumptions 3 and 4 give $\frac{DT}{Dt} = \frac{\partial T}{\partial t} + \mathbf{v} \cdot \nabla T = 0$. We are left with $\nabla \cdot k\nabla T = 0$.
5) Constant thermal conductivity (k) of glass $\Rightarrow \nabla \cdot k\nabla T = k\nabla^2 T = 0$, so $\nabla^2 T = 0$.
6) One-dimensional heat transfer in the z-direction $\Rightarrow T = T(z)$. Hence,

$$\nabla^2 T = \frac{\partial^2 T}{\partial z^2} = \frac{d^2 T}{dz^2} = 0 \tag{2}$$

It must be noted that the thermal conductivity of glass does indeed change with temperature, though this change has been neglected for simplicity, and an averaged value was used instead. Assuming Pyrex® glass properties, Welty reports that *k* ranges from 1.09 $\frac{\text{W}}{\text{m·K}}$ at 293 K to 1.45 $\frac{\text{W}}{\text{m·K}}$ at 573 K.[6] Assuming soda lime glass properties, Janssen reports that *k* ranges from 0.9 $\frac{\text{W}}{\text{m·K}}$ to 1.3 $\frac{\text{W}}{\text{m·K}}$ over a similar temperature range.[7] So, $k = 1.15\ \frac{\text{W}}{\text{m·K}}$ was taken as an approximate value over the entire temperature range used in this study. We require two boundary conditions on $T(z)$:

1) Taking $z = 0$ to be the bottom of the glass slide,

$$T(z = 0) = T_{\text{HP}} \tag{3}$$

where T_{HP} is the hot plate temperature.

2) Taking $z = l$ to be the thickness of the glass slide, the heat flux at the glass-air interface is given by

$$q_z = \frac{\dot{Q}}{A} = -k \frac{dT}{dz}\bigg|_{z=l} = h\Delta T \tag{4}$$

where ΔT is the temperature difference between the top surface of the glass slide and the ambient (glovebox) atmosphere, and *h* is the convective heat transfer coefficient computed using convective heat transfer correlations.

Regarding the second boundary condition (eq. 4), we note that a polymer thin film is sufficiently thin to safely assume that its temperature (T_s) is equal to that of the top

surface of the glass slide. Hence, $T(z = l) = T_s$. The temperature profile of the glass slide in the upwards direction from the hot plate, z, can be expressed as follows:

$$T(z) = \alpha z + \beta \tag{5}$$

where α and β are constants of integration; recall, we chose the z-axis pointing upwards with $z = 0$ at the surface of the hot plate (**Figure S2a**).

In light of the linear temperature profile (eq. 5), the first boundary condition (eq. 3) gives

$$T(z = 0) = \beta = T_{HP} \tag{6}$$

and the second (eq. 4) gives

$$-k \left.\frac{dT}{dz}\right|_{z=l} = -k\alpha = h(T_s - T_\infty) \approx h(T_{HP} - T_\infty) \tag{7}$$

where T_∞ is the bulk fluid temperature, measured to be 25 °C. We approximated T_s with T_{HP} to avoid having to iterate (recall, T_s is unknown). It follows that

$$\alpha = \alpha(T_{HP}) = \frac{h}{-k}(T_{HP} - T_\infty) \tag{8}$$

To compute α, we must first compute h using natural (free) convection correlations for a horizontal plate geometry with the hot surface facing up. Fluid properties are temperature dependent, and so the properties involved in the correlations were evaluated at the 'average' temperature $T_f = \frac{1}{2}(T_s + T_\infty) \approx \frac{1}{2}(T_{HP} + T_\infty)$. Although annealing occurred in a nitrogen atmosphere (i.e., in the glovebox), the properties of the ambient fluid were approximated with those of air (≈ 78%$_{vol}$ N_2), which are more readily available in the literature.[6] The following correlation for laminar heat transfer from a horizontal plate, developed by Raithby and Hollands,[8] was used to determine the average Nusselt number $\overline{\mathrm{Nu}}_{L^*}$:

$$\overline{\mathrm{Nu}}_{L^*} = \frac{0.560\ \mathrm{Ra}_{L^*}^{1/4}}{[1 + (0.492/\mathrm{Pr})^{9/16}]^{4/9}}, \qquad 1 < \mathrm{Ra}_{L^*} < 10^7 \tag{9}$$

where a characteristic length scale $L^* = Area/Perimeter$ is used in the Rayleigh (Ra) and Nusselt numbers, the Prandtl number $\mathrm{Pr} = \frac{\nu}{\alpha} = \frac{\mu/\rho}{k/c_p\rho} = \frac{c_p\mu}{k}$, μ is the dynamic viscosity, v is the kinematic viscosity, c_p is the specific heat (under constant pressure), $\mathrm{Ra}_{L^*} = \mathrm{Pr}\times\mathrm{Gr}_{L^*}$ and the Grashof number $\mathrm{Gr}_{L^*} = \frac{g\beta(T_{\mathrm{HP}}-T_\infty){L^*}^3}{\nu^2}$ (we assumed $T_\mathrm{s} \approx T_{\mathrm{HP}}$ for Gr_{L^*}), g is the acceleration due to Earth's gravity, and β is the coefficient of thermal expansion.[6,8] Also, the (Sail Brand) glass slides used in the study were 1 in long × 1 in wide and had an average thickness $l = 1.1$ mm. Raithby and Hollands suggested a correction for thick boundary layers (i.e., $\overline{\mathrm{Nu}}_{L^*} < 10$):

$$\overline{\mathrm{Nu}}_{\mathrm{corrected}} = \frac{1.4}{\ln\,(1 + 1.4/\overline{\mathrm{Nu}}_{L^*})} \tag{10}$$

It must be noted that many of the aforementioned parameters are highly temperature dependent, and so $\overline{\mathrm{Nu}}_{L^*}$, h , and α (eq. 8) are ultimately functions of T_{HP}. We computed h using the definition of the Nusselt number shown below,

$$\overline{\mathrm{Nu}}_{\mathrm{corrected}} \equiv \frac{hL^*}{k} \Rightarrow h = \frac{\overline{\mathrm{Nu}}_{\mathrm{corrected}}\times k}{L^*} \tag{11}$$

Substituting h into eq. 8, we were able to compute α and thus T_s (eq. 12) as functions of T_{HP}:

$$T_\mathrm{s} = T(z = l) = \alpha l + T_{\mathrm{HP}} \tag{12}$$

Plotting T_s against T_{HP} over an appropriate temperature range (55 °C to 255 °C), we were able to obtain a simple, linear correction factor for any value of T_{HP} (**Figure S2b**). As

mentioned in the full paper, the correction factor, although slight, was applied in the analysis of the UV-vis absorption spectra.

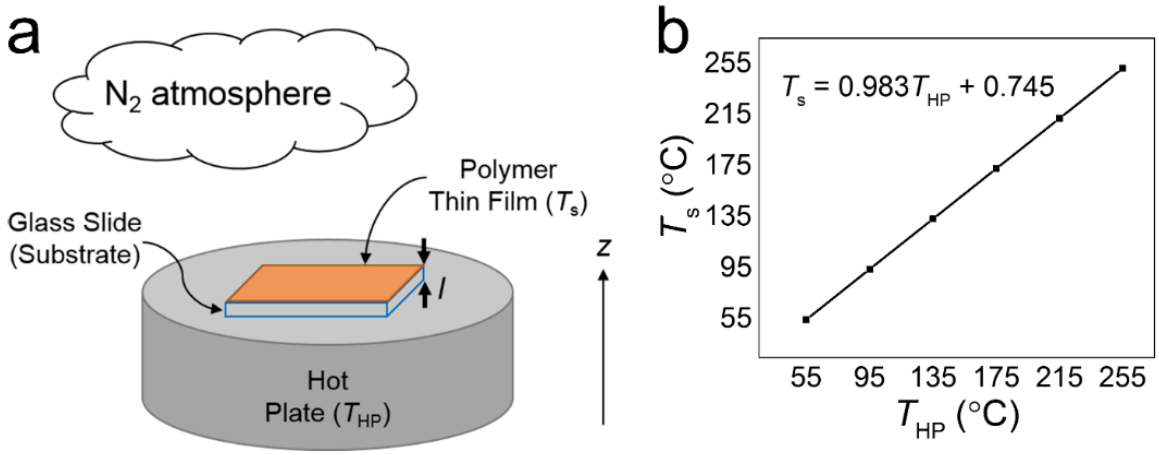

Figure C.2. Heat transfer corrections. (a) Conjugated polymer was spin-coated onto a glass slide (substrate) then placed onto a hot plate for annealing. (b) Heat transfer calculations produced a simple, linear relation between the polymer thin film temperature, T_s, and the hot plate temperature, T_{HP}.

C.3 Data Analysis

All data analysis was performed using the Python programming language. A script was developed to read in a list of .csv files containing the UV-Vis absorption spectra after annealing at the film at various temperatures. The deviation metric was computed and plotted against annealing temperature. A bilinear regression algorithm was implemented to determine the temperature that the transition occurred. The algorithm works by sweeping through all possible bilinear regressions and finding the best fit. The quality of each bilinear fit is judged by the sum of the R^2 weighted by the number of data points (i, j) associated with each line (a, b): $i * R_a^2 + j * R_b^2$. An example is shown in **Figure S3**. The code used to perform this analysis is openly available at https://github.com/seroot/UV_VIS_TG.

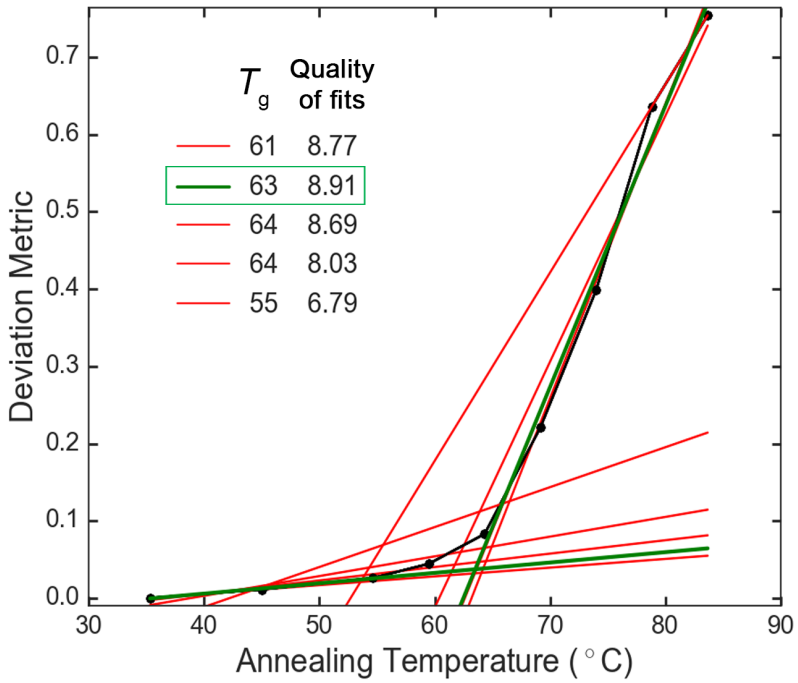

Figure C.3. Bilinear regression algorithm applied to P3BT. Plot showing various possible bilinear fits to the data, the green line indicates the best fit.

Although the T_g was obvious to determine from the deviation metric in almost all cases, PDTSTPD did not have as distinct of a transition as the other materials. In this case, it was important to use the algorithm to find the optimal bilinear regression. An example of the output is shown in **Figure S4**.

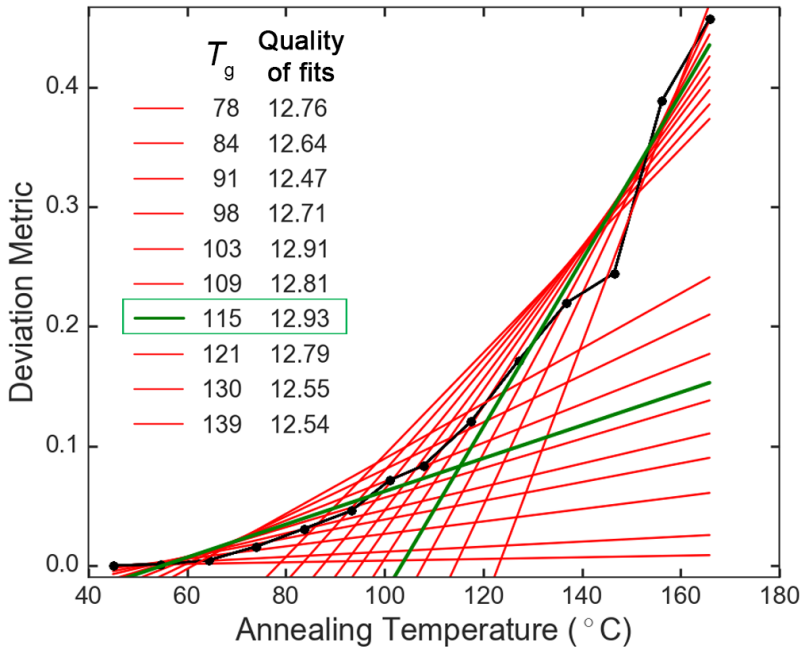

Figure C.4. Bilinear regression algorithm applied to PDTSTPD. Plot showing various possible bilinear fits to the data, the green line indicates the best fit.

C.4 Effect of Plasticizer

Solvent additives such as 1,8-diioodoctane (DIO) are ubiquitously used in the OPV literature as a facile processing strategy for controlling morphology and improving device performance.[9] The DIO is expected to act as a plasticizer to reduce the T_g, and so we tested the ability of our technique to measure this plasticization effect. DIO (2% by volume) was added to the P3BT:PCBM bulk heterojunction. As shown in **Figure S5**, the use of this additive resulted in a 20 ºC decrease in the T_g.

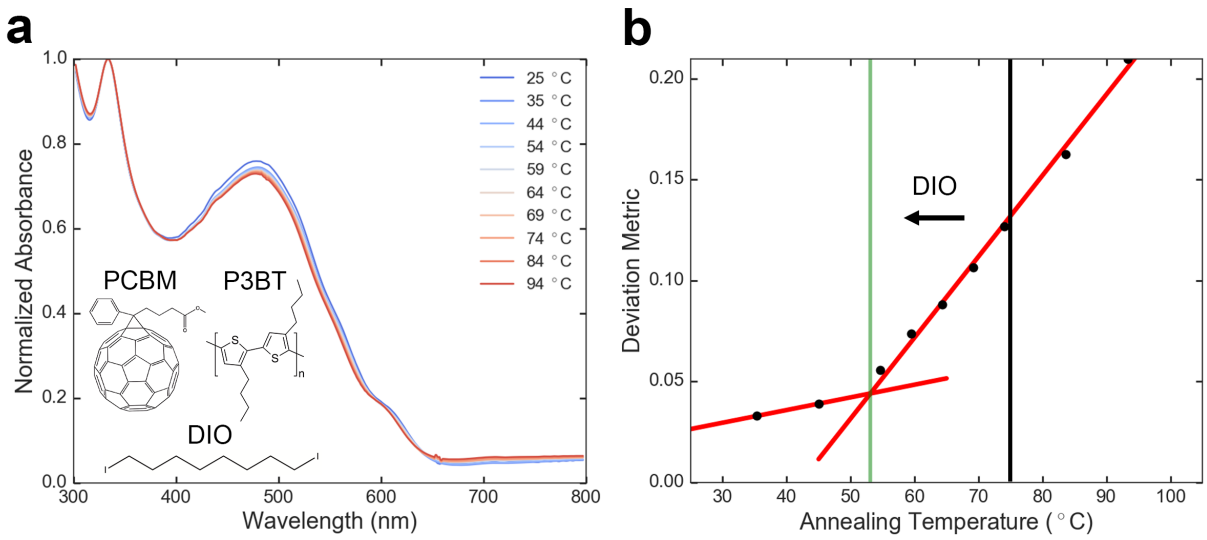

Figure C.5. Effect of processing additive, DIO, on the T_g of a P3BT:PCBM bulk heterojunction thin film. (a) Evolution of the thin-film absorption with thermal annealing. (b) Deviation metric as a function of annealing temperature. The addition of DIO to the bulk heterojunction results in a 20 ºC decrease in the T_g.

C.5 References

(1) Hsiao, Y. C.; Wu, T.; Li, M.; Qin, W.; Yu, L.; Hu, B. Revealing Optically Induced Dipole-Dipole Interaction Effects on Charge Dissociation at Donor: Acceptor Interfaces in Organic Solar Cells under Device-Operating Condition. *Nano Energy* **2016**, *26*, 595–602.

(2) Cho, S.; Seo, J. H.; Park, S. H.; Beaupré, S.; Leclerc, M.; Heeger, A. J. A Thermally Stable Semiconducting Polymer. *Adv. Mater.* **2010**, *22*, 1253–1257.

(3) Wang, E.; Hou, L.; Wang, Z.; Hellström, S.; Zhang, F.; Inganäs, O.; Andersson, M. R. An Easily Synthesized Blue Polymer for High-Performance Polymer Solar Cells. *Adv. Mater.* **2010**, *22*, 5240–5244.

(4) Yang, C. Y.; Heeger, A. J. Morphology of Composites of Semiconducting Polymers Mixed with C60. *Synth. Met.* **1996**, *83*, 85–88.

(5) Lu, X.; Hlaing, H.; Germack, D. S.; Peet, J.; Jo, W. H.; Andrienko, D.; Kremer, K.; Ocko, B. M. Bilayer Order in a Polycarbazole-Conjugated Polymer. *Nat. Commun.* **2012**, *3*, 795.

(6) Welty, J. R.; Wicks, C. E.; Wilson, R. E.; Rorrer, G. L. *Fundamentals of Momentum, Heat, and Mass Transfer*; 2008.

(7) Spalding, D. B. *Handbook of Heat Transfer*; 1975; Vol. 18.

(8) Iv, J. H. L.; Lienhard, J. H. A Heat Transfer Textbook. *J. Heat Transfer* **1986**, *108*, 198.

(9) Shao, M.; Keum, J. K.; Kumar, R.; Chen, J.; Browning, J. F.; Das, S.; Chen, W.; Hou, J.; Do, C.; Littrell, K. C.; Rondinone, A.; Geohegan, D. B.; Sumpter, B. G.; Xiao, K. Understanding How Processing Additives Tune the Nanoscale Morphology of High Efficiency Organic Photovoltaic Blends: From Casting Solution to Spun-Cast Thin Film. *Adv. Funct. Mater.* **2014**, *24*, 6647–6657.